High temperature volcanic gas uptake by rhyolite

Ana S. Casas Ramos

München, 2020

High temperature volcanic gas uptake by rhyolite

Ana S. Casas Ramos

Dissertation zur Erlangung des Doktorgrades
an der Fakultät für Geowissenschaften
der Ludwig-Maximilians-Universität
München

vorgelegt von
Ana S. Casas Ramos
aus Chiapas, Mexiko

München, den 4. März 2020

Erstgutachter: Prof. Dr. Donald B. Dingwell

Zweitgutachter: Dr. Fabian B. Wadsworth

Tag der mündlichen Prüfung: 21. September 2020

A mis padres, Miguel Ángel y Silvia Guadalupe.
Con mucho amor les dedico éste y todos mis logros.

Zusammenfassung

Das Hauptziel dieser Doktorarbeit ist die Untersuchung der komplexen und nicht ausreichend beschriebenen physikalisch-chemischen Wechselwirkungen, welche während vulkanischer Aktivität zwischen Asche und heißen Gasen auftreten. Gas-Asche-Wechselwirkungen sind allgegenwärtig in explosiven vulkanischen Eruptionen. Abhängig von der Magmazusammensetzung und Grad der Magmafragmentation werden verschiedene Mengen vulkanischer Gesteine und fragmentierter Magma (Asche und Pyroklasten), zusammen mit einer Mischung von heißen Gasen (im wesentlichen H_2O, CO_2, SO_2, HCl, H_2S und HF), produziert und in die Atmosphäre ausgeworfen. Im allgemeinen werden die größten Eruptionen, also diejenigen, die potentiell großskalige Auswirkungen auf die Umwelt hervorrufen, von Magmen mit hohem Gehalt an volatilen Elementen und Silizium (>65 SiO_2 Gew.%) erzeugt. SiO_2-reiche Magmen verhindern das effiziente Ausgasen flüchtiger Elemente. Dies führt zu einem Überdruck im über dem Magmareservoir liegenden Pfropfens und somit zu explosiven Eruptionen nach ausreichendem Druckaufbau.

Die Dynamik dieser Eruptionen ist typischerweise sub-plinisch oder plinisch und verbunden mit hochdifferenzierten kalk-alkalinen oder alkalinen Magmen. Bei der Eruption wird das hochviskose Magma durch die entmischten Gase rasch beschleunigt, was zu einer sehr effizienten Magmafragmentation (d.h. große Produktion feiner Asche) führt. In weiterer Folge bildet sich eine Aschewolke, welche, wenn sie zusammenfällt, pyroklastische Ströme erzeugt. In beiden Szenarien führt konstanter Kontakt zwischen Asche (<2 mm) und Gasen zur Entwicklung heterogener Reaktionen. Die entmischten Gase werden dabei von Aschepartikeln in Form von löslichen Produkten (z.B. Sulfat-, Halid- und Fluoridsalze) auf Ascheoberflächen "eingefangen". Das Auftreten von Gasaufnahme durch Aschepartikel ist ein bekanntes Phänomen und wird vorwiegend durch das chemische Auslaugen von Tephraablagerungen nachgewiesen. Dies wird auch häufig im vulkanischen Monitoring angewandt, jedoch sind die Mechanismen und Abläufe der Gasaufnahme ausreichend verstanden und es existieren keine Vorhersagemethoden zur Bestimmung der Zeitabhängigkeit der Aufnahme von Gas.

Bisher hat sich die Forschung um das Auftreten von Gasaufnahme zu untersuchen fast ausschließlich auf Asche-Gas-Wechselwirkungsprozesse bei niedrigen Temperaturen fokussiert. In diesem Fall reagieren vulkanische Gase zuerst mit atmosphärischem Wasser unter Bildung von Säuren (z.B. H_2SO_4), welche wiederum auf die Oberfläche der Asche kondensieren. Diese Säuren lösen zuerst das Silikatnetzwerk und Salze lagern sich nach der Evaporation des Wassers ab. Dennoch haben neue Studien experimentell gezeigt, daß Asche-Gas-Wechselwirkungen bei hohen Temperaturen (>200 °C) sehr effizient als Senke für Gase wirken können. Lösliche Salze können sich hier an der Oberfläche bilden ohne Kondensation von Gasen und Auflösung von Asche. Stattdessen besteht eine direkte Reaktion zwischen Festkörper und Gas. Eine weitere wesentliche Erkenntnis dieser Studien war die Identifikation des Glases als wichtigste in die Gasaufnahme involvierte reaktive Aschekomponente. Dies steht im Widerspruch zum allgemeinen Glauben, daß Mineralkomponenten der Asche hauptsächlich an der Gasaufnahme beteiligt sind. Inspiriert durch diese Ergebnisse und mit dem Ziel, die Aufnahme vulkanischer Gase durch Glas bei hohen Temperaturen zu untersuchen, habe ich einen umfangreichen experimentellen Aufbau zum Test der Effizienz der Abtrennung von zwei der wichtigsten vulkanischen Gase, SO_2 and HCl, an rhyolitischer (SiO_2-reicher) Gläser entwickelt.

Es wurden Experimente zum Test der Auswirkungen von Temperatur, Einwirkungsdauer, Korngrößenverteilung, Luftfeuchtigkeit und chemischer Zusammensetzung auf die Aufnahme von SO_2 und HCl entworfen und durchgeführt. Insgesamt wurden zu diesem Zweck 563 Experimente durchgeführt, und die gewonnenen Proben wurden mittels Ionenchromatographie, Elektronenstrahl-Mikrosonde, Rasterelektronenmikroskopie, Raman-Spektroskopie, Berechnung der Eisenmenge und Analysen der Verteilung der Teilchengröße charakterisiert. Die Ergebnisse der SO_2-Experimente haben das Auftreten von Gasaufnahme bei hohen Temperaturen bestätigt Es wurde festgestellt, daß diese durch Überschreiten des Glasübergangs der hier getesteten Rhyolite verstärkt wird. Tatsächlich führte die höchste experimentelle Temperatur (800 °C) zur effizientesten SO_2-Abtrennung. Es wurde beobachtet, daß aufgrund direkter Reaktionen zwischen SO_2 und dem in der Glasmatrix vorhandenem Kalzium die SO_2-Aufnahme nahezu ausschließlich durch die Bildung von $CaSO_4$ (Anhydrit) auf den Partikeloberflächen geschieht.

Die Ergebnisse der bei hohen Temperaturen durchgeführten HCl-Experimente haben gezeigt, daß nur eine geringe HCl-Aufnahme zu beobachten ist und es daher nicht relevant scheint diesen Prozess für diese spezielle Glaszusammensetzung weiter zu untersuchen. Die Charakterisierung von SO_2-behandelten Rhyolitpartikeln wies klar darauf hin, daß Ca^{2+}-Diffusion der Mechanismus ist, durch den Kationen bereitgestellt werden und die Bildung von $CaSO_4$ aufrechterhält. Die Zugabe von Wasserdampf zum Gasgemisch wirkt sich nicht auf diesen Prozeß aus. Auch die Bildung von Na_2SO_4 und K_2SO_4 wurde festgestellt, aber im Vergleich zu $CaSO_4$ in vernachlässigbaren Mengen. Dies deutet darauf hin, daß obwohl Na^+ und K^+ auch durch Diffusion mobilisiert werden, diese Kationen nur eine untergeordnete Rolle bei der SO_2-Aufnahme spielen, besonders unter wasserfreien Bedingungen.

Die Zeit- und Temperaturserie der Experimente erlaubte die Berechnung temperaturabhängiger Diffusionsgleichungen für Ca, Na und K in rhyolitischen Gläsern. Dies kann weiter angewandt werden um die experimentellen Daten für jede Temperatur zu skalieren. Außerdem wird hier vorgeschlagen, daß dieser Prozess nicht auf vulkanische Wolken oder die Umgebung pyroklastischer Ströme beschränkt werden kann, sondern, daß das passive Ausgasen zerklüfteter vulkanischer Kuppeln auch eine mögliche Umgebung für eine präeruptive SO_2-Aufnahme bietet, aufgrund der Gas -Asche-Wechselwirkungen bei hohen Temperaturen durch mit Asche gefüllten Kluftnetzwerks des ausgasenden magmatischen SO_2 und der relativ langen Verweildauern (Tage bis Jahre) von Kuppeln, während.

Die wesentlichen Schlußfolgerungen dieser Doktorarbeit sind, (1) daß Kalzium-Diffusion als der begrenzende Prozeß, der die SO_2-Aufnahme durch rhyolitisches Glas bei hohen Temperaturen kontrolliert, bestätigt wurde, (2) daß sich die Auswirkungen steigender Luftfeuchtigkeit im Gasgemisch auf die Kalzium-Diffusion als vernachlässigbar herausgestellt haben, und (3) daß die Beweglichkeit einwertiger Kationen stark eingeschränkt ist, wenn Fe^{2+}-Oxidation stattfindet. Aufgrund des Vorkommens von Kalzium und Eisen in vulkanischer Asche und der dampfreichen Natur vulkanischer Emissionen sind diese Erkenntnisse von großer Wichtigkeit, nicht nur weil sie zur Verbesserung unseres Verständnisses von Asche-Gas-Reaktionen bei hoher Temperatur beitragen, sondern auch weil sie die für die Entwicklung von Modellen zur Vorhersage der Gesamtmasse von Schwefel, der

während vulkanischer Eruptionen effektiv abgetrennt werden kann, notwendigen Eingabevariablen deutlich vereinfachen. Dies könnte für die Beurteilung der verschiedenen physikalischen, chemischen und biologischen Effekte, die vulkanische Eruptionen auf verschiedene aufnehmende Umgebungen haben, besonders nützlich sein. Zuletzt können Abschätzungen des globalen Budgets des geochemischen Schwefelkreislaufs möglicherweise von der Berücksichtigung der Abtrennung von Schwefel bei hoher Temperatur, die in vergangener, aktueller oder zukünftiger großer vulkanischer Eruptionen stattfindet, profitieren.

Abstract

The overarching aim of this thesis is to investigate the complex and under-constrained physicochemical interactions that can occur between ash and hot gas during volcanic activity. Gas-ash interactions are ubiquitous within explosive volcanic eruptions where, depending on the magma composition and efficiency of magma fragmentation, diverse quantities of volcanic rocks and fragmented magma (ash and pyroclasts) are produced and ejected into the atmosphere, together with a hot mixture of gases (principally H_2O, CO_2, SO_2, HCl, H_2S and HF). In general, the largest eruptions and therefore, those capable of inducing large-scale environmental effects on earth, are generated by volatile-rich and silica-rich (>70 SiO_2 wt.%) magmas. SiO_2-rich magmas impede efficient volatile outgassing resulting in overpressure of the overlying plug of the magma reservoir, which yields to very explosive eruptions. The dynamics of these eruptions is typically sub-Plinian or Plinian and is associated with highly differentiated calk-alkaline or alkaline magmas. Upon eruption, the highly viscous magma is rapidly accelerated by the exolved volatiles, resulting in very efficient magma fragmentation (i.e., large production of fine ash), followed by formation of a volcanic plume, which upon collapse, generates pyroclastic flows.

In both scenarios, constant contact between ash (D<2 mm) and gases, results in the development of heterogeneous reactions, by which exolved gases are "sequestrated" by ash particles and form soluble products (e.g., sulfate- halide- and fluoride-salts) on ash surfaces. Occurrence of gas uptake by ash is a well-known phenomenon, primarily detected by leaching of fallout ash and has been widely employed as a volcanic monitoring tool. However, the mechanisms and kinetics by which gas uptake occurs are not well understood, and no predictive tools exist to solve for the time-dependent scavenging of gas. Furthermore, the research to date that has investigated gas uptake occurrence, has almost exclusively been focused on low temperature ash-gas interactions processes, where volcanic gases first react with atmospheric water to form acids (e.g., H_2SO_4), which condense onto the ash surface, dissolve the silicate network and deposit surficial salts upon water evaporation.

Nevertheless, recent studies have experimentally shown, that high temperature (>200 °C) ash-gas interactions can very efficiently act as a sink for gases, by forming surficial soluble salts without condensation of gases and dissolution of ash, but instead by direct solid-gas reactions. Another crucial finding of these studies has been the recognition of the glass as the main reactive ash-component involved in gas uptake, which contrasts with the common belief that, it was the mineral component of ash that would mostly participate in gas uptake reactions. Inspired by these results and aiming to contribute to investigate high temperature volcanic gas uptake by glass, I developed an extensive experimental campaign aimed to test the potential of rhyolitic (SiO_2-rich) glasses to sequestrate two of the main volcanic gases exolved upon eruptions, SO_2 and HCl. Here, experiments were designed and performed to test the effects that temperature, exposure time, grain size distribution, humidity, and chemical composition had on SO_2 and HCl uptake.

A total of 563 experiments were conducted for this purpose and the resulting samples were characterized by ion chromatography, electron probe micro-analyzer, scanning electron microscopy, Raman spectrometry, bulk iron determination, and particle size distribution analyses. Results the SO_2 experiments, confirmed occurrence of gas uptake at high temperatures and was noticed to be enhanced by crossing the glass transition of the rhyolites tested here. In fact, the highest experimental temperature (800 °C) yielded the most efficient SO_2 sequestration. SO_2 uptake was observed to occur almost exclusively by formation of $CaSO_4$ (anhydrite) grown on the particle surfaces, due to direct reactions between SO_2 and calcium present in the bulk glass network.

Results of the high temperature HCl experiments showed that only minor HCl uptake occurs, and therefore it might not be relevant to further investigate this process for this particular glass composition. Characterization of SO_2-treated rhyolite particles clearly indicated that Ca^{2+} diffusion is the cation-supply mechanism that sustains $CaSO_4$ formation and that addition of water vapour to the gas mixture does not affect this process. Formation of Na_2SO_4 and K_2SO_4 were also detected, but only in negligible quantities, when compared to $CaSO_4$. This suggests that, although Na^+ and K^+ are also mobilized by diffusion, these cations play only a minor role in SO_2 uptake specially under anhydrous conditions.

Under hydrous conditions however, mobilization of Na^{+} and of K^{+} was observed to be higher than under anhydrous conditions, yet, still minor when compared to Ca^{2+}. Oxidation of iron Fe^{2+} (to Fe^{3+}) was observed to occur upon increasing temperatures, which seemed to coincide with the decreased mobility of both Na^{+} and K^{+} at T>600 °C and at T>700 °C under anhydrous and hydrous conditions, respectively. This was interpreted as a change in the structural role of monovalent cations above the glass transition from network modifiers to a charge compensating cations required by Fe^{3+} tetrahedra. The oxidation-limited mobility of monovalent cations observed here is of relevance, given the fact that Fe is an intrinsic component of volcanic ash. The time- and temperature-series of experiments, allowed the determination of temperature-dependent diffusion laws for Ca, Na and K in rhyolitic glasses, which can be further applied to scale the experimental data for any temperature.

Here is also proposed that, fractured volcanic domes provide feasible environments for pre-eruptive SO_2 uptake, given the high temperatures of degassed magmatic SO_2, and the relative long residence times of domes (from days to years), which allows longer timescales for interactions between SO_2 and ash-filled fracture networks. The main conclusions of this thesis are (1) that calcium diffusion was confirmed to be the limiting-process controlling high temperature SO_2 uptake by rhyolitic glass, (2) that the effect of increasing humidity in the gas mixture showed to be negligible to calcium diffusion (thus, to SO_2 uptake) and (3) that mobility of monovalent cations is strongly inhibited when Fe^{2+} oxidation takes place.

The ubiquity of calcium and iron in volcanic ash and the water vapour-rich nature of volcanic gas emissions, make these findings of great importance, not only because they contribute to the improvement of our understanding on high temperature ash-gas reactions, but also because they considerably simplify the input variables necessary for the development of models aimed to predict the total mass of sulfur that can be effectively sequestrated by ash during volcanic eruptions. This could be especially useful for better assessment of the various physical, chemical and biological effects that volcanic eruptions have on diverse receiving environments. Finally, estimations of the global budget of the geochemical sulfur cycle can potentially benefit by considering high temperature sulfur sequestration of past, current and future large volcanic eruptions.

Contents

List of Figures

List of Tables

Acknowledgments

This PhD has been much more exciting, challenging and gratifying than I thought it would be. Along my journey, a lot of people have provided me with support, care and advice that helped me to fulfill my goals. Here, I´d like to say thanks to all of you.

First of all, I would like to express my gratitude to Prof. Donald B. Dingwell, who believed in me, let me be part of the legendary LMU volcanology group, encouraged me to develop my research to its fullest, and who was always there, both as a supervisor and a friend. Thanks Don.

To Corrado Cimarelli, who helped build the bridge for me to come to Munich. Thanks for meeting me in Vienna in 2015 and for your constant support and care during these four years, Grazie caro amico! To Paul Ayris, who introduced me to the fascinating world of ash-gas reactions and who paved the way for this research. I´ve kept AGAR busy, but have been kind to him. To Fabian Wadsworth, whose contagious enthusiasm towards my work inspired me to always go further. Thanks for nurturing my research in ways only you could. To Pierre Delmelle, whose pioneering ideas fostered some of the research that have thrilled me during my PhD. Your feedback and advice have constantly improved my work.

To Elena Maters, my science sister and dear friend. Thanks for sharing ideas and kind words whenever I needed them. I´m very happy that we´ve crossed ways and hope to keep doing so in the future. To Jeremie Vasseur, whose commitment to improve the processing of my data contributed to the applicability of my results. Special thanks to the best group, Mat, Leti, Pancho and Damien; your friendship, support and silliness has filled my PhD with caring and happy moments. I´m forever thankful to you. #GroupHug, #CompositionMatters, #8to8, #TeamChocolatine. To my past and current officemates, Cristian, Shanjie, Lukas and Jieyan, for your company, patience and friendship. Cristian, you taught me to be tougher and unapologetic, so thanks for nothing (just kidding, thanks for your kind ways). Shanjie, I will always be grateful for the positivity you brought to our office every day. Lukas and Jieyan, you´ve been great company xiéxie/herzliches Dankscheen you both.

To all members of the mineralogy department, who have contributed to make my PhD more pleasant. Thanks to Loco Lukas, Jenny, Joan, Basti, Michaela, Christina, Sid, little Kai, Adrian, Caron, Zeynep, Taylor, Markus, Valeria, Ulli, big Kai, Betti, Dirk, Joa, Pablo, Guillem, Mila, Danilo, Arianna, Joanna, Andre, Tim, Rosa, Ira, Nataliya and many others for making this department so colorful and friendly.

To the national council for science and technology of México (CONACyT) and to the german academic exchange service (DAAD), who awarded me with the grant (Nr.409903) that funded this research. To Maria Aurora Armienta, Servando de la Cruz Reyna, Miguel Alatorre, Georgina Fernandez, Raymundo Martinez, Jesús Solé, Peter Haase, Johannes Köck and Romy Grimm for their support and encouragement during my grant application process.

Nun mal auf Deutsch, ich würde mich auch gern bei der Mensa Gruppe dafür bedanken, daß ihr mir den richtigen Weg zum Mittagsessen gezeigt habt(!) und für eure wunderbare Freundschaft. Michi, Diana, Iphi, Aline und Steffi danke euch für all die schöne Zeiten. Ich bedanke mich auch ganz herzlich bei Antonia Wimmer und Thomas Dorfner, die meine Arbeit im Chemielabor glücklicher gemacht haben.

Liebe Rike und Margot, eure Hilfsbereitschaft und Freundlichkeit hab´ ich immer sehr geschätzt. Herzliches dank auch zu den Mitarbeiter der Werkstatt: Markus, Hilger und Stefan für Eure Freundschaft und technische Hilfe. Günter und Carola Hesberg danke sehr für eure Unterstützung und wahre Freundschaft in guten und schwierigen Zeiten. Filomena und Mimoza, danke für all die freundlichen Unterhaltungen die wir hatten, ein nettes Lächeln von euch hat mir immer gutgetan. Zu meinen Freunden vom Goethe Institut in Mannheim, herzliches Dankeschön für die wunderbare sechs Monate dort. Auch bei den Ukulele Freunden, die ich in München getroffen hab, würde ich mich sehr für eure tolle Musik und fürs gemeinsame Spielen bedanken.

Ich bedanke mich auch ganz herzlich bei dem Freistaat Bayern und der Stadt München, deren Gastfreundlichkeit, inklusive Gesellschaft, traumhaften Landschaften, spannende Kultur und ausgezeichnetes Bier mein Promotionserlebnis genussvoller gemacht haben(!). Oda anders gsogt, vagelt´s God fia de scheene zeidn, i hob mi do dahoam gfuit.

Lieber Eduard, danke, daß du immer durch dick und dünn für mich da warst. Deine bedingungslose und liebevolle Unterstützung bei jedem Schritt meiner Promotionszeit hat mir sehr viel bedeutet. Danke für alles.

De vuelta a mi México lindo y querido, gracias a mis amigos de Chiapas y del D.F., Luna, Laura, Oli, Pechá, Thalía, Toñito, Ara, Atzin y muchos otros, por no olvidarse de mi, y estar al pendiente de mis aventuras en Baviera.

Más que a nadie, quiero darle gracias a mi maravillosa familia; a mis padres Miguel Ángel y Silvia Guadalupe, cuyo amor, paciencia y ánimos me han acompañado cada día y cuyo ejemplo de vida ha nutrido mi espíritu y me ha llenado de inspiración para desarrollarme con felicidad y plenitud en la vida. Los amo y admiro más allá de lo que las palabras pueden expresar. También, muchas gracias a mi hermano Migue y a mi cuñada Shenny por su cariño incondicional y constantes palabras de aliento.

Preamble

Some components of this thesis appear in published or submitted journal articles, and other components are in preparation for publication. These include:

- **Casas, A.S.,** Wadsworth, F.B., Ayris, P.M., Delmelle, P., Vasseur, J., Cimarelli, C. and Dingwell, D.B., 2019. SO_2 scrubbing during percolation through rhyolitic volcanic domes. Geochimica et Cosmochimica Acta, 257, pp.150-162. https://doi.org/10.1016/j.gca.2019.04.013.

- Maters, E.C., Cimarelli, C., **Casas, A.S.,** Dingwell, D.B., Murray, B.J., 2020. Volcanic ash ice-nucleating activity can be enhanced or depressed by ash-gas interaction in the eruption plume. Earth and Planetary Science Letters, 551,2020, https://doi.org/10.1016/j.epsl.2020.116587.

- **Casas, A.S.,** Wadsworth, F.B., Vasseur, J., Ayris, P.M., Delmelle, P., Hess, K.-U., Kaliwoda, M., Cimarelli, C., and Dingwell, D.B. Submitted. Rapid iron oxidation during high-temperature reactions between glassy volcanic ash and SO_2 gas. Under consideration at Chemical Geology.

- **Casas, A.S.,** Hornby, A., Cimarelli, C., Dingwell, D.B. In preparation. A multidisciplinary protocol for quantitative characterization of soluble salts on ash particles. For submission to Chemical Geology.

- Wadsworth, F.B., Vasseur, J., **Casas, A.S.,** Ayris, P.M., Delmelle, P., Hess, K.-U., and Dingwell, D.B. In revision. Time-dependent high temperature reactions between polydisperse rhyolite volcanic ash and gas. Under consideration at American Mineralogist.

As part of these collaborative works, I can confirm that I have performed all experiments and all analytical work, and taken the leading role in the data analysis and interpretation. The other collaborators on these projects provided insights, supervision, additional supporting analysis of data or analytical results to confirm my results, and technical assistance using microscopy or spectroscopy facilities.

In all cases where I am first author, the work is my own and represents a core component of this thesis. During my PhD I have also contributed to other studies in a leading or supporting role, which includes:

- Tomašek, I. Damby, D.E., Horwell, C.J., Ayris, P.M., Delmelle, P., Ottley, C.J., Cubillas, P., **Casas, A.S.,** Bisig, C., Petri-Fink, A., Dingwell, D.B., Clift, M.J., Drasler, B. and Rothen-Rutishauser, B. 2019. Assessment of the potential for in-plume sulphur dioxide gas-ash interactions to influence the respiratory toxicity of volcanic ash. Environmental Res.Volume 179, Part A,108798. https://doi.org/10.1016/j.envres.2019.108798.

- Wadsworth, F., Unwin, H., Vasseur, J., Kennedy, B., Holzmueller, J., Scheu, B., Witcher, T., Adolf, J., Cáceres, F., **Casas, A.S.,** et al. 2018. Trashcano: Developing a quantitative teaching tool to understand ballistics accelerated by explosive volcanic eruptions. Volcanica. 1(2), pp. 107-126. https://doi.org/10.30909/vol.01.02.107126

- Mueller, S.B., Ayris, P.M., Wadsworth, F.B., Kueppers, U., **Casas, A.S.,** Delmelle, P., Taddeucci, J., Jacob, M., and Dingwell, D.B. 2017. Ash aggregation enhanced by deposition and redistribution of salt on the surface of volcanic ash in eruption plumes. Scientific reports 7, 45762. https://doi.org/10.1038/srep45762.

- **Casas, A.S.,** Armienta, M.A., Ramos, S. 2016. Sulfur speciation with high performance liquid chromatography as a tool for El Chichón volcano, crater lake monitoring. Journal of South American Earth Sciences, 72, 241-249. https://doi.org/10.1016/j.jsames.2016.09.001.

Chapter 1

Gas uptake by ash during eruptive processes

1.1 Introduction

In this chapter, a review of the studies that first noticed the occurrence of gas uptake by ash during explosive volcanic activity, will be presented. The development of our understanding of volcanic gas uptake processes from qualitative observations (e.g., Lacroix, 1907) to quantitative measurements (e.g., Witham et al., 2005) will be analyzed. Finally, the relevance of investigating ash-gas interactions will be stressed from the point of view of the various short- and long-term environmental and climatic disturbances that volcanic gases and ash can induce upon release into the atmosphere and further receiving environments.

1.2 Magma fragmentation and production of ash

Release of gases is a distinctive feature of terrestrial and planetary volcanic activity (e.g., Wilson and Head, 1981; Oppenheimer et al., 2014; Wallace, 2003; Carlson et al., 1997; Renggli et al., 2017) in fact, the efficiency by which magma degasses and vesiculates during ascent within the volcanic conduit, is a key factor in determining the style of volcanic eruptions, thus, the characteristics of the eruptive products. Magma degassing can be broadly classified as passive or explosive. Passive degassing occurs mostly, but not exclusively, at Si-poor (low-viscosity) magmas from which dissolved gases can easily be discharged into the atmosphere or terrestrial environments. This type of volcanic activity generally occurs as formation of lava flows, lava lakes, lava fountains or as lava domes (Boudoire et al., 2018; Allard et al., 2016; Aiuppa et al., 2004; Sawyer et al., 2008).

Conversely, explosive degassing is characteristic for Si-rich magmas (dacite-rhyolite), whose high viscosity impedes efficient gas release, resulting in pressure build-up and energetic gas and magma release (Papale et al., 1998; Alidibirov, 1994; Klug and Cashman, 1996). Upon depressurization of the magma chamber (e.g., due to dome collapse or physical disruption of a confining plug on top of the conduit), Si-rich magma will ascend and accelerate as the exolved gas bubbles expand, magma fragmentation, will then occur if: (1) the pressure rises to the point, where the bubble growth rate exceeds the relaxation time of the melt around the bubble, which causes bubbles to burst, i.e., breakage of magma (Dingwell, 1996; Cashman et al., 2000), (2) the strain rate of magma column itself exceeds its inverse relaxation time (Dingwell, 1996; Papale, 1999), above which it will behave as a non-Newtonian fluid, leading to brittle fracture (Gonnermann & Manga, 2003; Wadsworth et al., 2018) or if, (3) magma interacts with water or ice, where conversion of thermal to kinetic energy results in magma fragmentation (Morrisey et al., 2000).

Each fragmentation mechanism will determine the properties of the produced material, however this can be broadly classified by its size as 'ash', 'pyroclasts' or 'lithics'. Here, 'ash' is the fine fraction of $P_d < 2$ mm (where P_d, represents particle diameter), 'pyroclasts' are often pumice, lapilli or scoria, and range from $2 < P_d < 64$ mm , while 'lithics' are thought to represent country rock material that is carried out of the conduit during explosive eruptions and have a size $P_d > 64$ mm (Rose and Durant, 2009; Fischer, 1961). The size of fragmented material produced during explosive eruptions is of importance for high temperature ash-gas reactions, because such reactions are believed to be only relevant for fine grained fragments, which have larger surface area, and can thus can react more rapidly than coarser particles.

Because of this, ash size-classification was expanded by Ayris and Delmelle (2012), by introducing the terms 'very fine' ($P_d < 63$ μm), 'fine' ($63 < P_d <$ 100 μm), 'coarse' ($100 < P_d <$2000 μm), and 'very coarse' ($P_d >$ 2,000 μm) ash. As ash size decreases, its specific surface area (a_s, $m^2\ g^{-1}$) increases, which provides larger reactive surface area per unit of ash, available for ash-gas interactions to occur (Delmelle et al. 2005). Due to the first-order control that particle size exerts on the rate of gas-ash reactions, in the present work, three different grain size distributions representative of fine and very fine and fine ash, i.e., <63, 63-90 and >90 μm, were

used to test the gas uptake potential of rhyolitic glass. More detailed information about the characterization of the experimental material particle size distribution will be presented in Chapter 2.

1.3 Volcanic gases

The amount and speciation of gases released during volcanic eruptions are controlled by their solubilities, the physicochemical properties of the magma (i.e., chemical composition, rheology), storage temperature and pressure. In Table 1.1. a compilation of measurements of discharged gases for various volcanoes is presented, and shows that the main components of volcanic emissions are: H_2O, CO_2, H_2, and SO_2, followed by H_2S, HCl, HF, and minor amounts of He, NH_4, Ar, O_2, N_2, CH_4, CO and HBr (Giggenbach et al., 2001; 1996; Oppenheimer et al., 2006;2014; Carn et al., 2016, and references therein; Johnson et al., 1993). Additional information about gas emissions can be obtained from degassing crater lakes, where magmatic gases, react with hydrothermal systems and dissociate (see Casas et al., 2016, and references therein) nevertheless, here only gaseous emissions will be considered.

As seen in Table 1.1, both SO_2 and HCl are ubiquitous in magmatic gas discharges, representing ~1-25 vol.% and ~1-10 vol.% of total volcanic gas emissions, respectively (Textor et al., 2004; Symonds et al., 1988; Cadle, 1980). Upon release to the atmosphere they can yield to short- and long-term atmospheric and climatic disturbances. Release of SO_2, for instance can lead to cooling of the earth surface (Robock et al., 2009). This occurs when SO_2 molecules react with atmospheric water to form sulfuric acid (H_2SO_4) droplets, which can absorb or scatter solar radiation, inducing cooling of the troposphere for variable time-scales (see Robock, 2000).

In addition, release of volcanogenic HCl into the atmosphere can promote destruction of ozone (O_3) molecules, when Cl^- radicals reach stratosphere levels (Crutzen, 1974; Stolarski and Cicerone, 1974). Occurrence of ash-gas interactions can, however, result in an effective reduction of volcanogenic SO_2 and HCl emissions available for atmospheric interactions, thus investigating this phenomenon is necessary in order to better assess the climate and environmental impacts of large volcanic eruptions (thus, large gas emissions).

Volcano	Kilauea	Kilauea	Erta Ale	Usu	Usu	White Island	Kudriavy
Location	Hawaii	Hawaii	Ethiopia	Japan	Japan	New-Zealand	Russia
Activity	Lava lake	Lava lake	Lava lake	Dome	Dome	Crater	Crater
Date	Mar 1918	Jan 1983	Jan 1974	Sep 1954	Jun 1985	Feb 1972	Aug 1995
Temp. (°C)	1,170	1,010	1,130	800	336	620	920
H_2O	370,900	798,000	794,000	980,000	999,000	911,000	953,000
CO_2	489,000	31,500	104,000	12,000	400	49,480	16,100
SO_2	118,400	149,000	67,800	430	32	18,180	10,600
HCl	800	1,000	4,200	530	170	11,570	2,000
HF	-	1,900	-	240	-	410	960
H_2S	400	6,220	6,200	4	35	7,190	2,100
H_2	4,900	9,025	14,900	6,300	390	925	5,760
N_2	-	-	1,800	570	14	-	220
NH_3	-	-	-	1.7	-	17.9	-
He	-	-	-	-	-	-	0.13
Ar	-	-	-	0.25	0.25	-	0.5
CH_4	-	-	-	17	0.44	-	0.03
CO	15,100	592	4,600	33	-	-	11

Table 1. 1 Composition and temperature data of some volcanic gas discharges (μmol mol^{-1}). Modified from Delmelle and Stix (2000).

Previous estimations of the annual volcanogenic emissions of SO_2 yielded to discharges ranging from ~1-50 Tg yr^{-1} (Textor et al., 2004, and references therein) however, recent studies suggest more conservative discharges of ~1-2 Tg yr^{-1} (Carn et al., 2016, and references therein). While, lack of monitoring in certain active volcanic areas, and non-reproducibility of measurements or of data processing procedures can lead to over- or under-estimations of the annual volcanogenic emissions, occurrence of low-and high-temperature gas sequestration by ash could also be potentially affecting estimations of gas budgets. Furthermore, as shown in Table 1.1, measured temperatures of released magmatic gases are above the dew point of both SO_2 and HCl acidic aerosols (190-200 °C), which implies that favorable thermal conditions naturally exist for high temperature ash-gas interactions.

Table 1.1. also shows the abundance of gas species for different magma compositions, which could lead to question whether investigating SO_2-uptake would be more relevant for mafic magma compositions (basaltic-andesitic) rather than for silicic magmas, given the fact that SO_2 is more abundant in mafic magmas.

Nevertheless, this work was focused on interactions between rhyolitic glass and SO_2, because Si-rich (highly viscous) magmas, tend to generate significant overpressure in the storage chamber over time (i.e., due to magma differentiation), which results in highly energetic magma fragmentation, thus large production of fine ash (Zimanowski et al., 2003), in comparison to more mafic magmas (Rose and Durant, 2009). Fine ash, as discussed in section 1.2, has a higher reaction potential due to its higher surface area, thus investigation of high temperature gas uptake by rhyolite is appears to be more pertinent than for basalt or andesite.

1.4 Gas uptake: previous studies

SO_2 sequestration at high temperatures by solid materials was first investigated given the industrial need to develop gas-solid interactions to mitigate SO_2 pollution from fossil fuels burning by power plants (Low et al., 1971; Allen and Hayhurst, 1996). The notion of volcanogenic gas sequestration by ash, however, began to receive attention after characterization of the ash (mostly by leachate analyses) collected from several erupting volcanoes during the 70s and 80s (i.e., Taylor and Stoiber, 1973; Rose et al., 1973; Rose ,1977;Varekamp et al., 1984; Óskarsson, 1980).

These studies extensively characterized fresh ash samples, and consistently noticed, that, not only large amounts of ionic species (Cl^-, SO_4^{2-}, Na^+, Ca^{2+}, F^-, Mg^{2+}, K^+, Mn^{2+}, etc.) were released upon leaching, but also that the concentration of anions (negatively charged ions) did not correspond to that of the original bulk ash composition. For instance, Taylor and Stoiber (1973), observed that the leached ash samples had concentrations of Cl^- and SO_4^{2-} of 7 and 14 g L^{-1} respectively, while the average volcanic rock composition was 0.06 and 0.25 g L^{-1} for Cl- and SO_4^{2-}, respectively. Imaging characterization of ash surfaces (enabled by the development of high-resolution microscopy) combined with leachate analyses has meant that the surface products of gas-ash reactions can be more precisely

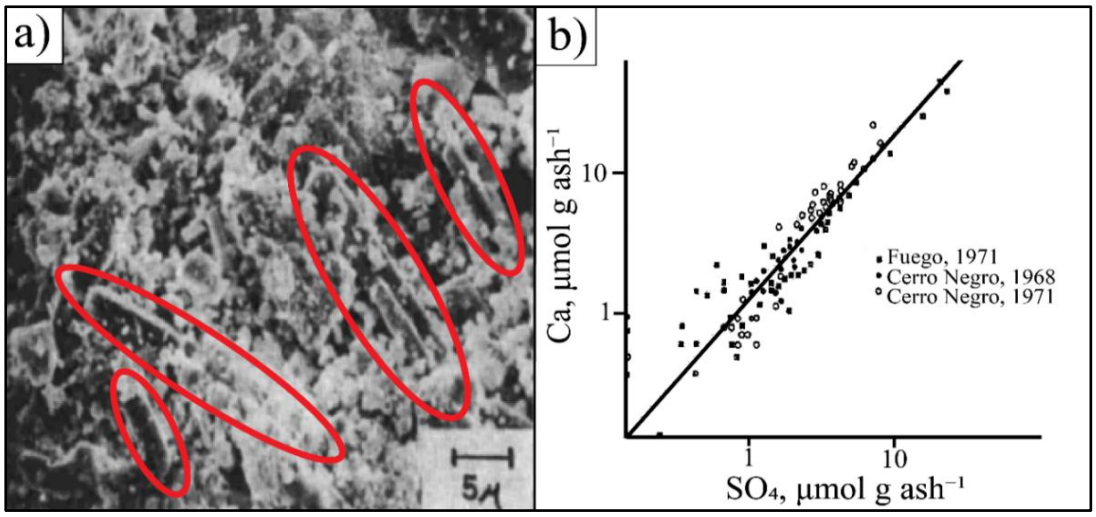

Figure 1. 1 SEM Image of an ash particle from the 1970 eruption of San Miguel volcano, El Salvador. Taken from Rose et al. (1973). This was one of the first ash-surface analysis ever made, and by combining a) SEM Imagery of ash particles and b) their leachate data (note molar ratios of calcium and sulfate are 1:1), the idea that ash-gas interactions were responsible for the formation of surface products began to develop. Elongated $CaSO_4$ crystals are marked inside the red ellipses.

identified (see Figure 1.1), for which $CaSO_2$ and NaCl were the most commonly found surficial products. Acknowledgment of gas sequestration by ash became increasingly evident and more studies focused on investigating the mechanism by which this would occur. For instance, a careful study of the fluorine and chlorine scavenged by ash, was performed by Óskarsson (1980), where they characterized the deposits of ash from the 1970 eruption of Hekla volcano.

Through mass- and particle size distribution analysis of the deposits and leachates analyses, they noticed that the salts formed on the ash were highly soluble and that there was a positive correlation between the amount of gas sequestrated by the particle surfaces (and leached as soluble salts) and the decrease of size distribution of ash, i.e., the smaller the particle was, the greater the concentrations of leached material. Moreover, they also performed some temperature-series of experiments to evaluate the hydrogen fluoride (HF) uptake potential of collected ash. Results of these experiments suggested that HF sequestration was temperature-dependent; since leachate and X-Ray diffraction analyses of treated samples showed marked differences in the amount and speciation of surficial products formed at different temperatures.

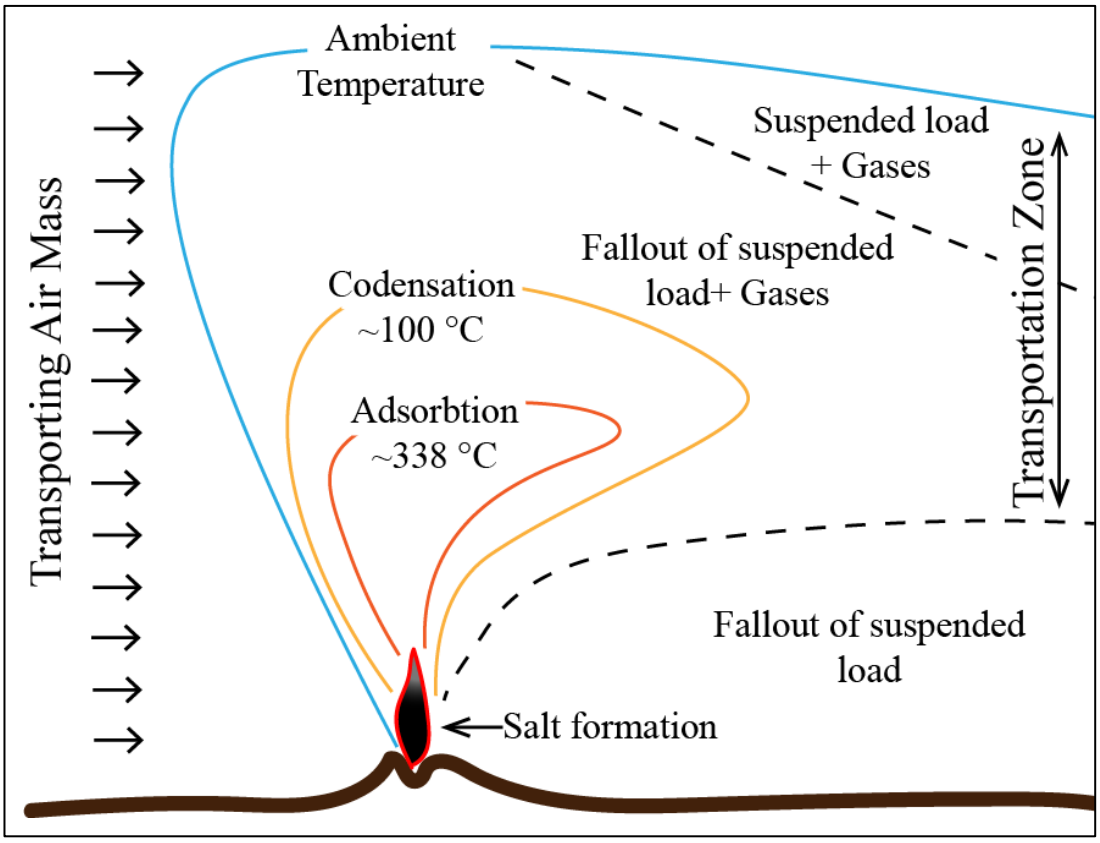

Figure 1. 2 Cross section of the three temperature-dependent zones of gas scavenging. (1) Salt formation zone (red line), takes place at magmatic temperatures in the vent and hottest core of the eruption column. HCl, SO_2 and HF are the primary anion donors that react with the alkalis and earth alkaline elements, like Ca and Mg. When the gases and volatiles are exsolved, they undergo an energy change; the surrounding has lower temperature and will change the stability of the gas phase; in which he surroundings have lower temperature exit the vent (Óskarsson et al., 1980, Naughton et al., 1974). (2) Adsorption zone (orange line), occurs at intermediate to high temperatures, where magmatic gases can be adsorbed onto the particle-surface reactive sites. (3) Condensation (yellow line), gaseous SO_2 oxidizes during atmospheric reactions and forms H_2SO_4, which can condense onto the ash surface, leading to acid-dissolution reactions. Modified from Óskarsson (1980).

For instance, at T > 700 °C, the most abundant compound formed was calcium fluoride (CaF_2), while at lower temperatures (T<600 °C), calcium fluosilicate ($CaSiF_6$) was predominantly formed. These results led Óskarsson (1980) to propose three temperature-dependent plume-zones where gas scavenging can occur, shown in Figure 1.2. From ash-leachates studies, it was further suggested that the concentration of leached anions (mainly SO_4^{2-}, Cl^- and F^-), could be used as proxy

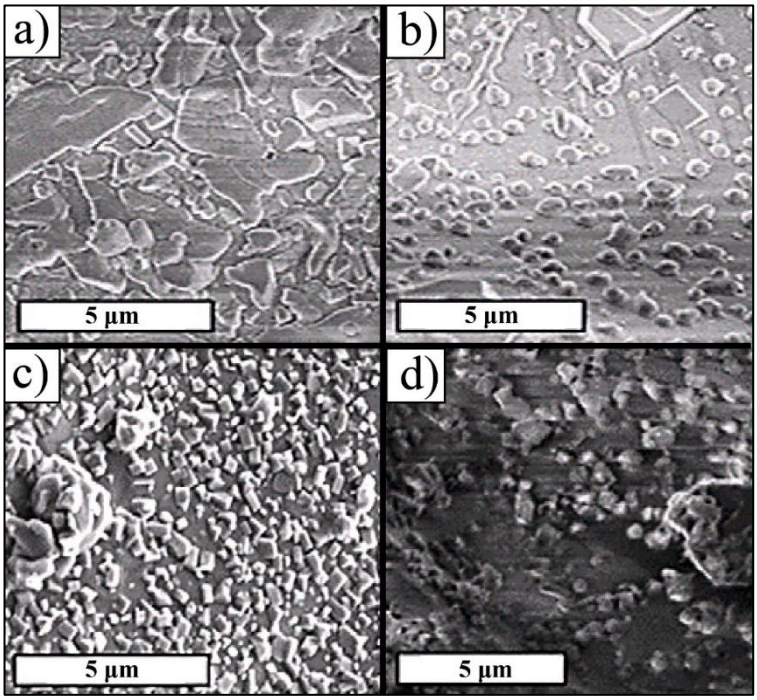

Figure 1. 3 Surface deposits on various glass compositions. Taken from Ayris et al. (2013). SEM analysis showed the presence of sulfur-bearing crystals, mostly in the form of $CaSO_4$, grown experimentally on the surfaces of a) tephrite, b) phonolite, c) dacite and d) rhyolite.

for the magmatic gas phase composition and therefore, different eruptive phases could be distinguished by analyzing changes in ash leachate concentrations (Edmonds et al., 2003; Nehring and Johnston, 1981; Stoiber et al., 1981). The converging explanation for this process was that ash could act as a "scavenger" agent for volcanic gases, evidenced by presence of surface salts. The mechanisms behind the gas uptake process, were however not well understood.

In the particular case of sulfur sequestration, the most accepted uptake mechanism, was that at low-temperature, SO_2 readily reacts with atmospheric water droplets, forming acid (H_2SO_4) aerosols, which when in contact with ash surfaces, condenses and causes dissolution of the bulk ash (minerals and glass network), which, upon evaporation of the water, leads to deposition of surface products observed, e.g., $CaSO_4$, $MgSO_4$, Na_2SO_4, etc. (Rose, 1977). This mechanism has been widely accepted and is believed to be the main sulfur uptake pathway for small- to intermediate-size eruptions, where the eruptive plume can be cooled relatively rapidly and SO_2 oxidation to H_2SO_4 takes place (Rose, 1977; Delmelle et al., 2007).

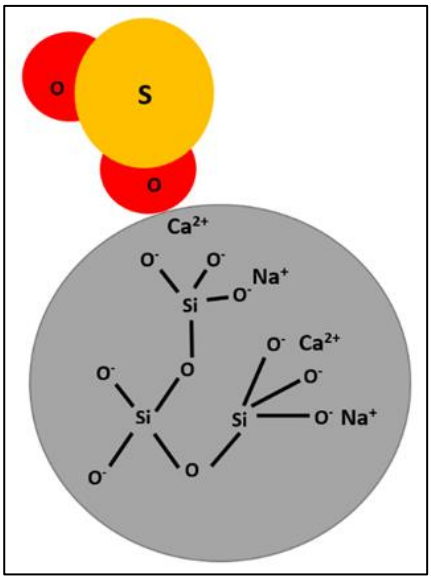

Figure 1. 4 Depiction of SO_2 adsorption onto a glass surface. Adsorption is believed to take place at alkalis- and alkali earth-oxides surface sites of the glass network, in the figure adsorption on a Ca-O site is shown.

However, Ayris et al. (2013) suggested that, at high temperature regimes, above the dew point of H_2SO_4 (~190-200 °C), sulfur sequestration could directly occur by reactions between SO_2 and ash. To test their hypothesis, they chose an experimental approach to evaluate the potential of glass to scavenge SO_2, by melting and quenching volcanic rocks of relevant compositions (tephrite, phonolite, dacite and rhyolite), and exposing them as grinded particles ($P_d \leq 63$ μm) to SO_2-air mixtures at high temperatures (200-800 °C), in order to reproduce the formation of soluble materials observed in volcanic ash (e.g., $CaSO_4$, $MgSO_4$, Na_2SO_2, etc.). Indeed, the experiments performed by Ayris et al. (2013) resulted in formation of surficial sulfate-bearing salts, seen in Figure 1.3a-d.

This findings led them to suggest that, (1) at temperatures above the dew point of H_2SO_4, sulfur uptake can directly occur in the form of SO_2 interactions with ash, as depicted in Figure 1.4, without undergoing previous oxidation reactions with water and that, (2) the glass present in ash, is potentially the most reactive component of ash for high temperature (T> 200 °C) sulfur uptake, and not the mineral components, as in the case of low-temperature sulfur uptake. Evidence of the high reactivity of silicate glasses to SO_2 had been shown by industrial studies of high temperature (≤1000 °C) SO_2 reactions with soda-lime silicate glass, which

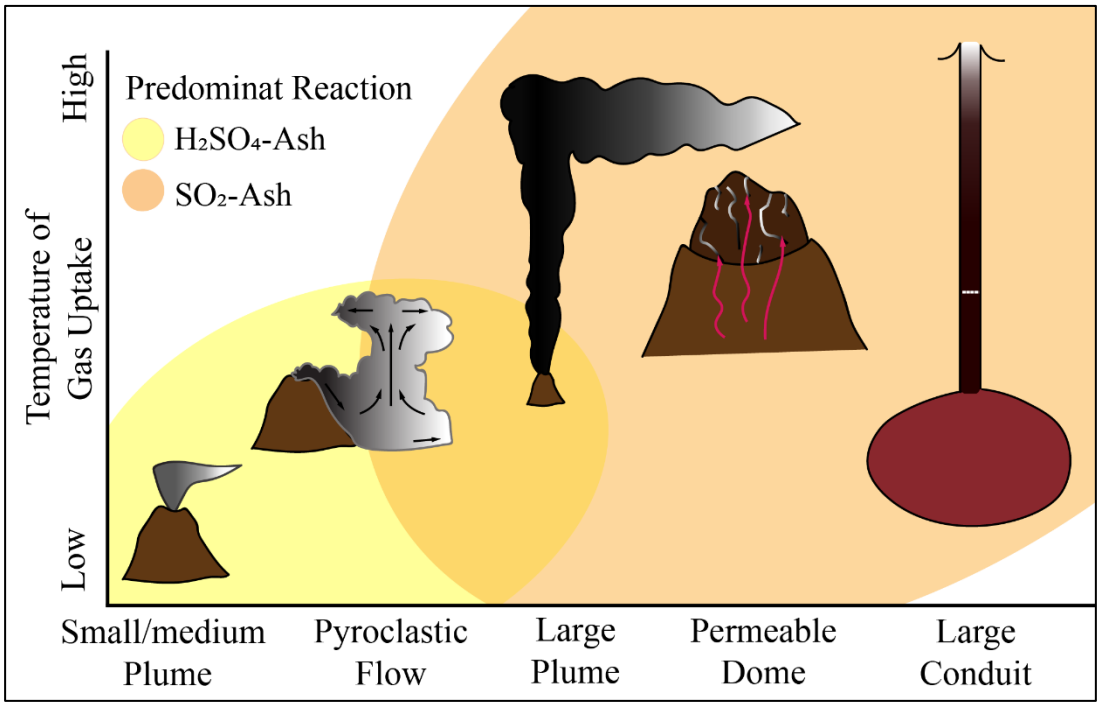

Figure 1. 5 Summary of the volcanic environments where sulfur, as SO_2 (gas) or H_2SO_4 (aerosol), uptake by ash can take place as a function of the temperature. At small to medium-size plumes (≤ Mt. St. Helens-size), the rising plume rapidly mixes with atmospheric air, prompting rich-H_2SO_4 aerosol formation (Rose, 1977). During pyroclastic flows, remobilization of ash and gases can also induce uptake reactions (Ayris et al., 2013). At larger plumes, direct chemisorption of gas onto ash surface occurs at the plume core, however at the umbrella region, acid aerosol formation also takes place (Óskarsson, 1980). Permeable, fractured, degassing domes, allow efficient high temperature ash-gas interactions, due by passing of magmatic SO_2 through ash-filled fractures (Casas et al., 2019). For caldera-forming eruptions, conduits can be large enough to allow high temperature SO_2-ash interactions above the fragmentation level, for reasonably long timescales (Ayris et al., 2013).

resulted in formation of surficial Na_2SO_4 on t glass surfaces (Douglas and Isard, 1949). In large volcanic eruption plumes, similar thermal reaction regimes are present and can be maintained long enough to impede SO_2-water reactions (i.e., H_2SO_4 aerosol formation) leading to direct gas-ash reactions. Furthermore, Ayris et al. (2013) applied their experimental findings to suggest that, relevant sulfur uptake by ash could also occur within the volcanic conduit, for large- to very large eruptions such as the Tambora (1815) or Krakatau (1883) eruptions . In both cases, the depth at which magma fragmentation takes place is large enough to almost reach the magma chamber (Foden, 1986; Mandeville et al., 1996).

At in-conduit scenarios, gas uptake could readily happen, once the fragmentation threshold is crossed (thus, once fine ash is produced), due to occurrence of energetic ash-gas mixing at magmatic temperatures (~ 1000 °C). Estimations of in-conduit SO_2 uptake made by Ayris et al. (2013) suggested that, for an eruption of the magnitude of the Krakatau (1883), where the conduit depth was estimated to be 4-5 km (Mandeville et al., 1996), up to 45 % of the magmatic SO_2 could have been removed by ash, before reaching the atmosphere. This has the implication that, in the case of large volcanic eruptions, to try to relate the composition of volcanic gas released to the atmosphere with the pre-eruptive magma composition, could lead to non-negligible underestimations of the initial magmatic gas content.

Moreover, Ayris et al. (2013) proposed that, another high temperature scenario for SO_2 uptake by ash could be during pyroclastic flows. These result from the partial to total collapse of volcanic plumes, which generates turbulent remobilization of ash and gases at relatively high temperatures (≥ 500 °C), which could also lead to gas uptake. More recently, gas uptake was also suggested to occur at permeable fractured degassing domes, (Casas et al., 2019) where, degassed magmatic SO_2 passing through fractures filled with fine grained pyroclastic material, could be an ideal environment for gas uptake, given the high temperatures of magmatic gases (Table 1.1) and the relatively long lifetimes of domes (from hours to years), which allow longer ash-gas reaction times. A summary of the volcanic environments where gas uptake, by reactions with ash, can occur is shown in Figure 1.5. In all scenarios, fine ash and high temperatures are present.

1.5 Environmental and climate implications of gas uptake

The need of understanding the fate of volcanic SO_2 and HCl emitted during volcanic eruptions arises from the diverse impacts that these gases can have on receiving environments. As mentioned in section 1.3, volcanogenic sulfur readily reacts with atmospheric water to form sulfuric acid (H_2SO_4) aerosols, which can affect the solar radiation budget at tropospheric levels (~ 10^4 m.a.s.l.) by causing temporal cooling of the earth surface (Charlson et al., 1991;1992), but also by inducing local warming, via reflecting the earth heat radiation (Robock, 2000, and references therein).

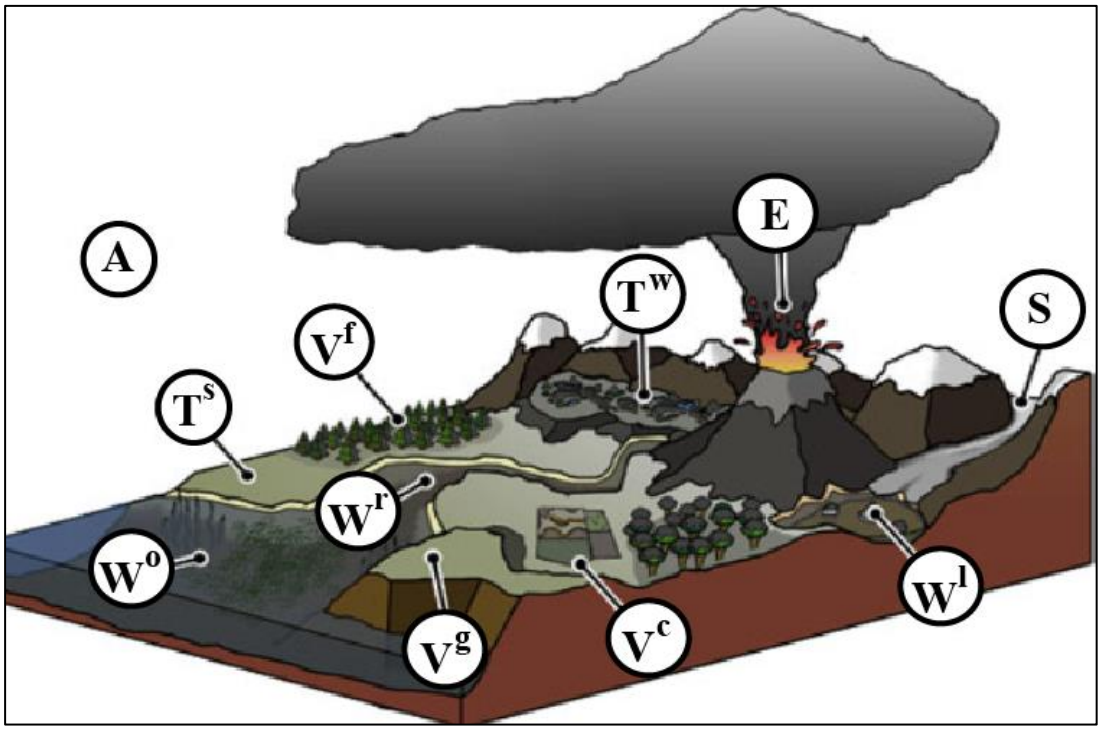

Figure 1. 6 Diagram of receiving environments of volcanic emissions (ash and gases). Taken from Ayris and Delmelle (2012). (E) represents the volcanic plume and cloud produced during a large volcanic eruption, where tephra is emitted to the atmosphere (A), and will eventually be deposit onto vegetation surfaces (V), such as forests (Vf), agriculture (Vc), and grassland (Vg), land surfaces (T), such as soil (Ts), wetlands (Tw), or into snow/ice (S).Tephra can also reach diverse aquatic systems (W), further reaching into ocean sediments (Wo), lakes and lake sediments (Wl), and river and river beds (Wr).

Cloud formation and evolution, can also be disturbed by the presence of H_2SO_4 aerosols in the atmosphere, since acid droplets can act as cloud condensation nuclei (Twomey, 1974), enhancing cloud formation, thus cloud albedo, which can ultimately alter the global dynamics of heat circulation (Nober et al., 2002).

Injection of HCl into the atmosphere can also pose serious environmental hazards, being perhaps the most relevant, that Cl^- radicals contribute to the destruction of atmospheric ozone molecules (O_3), thus to the depletion of the earth ozone layer (Molina and Rowland, 1974). Additionally, due to its high solubility, HCl can readily be dissolved in atmospheric water, which upon precipitation, contributes to the acidification of receiving terrestrial and aquatic environments, i.e., soil, vegetation, and water bodies (Pallister et al., 2010a; Swanson et al., 2010).

To improve our understanding of volcanic ash-gas reactions is therefore of relevance, because they can alter the effective amount of gases injected into the atmosphere, which can induce short- and large-scale climatic and environmental perturbations. Ayris and Delmelle (2012) brought attention to the complexity of the environmental effects of large volcanic eruptions, from the point of view of ash deposition on diverse environments. They did so, by compiling and reviewing post-eruptive data of 35 worldwide volcanic eruptions of diverse erupted volume (0.01 > km^3 >100) and reviewed the immediate physical, chemical and biological effects reported upon ash release.

Their work stressed the need for more multidisciplinary approaches to investigate and evaluate the diverse impacts of large volcanic eruptions. Figure 1.6 shows the various environments that are potentially affected by occurrence of explosive volcanic eruptions. Current assessment of the effects of volcanic eruptions are very complex to make, because of the many variables to be considered, i.e., the characteristics of the eruption, geographical location of the volcano, properties of the ash, composition of the gases emitted, weather conditions, etc. Assessment of the impacts of large or very large volcanic eruptions are of particular interest, since these eruptions produce considerable quantities of fragmented magma, such as

Toba eruption (74 ka) which produced an estimated volume of 2800 km^3 of erupted material. Furthermore, the fraction of fine ash ($P_d < 100\mu m$) for these eruptions is larger (0.3-0.5) than that of small- to medium-eruptions (Rose and Durant 2009). Occurrence of ash-gas interactions in large volcanic eruptions, is not only relevant because they can affect the gas budget injected to the atmosphere, but also because they change the chemistry of ash particle surfaces, thus its reactivity (Delmelle et al., 2007). The presence of soluble salts on ash surfaces, can exert important effects on ash transport within the volcanic plume, its dispersion dynamic within the cloud, and its overall residence time in the atmosphere (Carey and Sigurdsson, 1982; Sorem, 1982; Lane et al., 1993).

Ash aggregation is a primary mechanism that significantly affects the dispersal dynamics of volcanic ash (Brown et al., 2000, and references therein). The main agents that drive aggregation of volcanic ash are humidity (Sparks et al., 1997), electrostatic forces (James et al., 2003) and the presence of surficial salts produced during gas uptake (Gilbert and Lane, 1994 and Mueller et al., 2016).

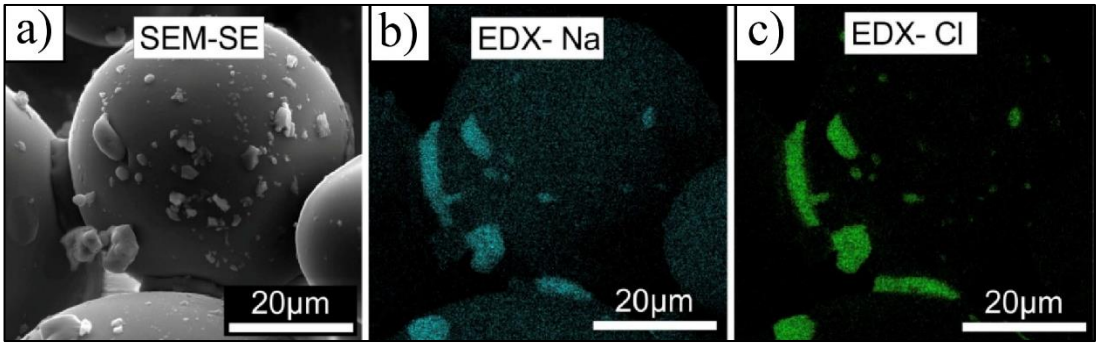

Figure 1. 7 Effect of surficial salts on particle aggregation. Experimental results of particle aggregation enhanced by NaCl deposits on soda-lime glass beads. SEM-EDX analysis showed that NaCl as the bridging agent for particles to aggregate. Taken from Mueller et al. (2017).

Once these soluble salts form, they act as bonding agents, cementing particles together and stabilizing aggregates, which results in higher removal rates of fine particles from the atmosphere (Lane et al., 1993; Mueller et al., 2017; Tomita et al., 1985). Figure 1.7 shows the results of aggregation experiments of particles doped with NaCl-loads, described in Mueller et al. (2017), where SEM-EDS images clearly show that NaCl surface deposits act like "bridges" among particles. When these particles interact with water bodies or atmospheric water droplets, the surface products can be readily leached, releasing a diverse array of species, mostly Ca^{2+}, Mg^{2+}, Na^{+}, K^{+}, Fe^{2+}, Fe^{3+}, Cl^{-}, SO_4^{2-} and F^{-}.

Finally, Figure 1.8 shows the relative concentrations of SO_4^{2-}, Cl- and F^{-}, leached from ash from various eruptions. Here, it is clear that formation of soluble material is ubiquitous during volcanic eruptions. Interestingly, Figure 1.8b also shows that Si-rich ash has typically higher SO_4^{2-} concentrations (see the data for dacite) than Si-poor ash. In order to improve our assessment of large volcanic eruption impacts, it is necessary to constrain the mechanisms by ash-gas reactions occur at high temperatures. Experimental data is crucial for this purpose, given natural ash-gas interactions cannot be directly observed, yet, they can be simplified, scaled and safely reproduced in the laboratory. The present work applied previous findings and hypothesis regarding high temperature gas uptake by ash, to design relevant series of experiments to help constrain the parameters by which SO_2 and HCl uptake occurs by rhyolite.

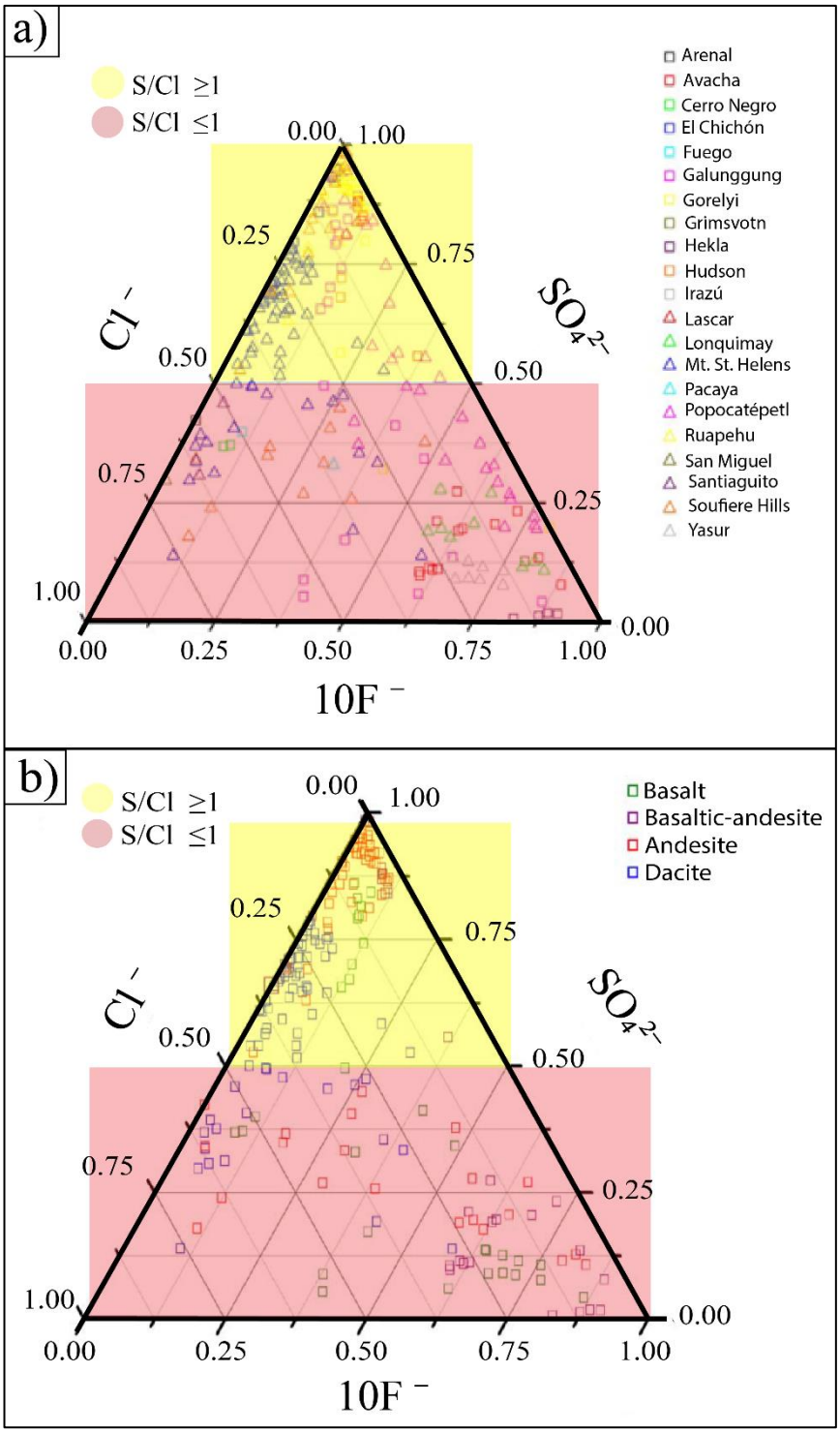

Figure 1. 8 Ternary diagram of relative SO_4^{2-}, Cl^- and F^- sequestrated by ash from various volcanoes. Modified from Witham et al. (2005). a) a total of 21 ash leachates (relative) compositions are plotted. Two main groups are shown in the diagram, based on their S/Cl ratio: for S/Cl ≥ 1 (yellow area), S/Cl≤1 (red area). Interestingly, in b), when the ash composition is also plotted, similar trends of the leachates can be observed; being the most S-rich samples (relative to Cl) those of the more silicic composition, i.e., andesite and dacite (red and blue squares, respectively.

Chapter 2

Experimental and Analytical Methods

2.1 Introduction

In this chapter the first studies aiming to reproduce ash-gas reactions observed in nature will be reviewed, along with the evolution of experimental techniques for this research. Next, the experimental apparatus used for this work (Advanced Gas-Ash Reactor) will be described (Ayris et al., 2015). Experimental conditions applied to sample preparation and treatment (i.e., gas mixtures, temperatures, exposure times, etc.), as well as the diverse characterization techniques will be described in detail.

The two sets of samples used to perform the gas uptake experiments, consisting in natural and synthetic rhyolitic glasses, will be described in terms of their origin, composition and preparation to make these materials suitable for experiments. Additionally, in the case of the synthetic glasses, the procedure and conditions by which these glasses where made will be shown. Finally, the analytical techniques through which samples (prior and after experiments), were characterized, will be also described.

2.2 Development of experimental techniques

One of the first attempts to experimentally replicate the formation the observed surface products produced during volcanogenic gas-ash interactions, was made by Óskarsson (1980). By analyzing ash leachates from the 1970 eruption of Hekla volcano, they observed very high concentrations of fluorine (F^-) and chlorine (Cl^-) and diverse cations (mainly calcium, Ca^{2+} aluminum, Al^{3+} and silicon, Si^{4+}), and suggested that these soluble compounds were formed during the eruption, as a result of reactions between the ash and the hot magmatic gases, particular HF. To test his hypothesis, they used washed and dried ash from the 1970 eruption, passed

a constant boiling flow of HF-H_2O over it at temperatures 150-1100 °C and analyzed leachates of the treated samples. Results of this simple test did not just succeed in replicating the soluble species found in the original ash, but also showed a temperature dependence of the soluble salts formed. The combined results and interpretation of the work of Óskarsson (1980) and observations made by Rose (1997) and Naughton et al. (1974), pointed out the relevance of experimental approaches to investigate gas sequestration mechanisms by ash. The work of Delmelle et al. (2005) provided new insights on the relevance of physicochemical properties of ash for interactions with gases, as well as on adsorption mechanisms of gases (including water vapor) at ash interfaces, by conducting several tests with natural ash samples.

In addition, Delmelle et al. (2007) further investigated the occurrence of dissolution of ash, mainly by fluorine, and its implications on later deposition of sulfate and halide salts also tested by using natural ash. These studies undoubtedly increased our understanding of the process by which ash and gases interact, by addressing many of the complexities of the mechanisms involved. More recently Ayris et al. (2013), focused their work on gas-glass reactions, instead of gas-ash reactions, proposing that the main cation source for the formation of the soluble salts was the glassy component of the ash.

They evaluated the SO_2-sequestration potential of four glasses made from melted volcanic rocks of relevant compositions (phonolite, tephrite, dacite and rhyolite). A strong correlation between the glass compositions and their reactivity with SO_2 under high temperatures, was observed as to occur by formation of surficial sulfate-bearing products. Most of such sulfates corresponded to $CaSO_4$, which was suggested to be formed by heterogeneous reactions between SO_2 molecules and surficial calcium reaction sites of aluminosilicates.

Nucleation and growth of $CaSO_4$ was also suggested to be controlled and limited by Ca diffusion from the bulk glass to the surface, and that this process, as also observed by Óskarsson (1980), was strongly temperature-dependent, and shows enhanced efficiency at temperatures above 600 °C. Following the previous findings pointing out the important role that glasses can play as cation donors for gas uptake processes, and aiming to constrain more factors relevant to gas-ash interactions, the effect of grain size distribution, humidity in the gas atmosphere were tested in this work.

For this, two sets of powdered rhyolitic glasses were treated with SO_2, SO_2-H_2O mixtures using the AGAR (Advanced Gas-Ash Reactor) apparatus developed by Ayris et al. (2015) illustrated in Figure 2.1. The post-treated material was extensively characterized and analyzed by various techniques prior and after SO_2-exposure. Sample characterization comprised analyses by ion chromatography, electron probe micro-analyzer, scanning electron microscopy, Raman spectrometry, bulk iron determination, and of particle size distribution.

2.3 Experimental apparatus

All gas-glass experiments were performed with the Advanced Gas-Ash Reactor device described in Ayris et al. (2015). A depiction of the components of the reactor is shown in Figure 2.1a. The AGAR reactor is a customized apparatus consisting of a horizontal three-zone furnace, containing a quartz tube in which a quartz bulb is inserted. The right side of the reactor has a narrow opening to let the gases into the reactor. Each gas is flowed into the reactor separately, to avoid interactions between them, prior to contact with the sample. Once the reactor bulb is loaded with the sample, it is inserted from the left side of the reactor into the quartz tube. The left end of the reactor is then sealed, leaving only the outlet of gases open, which is directed to the upper part of the fume hood. The temperature in the bulb and each of the heating zones was monitored using a K-type thermocouple accurate to within 2 K.

This device was exclusively design to perform experimental simulations of solid-gas reactions by providing mixing conditions similar to those occurring in volcanic eruptive environments. This device provides a unique method to experimentally evaluate the gas-uptake potential of ash, or in the case of this study, of glass, under high temperatures. The range of variables that can be tested in AGAR is wide; from the nature of the sample (composition, morphology, etc.), to the thermal treatments (room temperature to 800 °C), gas mixtures (the current set up allows usage of SO_2, HCl, H_2O, CO_2, air) and exposure times. In Figure 2.1b, a picture of the AGAR device is shown, together with the external components consisting in the gas bottles containing SO_2 and HCl (1, 2), the flow controllers of each gas (3) and the peristaltic pump used to control the flow of water entering the reactor (5).

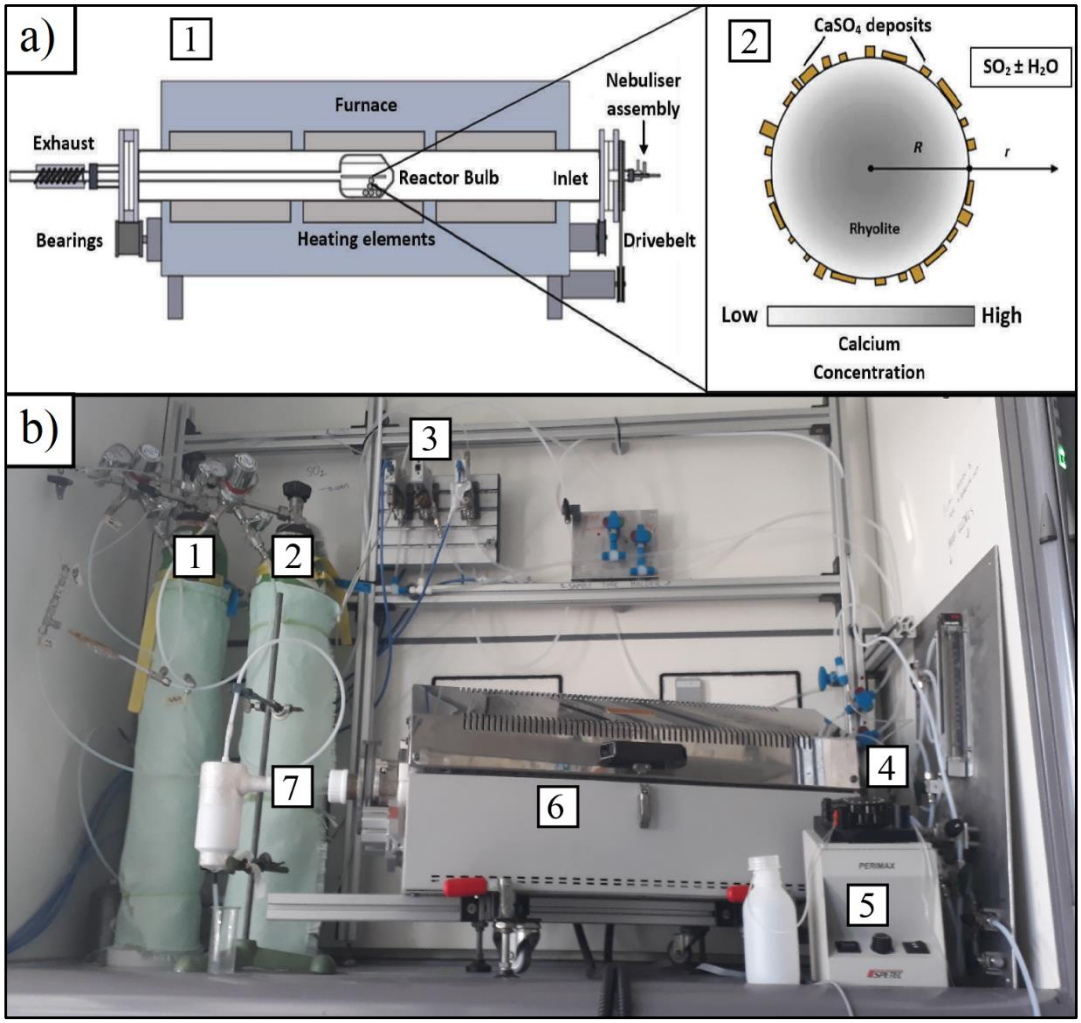

Figure 2. 1 Advanced Ash-Gas Reactor. a) Schematic of the experimental apparatus, modified from Ayris et al. (2015). 1) The apparatus consists of a split three-heating element tube furnace with a reactor tube inserted into it. At the end of the reactor tube is a bulbous sample holding head which is open at both ends to allow the flux of gas. The whole reactor tube rotates, tumbling particulate samples. Through the furnace assembly, SO_2-Ar gas mixtures and nebulized H_2O droplets are flushed at known concentrations. 2) A schematic approximation of the process examined in this study showing a spherical rhyolitic glass particle with radius R (radial position r) that has developed a strong concentration gradient of calcium as $CaSO_4$ crystals grow on the surface. b) Picture of then elements of AGAR used to perform gas-glass high temperature experiments. 1) and 2) Are the HCl-Ar and SO_2-Ar (1mol.% and 99 mol.% each) gas bottles, 3) the gas flowmeters, 4) the inlet of gases and/or water vapor to the reactor, 5) the peristaltic pump used to pump water into the reactor in the form of vapor aerosol (flown through a quartz nebulizer connected to the gas inlet), 6) the horizontal tube furnace, where the quartz reactor bulb containing the sample is inserted, and where the gas-glass reactions take place and 7) the gas outlet; let the gases leave the reactor directly to the top of the fume hood.

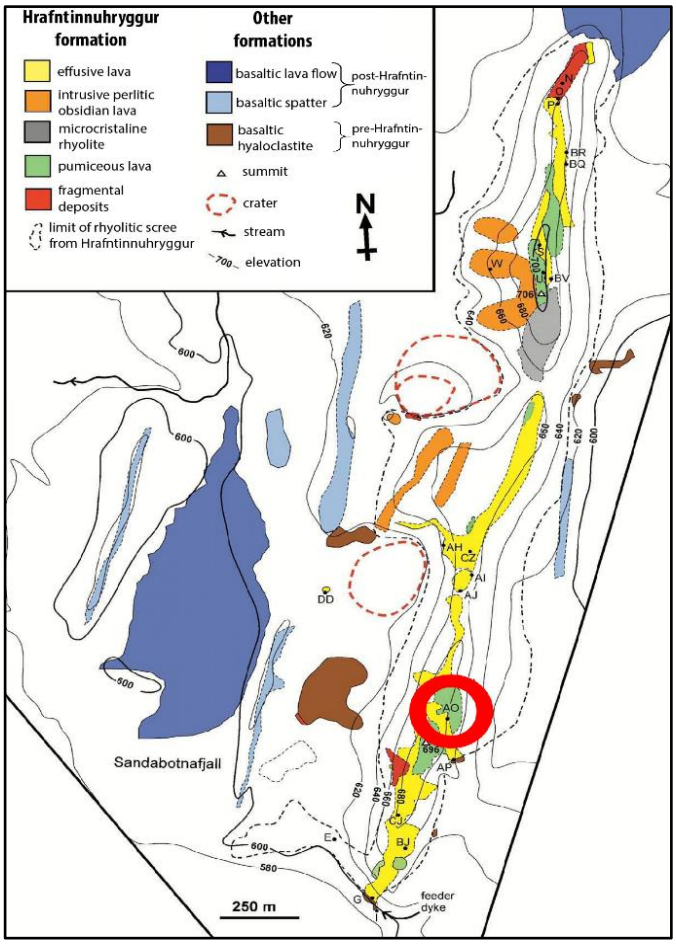

Figure 2. 2 Geological map of Hrafntinnuhryggur-ridge. The eruptive features are mostly lava flows and dome-like bodies, taken from Tuffen and Castro (2009). The sampling location "AO" of the rhyolite used in this work is indicated with a red hollow circle.

2.4 Sample material

In this work, the experimental evaluation of high temperature gas uptake, required a homogeneous, well characterized and isotropic material. Accordingly, a natural silicate glass was chosen, not only because it fits these requirements, but also due the important role that glass can play as cation donor to gas uptake-reactions, as experimentally determined by Ayris et al. (2013), Renggli et al. (2019), and Douglas and Isard (1949). Glass is a ubiquitous component of volcanic ash (Heiken and Wohletz, 1985; Heiken, 1972; Rogers and Hawkesworth, 2000).

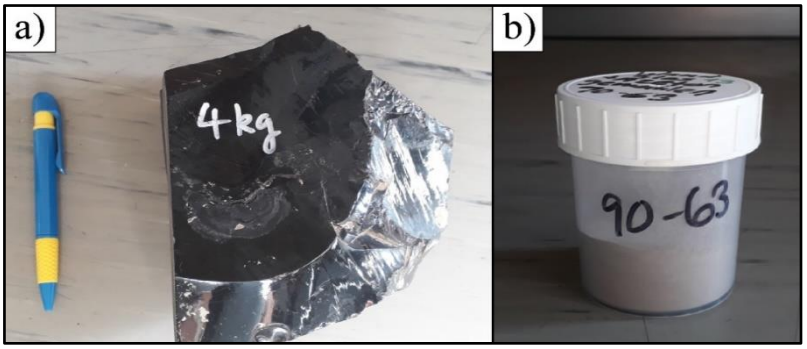

Figure 2. 3 Picture of the natural calc-alkaline Krafla Obsidian. a) As the original blocks collected, and b) as milled, sieved powder used to perform the SO_2-uptake experiments in AGAR.

The isotropic nature of silicate glasses, provides the further advantage that behavior of cations by diffusion and the oxidative changes in iron upon experimental exposure to gas, can be predicted using previous constraints (i.e. diffusivity of cations; see for example Mungall et al., 1997). Although the amount of glass within ash varies with the eruptive style and magma composition, it is well documented that ash invariably contains a glassy percentage, ranging from 50-100% (Heiken and Wohletz, 1992). The sample materials used for this work consisted in two sets of glasses: (1) a natural tholeittic rhyolitic glass and (2) synthesized haplogranitic glasses doped with excess CaO and FeO. The natural rhyolitic obsidian was collected from a dyke emplaced at Hrafntinnuhryggur, Iceland (taken at the sampling site known as "AO" in Tuffen and Castro (2009) as shown in Figure 2.2.

2.4.1 Sample preparation

2.4.1.1 Krafla obsidian

In order to make the sample material suitable for the subsequent experimental treatment, milling and sieving of the samples was done. Originally, the obsidian material was collected (from Hrafntinnuhryggur, Iceland) in the form of blocks of glass (dimensions of about 15x15x20 cm), as seen in Figure 2.3a. The blocks were then hammered to obtain smaller-size glass pieces which were then milled.

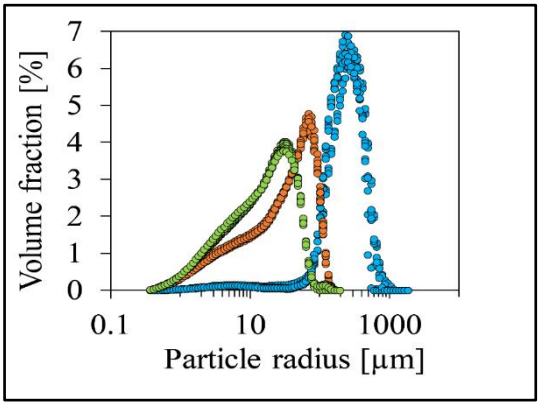

Figure 2. 4 Particle size distributions of the three sieved populations of the Krafla obsidian. In shades of green, orange and blue are, respectively, the size distribution ranges <63, 63–90, and >90 µm, referred to in the text.

The latter was done by using a centrifugal ball mill (Retsch GmbH, model S1000), where both, the milling container and balls, were made of zirconium dioxide (ZrO_2). The milling was done in batches of ~100 g each, by using three milling balls and a rotating speed of 40 revolutions per minute (rpm) for 3 minutes followed by a 5 minute-pause and repeating this until the glass powder had a fine-powder texture. The latter was done in order to avoid overheating of the powdered glass, which could affect its Fe redox state (more oxidized). All the milling was done under dry conditions, i.e., neither acetone nor water were used during the milling. This was to avoid alteration of the surface physicochemical properties, hence its reactivity and performance during the gas-uptake potential experiments.

Milling was followed by sieving the powdered glass to three grain size distributions: smaller than 63, between 63 and 90, and larger than 90 micrometers (i.e., <63, 63-90 and >90 µm), an example of the sieved glass powder can be seen in Figure 2.3b. After manual sieving, the powdered glasses were weighted (2 g per experiment), stored in sealed glass vials until the experiments were performed and labeled. Particle size distributions of the sieved powders were obtained by analyzing the samples with a Bettersizer S3 Plus laser particle size analyzer. For these analyses, a small amount of sample (~60 mg) was dissolved into ~4 mL of distilled water and manually injected into the instrument port. E ach sample was measured 9 times. Particle size distributions of the three sets of sieved samples are shown in Figure 2.4.

Sample	Fe_2O_3 (g)	$CaCO_3$ (g)	HPG8 mixture (g)
HPG8 + 1% CaO + 0% FeO_{total}	0	0.89	49.5
HPG8 + 1% CaO + 0.1% FeO_{total}	0.05	0.89	49.45
HPG8 + 1% CaO + 1% FeO_{total}	0.25	0.89	49.25
HPG8 + 1% CaO + 1.5% FeO_{total}	0.75	0.89	48.75
HPG8 + 1% CaO + 2% FeO_{total}	1	0.89	48.5
HPG8 + 1% CaO + 2.5% FeO_{total}	1.25	0.89	48.25
HPG8 + 2% CaO + 0% FeO_{total}	0	1.78	49
HPG8 + 2% CaO + 0.1% FeO_{total}	0.05	1.78	48.95
HPG8 + 2% CaO + 1% FeO_{total}	0.25	1.78	48.5
HPG8 + 2% CaO + 1.5% FeO_{total}	0.75	1.78	48.25
HPG8 + 2% CaO + 2% FeO_{total}	1	1.78	48
HPG8 + 2% CaO + 2.5% FeO_{total}	1.25	1.78	47.75

Table 2. 1 Composition of HPG8 samples doped with CaO and FeOtotal. Amounts of $CaCO_3$ and Fe_2O_3 to be added to the HPG8 oxide mixture, to achieve the theoretical compositions HPG8 + 1,2 wt.% CaO + 0, 0.1, 1, 1.5, 2 and 2.5 wt.%FeOtotal.

2.4.1.2 HPG8 glasses

The synthetic glasses were produced to have a similar composition to the natural Krafla calc-alkaline obsidian but different contents of CaO and total Fe-bearing oxides. For this, the haplogranitic composition designated as HPG8 by Holtz et al. (1992) were synthesized from reagent-grade oxides to have the following composition: 79.1 wt.% SiO_2, 12.07 wt.% Al_2O_3, 4.23 wt.% K_2O and 4.6 wt.% of Na_2O, and additionally doped with 1 and 2 wt.% CaO, and 0, 0.1, 1, 1.5, 2, 2.5 wt.% total FeO each. The powder preparation to make the glasses, was done first by making a 1 kg-batch of pure HPG8 composition. This batch of pristine HPG8 composition, was later mixed with the CaO and FeO to obtain the compositions mentioned above. The HPG8 batch was prepared by weighing 791 g of SiO_2, 120.7 g of Al_2O_3, 62.06 g of K_2CO_3 (i.e., K_2O) and 78.66 g of Na_2CO_3 (i.e., Na_2O). The oxides were mixed and also milled with the method described in section 2.3.1.2. Once the 1 kg-batch of oxides mixture with HPG8 composition was milled, a sub-set of HPG8 + CaO + FeO was weighted with the amounts shown in Table 2.1.

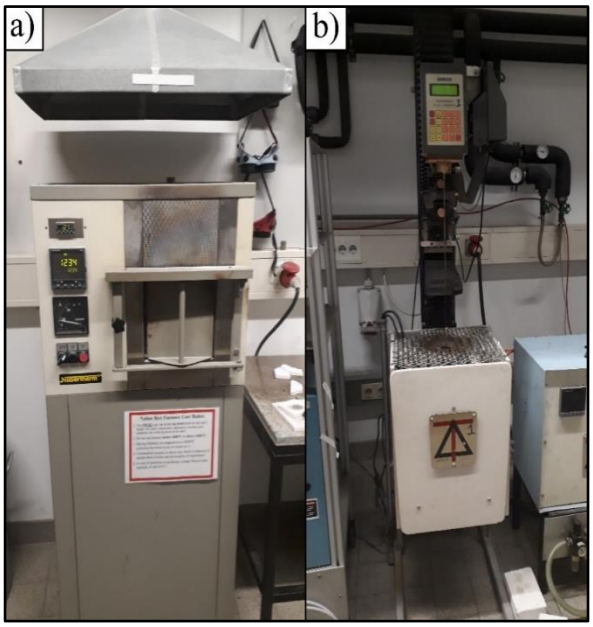

Figure 2. 6 Furnaces used to synthesize the HPG8 set of glasses. a) The box-furnace used to melt the oxide powders and b) The stirring-furnace to ensure that the glasses were homogeneous and bubble-free.

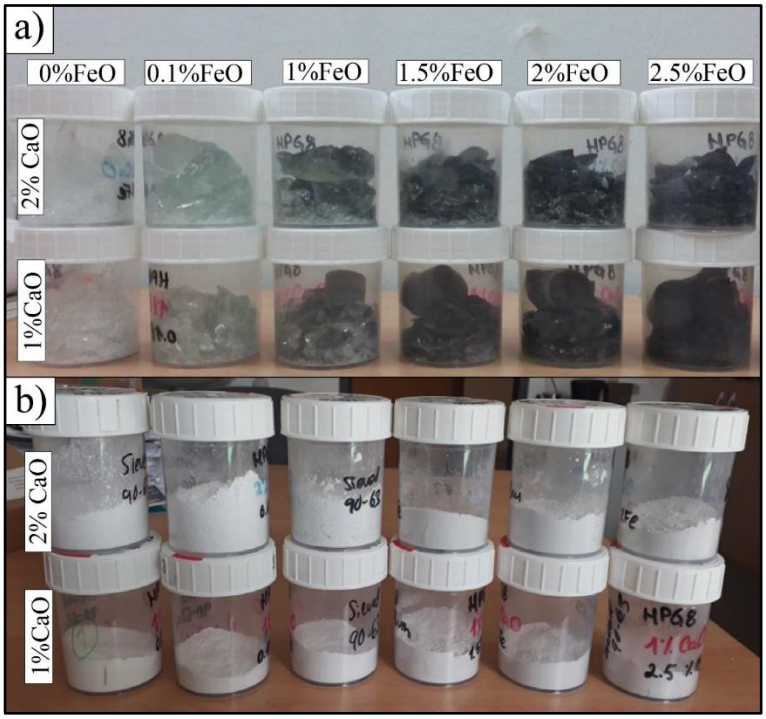

Figure 2. 5 Synthesized HPG8 glasses. a) Quenched HPG8 glasses doped with 1 wt.%CaO (lower row) and 2 wt.% of CaO (upper row) and 0, 0.1, 1, 1.5, 2 and 2.5 wt%. FeO (form left to right) each. Approximate mass of each sample was 50 g. b) HPG8 glasses after milling pictured in the same order as in a).

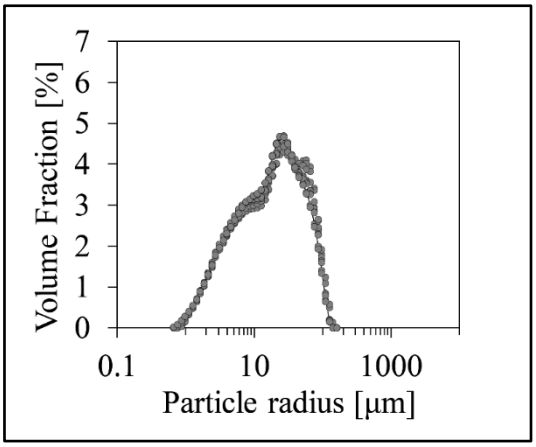

Figure 2. 7 Particle size distribution of the HPG8 glasses sieved for the particle diameter of 63-90 µm, this was obtained from a total of 9 measurements.

Doping of the samples with FeO and CaO was made in the form of ferric oxide (Fe_2O_3) and calcium carbonate ($CaCO_3$). All oxides were dried, at T=110 °C, overnight prior to weighing. The dried Fe_2O_3 and $CaCO_3$ were then weighted according to Table 2.1, to have the aimed HPG8 + CaO + FeO_{total} compositions, afterwards the oxide mixture was manually mixed in plastic bottles. The samples were milled under the same procedure as for the Krafla obsidian (see section 2.3.1.2), placed in a thin-walled platinum crucible and melted stepwise at 1550 °C in an electrical $MoSi_2$ muffle furnace pictured in Figure 2.5a, at atmospheric pressure.

After the initial melting, each sample was taken to a concentric furnace to be stirred with a Pt_{80} Rh_{20} spindle 1600 °C, at atmospheric pressure (Figure 2.5b). This had as main purpose to ensure chemical homogeneity of the glasses, as well as to remove any bubbles contained in the melts, remained from the initial melting. Absence of bubbles was confirmed by constantly checking the tip of the spindle, quickly removing it from the melt, quenching it and visually inspecting if the glass had any bubbles. Once the melts were bubble-free, the melts were taken out of the furnace and quenched rapidly by immersion of the crucible containing the melt, in deionized water. The resulting glasses where removed from the crucible by drilling and gently hammering out the glass rests. Figure 2.6a shows the two sets of HPG8 glasses (doped with 1 and 2 wt.% CaO and doped with different amounts of FeO wt.%).

The glasses were then milled, sieved to only one particle diameter size (63-90 μm), weighted and stored in sealed plastic vials (Figure 2.6b) until experiments were carried out. The powdered and sieved HPG8 glasses were also analyzed with the Bettersizer S3 Plus laser particle size analyzer, to constrain its grain size distribution (see Figure 2.7).

2.5 Experimental design

2.5.1 Krafla obsidian

Experiments were planned to assess the potential of the rhyolitic glasses (both the natural calc-alkaline and the synthetic HPG8) to uptake SO_2 at high temperatures, and to constrain the cation-diffusion kinetics of the process. This was done by exposing 2 g of each sample to SO_2-Ar, SO_2-H_2O-Ar mixtures for various time- and temperature-series of experiments in the AGAR apparatus at the Ludwig-Maximilians-Universität, pictured in Figure 2.1b. Each one of the particle size distributions (<63, 63-90 and >90 μm) to an isothermal range of temperatures 200, 300, 400, 500, 600, 700 and 800 °C, for the exposure times of 1, 3, 5, 15, 30 and 60 min.

The sample material was placed inside the reactor bulb in a split three-zone Carbolite HZS-12/-/900/E301 horizontal tube furnace (Figure 2.1b-6). For the hydrous experiments, a SPETEC Perimax-12 low-flow peristaltic pump (Figure 2.1b-5) connected to a Meinhard Glass Products Q-HEN-150-A quartz nebulizer, fed water into the reactor as an aerosol. The gas mixture used for anhydrous conditions consisted in a 100 standard cubic centimeter per minute (sccm) gas stream consisting of 99 mol.% Ar and 1 mol.% SO_2 (see SO_2 bottle in Figure 2.1b-2), plus a 225 sccm CP grade Ar flow as carrier gas. To also test the behavior of monovalent cations (i.e., Na^+, K^+) diffusion under more oxidizing conditions, an experiment was conducted with pre-oxidized material. This is of relevance, given the fact that, diffusion of monovalent cations strongly depends on their role in the melt (e.g., as charge compensating cations or network modifiers), which is in turn also influenced by the redox state of network former cations like iron (Mysen et al., 1980). Consequently, an experiment where the redox state of iron, expressed as $Fe^{3+}/\Sigma Fe$ of the initial material, was higher, than its original value 0.153, was designed.

This was achieved by pre-heating 2 g of original powdered glass, of the grain size distribution 63-90 μm at 700 °C for 1 h. Following the pre-heating, the sample was treated under anhydrous conditions (SO_2-Ar) at 600 °C for 1 h. For the hydrous conditions, only the grain size distribution of 63–90 μm was used. This is justified because the underlying mechanisms of gas scavenging were elucidated in the anhydrous experiments, and the hydrous experiments are simply designed to test the difference that results from the addition of water. The temperature-series experiments were performed at 400–800 °C for 60 minutes. Eleven different flow rates of H_2O were used, ranging from 0.05 to 7 ml min^{-1} using the constant 1 mol.% SO_2 and 99 mol.% Ar.

Under the conditions tested, this resulted in a mol. % of water vapour of 0.01–96.41, these were selected by taking the flow rate range available of the peristatic pump used to nebulize water flow. At one flow rate of water (0.4 ml min^{-1}) time-series experiments (1–60 min.) at 600–800 °C were conducted. An additional set of HCl, and HCl-H_2O experiments was conducted, using the same material described above. Analogous to the SO_2 anhydrous experiments, the HCl experiments were conducted in a 100 sccm gas stream of 99 mol.% Ar and 1 mol.% HCl (see HCl bottle in Figure 2.1b-1), an additional 225 sccm CP grade Ar stream was used as carrier gas. For the anhydrous experiments, the HCl uptake of the material was tested for the three grain size distributions (<63, 63–90, >90 μm), also 2 g of each grain size distribution were exposed to the HCl-Ar gas mixture for between 1 and 60 minutes, at between 200 and 800 °C. For the hydrous experiments, additional to the above-mentioned gas mixture, eleven water vapor mol.% (0.01–96.41) were added. As in the case of the SO_2-H_2O experiments, only a single grain between 63 and 90 μm chosen to be tested at hydrous conditions.

2.5.2 HPG8 glasses

For the HPG8 set of samples, the same experimental protocol, to test its SO_2-sequestration potential at high temperatures, was done as for the Krafla obsidian, but the number of experiments was slightly reduced. This is because the Krafla-set of experiments were done previous to the HPG8 and the result I got showed clear experimental trends where SO_2 uptake efficiency was higher, so the

number of experiments were reduced to focus on the most relevant ranges of time and temperature for the HPG8 samples. For this, only one grain size distribution was used (63-90 μm), the temperature range was reduced to 600, 700 and 800 °C as well as the the exposure time, to only 5, 15 and 30 min. Also, only anhydrous experiments were conducted for this set of glasses. All experiments were terminated by rapid quenching in air by removing the sample bulb quickly from the AGAR. After each experiment, the samples were taken out of the reactor and left to cool to room temperature. The quenched samples were collected and stored in glass vials.

2.6 Analytical techniques

After the experiments were performed, various analytical techniques were used to characterize surficial changes of the material (e.g., nature, shape and abundance of surface products, changes in the surface morphology) as well as bulk changes (e.g., cation diffusion, redox state of iron, glass network).

2.6.1 Ion-exchange chromatography

This is an analytical technique, that allows physicochemical separation and identification of analytes (chemical species of interest) dissolved in a liquid sample. The basic elements of ion-chromatography are the liquid sample, the mobile phase (or eluent), a stationary phase (or separation column) and a detector. The mobile phase, is a liquid solution that flows together with the sample though the stationary phase. The separation occurs when the surface of the stationary phase, containing radical groups that have affinity with the ions in the sample, interacts and forms short-lived bonds with the analyte. These bonds result in retention of the ions at the stationary phase surface. The mobile phase however, continues to flow and has also an affinity to the stationary phase material, so that after a time lapse, called "retention time", the analyte species retained at the stationary phase will be released, replaced by the affine species from the mobile phase, and will leave the stationary phase, flow into the detector (in the case of ion chromatography, a conductivity detector is used) and the detector will send a signal proportional to the concentration of the ion. A depiction of cation ion-exchange is shown in Figure 2.8a. Each ion will have a distinctive retention time, at which it leaves the stationary phase, which allows a precise qualitative identification of the ion.

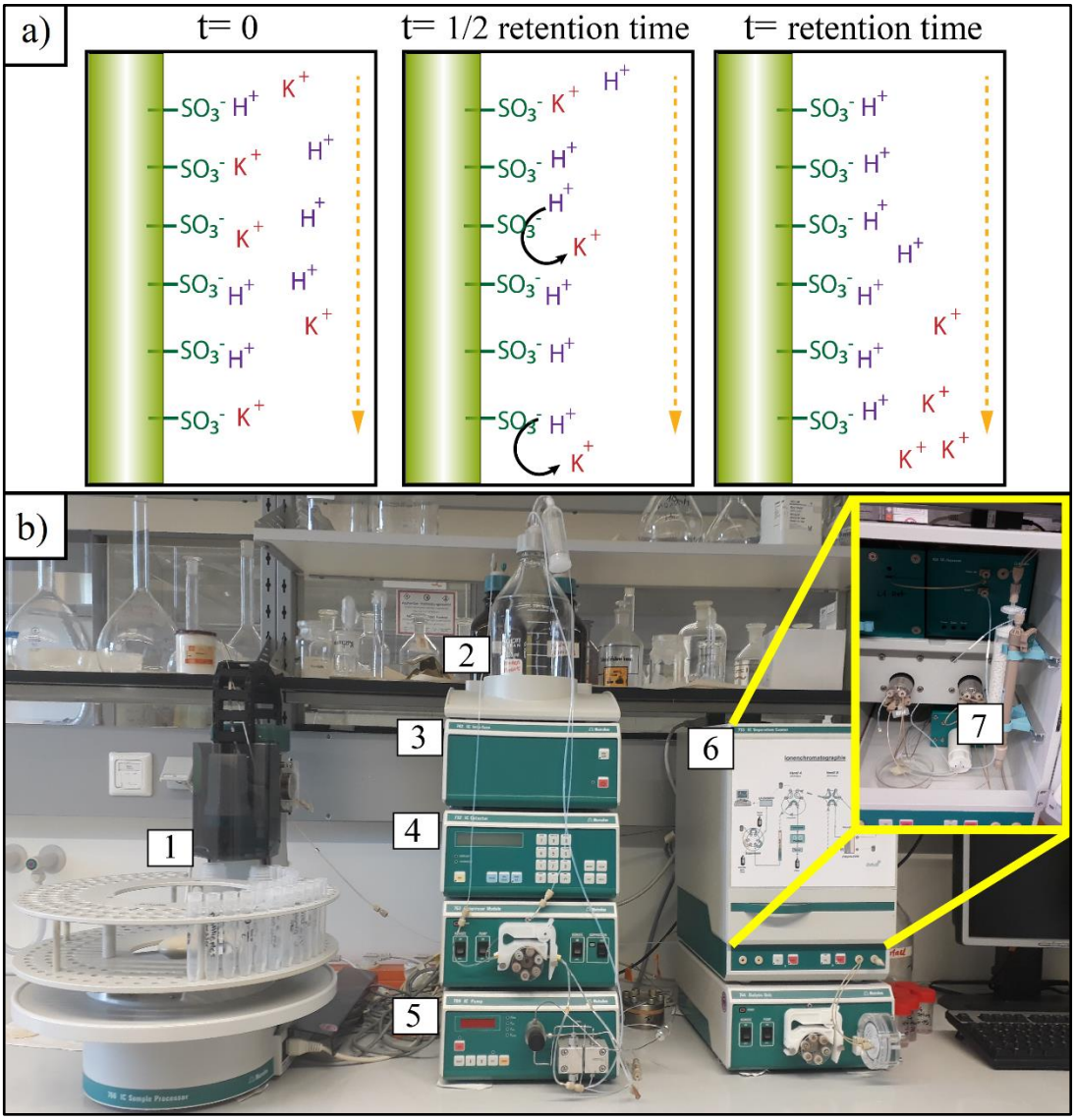

Figure 2. 8 Ion Chromatography system. a) Stages of ion-exchange (in this case, cation) chromatography. The green column represents the stationary phase, which surface consists in sulfite (SO_3^-) radicals with affinity to positive charges. The protons (H^+, in purple), represent the dissociated mobile phase, which originally consisted in HNO_3. The potassium cation (K^+ in red) represents the cation of interest dissolved in the sample. The orange dotted arrow shows the flow of the sample-mobile phase solution. At t=0, the sample is flown to the stationary phase and some potassium cations are retained, as well as some H^+. At t=1/2 retention time, all potassium cations have been retained, and as the mobile phase continues to flow, the cation exchange starts (black curved arrows). At t=retention time, all the potassium cations have been released and start flowing to the detector. b) Picture of the elements of the Ion Chromatography system: 1) 706 IC Sample Processor, 2) Eluent, 3) 762 IC Interface, 4) 732 Conductivity Detector, 5) 709 IC Pump, 6) 733 Separation Center and 7) the separation column.

	Ion Analysis	
Analytical Conditions	**Anions**	**Cations**
Separation Column (Stationary Phase)	Metrosep A Supp 5–150/4.0	Metrosep C4-150/4.0
Pre-column	Metrosep A SUPP 4/5 Guard/4.0	Metrosep C4 Guard/4.0
Eluent solution (Mobile Phase)	Na_2CO_3 3.2 mM + $NaHCO_3$ 1 mM	HNO_3 34mM + $C_7H_5NO_4$ 14 mM
Flow Rate (mL min^{-1})	0.7	0.9
Temperature (°C)	25	
Sample Size (µL)	20	

Table 2. 2 Analytical conditions for the ion-chromatography determinations. Leached samples were analyzed for anions and cations

To quantify the amount (concentration of each ion), analysis of known concentrations of ions are flown into the system and though a conductivity detector, the concentration can be directly linked to an electrical conductivity signal, thus calibration curves can be created to develop a quantitation method.

All samples were leached at room temperature with deionized water (conductivity ≤ 4.3 µS cm^{-1}) for 1 h at a 1:250 solid:water ratio, followed by vacuum filtration through a 0.22 µm mixed cellulose ester membrane. Ion analysis for anions (F^-, Cl^-, SO_4^{2-}, NO_3^-) and cations (Li^+, K^+ Na^+, NH_4^+, Ca^{2+} and Mg^{2+}, Mn^{2+}), were performed with a Metrohm Ion Chromatography system. The later consisted in a 706 IC Sample Processor, 762 IC Interface, 732 Conductivity Detector, 709 IC Pump, 733 Separation Center, as seen in figure 2.8b-1-6, respectively at the Ludwig-Maximilians-Universität. Detailed analytical conditions are shown in Table 2.2

2.6.2 Bulk FeO determination ($K_2Cr_2O_7$ potentiometric titration)

The redox state of iron, was determined as FeO wt.% by potentiometric titration based on the method described by Shapiro and Brannock (1956), using a 665 Metrohm Titroprocessor, a 685 Dosimat automatic titrator connected to an 649 Magnetic Swing-out Stirrer with an electrode holder and a platinum reference (silver-silver) electrode, pictured in Figure 2.9b-1,3,6,4 respectively.

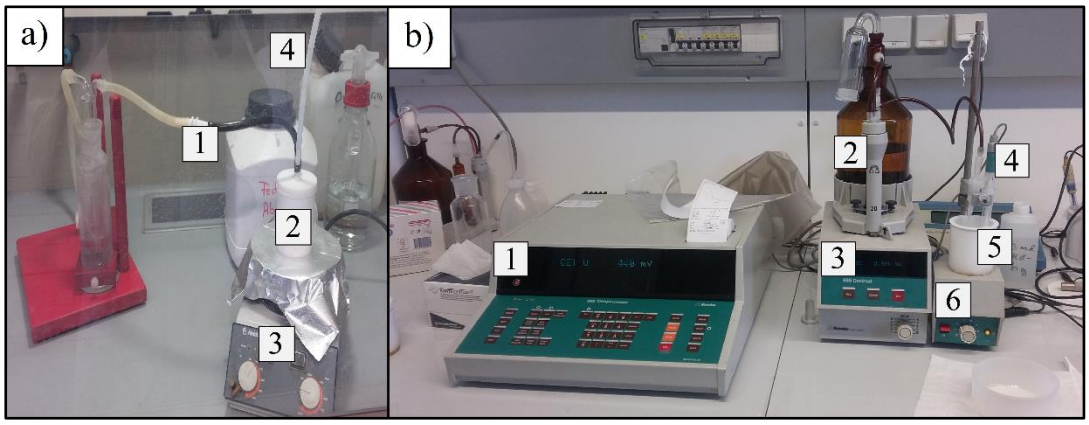

Figure 2. 9 Picture of the potentiometric titration system. The pre-step of dissolving the sample takes place in the set up showed in a) which is composed of : 1) is the hose connected to the Teflon crucible that feeds CO_2 into the crucible in order to avoid oxidation of the sample by contact with air during the dissolution, 2) is the Teflon crucible containing the sample, and the acid mixture (HF+ H_2SO_4+ H_3BO_3), 3) is the hot plate to heat the crucible, i.e., the sample, and 4) is the output-hose for the CO_2 flux. Once the sample is dissolved, the titration takes place in the system showed in b), which is composed of 1) The data processing system (686Titroprocessor), 2) the $K_2Cr_2O_7$ 0.01N solution, 3) the automatic titrator (665 Dosimat), 4) the reference electrode, 5) the crucible with the dissolved sample and a magnetic stirrer inside, and 6) the magnetic stirrer plate.

The analysis consisted in acid dissolution of approximately 25 mg of sample, by placing the weighted sample in a Teflon crucible, adding ~5 mL of deionized water (to bring the sample in solution) and 10 mL of a solution containing hydrofluoric acid (HF), sulfuric acid (H_2SO_4) and deionized water in a in proportion of 0.8:1:3. The Teflon crucible was then covered with a Teflon cap with two Teflon hoses on top. One of the hoses lets CO_2 flow into the crucible (the black hose shown in Figure 2.9a-1), to avoid additional oxidation of the solution, to the interior of the crucible (without contact with the sample-solution), while the other serves as output for the gas (white hose Figure 2.9a-4).

The crucible was brought to ~100 °C and the sample was let to boil for approximately 30 minutes, after which, the crucible was partially immersed into a container filled with cold water, and left to cool for ~20 min. Once the Teflon crucible was cooled to room temperature, the sample crucible was disconnected from the CO_2 flux, 15 mL of boric acid (H_3BO_3) were immediately added, a small magnetic stirring bar was put into the crucible, the electrode was put in contact with the

solution and the titration was started (Figure 2.9b-5). The titration solution was $K_2Cr_2O_7$ 0.01N (Figure 2.9b-2), when in contact with the dissolved ferrous iron, the following redox reaction occurs:

$$6Fe^{2+} + Cr_2O_7^{2-} + 14H^+ = 2Cr^{3+} + 6Fe^{3+} + 7H_2O \qquad \textbf{Equation 2. 1}$$

The dichromate ion ($Cr_2O_7^{2-}$) acts as the oxidizing agent for the ferrous iron (Fe^{2+}). When the all $Cr_2O_7^{2-}$ has reduced to Cr^{3+} (i.e., all Fe^{2+} has oxidized to Fe^{3+}), the sample-solution will change its color, from an initial translucid color to light yellow, when the oxidation is complete. The electrical voltage measured with the electrode, increases accordingly with the change of color and records an "endpoint" when the color no longer changes. At this point the titration stops and the mL of the $K_2Cr_2O_7$ 0.01N solution consumed are calculated in wt.% of FeO. Next, the concentration of ferrous iron, Fe^{2+}, can be obtained as shown in Equation 2.2:

$$(wt.\%FeO_{titrated})*0.77 = wt.\%\ Fe^{2+} \qquad \textbf{Equation 2. 2}$$

where, 0.77 is the ratio between the molecular weights of ferrous iron and ferrous oxide, i.e., Fe^{2+}/FeO. The concentration of ferric oxide, Fe_2O_3, can also be obtained from the ferrous oxide value obtained by titration (wt.% FeO), and knowing the amount of total iron (FeO_{total} = FeO + Fe_2O_3, in wt.%), as seen in Equation 2.3:

$$(wt.\%\ FeO_{total} - wt.\%\ FeO_{titrated})*1.111342 = wt.\%\ Fe_2O_3 \qquad \textbf{Equation 2. 3}$$

where, FeO_{total} is the total iron oxide content, obtained by electron probe micro analyzer (EPMA) analysis, $FeO_{titrated}$ is, as for the previous equations, the value directly obtained by the potentiometric titration and 1.111342 is the molecular weight ratio Fe_2O_3/2FeO. Once the concentration of ferric oxide has been calculated, according to Equation 2.3, the concentration of ferric iron, Fe^{3+}, can be obtained by applying Equation 2.4, as follows:

$$(wt.\%\ Fe_2O_3)*0.69=wt.\%Fe^{3+} \qquad \textbf{Equation } \textbf{\textit{2. 4}}$$

where, wt.% Fe_2O_3 is the concentration obtained from Equation 2.3 and 0.69 is the molecular weight ratio between ferric iron and ferric oxide, i.e., $2Fe^{3+}/Fe_2O_3$. Once the ferrous and ferric iron concentrations were calculated, from Equations 2.2 and 2.4, respectively, the bulk redox state iron of the samples could be expressed as the ferric iron, relative to the abundance of the sum of both cations, i.e., $Fe^{3+}/(Fe^{3+}+Fe^{2+})$ or $Fe^{3+}/\Sigma Fe$. Determination of FeO of a synthetic reference material containing 18.8 wt.% FeO, was used to evaluate the accuracy of the method. The standard deviation of the measurements was less than 0.2.

2.6.3 Field-emission scanning electron microscope

This method allows the determination of mineral structures and micro-scale imaging of samples. The scanning electron microscope works with a focused beam of high-energy electrons directed to the sample surface. The impact (kinetic) energy is dissipated in the form of emission of secondary electrons (resulting in surface imaging), backscattered electrons and diffracted backscattered electrons, which give information about in mineral structures and orientation), among others, which are detected by mass spectrometers.

Approximate spot-analyses of particle glass chemistry and images of pre- and post-treated samples, as polished thick sections and powder, were determined using the back-scattered electron detector (BSED) on a Hitachi field-emission scanning electron microscope (FE-SEM) SU5000 equipped with energy dispersive spectrometers, at the Ludwig-Maximilians-Universität.

2.6.4 Electron probe micro-analyzer (EPMA)

This device operates under the same fundamental principles as the field-emission scanning electron microprobe, with the difference that it additionally allows the acquisition of chemical data by spot-size analysis (1-2 μm), which was useful to determine chemical diffusion profiles in our samples. The bulk chemical composition of the glasses, prepared as carbon-coated thick polished sections, was measured with a Cameca SX-100 electron probe micro-analyzer at the Ludwig-Maximilians-Universität, with a LaB6 cathode and five spectrometers.

HPG8 + 1% CaO												
Sample	+ 0%FeO		+ 0.1%FeO		+ 1%FeO		+ 1.5%FeO		+ 2%FeO		+ 2.5%FeO	
	Mean	St Dev	Mean	St Dev	Mean	St Dev	Mean	St Dev	Mean	St Dev	Mean	St Dev
SiO_2	78.28	0.36	77.41	0.48	78.19	0.34	76.88	0.54	77.47	0.53	77.08	0.31
TiO_2	0.02	0.02	0.02	0.03	0.02	0.02	0.02	0.02	0.03	0.03	0.03	0.03
Al_2O_3	11.76	0.13	11.7	0.15	11.66	0.25	11.42	0.36	11.45	0.17	11.35	0.13
FeO_T	0.09	0.06	0.15	0.04	1.04	0.06	1.57	0.14	2.04	0.06	2.59	0.16
MgO	0.02	0.01	0.02	0.01	0.02	0.01	0.02	0.01	0.02	0.01	0.01	0.01
CaO	1.14	0.06	1.11	0.05	1.12	0.03	1.1	0.04	1.11	0.04	1.14	0.04
Na_2O	4.58	0.11	4.58	0.07	4.43	0.11	4.29	0.16	4.23	0.1	4.1	0.1
K_2O	4.07	0.06	4.04	0.05	4.01	0.05	3.98	0.08	3.93	0.06	3.96	0.04
SO_2	0.01	0.01	0	0	0.01	0.01	0.01	0.01	0.01	0.01	0.01	0.01
P_2O_5	0.04	0.02	0.05	0.02	0.04	0.02	0.04	0.01	0.04	0.01	0.03	0.01
Total	100		99.07		100.55		99.32		100.31		100.29	

HPG8 + 2% CaO												
Sample	+ 0%FeO		+ 0.1%FeO		+ 1%FeO		+ 1.5%FeO		+ 2%FeO		+ 2.5%FeO	
	Mean	St Dev	Mean	St Dev	Mean	St Dev	Mean	St Dev	Mean	St Dev	Mean	St Dev
SiO_2	76.34	0.64	76.48	0.45	75.38	0.55	75.5	0.26	76.32	0.4	74.36	0.79
TiO_2	0.03	0.03	0.02	0.03	0.04	0.03	0.02	0.02	0.01	0.02	0.04	0.04
Al_2O_3	11.78	0.22	12.02	0.17	11.44	0.11	11.25	0.15	10.89	0.09	11.44	0.07
FeO_T	0.04	0.02	0.15	0.02	1.02	0.02	1.51	0.04	2	0.07	2.45	0.08
MgO	0.01	0.01	0.02	0.01	0.01	0.01	0.02	0.01	0.02	0.01	0.02	0.01
CaO	2.19	0.06	2.19	0.03	2.14	0.05	2.17	0.05	2.18	0.04	2.15	0.05
Na_2O	4.43	0.1	4.69	0.04	4.36	0.06	4.27	0.07	3.94	0.05	4.2	0.1
K_2O	4.22	0.05	4.15	0.04	3.99	0.06	3.8	0.05	3.93	0.03	3.95	0.06
SO_2	0.01	0.01	0.01	0.01	0.01	0.01	0.01	0.02	0.01	0.01	0.01	0.01
P_2O_5	0.04	0.02	0.04	0.02	0.05	0.02	0.04	0.02	0.03	0.02	0.02	0.02
Total	99.11		99.77		98.45		98.59		99.32		98.63	

Sample	Krafla natural calc-alkaline obsidian	
	Mean	St Dev
SiO_2	75.95	0.61
TiO_2	0.22	0.03
Al_2O_3	11.91	0.12
FeO_T	3.26	0.08
MgO	0.09	0.01
CaO	1.7	0.04
Na_2O	3.74	0.5
K_2O	2.65	0.04
SO_2	**0**	**0**
P_2O_5	0.02	0.01
Total	99.54	0.14

Table 2. 3 Bulk chemical composition of the experimental glasses as determined by electron probe micro-analyzer spot-analysis. Mean composition values were obtained by measuring 10-15 spots per sample. The upper and middle tables show the HPG8 sub-set of samples containing 1 and 2 wt.% CaO, respectively, each one with different wt.% FeOtotal amounts (0-2.5). The lower part of the table shows the Krafla obsidian composition.

Measurements for were carried out with a 15 kV acceleration voltage and a 10 μm diameter defocused beam with 5 nA beam current. In the case of the HPG8 glasses the beam has a diameter of 5 μm. The defocused beam was used for all elements to minimize alkali loss. The standards used to calibrate the measurements were: synthetic wollastonite (for calcium and silicium), periclase (for magnesium), hematite (for total iron ´Fe_{total}´), natural orthoclase (for potassium und aluminum), and albite (for sodium).

Chemical homogeneity was confirmed for all HPG8 and for the natural calc-alkaline rhyolitic obsidian, by performing 20 spot analysis on each glass; in the case of the set of HPG8 glasses each one of the twelve samples (doped with 1 and 2 wt.% CaO and 0, 0.1, 1, 1.5, 2 and 2.5 wt.% FeO each) were measured. Bulk chemistry results of each glass are shown in Table 2.3. Measured compositions of HPG8 glasses agree with the desired compositions (calcium and iron oxide contents), while the measured composition for the calc-alkaline rhyolite is also in agreement with the bulk composition reported by Tuffen and Castro (2009).

2.6.5 Raman spectroscopy

This method allows the detection of vibrations associated with structural features of materials, due the Raman scattering phenomenon. In the particular case of silicate glasses, this analytical technique can be applied to identify compositional and structural features by analyzing the obtained glass spectra. The principle of this technique is that, when a radiation source (photons), in this case a laser (monochromatic radiation), is contact with a material, most of the energy will pass through the system, i.e., will be transmitted, exactly as it was emitted, while some of this energy will not be conserved and will instead be adsorbed or scattered.

Scattering of photons by a material, can occur elastically, if the scattered photons conserve the energy of the incident photons, and only their direction changes (Rayleigh scattering), but if the photons also change their direction, the scattering is said to be inelastic. Scattering of inelastic photons produces a shift in energy, called Raman shift, which is expressed as wavenumber (cm^{-1}). The Raman spectra of a material, consists of Raman "peaks" or bands, which are related to the vibrations of the constituents of the material (atoms, molecules, ions).

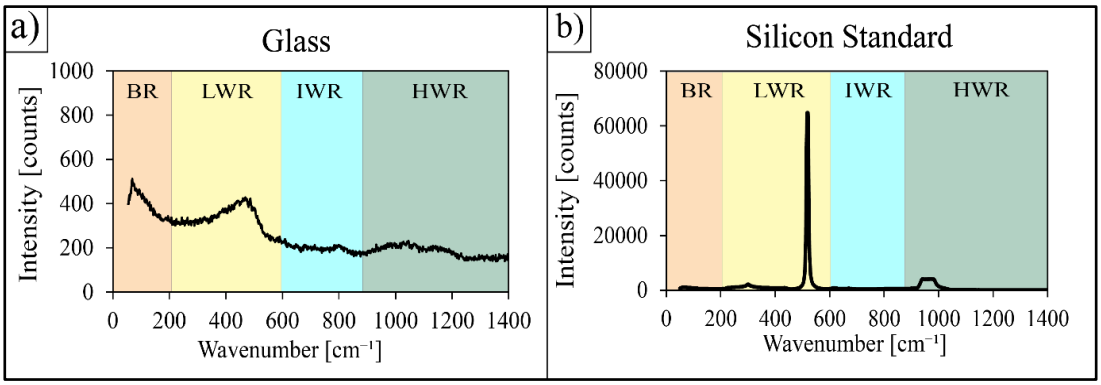

Figure 2. 10 Example of a Raman spectra. Four distinctive regions for structural/compositional glass features can be seen, the orange band corresponds to the Boson region (BR), the yellow band corresponds to the low wavenumber region (LWR), the blue band corresponds to the Intermediate wavenumber region (IWR) and the green band corresponds to the high wavenumber region (HWR). In a) the Raman spectra of the pristine obsidian can be seen. At the LWR, a peak at ~500 cm^{-1} indicated the presence of bonding oxygen bonds. In b), the spectra of the Silicon standard used as reference material to corroborate the accuracy of the measurements, can be seen. It displays a high-intensity peak (note the difference on the axis scale, with respect to that of the glass chip), at the wavenumber of 521 cm^{-1}, i.e., in the LWR.

As each material interacts distinctively to the incident radiation, this effect is used to "finger print" their structures, since each spectrum reflects specific chemical bond vibrations of a material. This technique has been applied to study the structure of silicate glasses (e.g., McMillan and Piriou, 1983; Mysen and Toplis, 2007; Bell and Dean, 1972; Furukawa et al., 1981; McMillan, 1984; Neuville et al., 2014; Rossano and Mysen, 2012), and have recognized recurrent features in silicate glasses spectra.

In general, four regions can be distinguished for silicate glasses spectra that correspond to vibrations caused by differences in the glass network structure: (1) The Boson Region, from 10-250 cm^{-1}, comprises the region dominated by a scattering continuum and the Rayleigh tail of the excitation source (Bell et al., 1968; McMillan et al., 1994), this region is however, not related to the glass structure and will be dismissed in the following figures, (2) the low wavenumber region (LWR), from ~250-600 cm^{-1}, which is associated with vibration modes of bridging oxygen atoms (BO) with poly-membered rings of tetrahedra (i.e., 4+ cations), that forms silicate networks, (3) the intermediate wavenumber region (IWR) located at ~600-

Parameter	Value
Laser Wavelength (mm)	532
Laser Filter (%)	50
Grating	1800T
Confocal Hole	500
Spectral slit	100
Central Position	3085.62
Spectral Range (cm^{-1})	50-400
Exposure Time (sec)	8
Accumulation Number	2
Spike Removal	Multi
Objective	x100

Table 2. 4 Analytical parameters used for Raman spectroscopy measurements of HPG8 glasses and the Krafla obsidian.

850 cm^{-1}, represents the structural contribution of the Si-O bond stretching; specifically, the vibrations in the Si-O-Si plane or vibrations of the encaged Si-atom in the tetrahedra (McMillan et al., 1994) and finally, (4) the high wavenumber region (HWR), seen at ~850-1300 cm^{-1}, its related to the vibration modes of bonds between non-bridging oxygens (NBO) and fourfold-coordinated cations, i.e, Si^{4+}, Al^{4+}, Ti^{4+}, Fe^{3+}, (McMillan, 1984; Mysen, 2003).

Additionally, some spectra of hydrous glasses display a water region (WR) in the range ~2800-3800 cm^{-1}, which relates to vibrations of the O-H bond. In Figure 2.10a, an example of a Raman spectra acquired for the pristine Krafla Obsidian used in this work is shown. The vertical axis represents the intensity counts (arbitrary units) of the signal, and the horizontal axis the wavenumber (cm^{-1}). Raman spectra were acquired for both thick polished sections and glasses with a for which a green argon ion laser (532 nm) was used. The laser provided a power at the sample surface of ~2.5 mW, was focused through the 100× objective to a ~1 μm spot. A silicon standard was used as reference material to ensure the reproducibility of the measurements (Figure 2.10b). In all cases, the standard deviation of the measurements was less than 0.4. Specific measuring parameters are listed in Table 2.4.

Chapter 3

Results of SO_2 and HCl uptake by rhyolitic glasses

3.1 Introduction

In this chapter, the results of the gas (i.e., gas mixtures of SO_2-Ar, SO_2-Ar-H_2O, HCl-Ar and HCl-Ar-H_2O) uptake experiments by rhyolitic glasses will be presented. These results were obtained by analyzing both the pristine glasses (the initial untreated glasses) and treated samples by a wide range of techniques. High temperature SO_2 uptake potential of rhyolitic glasses was tested for two sets of glasses: the first one consisted of a natural calc-alkaline obsidian, while the second one consisted of a set of synthesized haplogranitic glasses, doped with diverse amounts of CaO and FeO (wt.%). HCl uptake potential was only tested for the calc-alkaline rhyolitic glass. The gas uptake experiments consisted of exposing powdered glass samples to SO_2-Ar and HCl-Ar gas mixtures (under hydrous and anhydrous conditions) in the AGAR device (described in section 2.2, Chapter 2,) for diverse time- and temperature-series (1-60 minutes and 200-800 °C, respectively).

Assessment of the uptake potential of all glasses was based, to a great extent on results obtained from ion chromatography analysis of leachates of treated samples, which provided precise information about the chemistry of the soluble products formed on the surface of the sample-particles treated under the various variables tested here. Further characterization of non-treated and treated samples, consisted on scanning electron microscope analysis with back-scattered electrons (SEM-BSE) and energy- dispersive X-rays (SEM-EDS), bulk iron redox state measurements (wt.% FeO determinations), Raman spectroscopy and electron probe micro-analyzer (EPMA) analyses.

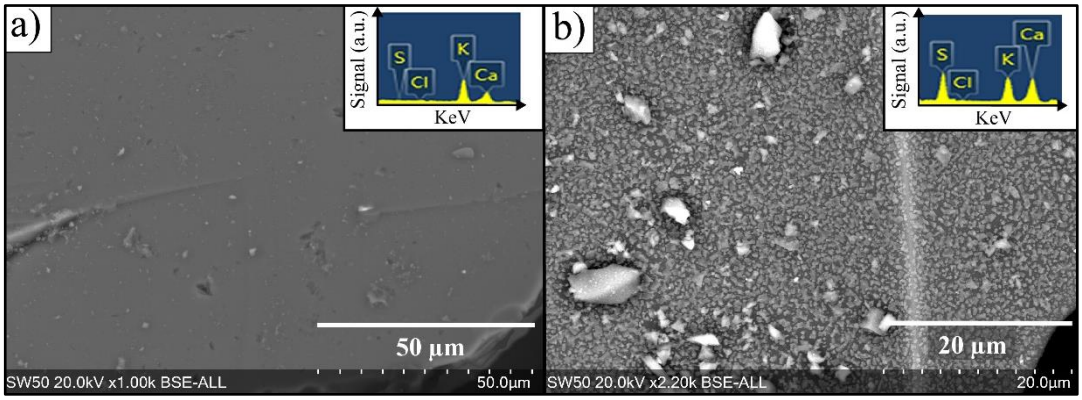

Figure 3. 1 SEM-BSE images of non-treated and treated samples. a) Surface of a non-treated sample grain of the sieved grain size distribution >90 µm is pictured. Small surficial particles are simply fragments of the material. On the top right of the picture, the EDS signals are shown for the surface of the grain, confirming no sulfur is present on the surface of the untreated material. b) surface of a treated sample grain of the grain size distribution >90 µm, with SO_2-Ar mixture at 800 °C for 60 min. on top right of this figure, the EDS spectra can also be seen and shows both the appearance of the sulfur peak, as well as an increase in the surficial calcium signal.

3.2 SO_2 uptake by natural calc-alkaline rhyolitic obsidian

3.2.1 SO_2-anhydrous experiments

The first set of SO_2 uptake experiments consisted in exposing powdered calc-alkaline rhyolite particles to a gas mixture of SO_2-Ar (1 mol.% SO_2 and 99 mol.% Ar), at diverse temperatures and exposure times (see section 2.4.1 in Chapter 2).

3.2.1.1 Scanning electron microscope (SEM) analysis

Formation of surficial products resulting from the SO_2-glass particles reactions was visually and qualitatively evaluated with the SEM. Visual evaluation of the surficial products formed on the glass particles was done by acquiring images of non-treated and treated samples, both analyzed as without any sample preparation.

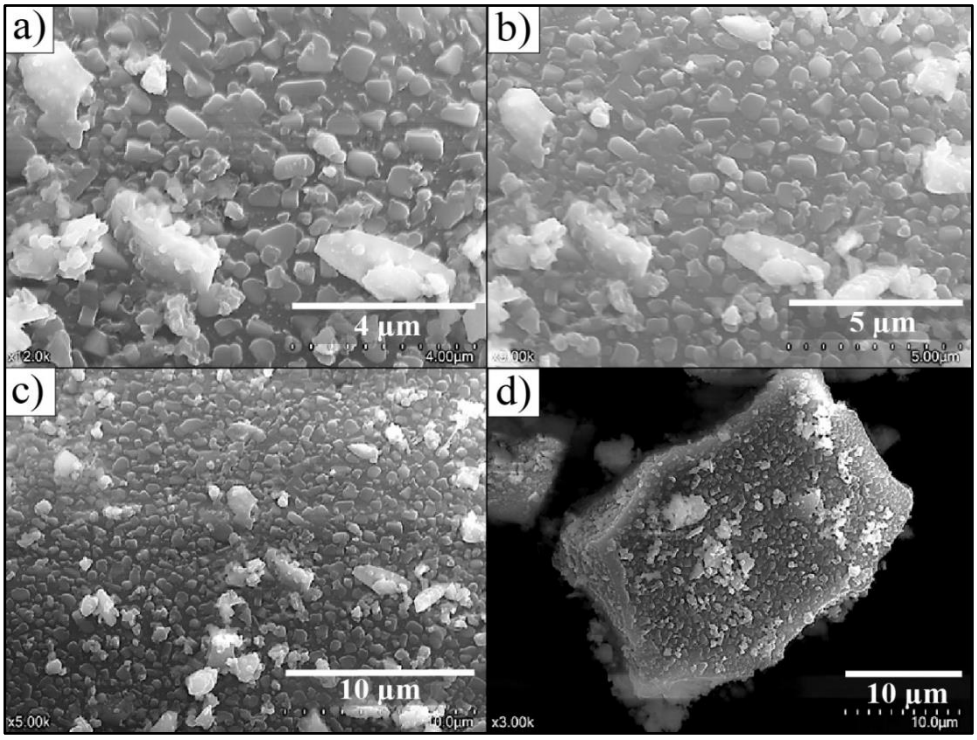

Figure 3. 2 SEM-BSE images of the morphology of surficial sulfate-bearing salts. Surfaces of samples of the grain size distribution 63-90 µm, treated at 800 ℃ for 60 min. The surface products have mostly sharp angular cubic-like shapes and seem to cover the surface of the glass particles uniformly. The two upper images were made with an increased zoom with respect to the lower pictures, to show more closely the characteristics of the surficial grown salts.

Also, to qualitatively assess the chemistry of the non-treated glass particles and of the surficial products formed during the experiments, samples were analyzed with energy-dispersive X-rays (SEM-EDS). Treated samples were mounted in epoxy as thick sections and polished to be also analyzed with SEM-EDS. The thick sections had a diameter of 2.5 cm and a height of 0.7 cm. This was done because previous studies on SO_2-glass reactions (i.e., Ayris et al., 2013) have suggested that the main mechanisms for high temperature SO_2 uptake by glass is cation (mainly calcium) which react with SO_2 molecules at the particle surface interface to form surficial S-bearing products. Therefore, occurrence of cation diffusion would be evidenced for the treated samples if internal bulk chemistry is also analyzed. Results of the SEM-BSE images of non-treated and treated samples- can be seen in Figure 3.1.

Here, non-treated sample-grain (Figure 3.1a) showed nominally featureless glassy surfaces, while the grain shown in panel b, corresponding to a sample treated at 800 °C for 60 minutes, displays on its surface multiple small angular crystals. Energy dispersive (EDS) X-ray spectra are shown in an inset in both images, which show absence of volatiles S, Cl, on the surface for the non-treated sample, while for the treated sample, the signal of sulfur appears along with an increase of the calcium signal. Further SEM-BSE images of treated samples can be seen in Figure 3.2a-d, where four sample-grains images were taken with different magnifications. The products appear to be angular cubic-like crystals of different sizes in the order of tenths of nanometers, and be uniformly distributed on the glass surface, without any preferential formation sites.

SEM-BSE and -EDS analyses of polished thick sections were done also for the non-treated and treated glass powders to gain insights into internal particle bulk chemistry changes resulting from the formation of surficial products. Figure 3.3 shows images of elemental maps of S, Ca, Na, and K obtained for polished surfaces of non-treated and treated samples. In the case of the non-treated surfaces (Figure 3.3a-e) a homogeneous distribution of the analyzed alkali and alkaline-earth elements can be observed, as well as negligible presence of sulfur. For the treated sample surfaces (Figure 3.3f-j), an overall increase of the signal of Ca and S.

In the case of sulfur, its presence in the sample appears only in the treated samples, and seems to be notably high at the edges of the particles (Figure 3.3g), whereas the presence of calcium noticed both in the non-treated and treated samples, shows an increased spatial distribution at the edges of the particles. Regarding the spatial distribution of sodium and potassium (Figure 3.3i,j), both non-treated and treated samples, do not show a noticeable increased signal on the particle edges (as observed for calcium and sodium), suggesting preferential formation of sulfur bearing Ca products, e.g., $CaSO_4$.

Another interesting feature is that, in the case of the calcium mapping, dark zonings are seen on the polished surfaces, just below of the enriched calcium layer of the polished particles (see Figure 3.3h). In panels k,l and m of Figure 3.3, this is further shown with magnified images of calcium elemental maps. This observation could only be made for calcium, and was not seen for any other cation.

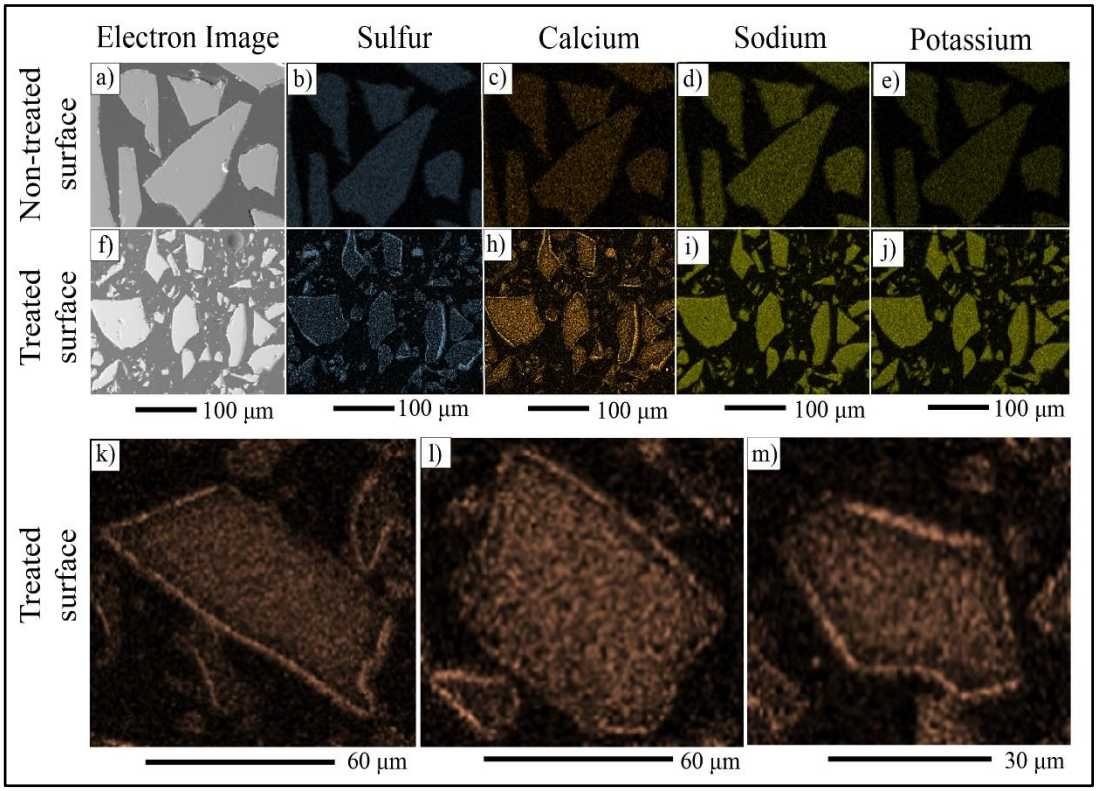

Figure 3. 3 Energy dispersive X-ray spectroscopy maps for S, Ca, Na and K of polished particle surfaces. Elemental maps showing the spatial distribution of S, Ca, Na and K of polished sample surfaces were obtained for a non-treated sample (a-e), and a sample treated with SO_2 at 800 for 60 minutes (f-j). Both samples are of the particle size distribution of 63-90 µm. In panels k, l and m, show elemental maps of calcium of treated samples.

Apparent spatial depletion of calcium for treated samples, (not observed for the untreated samples) suggests migration towards the surface (edges of particles in Figure 3.3), due to diffusion.

3.2.1.2 Leachate analysis

SEM-BSE analysis visually confirmed the presence of multiple surficial products grown on sample surfaces after the time- and temperature-series of experiments, and SEM-EDS analysis provided me with preliminary qualitatively information about the bulk chemistry of such surficial products and the particle bulk element distribution.

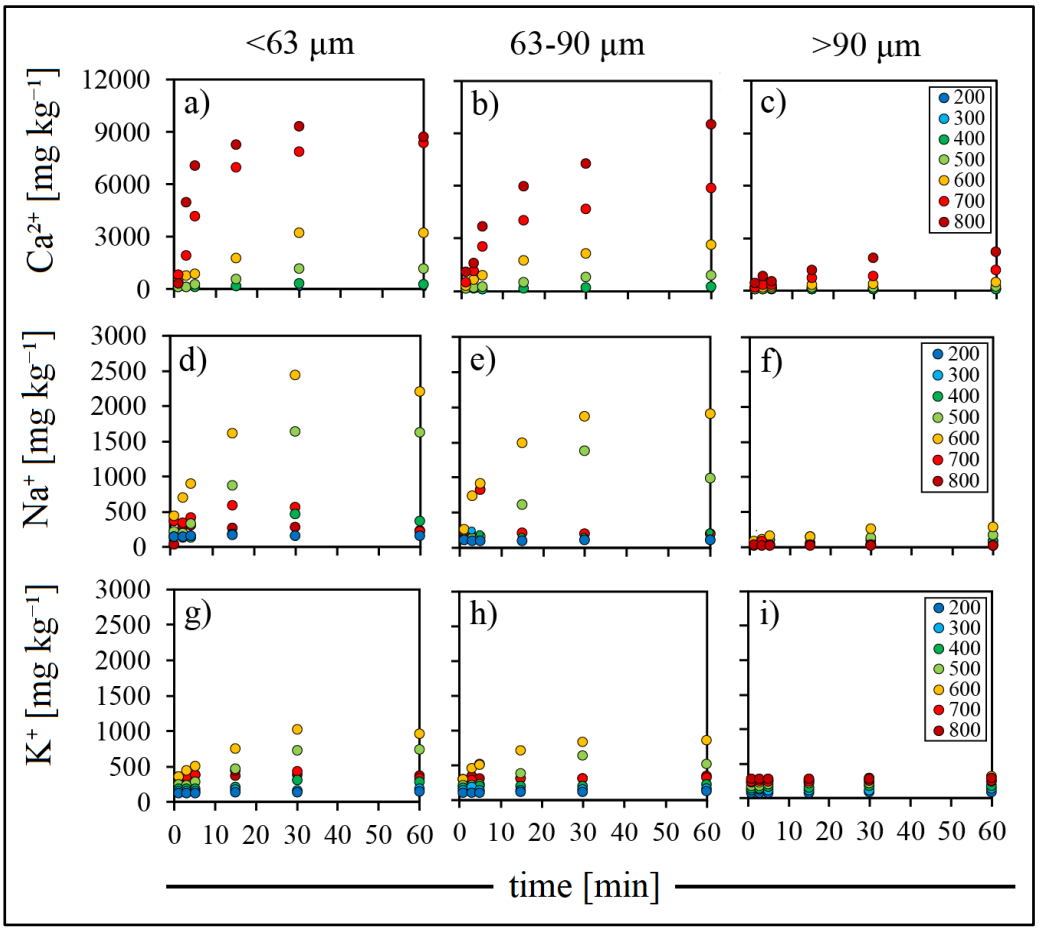

Figure 3. 4 Concentrations of leached cations from the anhydrous SO_2 experiments. Concentrations of leached Ca^{2+}, Na^{+} and K^{+} from treated samples are plotted against the exposure times (1-60 min.), for the three grain size distributions, <63 (a,d,g), 63-90 (b,e,h) and >90 µm (c,f,i). Treatment temperature of the experiments (200-800 °C) is indicated by the color -coding shown in the inset of plots c,f,I, where the colder colors represent the lower temperatures and the warmer colors, represent the highest temperatures. Also note that, the scale for the Y-axis, i.e., concentration of leached cation (mg kg^{-1}) is the same for Na^{+} and K^{+}, and different for Ca^{2+}. This aimed to show more clearly the evolution of concentrations of each cation, since concentrations of leached calcium were up to one order of magnitude greater than those of the leached monovalent cations.

However, quantitatively analysis of the surficial products was still to be determined. For this, I also analyzed the treated samples leachates with the ion chromatography analytical technique described in Chapter 2, section 2.5.1. Analyses of leachates were performed for of all time- and temperature- series of experiments, of the three grain size distributions <63, 63-90, >90 µm, in order to gain precise

information about the chemistry of the soluble surficial products formed during high temperature SO_2-glass interactions. Results of the ion chromatography analyses for calcium, sodium and potassium (Ca^{2+}, Na^{+} and K^{+}, respectively) are shown in Figure 3.4. Only these three cations were detected in the leachates and could therefore be measured. Concentration of leached cations are expressed as mg kg^{-1}, i.e., mg of the leached cation per kg of sample.

The concentrations of leached cations show good agreement with the SEM-EDS element spectra, where calcium was the only cation with significant presence on the edges that hinted at predominant surficial calcium bearing-products formed (see Figure 3.3h). Indeed, the main leached cation in all samples of all grain size distributions, exposure times and treatment temperatures tested (see Figure 3.4a,b,c), was calcium, reaching a maximum leached concentration of 9,488 mg kg^{-1}) for the experiment performed with the grain size distribution of 63-90 μm, at 800 °C for 60 min (Figure 3.4b). This concentration accounts for ~80% (79.97%, precisely) of the total bulk Ca in the particle, which was 11,864 mg kg^{-1} (i.e., 1.7 wt.% CaO, as seen in Chapter 2, section 2.5.4).

Behavior of leached calcium concentrations (Figure 3.4a-c) can lead to the general observation that leached calcium concentrations show higher values upon increasing temperatures, looking at the a-c plots, is clear that temperatures of 700 and 800 °C, were two to three times greater than for example, those obtained at 600 °C, while temperatures lower than 600 °C displayed rather negligible concentrations (see the filled blue and dark green circles). Increasing of the exposure time of the experiments also show a positive correlation with the concentrations obtained, since samples treated for short exposure times, i.e., 1, 3 and 5 minutes consistently showed the lowest concentrations of leached cations, while exposures times of 15, 30 and 60 minutes resulted in overall high cation concentrations.

The effect of grain size distribution of the samples showed to play also a strong role on concentrations of leached calcium, although the highest concentration value was obtained for the grain size distribution 63-90 μm, an overall enhancement of concentrations is seen, as the particle size distribution of the samples decreases. For instance, leached calcium concentrations of the grain size distribution <63 μm (Figure 3.4a) able to reach higher values in less time than those for 63-90 μm, while the grain size distribution >90 μm leads to the overall lowest concentration values.

Concentrations of leached sodium and potassium were minor when compared to those obtained for calcium (see the concentration scale in Figure 3.4d-i). This is noteworthy, given the fact that the bulk concentration of both sodium and potassium in the glass were 30,782 (3.74 wt.% Na_2O) and 23,273 (2.65 wt.% K_2O) mg kg^{-1}, thus greater than that of calcium, which was 11,864 mg kg^{-1} (1.7 wt.% CaO). In the case of Na^+ concentration, the maximum value obtained was 2430 mg kg^{-1}, for the sample of grain size distribution <63 μm exposed at 600°C for 30 minutes (see the yellow-filled circles in Figure 3.4d), which accounts for only 7.8 % of the bulk Na content in the glass. Leached concentrations of potassium were even lower when compared to the those of calcium or even with those of sodium, being the maximum leached concentration 1,020 mg kg^{-1}, for the sample of the grain size distribution <63 μm, exposed at 600°C for 30 minutes (see the yellow series in Figure 3.4g), which represents only 4.38 % of the total potassium in the glass.

Concentrations of leached monovalent cations Na^+ and K^+ clearly differ to those obtained for calcium, being the firsts much lower than the latter. Their concentrations display, however, noteworthy trends regarding the effect of the tested variables (exposure time, temperature and grain size distribution) on the obtained concentrations, and even share some similarities with some trends observed for calcium. A similar trend between monovalent cations and calcium concentrations, is that, both Na^+ and K^+ leached concentrations increase with decreasing grain size distribution of the samples, as for calcium concentrations, being the highest Na^+ and K^+ concentrations those obtained for samples of the grain size distribution <63 μm (see Figure 3.4d and g).

In addition, the effect of increasing exposure time also seems to have a positive effect on the concentrations of leached sodium (Figure 3.4d-f) and potassium (Figure 3.4g-i), as in the case of calcium (Figure 3.4da-c). The effect of temperature on leached sodium and potassium concentrations, initially seems to be similar to that observed for calcium, in that higher exposure temperatures led to higher concentrations, and increasing temperatures resulted in higher concentrations of both monovalent cations, however, this observation is only true for the temperature range 200-600 °C, unlike in the case of calcium, where this trend was consistent from 200 to 800 °C. At higher temperatures, i.e., 700 and 800 °C, both sodium and potassium concentrations decrease up to values of concentrations obtained at lower temperatures (i.e., 200-400 °C).

This consistently negative effect of temperature treatments of 700 and 800 °C on the leached monovalent cations concentrations, might be an indication that, formation of surficial Na- and K- bearing surficial products is less favorable at T> 600 °C. Besides analyzing the leachates for cations, analyses for a wide range of anions (F^-, Cl^-, SO_4^{2-}, NO_3^-) were also carried out by the ion chromatographic technique described in Chapter 2, section 2.5.1. Analyses for anions were performed, as in the case of cations, for all time- and temperature series of experiments of the three grain size distributions (<63, 63-90, >90 μm). As expected, the only detectable and measurable anion was sulfate (SO_4^{2-}), since the samples were exposed only to SO_2.

Concentrations of leached sulfate are plotted in Figure 3.5, and expressed as molal concentrations (mmol kg^{-1}) against the molal concentrations of each cation. This way of plotting leached sulfate and cations served the purpose to evaluate the molal ratios between cations and sulfate and be able to precisely determine which chemical compound (formed during the SO_2 exposure and leached afterwards) was formed. Molal ratios of $CaSO_4$ require a 1:1 behavior between calcium and sulfate, given the fact that one mole of leached calcium sulfate, requires one mole of calcium and one mole of sulfate, while both sodium and potassium should display 2:1 molar ratio, given the fact that one mole of either Na_2SO_4 or K_2SO_4 would require two moles of sodium or potassium and one mole of sulfate.

From previous results of characterization of treated samples, it was clear that calcium was the most reactive cation involved in SO_2-glass interactions; considering, for example, the high calcium concentrations obtained from the leached samples, in comparison with the other cations, its increased spatial distribution at the edges of treated samples, as seen with the SEM-EDS in Figure 3.3h, and the enhancement of the Ca spectra shown for treated samples in Figure 3.1b. Consequently, the most abundant surficial product formed during the SO_2-glass experiments was expected to be calcium sulfate. This seems indeed to be the case, by looking at the molal concentration graphics of Ca^{2+} and SO_4^{2-}, as seen in Figure 3.5a-c, which show strongest linear behavior among all cations and sulfate, strongly indicating predominant $CaSO_4$ formation as a result of the SO_2-glass high temperature interactions. The linear relationship between Ca^{2+} and SO_4^{2-} becomes even more linear for the samples treated with the temperatures i.e., 700 and 800 °C. Interestingly, at T≤600 °C, this linear behavior seems to show a slight decline.

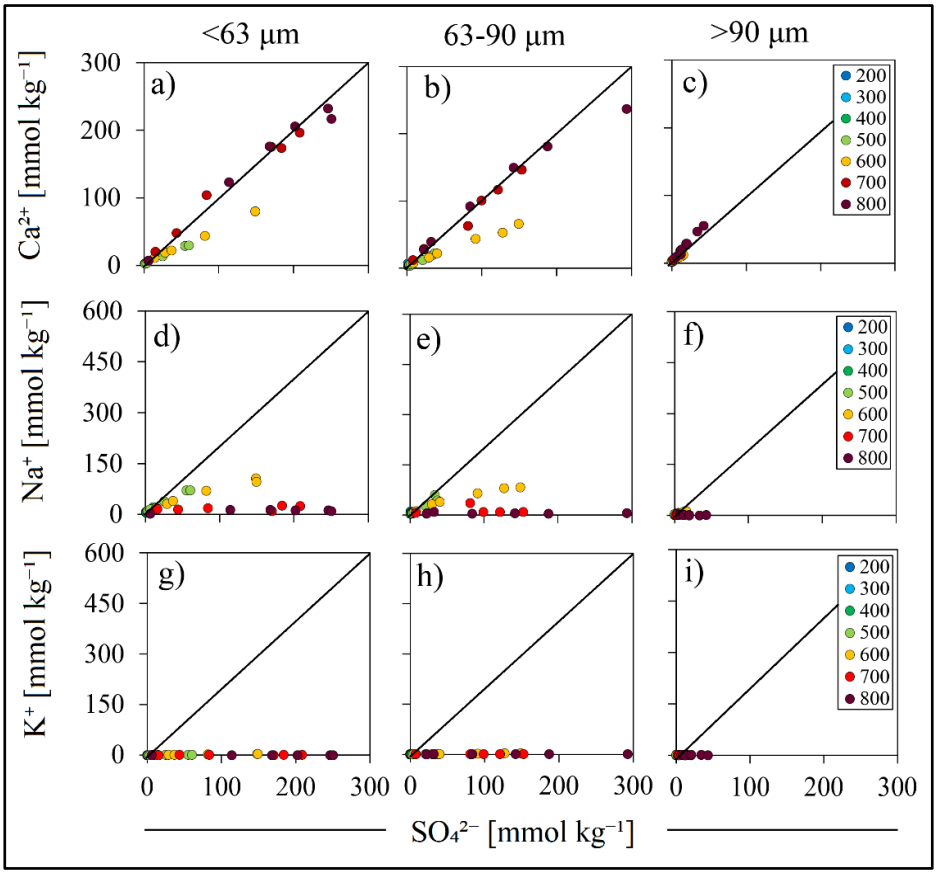

Figure 3. 5 Molal concentrations of leached cations and sulfate from the anhydrous SO_2 experiments. Molal concentrations (mmol kg^{-1}) of leached cations, Ca^{2+} (a-c), Na^+ (d-f) and K^+ (g-i) are plotted against concentrations of leached sulfate for the three grain size distributions. To simplify the graphics, time-series of experiments are not distincted, and only temperature-series are color coded, according to the legend of seen in plots c, f and i. For Na^+ and K^+, the molal relation with SO_4^{2-}- is 2:1, i.e., two moles of Na^+ or K^+ react each with one mole of SO_4^{2-}, therefore the y- and x-axis are different. Ca^{2+} molal reaction with SO_4^{2-} is 1:1, thus the y- and x-axis are identical, in each case the molal ratios 1:1 and 2:1 are shown with a black line.

Coefficient of correlation R^2																							
PSD (µm)	<63							63-90							>90								
T (°C)	200	300	400	500	600	700	800	200	300	400	500	600	700	800	200	300	400	500	600	700	800		
Ca	0.007	0.413	0.982	0.993	0.999	0.984	0.973	0.607	0.041	0.981	0.981	0.993	0.978	0.975	0.919	0.497	0.962	0.97	0.994	0.999	0.986		
Na	0.197	0.4	0.993	0.9924	0.992	0.189	0.538	0.315	0.042	0.638	0.905	0.964	0.007	0.002	0.429	0.199	0.334	0.758	0.912	0.155	0.11		
K	0.084	0.001	0.912	0.962	0.995	0.612	0.49	0.008	0.205	0.092	0.929	0.961	0.04	0.428	0.043	0.09	0.876	0.414	0.221	0.168	0.136		

Table 3. 1 Correlation coefficient values for molal ratios of leachates of the calc-alkaline rhyolite samples treated with SO_2. R^2values of the molal ratios obtained for concentrations of each cation versus sulfate were calculated for all three grain size distributions, temperatures and exposure times (these values are integrated indistinctively in the temperature data), i.e., from the plots in Figure 3.5.

Moreover, molar ratios of sodium show the most linear behavior for samples treated at 600 °C, which is also in agreement with the high concentrations of leached sodium obtained at this temperature (see in Figure 3.4d-f). This could be an indication that at T= 600 °C, formation of Na_2SO_4 is not negligible. Finally, molal ratios of potassium did not show any strong trend, when compared to those observed of sodium or calcium (see Figure 3.5g-i). This was not surprising, considering that the negligible concentrations obtained for this cation, as seen in Figure 3.4g-i.This strongly suggests that K_2SO_4 is the less favorable product formed due SO_2-glass reactions at high temperatures, amongst the cations tested.

In addition to plotting the molal ratios between cations and sulfate, the coefficient of correlation, R^2, was calculated for the molal ratio (cation/sulfate) of each temperature and grain size distribution, and can be seen in Table 3.1. The best correlation was continuously that of calcium (i.e., Ca^{2+}/SO_4^{2-}), being for all three grain size distributions and at T≥ 400 °C, always greater than 0.9. For sodium ($2Na^{+}/SO_4^{2-}$), and potassium ($2K^{+}/SO_4^{2-}$), the strongest correlations are obtained inconsistently for distinct grain size distributions and temperatures. For example, R^2 values greater than 0.9 obtained for both Na and K of the grain size distribution <63 μm, were obtained only in the temperature range of 400-600 °C. Similarly, for the grain size distribution 63-90 μm, R^2 values are greater than 0.9 only for the temperature range of 500 and 600 °C for both monovalent cations, while for the grain size distribution >90 μm, the only R^2 value greater than 0.9 is obtained for sodium at 600 °C.

3.2.1.3 Bulk FeO determination (iron redox state)

One observation made after performing the time- and temperature-series of experiments, was that most of the samples would display changes in their color. To exemplify this phenomenon, a comparison of a non-treated sample and several treated samples is seen in Figure 3.6. The observed change in color of samples was systematic upon longer exposure times, and especially upon higher treatment temperatures. An increase of both experimental variables, would cause the sample acquiring a more reddish tonality (Figure 3.6b), when compared with the non-treated sample powder. This bulk change in the sample color can be clearly seen in

Figure 3. 6 Color change of the treated samples. Upon performing the experiments with a) the powdered glass and b) collecting the samples, visible variations in the color of the powders were observed, in comparison with the original powder. Different sample treatments produced different sample tonalities; the enhanced reddish tone was obtained for the samples exposed for longer times, and higher temperatures.

Figure 3.6, where diverse treated samples are pictured in panel b, while the initial powdered material is also shown in panel b for comparison. This led me to think that the post-experimental change in color of the samples, could hint at changes in the redox state of iron in the glass, given the fact that the experimental material had a rather high amount of total iron, i.e., 3.26 wt.%, as reported in Table 2.3 (see Chapter 2).

In order to identify if the redox state of iron present in the treated samples was changing upon preforming high temperature experiments, the bulk redox state of iron was measured for the treated samples of all time- and temperature- series of experiments, of the three grain size distributions <63, 63-90, >90 μm and for the non-treated materials (as glass and powder) to have an initial redox state of iron value and of the initial redox state of iron. The bulk iron oxidation was obtained as wt.% FeO, by the potassium dichromate ($K_2Cr_2O_7$) potentiometric titration method described in Chapter 2, section 2.5.2.

Once the wt.% FeO was determined, and knowing the total iron content in the sample (expressed as FeOtotal wt.%), Fe_2O_3 could be calculated using Equation 2.3, in section 2.5.2 of Chapter 2. Once the bulk concentrations of ferrous oxide, FeO, the ferric oxide, Fe_2O_3 were known, simple calculations were made to obtain the ferric iron to total iron ratio i.e., $Fe^{3+}/\Sigma Fe$ of the samples, which was then used to express the bulk redox state of the samples.

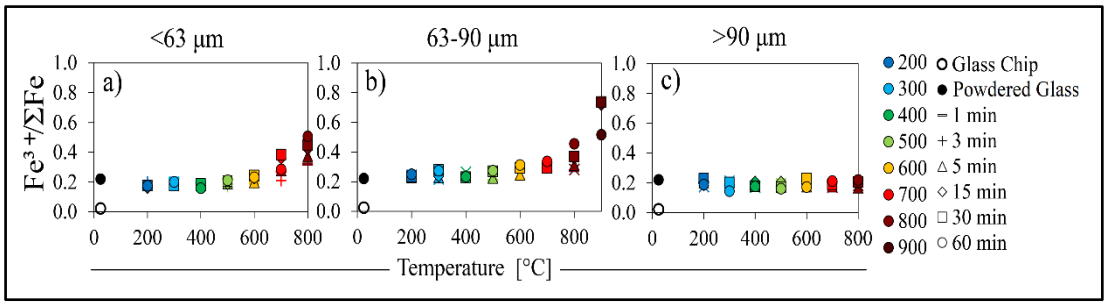

Figure 3. 7 Bulk iron redox state of the initial material and the treated samples. Measured bulk iron redox state is expressed as the ratio of ferric iron (Fe^{3+}) over total iron (ΣFe), for the initial material, analyzed as a fragment of the pristine obsidian and as powdered glass, referred in the legend as ´Glass Chip´ and ´Powdered Glass´, respectively. Treated samples, of all three grain size distributions, exposure times and temperatures are also plotted. All $Fe^{3+}/\Sigma Fe$ data points are plotted against temperature (°C). For all treated samples, exposure times (min.) are represented by the diverse marker types, as shown in the legend.

Figure 3.7 shows the results of the iron redox state determinations obtained for all time- and temperature- series of experiments of all three grain size distributions, and for the starting material, analyzed both as glass and as powdered glass. The $Fe^{3+}/\Sigma Fe$ values obtained are plotted against the treatment temperature, and the exposure times of each series of experiments are shown with different types of markers (see the legend on the right side of Figure 3.7). Iron redox state of the starting material was determined for the pristine obsidian (referred as ´Glass Chip´ in Figure 3.7), for which a small chip of glass was analyzed, and for the powdered, sieved glass (referred as ´Powdered Glass´ in Figure 3.7).

Results for the redox state of the initial materials (glass and powder) showed to be different, as the measured redox state of the glass chip was $Fe^{3+}/\Sigma Fe$=0.023 and 0.219 for the powdered glass, thus the powdered sample was more oxidized than the original glass. Results of the bulk redox state of iron of the pristine glass ($Fe^{3+}/\Sigma Fe$= 0.023), indicates that the original material was initially very reduced when quenched, since the ferrous iron (Fe^{2+}), accounts for 97% of the total iron. The discrepancy between the redox state of the starting material measured as glass and as powdered glass, was most likely due to heating caused by milling of the material, despite caution taken to prevent sample overheating.

Iron redox state results presented in Figure 3.7 seem to confirm the occurrence of changes in the redox state of iron of the samples, indeed towards increased $Fe^{3+}/\Sigma Fe$ values; i.e., more oxidized redox states, since most $Fe^{3+}/\Sigma Fe$ ratios display an increase upon increasing temperature. The change in the bulk redox state of iron is more evident for the grain size distributions of <63 and 63-90 μm, and almost negligible for samples of the >90 μm particle size distribution. This behavior shares similarities with that of the leached calcium concentrations, in that higher concentrations of leached calcium were consistently obtained upon increasing temperature treatments.

Increase of the redox state of iron can be observed for the grain size distribution of <63 μm (Figure 3.7a), where a rather parabolic curve seems to rise at T= 600 °C, and significantly increase at T≥700 °C. A similar behavior can be seen for the measured redox state of samples of the grain size distribution of 63-90 μm (Figure 3.7b). Finally, treated samples of the particle size distribution of >90 μm (Figure 3.7c) display no appreciable increase of the iron redox state. The extent of iron redox sate changes of the treated samples, when considering the initial redox state of the experimental material, is also noteworthy.

The non-treated powdered glass (´Powdered Glass´ in Figure 3.7) has a $Fe^{3+}/\Sigma Fe$ value of 0.219, meaning that ferric iron, Fe^{3+}, accounts for ~22% of the total iron. For treated samples, this value shows little to no variation in the range of 200-500 °C, for all exposure times, and all grain size distributions (Figure 3.7a-c). At T= 600 °C, the $Fe^{3+}/\Sigma Fe$ started to increase, especially for the samples treated for the highest exposure times (i.e., 30 and 60 min.) and for the grain size distributions of <63 and 63-90 μm, while for those >90 μm, the increase in redox state is minor.

The maximum $Fe^{3+}/\Sigma Fe$ value obtained at T=600 °C was 0.312 for the grain size distribution 63-90 μm of the sample treated during 60 minutes. At T=700 °C, a maximum value of 0.384 was obtained for the grain size distribution <63 μm, for the experimental time of 30 min., while at T=800 °C, the highest value amongst all treated samples was 0.507 for the grain size distribution <63 μm for the experimental time of 60 min. To further test the effect of experimental temperature on iron oxidation during SO_2-glass interactions, and to assess if an even higher oxidation state of a treated sample could be achieved than the maximum value obtained so far (i.e., $Fe^{3+}/\Sigma Fe > 0.507$), an additional experiment was design, in that a powdered glass sample of the grain size distribution 63-90 μm was treated for 60

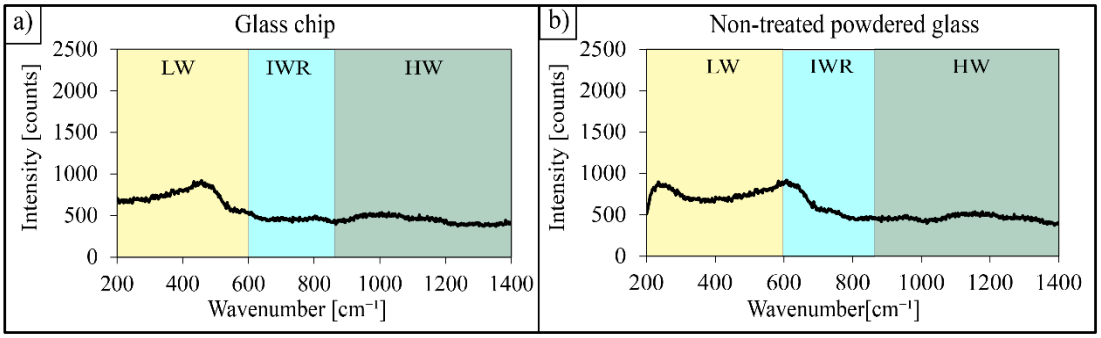

Figure 3. 8 Average Raman spectra of the initial material. Average spectrum for the initial material was acquired by measuring each material 5 times. a) The pristine obsidian, analyzed as small glass chip, showed a low intensity signal for all wavenumber regions low wavenumber region (LWR, 250-600 cm^{-1}), intermediate wavenumber region (IWR, 600-850 cm^{-1}) and the high wavenumber region (HWR, 850-1300 cm^{-1}). In the case of the milled obsidian, i.e. b) the non-treated powdered glass, the spectrum showed a general increase of the signal intensity in all regions, especially in the LWR.

minutes under the previously used SO_2 atmosphere, with the difference that the treatment temperature was increased to 900 °C. The measured iron redox state of the sample was, higher than that of the non-treated powdered glass, being $Fe^{3+}/\Sigma Fe = 0.517$, which was similar than values obtained at T=800 °C. By looking at the data point at 900 °C (in Figure 3.7b), it is obvious that the parabolic behavior of the plotted data becomes flat and displays a plateau. This might be an indication that, for this material, at T≥800 °C, iron oxidation state higher than $Fe^{3+}/\Sigma Fe \sim 0.5$ are not possible to achieve.

3.2.1.4 Raman spectroscopy

Raman spectra was acquired for both non-treated material (pristine obsidian and powdered glass), and treated samples (as only treated powders and as polished thick sections of these powders) using the analytical Raman spectroscopic system and measuring conditions (see Table 2.4), described in section 2.5.5, in Chapter 2. This had the aim to gain insights into the sample structure and to assess if changes in the spectra of treated samples could be correlated to the experimental parameters. Furthermore, after identifying occurrence of changes in the redox state of treated samples, Raman spectroscopy was also used to assess if iron oxidation would have a distinctive signal in the Raman spectra acquired for treated samples.

Besides performing single ´spot´ analysis of the samples, for the polished thick sections, transect measurements were also carried out (see Figure 3.11). Transect spot-analysis were acquired to have profile measurements of the interior of the particles and to try to correlate spectra changes, with the experimental variables. Additionally, Raman spectra were also performed to determine the mineralogy of the surficial products grown on the treated particles.

This was done by acquiring spectra of reference materials of anhydrite, ($CaSO_4$) and gypsum, ($Ca[SO_4]\cdot 2H_2O$), and later comparing them with the spectra of the surface of treated samples. Figure 3.8 shows the spectra acquired for the original (non-treated material) in the form of obsidian glass and the powdered glass. Spectrum of the glass chip (Figure 3.8a) displays a low signal at both low- and high-wavenumber regions (LWR and HWR), whereas for the non-treated powdered glass, at the LWR, two peaks seem to appear or be more visible than for the glass chip; at 200-300 and 500-600 cm^{-1}.

At the HWR, an increased signal is also observed, and also two peaks seem to appear; at 900-1000 and 1100-1200 cm^{-1}. The low wavenumber region (LWR) in silicate glasses is associated to vibrations of bridging oxygens (BO), specifically with three- or higher-membered rings of tetrahedra forming silicate networks. Lastly, the high wavenumber region (HWR) represents the vibrations of tetrahedra of tetra or trivalent cations) with non-bridging oxygens (NBO).

3.2.1.4.1 Raman spectra of reference materials and surficial products formed

Raman spectra were acquired for the reference materials anhydrite and gypsum and of the surficial products formed on the samples after SO_2- and SO_2+H_2O high temperature treatments (see Figure 3.2), to gain certainty on the mineralogy of the surficial salts. These minerals were used as reference materials to determine more precisely the mineralogy of the surficial products. Whereas results of previous analysis consistently showed that the surficial products formed on the treated samples, were mainly calcium sulfate, the specific mineralogy was not clear, i.e., if the products were formed as anhydrite or gypsum. For this, reference materials of both minerals were directly analyzed as powders without any preparation, under the same analytical conditions described in section 2.5.5, Chapter 2.

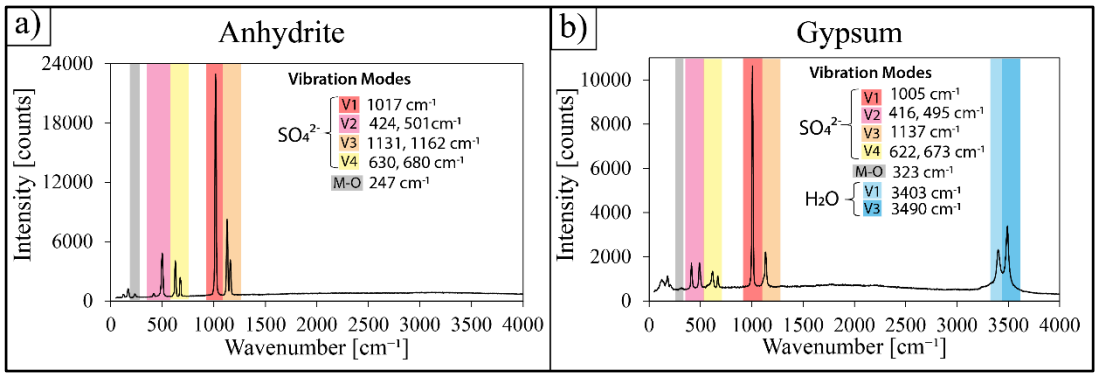

Figure 3. 9 Average Raman spectra of anhydrite and gypsum. The relevant peaks are emphasized with color bands in both cases and described in the inset. Each color band represents a characteristic bond-vibration of the constituents of each material. Sulfate (SO_4^{2-}), displays four distinctive vibration modes: symmetric stretching (V1, in red), symmetric bending (V2, in pink), asymmetric stretching (V3, in orange) and asymmetric bending (V4, in yellow); the metal-oxygen bond (M-O), in this case the bond between calcium and one of the sulfate-oxygens; and the water molecule shows the vibration modes V1 (light blue) and V3 (dark blue), this was only shown in gypsum spectra.

Material	Specie	Associated Vibration	Raman peak wavenumber (cm^{-1})		
			This work	Buzgar et al., 2009	White, 2008
Anhydrite	Ca-O		242	235	-
	SO_4^{2-}	V1	1,019	1,017	-
		V2	424-501	419-503	-
		V3	1,129-1,163	1,129-1,160	-
		V4	630-680	630-678	-
Gypsum	Ca-O		323	316	Not reported
	SO_4^{2-}	V1	1,005	1,010	1,008
		V2	416-495	416-495	415-494
		V3	1,137	1,143	1,136
		V4	620-673	622-674	624-671
	H_2O	V1	3,403	Not reported	3,406
		V3	3,490	Not reported	3,949

Table 3. 2 Comparison of reported values of anhydrite and gypsum spectra with this work. The spectra of anhydrite (taken from Buzgar et al., 2009) and gypsum (taken from Buzgar et al., 2009 and White, 2009) are described as Raman peak wavenumber (cm^{-1}) of the characteristic vibration modes of the mineral components. The reported wavenumber of the relevant peaks show strongly agreement with those obtained by analyzing the reference materials in this work.

In Figure 3.9 the spectra of anhydrite and gypsum are shown with the description and location of each characteristic peak, also described in Table 2.3. Unsurprisingly, the wavenumber of the peaks appearing in both spectra are very similar. Previous studies of Raman spectrum of sulfate, have identified four characteristic vibration modes for this specie; V1 and V2, are the symmetrical stretching and symmetrical bending, respectively, and V4 are the asymmetric stretching and asymmetric bending, respectively.

The anhydrite spectrum also shows these vibration modes, being V1 at 1017 cm^{-1}, the peak with the highest intensity of all, followed by V3, represented by two peaks at 1131 and 1162 cm^{-1}, and V2 and V4 are also described by two peaks at 424 and 501 cm^{-1}, and 630 and 680 cm^{-1}, respectively. The spectra show the Ca-O (M-O) peak, at a much lower intensity at 247 cm^{-1}. Gypsum spectra appears to be very similar to that of anhydrite, despite the noticeable lower intensity of the peak signals (see the y-axis in Figure 3.9a-b). Location of the peaks in both spectra is, however comparable. The main peak is again that related to the vibration mode V1 at 1005 cm^{-1}, followed again by V3, which in this case consists of only one peak at 1137 cm^{-1}, while V2 and V4 consist of 2 peaks each, as in the case of anhydrite, at 416 and 495 cm^{-1} and 622 and 673 cm^{-1}, respectively.

The M-O peak is in this case, slightly shifted to the right at 323 cm^{-1} but much less intense than the other peaks, as in the case of anhydrite. Yet, the most notorious difference is the appearance of the water-region at the right side of the gypsum spectra. The water region displays two peaks at 3403 and 3490 cm^{-1}, which represent the vibration modes V1 and V3, respectively, of the O-H bonds. These water-related signals were clearly absent in the anhydrite spectrum, and provide a powerful tool to differentiate the spectra between the two minerals. Once the reference materials were characterized, a thoroughly comparison of previously reported wavenumbers of anhydrite and gypsum was done, as seen in Table 3.2.

The reported location of peaks representing each one of the characteristic vibration modes related to anhydrite or gypsum bonding structure show great agreement with those obtained in this work for these reference materials. After characterizing the reference materials, acquisition of Raman spectra was carried out for surface products of samples treated under both anhydrous and hydrous SO_2 atmospheres

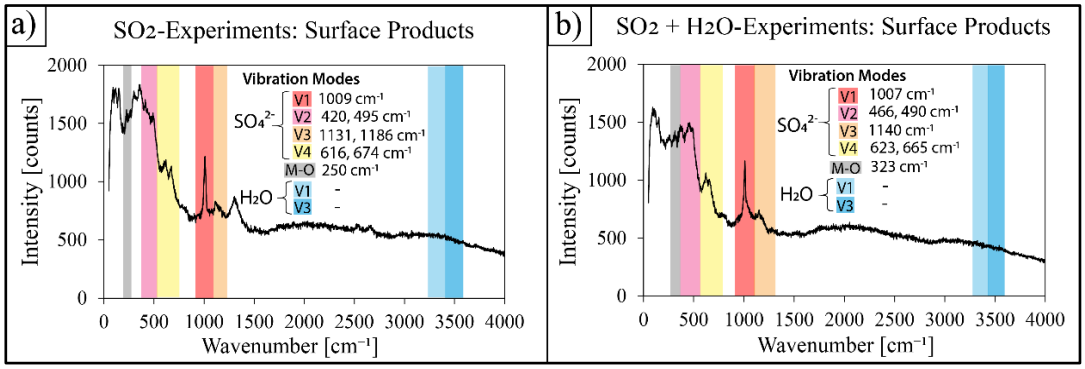

Figure 3. 10 Average Raman spectra of the surficial products formed on the samples after high temperature SO_2- and SO_2 + H_2O-treatments with the characteristic vibration modes of anhydrite and gypsum are high lightened and the location of the peaks described in the inset. While the spectra of treated samples appear noisier that than of the reference materials, no normalizing or correction to the spectra was done to avoid losing resolution on relevant peaks. Shown in a) is the averaged spectra of samples of three grain size distributions, treated at 600, 700 and 800 °C for 60 minutes each, under anhydrous SO_2 conditions. In b) averaged spectra of the SO_2-H_2O experiments of the grain size distribution 63-90 μm treated at 600, 700 and 800 °C for 60 min is shown. In both cases, the spectra show peaks observed in the reference materials, attributed to the vibration modes of sulfate, and Ca-O bonds. The vibration modes V1,2,3 and V4, at the expected wavenumbers, corresponding to the sulfate signal are featured in the spectra along with the Ca-O peak. Absence of the peaks related to vibration of water molecules in both spectra, indicates that gypsum was neither formed under anhydrous nor in hydrous conditions.

For the SO_2 anhydrous experiments, samples treated at 600, 700 and 800 °C, of the three grain size distributions; <63, 63-90 and >90 μm, were analyzed. For the hydrous experiments, only the 63-90 μm grain size was analyzed, of samples treated at 600, 700 and 800 °C. For both (anhydrous and hydrous conditions, all analyzed samples where those treated for 60 minutes, in order to guarantee that there was enough material formed at the particles surfaces, to acquire a detectable signal. Results of are presented in Figure 3.10, which shows the average spectra obtained for each treatment, anhydrous and hydrous SO_2 atmospheres. To average the spectra obtained for samples of each SO_2 experimental condition (anhydrous and hydrous) served to reduce the amount of data presented and visually simplify the graphic, given the fact that, in each case (anhydrous and hydrous treated samples), the signals obtained for all analyzed samples were corresponding with each other.

In both spectra, most of the peaks observed previously from the reference materials (see Figure 3.9) are also observed for the spectra acquired for the treated samples, with the exception of the peaks attributed to water, seen for the gypsum average spectra (Figure 3.9b). The increased signal obtained at the beginning of the spectra (Figure 3.10a,b), relates to the underlaying glass surface, as seen in Figure 3.8b. The spectra of the samples treated under anhydrous SO_2 atmospheres were expected to be similar to that of anhydrite, since there was no water vapor added to the gas mixture and therefore the most likely product to have formed on the surface would be anhydrite.

However, post-treatment hydration of samples could have occurred, as water from the air could have been adsorbed and leading to formation of gypsum, even under anhydrous experimental conditions. Yet, spectra acquired for all samples treated under anhydrous conditions, shown in Figure 3.10a, lacked any signal of the water peaks seen for gypsum in Figure 3.9b. The spectra of samples treated under SO_2 anhydrous conditions, did however, display all the sulfate- and Ca-related peaks seen for anhydrite, seemingly confirming that, the mineralogy of the surficial deposits was indeed anhydrite-dominated. In the case of the $SO_2 + H_2O$-experiments, spectra of treated samples were expected to feature the water-related peaks, since under hydrous condition, at least to some extent, gypsum could have formed.

However, when inspecting the resulting spectra, presented in Figure 3.10b, no peak could be distinguished in the water region for any of the analyzed samples, and the acquired spectra appears to be almost identical to those of samples treated with SO_2 under anhydrous conditions. This led to the preliminary observation, that the products formed during the experiments consisted, in both cases (anhydrous and hydrous SO_2 atmospheres), of anhydrite, and that no detectable post-experimental hydration of the surface products occurred.

3.2.1.4.2 Raman spectra of the transect measurements of the treated and untreated samples

Once the characterization of the mineralogy of the surface products was done, I preformed also Raman spectroscopy on the polished surfaces of treated samples, to study the effects of SO_2 treatments on the internal glass structure and try to profile the extent of their occurrence.

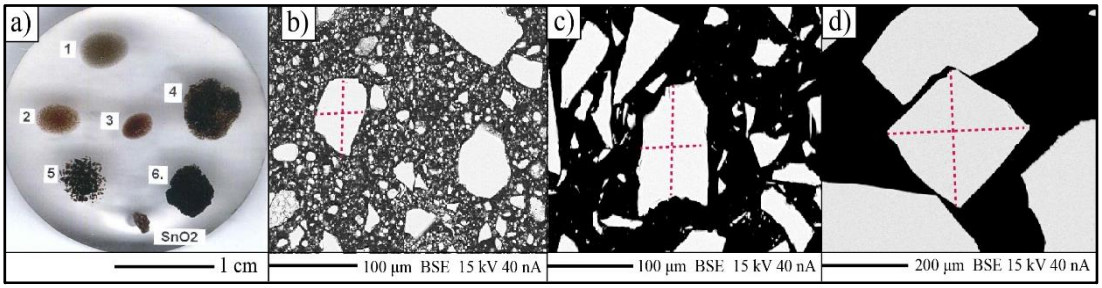

Figure 3. 11 Polished thick sections of treated samples. a) a polished epoxy-mount with treated samples is pictured. The change in color of treated samples mentioned before, from grey to diverse red tones, is also evident here. On the bottom of the mount, a small SnO_2 particle was placed, as a reference spot to locate better each sample. b), c) and d) are pictures taken with an Electron Probe Micro-Analyzer, and show grains of the grain size distributions <63, 63-90 and >90 µm, respectively. The dotted red lines show the trajectory of the transect analysis.

This was achieved by applying the same analytical conditions used in the previous Raman analysis (see Table 2.4), with the difference that, in order to expose the interior of treated particles, samples were embedded in epoxy within a mold and prepared as the polished thick section shown in Figure 3.11a. The samples chosen to be analyzed were those that would, most likely, show noticeable internal changes, based on previous characterization of treated samples, i.e., samples that showed the strongest evidence of reaction with SO_2, i.e., samples of the grain size distributions (<63, 63-90 and >90µm), treated with SO_2 at 600, 700 and 800 °C, all treated for 60 minutes. The measurements were done by analyzing approximately 13 spots along perpendicular transects of grain surfaces of each sample, as is depicted with red dotted lines in Figure 3.11b,c,d.

The resulting spectra is shown in Figure 3.12, where, for each plot, spectra of transect measurements are shown as well as the spectrum of the non-treated material (seen in Figure 3.8a as ´Glass chip´), for compassion purposes. The spectrum of the non-treated glass is shown simply with a black line, while spectra of treated samples are shown with two different colors, to describe their spatial location within one transect, being the blue spectra that of measurements performed at center-, and close to the center-distances and the red spectra that of edge-, close to the edge-distances, see legend at the right side of Figure 3.12. Spectra of treated samples of all grain size distributions treated at 600, 700 and 800 °C, clearly differ from the spectrum of the non-treated glass.

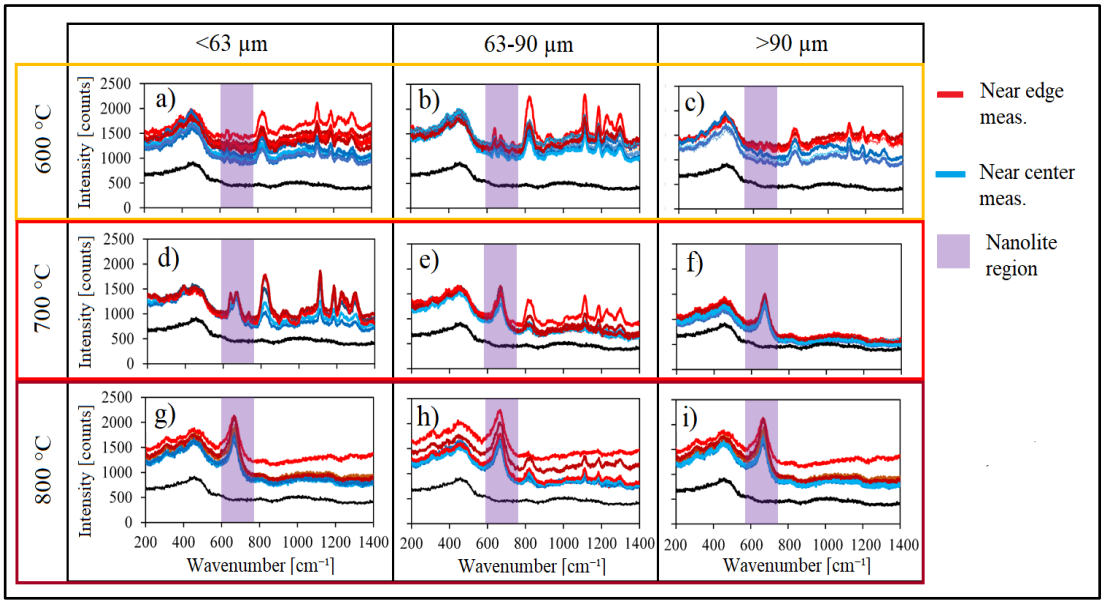

Figure 3. 12 Raman spectra of polished particle surfaces. Raman spectroscopy measurements performed along transects of particle surfaces embedded in a polished thick section are shown. Raw spectra for particles of the three grain size distributions <63 (a,d,g), 63-90 (b,e,h) and >90 µm (c,f,i) also arranged by the treatment temperature can be seen as the horizontal images for 600 (a.c), 700 (d-f) and 800 °C (g-i). The spectra acquired for each transect (consisting in at least 12 points each) is plotted in each case as blue spectra (far from the particle edges) and red spectra (near the edges), as well as the spectra of the non-treated (initial) material. The most distinctive change among the spectra, the peak located at ~ 670 cm^{-1}, is highlighted with a violet band in each spectrum. In silicate glasses, this peak is associated vibrations of Fe-bearing nanolitic structures.

The non-treated glass displays a rather simple spectra, featuring a prominent peak located at ~430 cm^{-1}, within the low wavenumber region (LWR, 250-600 cm^{-1}). This signal arises from the vibrations of bonding oxygens with tetravalent cations and indicates a polymerized glass structure, which agrees with the rhyolitic composition of the glass (~76 wt.% SiO_2).

Spectra of treated samples display, on the other hand, several other more complex features located within the intermediate- and high wavenumber regions, located at ~600-850 and ~850-1300 cm^{-1}, respectively. While spectra of treated samples initially appear to display a rather random arrangement of peaks, as seen for example, for the spectra of samples of all grain size distributions treated at 600 °C (Figure 3.12a-c), when Figure 3.12 is carefully inspected, there is one

changing feature shared by all samples, that differs from that of the non-treated glass, namely the peak found at ~670 cm^{-1} and high lightened for all spectra with a translucid purple band. This peak appears to be completely absent from the spectrum of the non-treated glass (see the black line spectra), while spectra of treated samples tend to display, in greater or lesser degree, a peak at ~670 cm^{-1}; samples treated at 600 °C, appear to display this peak only for the grain size distribution of 63-90 μm (see Figure 3.12b), while the grain size distributions of <63 and >90 μm show rather absence of this peak or a very week signal.

Furthermore, the intensity of the peak seems to consistently increase for all grain size distributions upon increasing temperature, as the 670 cm^{-1} peak becomes more intense and broader, becoming particularly evident in spectra of samples treated at 800 °C, (as seen in Figure 3.12g-i), than for samples treated at 600, 700 °C. Previous studies focused on structural and chemical characterization of silicate glasses using Raman spectroscopy, have also detected this peak and have associated it with structural features of Fe-bearing nanolites (DiGenova et al. 2017b;2018 and references therein). Nanolites, are nanoscale mineral phases present in some quenched products of volcanic eruptions (e.g., Mujin and Nakamura, 2014, Sharp et al., 1996, Zellmer et al., 2016; Barone et al., 2016; Schlinger et al., 1986;1988a,b).

They were first characterized by Sharp et al. (1996) as crystals smaller than microlites (0.6-1.2 μm), i.e., <0.6 μm wide size crystals. Further classification of nanolites was made by Mujin et al. (2017) who then designated nanolites, as crystals of width between 30 nm up to 1 μm. Another relevant peak found in Fe-bearing silicate glasses, is that linked to ferric iron (Fe^{3+}), dissolved in the silicate glass structure, located at ~970 cm^{-1} an is emphasized with a green band in the spectra of Figure 3.12.

This peak has been observed to correspond to the signals of an asymmetric coupled mode of Fe^{3+} vibrations in four-coordination state (Di Genova et al., 2016a; Di Muro et al., 2009). Detection and analysis of the behavior of both the Fe^{3+}- and nanolite-related peaks is of relevance for Fe-bearing glasses, since nucleation of Fe-bearing nanolites, incorporate mostly ferric iron, Fe^{3+}, in their structure. By inspecting spectra shown in Figure 3.12, the ferric iron peak seems to be absent from the non-treated glass spectrum, which is in is a congruent result, when considering the measured iron redox state ($Fe^{3+}/\Sigma Fe$) of the non-treated glass,

0.023, which (see section 3.1.1.3), which showed that the bulk iron of the initial material was nominally ferrous iron (Fe^{2+}), i.e., reduced iron, which upon milling and high temperature SO_2 treatments, would consistently show higher redox values (see Figure 3.7). Yet, this peak seems to appear for some treated samples, in particular those of the smallest and intermediate grain size distributions, i.e., <63 and 63-90 μm, for the treatment temperatures of 600 and 700 °C (seen in Figure 3.12 a,b,d,e). Spectra of samples treated at 800 °C however, do not seem display the ferric iron peak, (see Figure 3.12g-i). Interestingly, these spectra display the most intense and broader nanolite-related peaks (see purple band on spectra of Figure 3.12g-i) amongst all spectra.

This might be an indication that, when the ferrous iron of the samples oxidizes, it does not remain dissolved in the glass structure, but rather incorporates into a Fe^{3+}-bearing nanolite crystal phase. The latter seems to be increase at $T \geq 600$ °C, and appears to be especially clear for T= 800 °C. This range of temperatures, was also, that at which formation of surficial $CaSO_4$ appeared to be more efficient than at T<600 °C (see Figure 3.4a-c, section 3.1.1.2). This led to the possibility that the two processes, Ca^{2+} diffusion and Fe^{2+} oxidation could be linked in a cause/effect-like dynamic.

3.2.1.5 Electron probe micro-analyzer (EPMA) transect measurements

Transect measurements of treated samples were also performed with the Cameca SX-100 electron probe micro-analyzer (described in section 2.5.4 of Chapter 2) to obtain quantitative information about cation diffusion occurring during high temperature SO_2 uptake. Of particular interest was the diffusion of calcium, since it was clear from previous analysis and chemical characterization of treated samples, that this was the main cation present in the surficial products formed after the high temperature SO_2-treatments. Whereas evidence of calcium diffusion (and, in a minor degree sodium and potassium diffusion) was expected to be shown with EPMA analyses, the extent to which this occurred, was unknown, and therefore precise spot-measurements along perpendicular pathways were performed on polished surfaces.

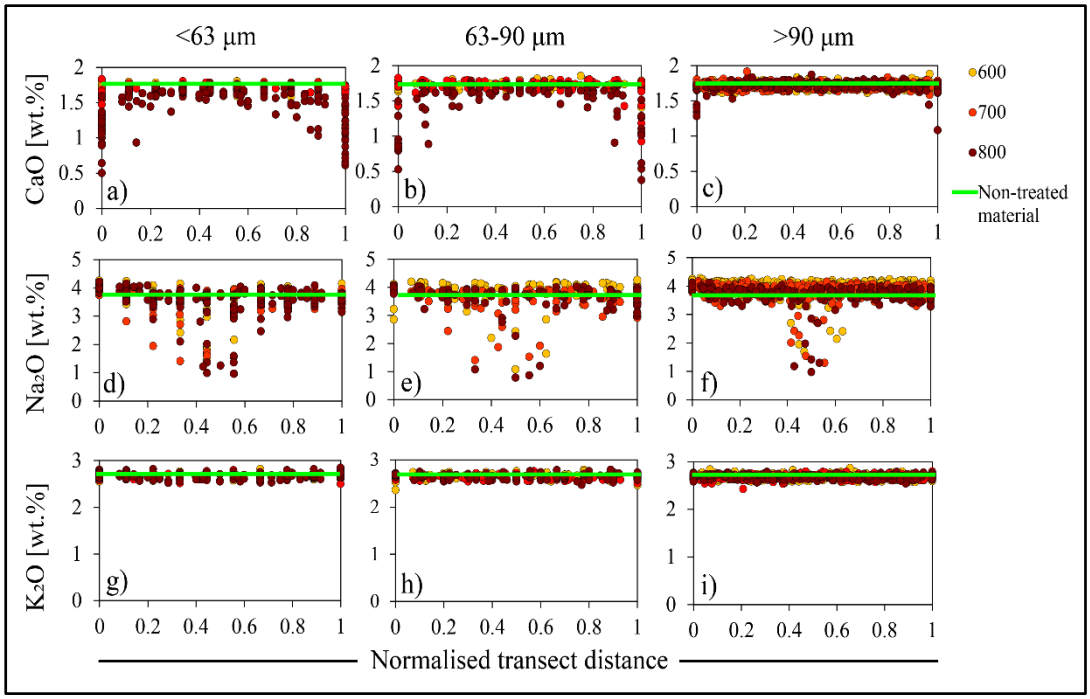

Figure 3. 13 Transect EPMA spot-measurements for Ca, Na and K of treated samples. Spot-measurements of samples of the three grain size distributions treated at 600, 700 and 800 °C each, under SO_2-anhydrous atmospheres, are shown as wt.% of the measured calcium (a-c), sodium (d-f) and potassium (g-i), measured as oxides, and plotted against the normalised distance of the transects. The latter is an arbitrary parameter, used to dismiss the difference between the length of the different transect measurements of all grain sizes, by dividing the spot-measurements distance by the total transect distance. Thereby, the normalised transect distance values of 0 and 1 represent the edges of the particles, and 0.5 represents the middle. Spot-measurements are also color coded to represent the treatment temperature of the sample, (see the legend panel). Additionally, and for comparison purposes, the average value of Ca, Na and K (wt.%, as oxides) of the untreated material is plotted as a horizontal green line.

The samples chosen to be analyzed by this technique, were again those that, by previous analysis, showed to have formed the highest amount of salts for each grain size distribution, this is, samples treated at 600, 700 and 800 °C for 60 minutes each. For each grain size distribution, ten grains were analyzed, and, depending on the gain size, each perpendicular transect consisted in ~ 10, ~ 15 and ~ 30 spot analysis, for the grain size distributions of <63, 63-90 and >90 µm, respectively. Analysis were carried out according to the measuring conditions described in section 2.5.4 of Chapter 2.

The plots shown in Figure 3.13 correspond to transect analysis results of calcium (a-c), sodium (d-f) and potassium (g-i), obtained for the ten grains analyzed for each one of the three-grain size distributions, each treated at 600, 700 and 800 °C. The spot analyses are color-coded to indicate the temperature at which the samples were treated and exposed to the SO_2 atmosphere, as in the previous plots. Additionally, in order to clearly distinguish the degree of depletion of each cation, the average value measured (wt.% of the oxide) each element of the untreated powdered glass (i.e., initial concentration of each element) is expressed as a constant green line with the value of 1.21, 2.73 and 2.2 wt.% for CaO, Na_2O and K_2O, respectively.

The graphics are plotted in weight percent of the cation (expressed as oxide), versus what I called a ´normalised transect distance´, this is, an adjusted that expresses the distance of each spot-analysis of each perpendicular transect of in a zero to one-scale, where ´zero´, corresponds to the value measured on the first spot of a transect and ´one´, to the last of each transects. This was done by dividing the distance of each spot analysis by the total distance of the complete transect.

This had the purpose to be able to better compare the extent of diffusion amongst the analyzed samples, regardless of the particle size distribution or the number and distances of the spot analysis. By looking at the plots of calcium in Figure 3.13a-c, depletion is evident, and seems to systematically increase from the center of the particle (normalised transect distance of 0.5) to the particle edges (i.e. surface), represented by the vertical axis values of 0 and 1. This near edge-depletion also appears to occur to a greater extent within decreasing particle size (Figure 3.13a and b), as well as within increasing of the treatment temperatures.

Maximum depletion of calcium reaches a value of 0.27 wt.% for the grain size distribution 63-90 μm grains treated at 800 °C for 60 minutes, meaning that a fraction of 0.77 of the original calcium content has migrated from the bulk glass structure to the particle surface. Interestingly, a strikingly similar result was observed for the leached calcium data of this same sample, where the amount of calcium leached accounted for 0.79 of the total bulk calcium in the particle (see Figure 3.4b, in section 3.1.1.2). This behavior was consistently observed for calcium spot-measurements for the three gain size distributions, and will be further addressed in Chapter 4.

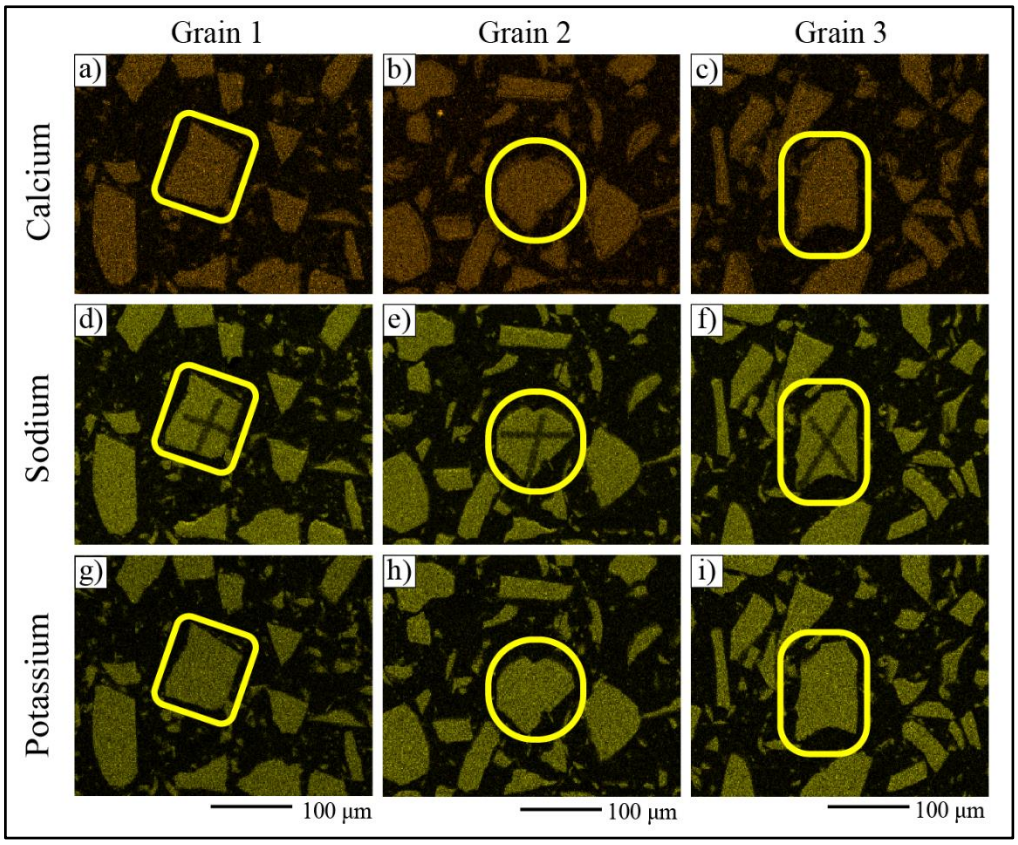

Figure 3. 14 Energy dispersive X-ray spectroscopy maps for Ca, Na and K of polished particle surfaces of samples previously analyzed with EPMA. SEM-EDS Element mapping was done for grains previously analyzed with the EPMA to examine if this analysis was responsible for the unexpected depletion of Na observed for the transect EPMA measurements. Three grains were mapped for Ca (a-c), Na (d-f) and K (g-i). Each grain of interest is highlighted with a yellow contour. Sodium loss is indeed evident when observing the corresponding element map images (d-f), where the spot-measurements of the transects can only be seen for sodium, seemingly agreeing with the inward Na depletion observed in Figure 3.13.

Conversely, interpretation of sodium EPMA transect measurement results, requires a rather more careful reading. As mentioned before, calcium was by far, the cation that showed to be primarily responsible for surficial products formation, upon high temperature SO_2 treatments, while sodium and potassium did not show to be as reactive to the SO_2 high temperature treatments.

In view of this, no dramatic depletion of sodium was expected, according to the minor concentrations of Na obtained from the leachate data (see Figure 3.4d-f). Yet, by observing Figure 3.13d-f, depletion of Na seems to indeed occur, but shows an opposite depletion behavior than that of calcium.

While calcium depletion was seen to occur at near-edge distances, depletion of sodium appears to occur at near-center distances. Furthermore, the observed depletion appears to occur regardless of the grain size distributions and treatment temperatures, unlike in the case of calcium, where both increasing temperatures and decreasing of the grain size distribution would lead to higher near-edge depletion (see Figure 3.13a-c). If in fact, the sodium depletion observed in Figure 3.13d-f, was due to diffusion triggered by the high temperature SO_2 treatments of the sample, this behavior would contradict our proposed high-temperature SO_2 uptake mechanism which implies cation diffusion form the bulk glass network towards the surface of the particle. This result, was later observed to be an artefact of the EPMA measurements, which, despite the care taken in the setting the measuring parameters, caused loss of sodium.

The latter became clear by acquiring SEM-EDS element distribution maps for Ca, Na and K of polished particle surfaces of samples previously analyzed with the EPMA. Figure 3.14 shows the resulting element maps for Ca (a-c), Na (d-f) and K (g-i) of three grains (enclosed in hollow yellow outlines) on which EPMA analyzed were performed. In the case of calcium (a-c) and potassium (g-i), transect spot-analysis show no significant evidence of absence or reduction of the element signal, however, in the case of Na (d-f), the element map shows clear signs of surface alteration (i.e., element loss), on the three different grains, for which the EPMA transects can easily be seen. Nevertheless, the robust set of leachate data (time- and temperature-series) helped to outweigh this result, in terms of determining the amounts of Na present in the surface, thus diffused.

3.2.2 SO_2-anhydrous experiments

The first set of high temperature SO_2 uptake, performed under hydrous conditions, provided me with relevant information about SO_2 uptake by powdered natural rhyolitic glass, in terms of the effect of the tested variables (temperature, grain size distribution and exposure time). Consequently, to perform the next set of SO_2 uptake experiments under hydrous conditions, the experimental design was changed and optimized based on the observations made from the results obtained from the anhydrous set of experiments.

For instance, since the effect of the grain size distribution of the samples showed to play an important role on the SO_2 uptake experiments, being the samples of largest grain size distribution (i.e., >90 μm) the ones that, upon SO_2 treatments, produced the lowest amounts of surficial sulfur-bearing products (see Figure 3.4c,f,i), I chose to only test samples of the intermediate grain size distribution 63-90 μm to perform the time- and temperature-series of SO_2- uptake experiments under hydrous conditions. The exposure temperature range was also adjusted to a more efficient range, given the fact that experiments performed at 200-300 °C, resulted in low to negligible sulfur uptake, as reflected in the leachate data shown in Figure 3.4, and therefore experiments under hydrous conditions were only tested for 400, 500, 600, 700, and 800 °C.

Regarding the exposure time, it was initially reduced to only that of 60 minutes, in order to have an overview of the behavior of the samples under hydrous SO_2-atmospheres. Upon analysis of the samples a second subset of experiments were also performed with the original exposure times, i.e., 1, 3, 5, 15, 30 and 60 minutes, so that total of two sets of SO_2 uptake experiments under hydrous conditions were performed; the first set aimed to test the effect of addition of humidity to the SO_2-Ar mixture (1 mol.% SO_2 and 99 mol.% Ar) on the SO_2 uptake by the samples, and consisted in humidity- and temperature-series of experiments performed all for 60 minutes.

To test the effect of humidity on SO_2 uptake, a wide range of water vapour was let into the reactor, together with the SO_2-Ar gas mixture, namely 0.01, 24.32, 38.16, 47.72, 62.3, 82.17, 90.04, 93.09, 94.71 and 96.41 mol.% H_2O, at the temperature range of 400-800 °C for 60 minutes each. The second set aimed, however, to test the temporal variation of the effect of adding humidity to the SO_2-atmosphere. This was done by performing time-series of experiments with the original exposure times: 1, 3, 5, 15, 30 and 60 minutes, however, only for the most relevant ranges of temperature; 600-800 °C and only for a single water vapour value (62.29 mol.% H_2O), selected after inspecting the results of the first set of hydrous experiments.

Addition of water vapour to the AGAR reactor to perform both sets of hydrous experiments was done by coupling a quartz nebulizer to the gas inlet of the reactor, which was fed by deionized water pumped from a peristaltic pump (described in detail in Chapter 2, section 2.4.1).

After performing the experiments, samples where left to cool to room temperature within the reactor bulb, then placed in sealed glass vials.

3.2.2.1 Scanning electron microscope (SEM) analysis

SEM-analysis of treated samples was done to evaluate if formation of surficial products occurred, as for samples treated under anhydrous conditions, and to detect if, increasing humidity in the gas mixture would influence the morphology, shape or size of the surficial products formed. Images obtained with the SEM-BSE are shown in Figure 3.15a-k, of samples exposed to each one of the water vapour contents (mol.% H_2O), treated at 600 °C for 60 minutes each. Furthermore, an image showing the surface of a sample treated under SO_2-anhydrous conditions for the same exposure time and temperature is shown in panel l for visual comparison.

Addition of humidity to the SO_2 atmosphere does seem to exert an influence on the morphology of the surficial products, as seen in the images shown in Figure 3.15a-k. To highlight some of the features observed on the particle surfaces, yellow lines were drawn around them. Samples treated with the lowest amount of water vapour (0.01 mol.% H_2O), seen in Figure 3.15a, already show a different arrangement of the surficial products than that observed for samples treated under anhydrous conditions (see panel l).

For the sample shown in panel "a" the surficial products, display a ring-network arrangement that seems to incorporate most of the surficial products. An average diameter of the rings was found to be ~1 μm. The pattern of surficial product arrangement shown in Figure 3.15a, strongly differs from that observed for the surficial products formed under anhydrous SO_2- experiments, which showed overall bigger and blockier minerals, grown seemingly detached from each other (see panel l and Figures 3.1 and 3.2). Upon further increase of humidity (see panel b), surficial products start to also display round-shaped morphologies, in addition to the initially observed ring-network arrangement.

Moreover, these round-shaped products seem to have formed as single products, instead of being formed within connected a network. Occurrence of round-shaped and ring-network arranged products are emphasized with yellow lines on the left and right side of panel b, respectively.

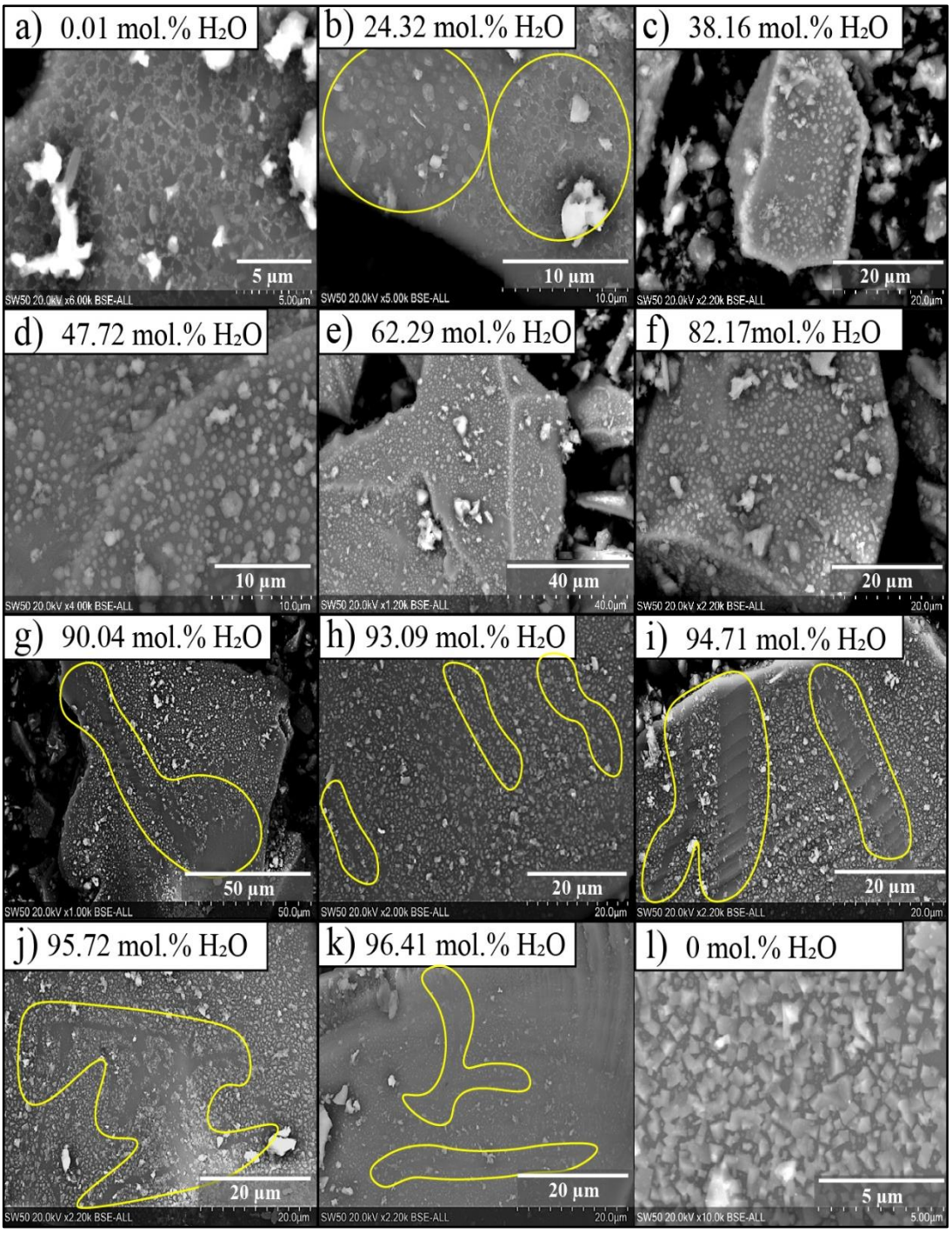

Figure 3. 15 Effect of hydrous SO_2-atmospheres on formation of surficial products on treated samples. SEM-BSE images were taken for samples treated with the SO_2-hydrous gas mixtures for all water vapour amounts tested, i.e., 0.01-96.41 (mol.% H_2O). All shown hydrous-treated samples were treated at 600 °C for 60 min (a-k). Furthermore, in panel l, a sample surface treated under anhydrous conditions (i.e., 0 mol.% H_2O added) is pictured to compare the morphology, size abundance etc. of surficial products formed under both gas mixtures. Noteworthy features are emphasized with yellow contours, as in the case of panels b, g-k.

Within the range of 38.16-82.17 mol.% H_2O added to the SO_2 atmospheres (panels c-f), the round-shapes appear to be the predominant morphology of all surficial products, since no further ring-network arrangements could be observed. Regarding the size of these products, it seems to show a general increase, in comparison to that of products formed under lower water content (<38.16 mol.% H_2O), with widths of the products ranging from 1-2 μm to a few hundred nanometers.

At even higher humidity conditions (≥90.04 mol.% H_2O), an interesting feature could be observed for most of the treated samples (see panels g-k), namely, the occurrence of delimited pathways, along which surficial products seem to be absent from the surface, despite the fact that, these product-free pathways are surrounded by surficial products.

This feature can be seen specially clearly for the surfaces displayed in panels g, i, and j, (90.04, 94.71 and 95.72 mol.% H_2O) where lined-shaped pathways (within covered surfaces), appear to be lacking of any surficial product. Careful observation of these images leads to hypothesize that the absence of surficial products along some linear pathways was an indication of super saturation of water in the gas mixture during the experiments, which perhaps led to rapid condensation of water microdroplets on the particle surfaces once the samples were taken out of the reactor, which could have caused some leaching of surficial products.

Another interesting observation made for the samples treated with high humidity (panels g-k), is that the shape of the surficial products becomes less rounded and more angular. Increasing of humidity in the SO_2 atmospheres, also seems to exert an influence on the size of the surficial products, since the general size of the products formed appear to decrease proportionally to increasing water vapour contents.

See for example the size difference shown for surficial products treated with 38.16 mol.% (panel c), where the average size of the surficial products was ~2.5 μm, and those treated with the highest amount of water vapour, 96.41 mol.% (panel k), where all products had a size smaller than one micrometer. The decrease in the size of the surficial products formed under high amount of water vapour added to the gas mixture, will be further addressed in Chapter 4.

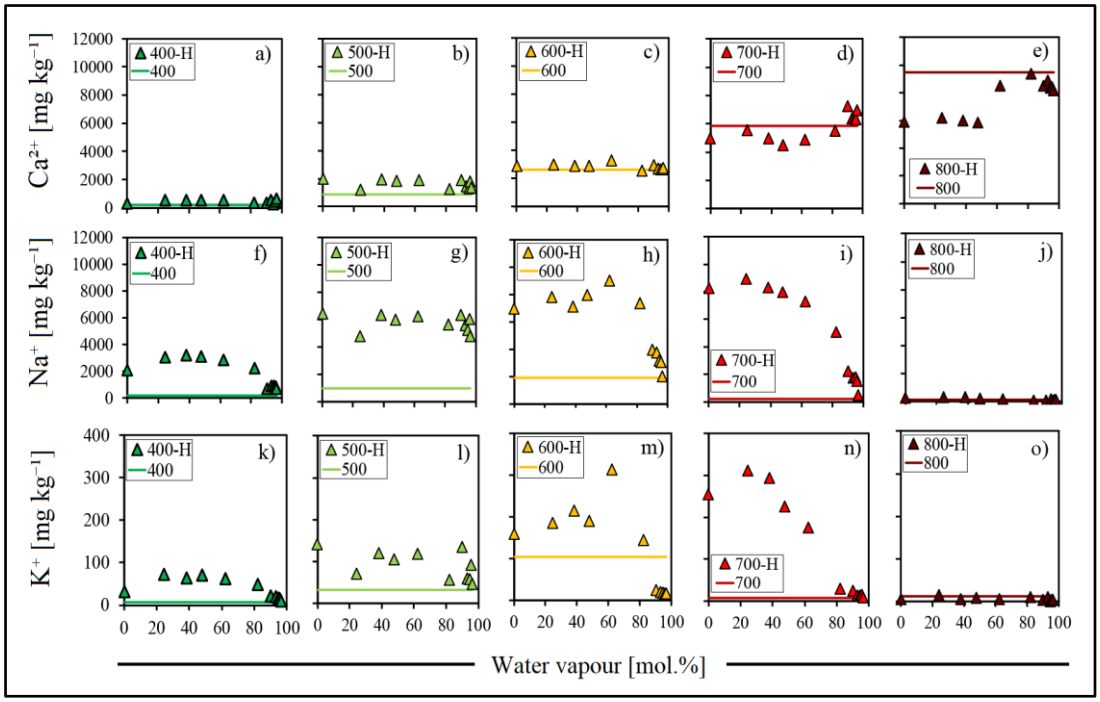

Figure 3. 16 Concentration of leached cations from the water vapour- and temperature-series of hydrous SO_2 experiments. Leachate data for the first set of hydrous experiments is shown, i.e., of samples treated at 400-800 °C, for 60 minutes each under SO_2-hydrous gas mixtures are plotted for Ca^{2+} (a-e), Na^+ (f-j) and K^+ (k-o) as a function of the range of water vapour tested (0.01-96.41 mol.% H_2O). For each temperature, leachate data of both hydrous and anhydrous conditions are plotted. Hydrous data are plotted as filled (filling colors represent the treatment temperatures) triangles and represent the concentration of a leached cation obtained for each water vapour amount (mol.%) tested, while anhydrous data is plotted as a constant concentration value (no water vapour was added), described by a colored line (color of the line also represents treatment temperatures). The legend inset in each graph shows the hydrous data as the temperature value plus an "H" and the anhydrous data as only the temperature value.

3.2.2.2 Leachate analyses

After observing how distinct the surficial products formed of SO_2-hydrous experiments were, compared to the results obtained under anhydrous conditions, samples leachates were analyzed. Results of the leachate analysis are shown in Figure 3.16. Concentrations of calcium, sodium and potassium are plotted against each water content tested, for all treatment temperatures (400-800 °C) of the first set of hydrous experiments, i.e., the set of water vapour- and temperature-series

of experiments, which were performed for the only the experimental time of 60 min. Concentrations of leached calcium (a-e), sodium (f-j) and potassium (k-o) are expressed as mg of the leached cation over kg of the glass (mg kg^{-1}). Leachate data points of the hydrous experiments are shown as filled triangles to difference this data points from those of the SO_2 anhydrous experiments, which were filled circles. The filling of the triangles corresponds to the treatment temperature, according to the color-coding of temperature previously used (see legend in Figure 3.4), also shown in the upper left insets on the plots. Additionally, in order to make a direct comparison between the leachate data obtained under anhydrous conditions, a prolonged colored line is plotted in each graphic, which represents the concentration value of the cation obtained for the same sample treatment (temperature and experimental time of 60 minutes) but under anhydrous conditions.

For example, in the panel a, each filled triangle represents the concentration of calcium obtained for at each water vapour content (mol.%), treated at 400 °C for 60 minutes each, while the green colored line represents the value of leached calcium obtained also at 400 °C and for 60 minutes, but under anhydrous conditions (i.e., only SO_2-Ar). Inspection of Figure 3.16 leads to the several noteworthy observations; for instance, that for leached calcium concentrations (panel a-e), the effect of addition and increase of humidity to the SO_2-Ar gas mixture, appears to be negligible for temperatures, given the fact that, for each temperature, the data points of the hydrous experiments seem to match to almost the exact values of the concentration obtained under anhydrous conditions.

Despite the fact that, some hydrous experiments preformed at 800 °C (e.g., panel e) showed calcium concentrations values lower than that obtained under anhydrous conditions, nearly all concentrations of leached calcium exhibited values close to those obtained under anhydrous conditions, suggesting that surficial Ca-bearing product formation occurs apparently independently of humidity present in the SO_2 atmosphere, during high temperature experiments. Leached concentrations of monovalent cations obtained from samples treated under hydrous conditions showed, a different behavior than that observed for calcium. Conversely to the latter, addition of certain amounts of water vapor considerably increased concentrations of leached sodium (see panels f-j) and potassium (see panels k-o), in comparison to concentrations obtained under anhydrous conditions.

For instance, under hydrous conditions, concentrations of leached sodium from samples treated at 400, 500, 600, 700 and 800 °C (panels f-j), yielded to values of 1563, 651, 476, 4746 mg kg^{-1}, respectively, were up to 232 % higher than those obtained under anhydrous conditions. Similarly, concentrations of leached potassium, were up to 1017, 442, 300, 4458 and 134 % greater under hydrous conditions than under anhydrous conditions, for temperature treatments of 400, 500, 600, 700 and 800 °C (panels k-o), respectively.

The enhanced concentrations of monovalent cations seem to occur only for a range of water vapour amounts, namely: 0.01-82.17 wt.% H_2O, whereas at higher humidity values (≥90.04 mol.% H_2O), concentrations of sodium (panels h-i) and potassium (panels m-n), start to decrease towards the values obtained under anhydrous conditions, or even below these, as in the case of potassium (see panels m and n). The increased concentrations of leached Na and K show another interesting feature; namely that samples treated at 700 and 800 °C under hydrous conditions, seem to have overcome the negative effect that these temperatures previously had on formation of Na- and K-bearing products (see Figure 3.4, panels d-f and g-i).

Concentrations of leached Na and K from samples of the same grain size distribution (63-90 μm) treated at 700 °C for 60 minutes, but under anhydrous SO_2 atmospheres, were minor to negligible, when compared to concentrations obtained at lower temperatures (T<700 °C). While for samples treated under anhydrous conditions at 700 °C, concentrations of leached Na and K represented only 0.6 and 0.03 % of the total bulk Na and K present in the glass, respectively, under hydrous conditions, leachate concentrations obtained also at 700 °C, accounted for up to 28 and 1.3 % of the initial bulk concentrations of Na and K, respectively.

Yet, the leachate data of Na and K of samples treated at 800 °C (Figure 3.16j,o), seems to be similar under both hydrous and anhydrous conditions. despite the fact that some concentrations of Na and K do show a slight increase under hydrous conditions, namely 1.12 and 0.06 % of the total Na and K, in comparison to the 0.48 and 0.5 % obtained under anhydrous conditions. In both cases, however, the amounts of leached monovalent cations for treatments of 800° C can be considered to be negligible under hydrous and anhydrous SO_2 atmospheres.

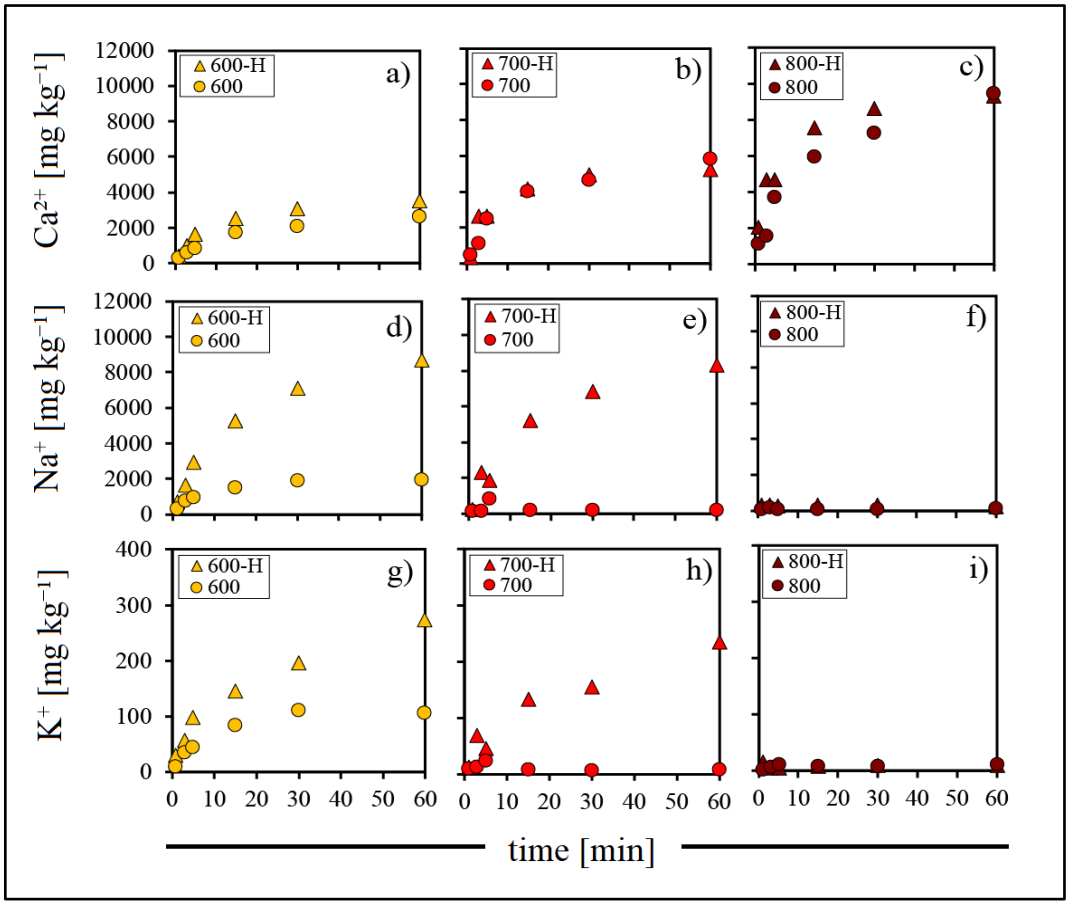

Figure 3. 17 Concentrations of leached cations from the time- and temperature-series of hydrous SO_2 experiments. Concentrations of leached calcium (a-c), sodium (d-f) and potassium (g-i) from the second set of hydrous experiments are shown, i.e., for the time- and temperature series of experiments conducted at the constant water vapour amount of 62.29 mol.%. Concentration data is plotted against the exposure times (1-60 min.). Data points of the samples treated under SO_2-hydrous conditions are symbolized again as filled triangles and the anhydrous data points are represented by the filled circles, as described in the legend inset for each plot.

Leachate data of the second set of hydrous experiments consisting of time- and temperature-series (1-60 minutes and 600-800 °C, respectively), tested only under one amount of water vapour (62.29 mol.% H_2O), are shown in Figure 3.17. Concentration of calcium (a-c), sodium (d-f) and potassium (g-i) are plotted against the exposure time for the three temperatures tested. The leachate data of the samples treated under hydrous experiments are symbolized with filled triangles (as in Figure 3.16), while the data points of samples treated with anhydrous SO_2-Ar mixtures are symbolized with filled circles.

The filling color of both circles and triangles indicate the temperature of the sample treatment, which is also shown as insets on the upper left side of each plot. The set of time- and temperature-series of experiments exhibited very similar trends than those observed for the first set of hydrous experiments (humidity- and temperature series). First, that the concentrations of leached calcium, seem to be broadly unaffected by addition of water vapor to the SO_2-Ar atmosphere, and show to be rather strongly dependent on temperature and exposure times (see panels a-c), as previously noticed for the anhydrous set of experiments (see Figure 3.4a-c).

Second, that concentrations of leached sodium and potassium show a considerable increase upon addition of water (in this case 62.29 mol.% H_2O), even for experiments performed at T=700 °C, which, in the previous anhydrous experiments, led to minor amounts of leached sodium (panels d and e) and potassium (panels g and h), when compared to concentrations of both cations obtained at T>600 °C (see Figure 3.4f-o in section 3.1.1.2). Lastly, that samples treated at 800 °C, produced minor concentrations of leached sodium (panel f) and potassium (panel i), when compared to concentrations obtained at lower temperatures, as was also the case of anhydrous experiments.

Additionally, the time-dependency of concentrations of leached cations upon high temperature treatments displays the same parabolic behavior for both hydrous and anhydrous SO_2 sets of experiments. Both sets of SO_2 uptake experiments under hydrous conditions yielded to very interesting leachate results, being perhaps the most relevant, the enhancing effect that addition of certain water vapour contents had on concentrations of sodium and potassium (see Figure 3.16f-o, and Figure 3.17d-i), even at T=700 °C, at which anhydrous experiments led to negligible concentrations of both monovalent cations (see Figure 3.4 d-I in section 3.1.1.2).

Considering that, leached cation concentrations result from dissolution of soluble surficial salts (i.e., $CaSO_4$, Na_2SO_4, and K_2SO_4), formed during high temperature SO_2 exposure of samples, a concentration increase of any cation, implies that more surficial salts were formed, thus, mobilization of this cation within the silicate network of the samples occurred more efficiently. This could be an indication that upon presence of water vapour, a different mechanism for Na and K mobilization within the glass network takes place, which might no longer be cation diffusion, as it was previously suggested.

Furthermore, the fact that, at T=800 °C, under both hydrous and anhydrous exposure to SO_2 atmospheres, no significant amounts of Na and K could be leached, i.e., no significant Na-, K-bearing surface products were formed, suggests the occurrence of a strong internal mechanism by which monovalent cation mobility is effectively reduced, impeding further Na and K reactions with SO_2, hence Na- and K- surficial products formation. Finally, as calcium concentrations showed to be broadly unaffected by addition of humidity to the SO_2 atmospheres, it can be assumed that the controlling mechanism that drives calcium outward motion to react with SO_2, is the same under both hydrous and anhydrous conditions. These results will be further addressed in Chapter 4.

3.2.2.3 Bulk FeO determination (iron redox state)

Considering that, changes in the bulk redox state of iron were observed for samples treated with SO_2 under anhydrous conditions (see Figure 3.7 in section 3.1.1.3), I also measured this parameter for treated samples treated of the two sets of SO_2-hydrous experiments, i.e., those performed at a constant exposure time, varying the temperature and amount of water vapour (mol.%) and those performed at a constant water vapour amount, varying the exposure times and temperatures.

For the first set of SO_2-hydrous treated samples, I chose to measure the redox state of iron of samples treated with six amounts of water instead of the whole range of eleven water vapour mo.% tested, since the six amounts (0.01, 47.72, 62.29, 82.17, 93.09 and 96.41 mol.% H_2O) seemed to be representative enough of the variety of effects observed for the eleven amounts of water vapour. In Figure 3.18, the results iron redox state determinations are shown, for this first set of samples.

Redox state of iron is expressed as $Fe^{3+}/\Sigma Fe$, versus the water vapour amounts tested (mol.%), for the temperatures of 600, 700 and 800 °C. Exposure time for all treated samples was 60 minutes. The data points corresponding to the results obtained under hydrous conditions are represented by filled triangles color-coded according to the experimental temperature, and the prolonged horizontal lines correspond to the single redox state value of the experiments performed at each temperature (600, 700, 800 °C), for 60 minutes, under SO_2-anhydrous atmospheres.

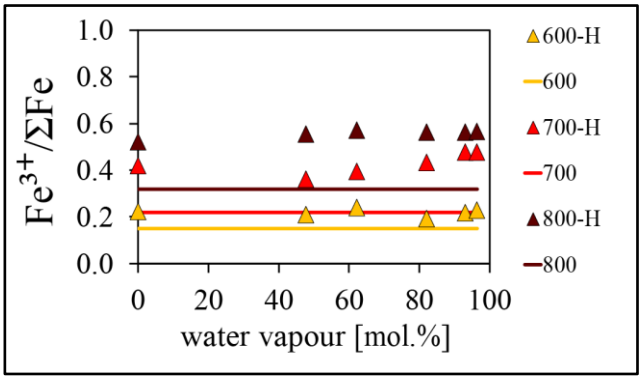

Figure 3. 18 Bulk iron redox state of iron of samples treated with the water vapour- and temperature-series of experiments. For the first set of SO_2-hydrous experiments (i.e., water vapour- and temperature series), FeO was determined and the redox state of iron, expressed as $Fe^{3+}/\Sigma Fe$, is plotted against the water vapour amounts (mol.%) for samples treated with at 600, 700 and 800 °C, for the constant exposure time of 60 min. As reference values of comparison, the $Fe^{3+}/\Sigma Fe$ values from samples treated under anhydrous conditions are also plotted. Data points of samples treated under hydrous experiments are represented by filled triangles, and the values obtained under anhydrous conditions are shown as constant colored lines.

Interestingly, the data points of hydrous experiments display a higher $Fe^{3+}/\Sigma Fe$ ratio (i.e., more oxidized iron) for all treatment temperatures, than the data points of the experiments performed at anhydrous conditions. Also, the increase of redox state of iron for the hydrous experiment data points, appears to be rather constant for all data points, for each temperature, independently of the water vapor (mol.%) added.

For example, the $Fe^{3+}/\Sigma Fe$ values obtained for the hydrous experiments of the samples treated with 0.01 and 96.41 mol.% H_2O (i.e., the lowest and highest humidity tested) are 0.223 and 0.228, 0.419 and 0.478, 0.523 and 0.565, for the samples treated at 600, 700 and 800 °C, respectively. Indeed, when the standard deviation of the $Fe^{3+}/\Sigma Fe$ values was calculated for all the water vapour mol.%, very small values were obtained; 0.003, 0.041 and 0.029, for the data obtained at 600, 700 and 800 °C, accordingly. The fact that, the hydrous treatment of the samples for all temperatures, produced a higher bulk oxidation of the iron present in the sample, points towards the occurrence of an enhanced redox dynamics of the iron in the glass particles.

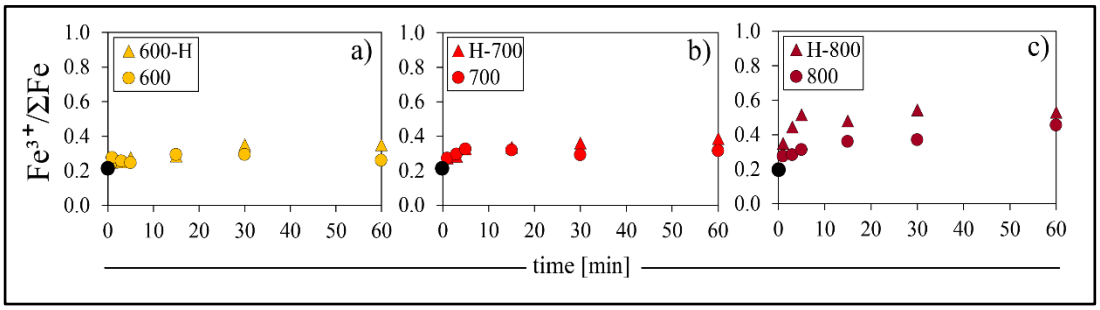

Figure 3. 19 Bulk iron redox state of samples treated with time- and temperature-series of hydrous SO_2 experiments. $Fe^{3+}/\Sigma Fe$ data is plotted of samples treated under hydrous conditions (represented by filled triangles), at 600 (a), 700 (b) and 800 °C (c), for 1-60 minutes with the constant added water vapour amount of 62.29 mol.%. $Fe^{3+}/\Sigma Fe$ data of the anhydrous experiments is also plotted, as filled circles, as well as the value corresponding to the initial (no-treated powdered glass), symbolized by a black filled circle.

	Measured $Fe^{3+}/\Sigma Fe$			Relative increase (%)		
T (°C)	600	700	800	600	700	800
Anhydrous	0.293	0.325	0.455	134	148	208
Hydrous	0.350	0.386	0.544	160	176	248
Initial $Fe^{3+}/\Sigma Fe$	0.219					

Table 3. 3 Maximum iron redox states obtained under hydrous and anhydrous conditions. The maximum $Fe^{3+}/\Sigma Fe$ values of samples treated at 600, 700 and 800 °C under hydrous and anhydrous SO_2 atmospheres are shown, along with the relative increase (in percentage) that these values represent, considering the initial $Fe^{3+}/\Sigma Fe$ value of the non-treated powdered material. For all temperatures the highest $Fe^{3+}/\Sigma Fe$ value was obtained for the samples treated under hydrous conditions.

Bulk oxidation of the hydrous-treated samples, is apparently unaffected by the increase of humidity in the gas-atmosphere, which might indicate that redox reactions of this material requires only a certain amount of water vapour to proceed above which, the effect of increased humidity on Fe oxidation can be neglected. Moreover, redox state of iron was also measured for the second set of hydrous experiments, as seen in Figure 3.19. Here, the redox state of iron ($Fe^{3+}/\Sigma Fe$) is plotted against the exposure times (1-60 minutes) for hydrous (62.29 mol.% H_2O) and anhydrous data points. Furthermore, the $Fe^{3+}/\Sigma Fe$ value of the pre-treated material (powdered glass) is also plotted (0.219) as a black filled circle, for a better comparison of the data.

At T= 600 and 700 °C (Figure 3.19a,b) the results obtained for time-series of experiments under both hydrous and anhydrous gas-mixtures seems to be similar, although the $Fe^{3+}/\Sigma Fe$ values of samples treated under hydrous conditions are slightly higher than those of anhydrous experiments for the exposure times of 30 and 60 minutes; 20 and 28% higher for T=600 °C and 20 and 18 % for T=700 °C. In both cases the highest $Fe^{3+}/\Sigma Fe$ values were obtained for samples treated under hydrous atmospheres for the longest exposure time, 0.35 and 0.38 for T=600 and 700 °C, respectively. At T=800 °C (Figure 3.19c), the deviation of $Fe^{3+}/\Sigma Fe$ values obtained under hydrous and anhydrous conditions is more evident.

The data point of the hydrous experiments is clearly higher for the exposure times of 1-30 minutes, and at t= 60 minutes, the values of both conditions show less variation from each other. The highest $Fe^{3+}/\Sigma Fe$ values of samples treated under hydrous and anhydrous conditions for all three temperatures were obtained at T=800 °C, namely 0.544 at t=30 min under hydrous conditions and 0.455 at t=60 minutes, for the anhydrous conditions. Both values represent a significant change in the bulk iron redox state of the samples, when considering the original iron redox state of the pre-treated material ($Fe^{3+}/\Sigma Fe$=0.219).

Table 3.3 summarizes the maximum $Fe^{3+}/\Sigma Fe$ values obtained for samples treated a 600, 700 ad 800 °C, under hydrous and anhydrous conditions. The increase in the redox state of iron in Table 3.3, is also expressed as percentages relative to the $Fe^{3+}/\Sigma Fe$ value of the initial (non-treated material). For all temperatures, the highest $Fe^{3+}/\Sigma Fe$ values (higher Fe oxidation), were obtained for samples treated under hydrous conditions, although, as mentioned before, the difference between among values obtain under hydrous and anhydrous conditions is overly high.

3.3 SO_2 uptake by synthetic haplogranitic glasses (HPG8)

Based on the results obtained from the first set of high temperature SO_2-uptake experiments by natural calk-alkaline obsidian, some preliminary premises could be made. The most concise and relevant was that, the role of calcium seemed to be essential for the glass-sulfur reactions responsible for SO_2 uptake by the calc-alkaline rhyolite used, since $CaSO_4$ was, by far, the most abundant product formed on the surfaces of the glass particles, for both hydrous and anhydrous SO_2 gas

atmospheres, for all time- and temperature-series of experiments. This conclusion was consistently reached upon extensive characterization of both surficial products (from leachate, SEM-BSE data) and internal glass chemical/structural changes (EPMA and SEM-EDS).

Furthermore, another very interesting result of the calk-alkaline obsidian set of experiments was the observed change in the iron redox state of the samples upon high temperature SO_2-treatments (both hydrous and anhydrous). Iron oxidation observed for the time- and temperature-series of experiments seemed to share the same trends observed for mobility of calcium (seen from the leachate data), since it increased also with exposure time and temperature, especially at T≥ 600 °C (like concentrations of leached calcium).

This led me to think that maybe mobility of calcium and iron oxidation are processes that might be linked. Is calcium outward diffusion causing iron oxidation, is iron oxidation instead calcium diffusion, or are the two processes not liked at all?. In order to bring insights into this issue, I decided to design a new set of SO_2-glass experiments, by making synthetic rhyolitic glasses, with the haplogranitic composition termed ´HPG8´ by Holz et al. (1992) described in section 2.3.1.2 of Chapter 2.

A total of twelve HPG8 glasses were synthesized, consisting of two sets doped with 1 and 2 wt.% CaO, each doped with 0, 0.1, 1, 1.5, 2, and 2.5 wt.% of FeO. After the glasses were synthesized, they were also milled and sieved to have a controlled grain size distribution of 63-90 μm. The time- and temperature series of SO_2-uptake experiments were designed similarly those of the calc-alkaline rhyolite, with some modifications, however, due to the large number of samples and the need to prioritize the number of experiments, thus the analytical characterization of samples.

In favor of prioritizing the number of experiments, the exposure times and temperatures tested were reduced, by choosing to only test the conditions at which SO_2-uptake showed to be more efficient for the calc-alkaline rhyolite, i.e., only the exposure times of 5, 15, and 30 minutes were chosen. Regarding the temperatures, only 600, 700 and 800 °C were tested, since they showed to strongly enhance formation of surficial products (see Figure 3.4), when compared with lower temperatures (T<600 °C).

The gas mixture remained the same: 1 mol.% SO_2 and 99 mol.% Ar. For this set of samples, experiments were only performed under anhydrous conditions, since leachate data results for the calc-alkaline rhyolite showed that the effect of adding water vapour to the gas-mixture was practically negligible for formation of surficial $CaSO_4$, thus the main product of high temperature SO_2-uptake.

3.3.1 Scanning electron microscope (SEM) analysis

SEM-BSE images were taken for samples of the two sets of HPG8 + 1 wt.%CaO and HPG8 + 2 wt.%CaO, each doped with 0, 1 and 2.5 wt.% FeO and treated at 600, 700 and 800 °C, for the exposure time of 30 minutes (i.e., the maximum exposure time). Only samples treated at 30 minutes were analyzed with the SEM, in order to ensure that enough surficial products were formed, and could be therefore detected and observed.

The obtained images are organized by composition and treatment temperature in Figure 3.20, where the three vertical sections from left to right can be seen, showing the samples treated at 600 °C (a-p), 700 °C (b-q) and 800 °C (c-r). The composition of the samples can be seen at the two horizontal sections corresponding to the two sets of HPG8 samples 1 and 2 wt.% CaO, and their corresponding content of wt.% of FeO. Several observations can be done regarding the shape, size, morphology and abundance of the surficial products formed on the treated HPG8 particles shown in Figure 3.20.

For instance, the effect of high temperature seems to be, as in was int the case of the calc-alkaline rhyolite, to enhance formation of larger and more abundant surface products. At T=800 °C, for both sets of HPG8 glasses, particle surfaces appear to be almost entirely occupied with surficial products of relatively large sizes (~1 μm in width) as those formed at 700 and 600 °C. For example, in panels c,f and i, corresponding to HPG8 samples doped with 1 wt.% CaO and 0, 1 and 2.5 wt.% FeO, respectively and treated at 800 °C, the surface products are consistently of larger size (~1 μm in width) and appear to have larger coverage areas than samples treated at 600 ° C, i.e., panels a, d and g or at 700°C, i.e., panels b, e and h.

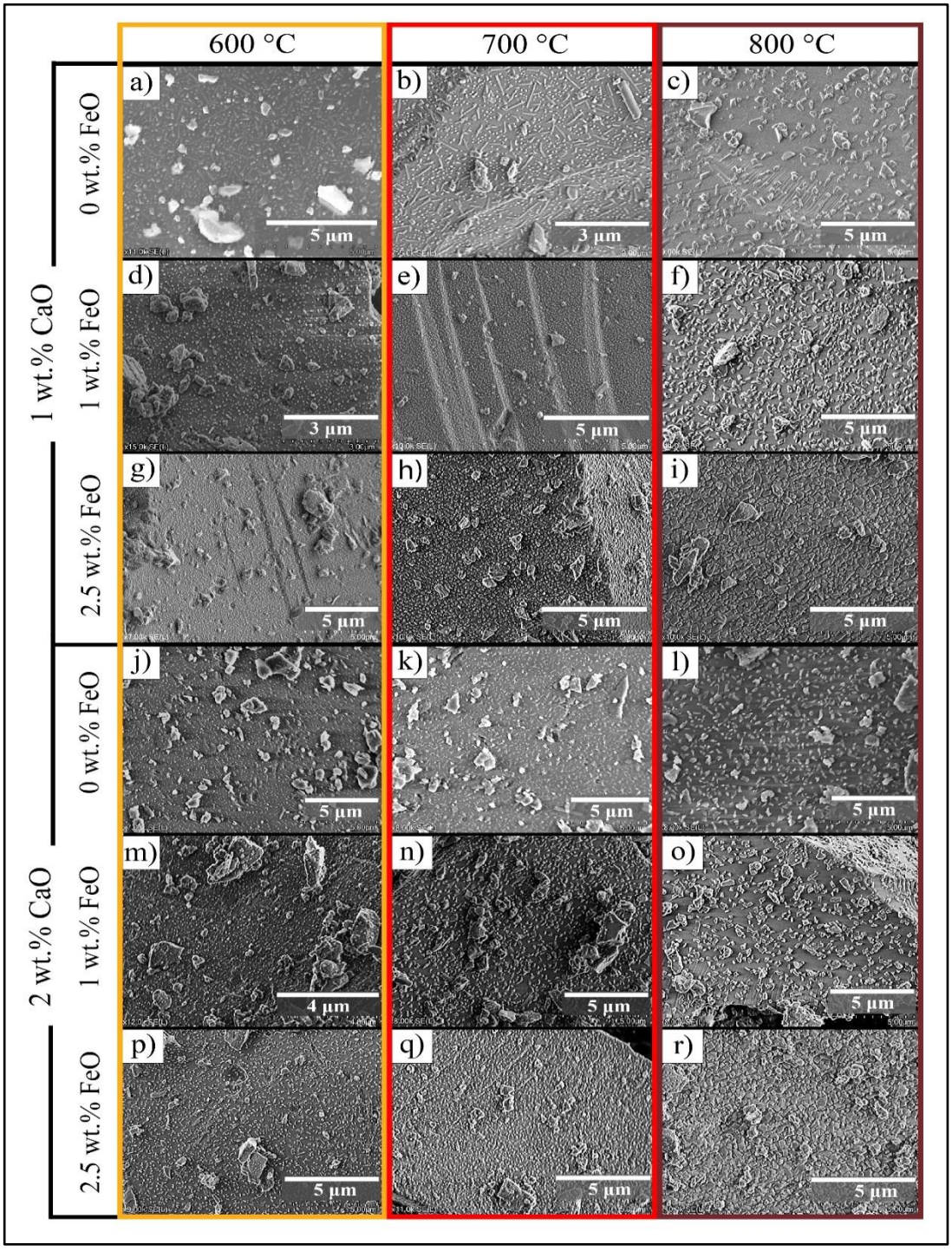

Figure 3. 20 SEM images of the SO_2-treated HPG8 samples. Samples of the two sets of HPG8 samples treated under SO_2-anhydrous conditions are shown and grouped according to the treatment temperature and composition. The sub set of HPG8 samples doped with 1 wt.% of CaO are shown in the first block (a-i), and grouped according to the iron oxide contents; 0 (a-c), 1 (d-f) and 2.5 (g-i) wt.% FeO, respectively. Analogously, HPG8 samples doped with 2 wt.% of CaO and 0 (j-l), 1 (m-o) and 2.5 (p-r) wt.% *of* FeO are shown. Treatment temperatures are color coded and shown as vertical sections; 600 (a,d,g,j,m,p), 700 (b,e,h,k,n,q) and 800 °C (c,f,i,l,o,r).

The same observation can be made for HPG8 samples doped with 2 wt.% CaO, where temperature treatments of 800 °C resulted in formation of larger and more abundant surface products as seen in panels l, o and r (0, 1 and 2.5 wt.% FeO), when compared to the same samples treated at 600 °C (see panels j, m and p) and 700 °C (panels k, n and q). Regarding the effect of the sample composition on the surficial products (addition of CaO and FeO) formed on the surface of samples, some noteworthy features were observed.

First, that the iron-free samples, from both sets of HPG8 glasses (doped with 1 and 2 wt.% of CaO), treated at 600 and 700 °C (see panels a,b and j,k respectively), appear to display surficial products with greater aspect ratios than the iron-bearing samples (doped with 1 and 2.5 wt.% FeO), and have a rather spike-like morphology (up to ~1 μm in length). This is especially evident for samples doped with only 1 wt.% CaO, treated at 600 and 700 °C (see panels a and b), for which several spike-shaped products appear on the particle surfaces, together with other surficial products of smaller aspect ratios and sizes (up to ~200 nm).

Samples doped with 2 wt.% of CaO show a similar behavior, in that, the products formed at 600 and 700 °C (see panels j and k), also appear to be spike-shaped, however these products seem to be slightly wider than those formed on samples doped with 1 wt.% CaO. Addition of 1 and 2.5 wt.% FeO in samples doped with 1 wt.% CaO appears to result in formation of surface products with a smaller aspect ratio (see panels d and g), showing a clearly different morphology than that observed for samples with 0 wt.% FeO. This is also the case for samples doped with 2 wt.% CaO, where addition of 1 and 2.5 wt.% of FeO results in a change of the morphology of the surficial products towards more cubic/angular shapes, as seen in panels m and p for samples treated at 600 °C and panels n and q, for samples treated at 700 °C.

Also, abundance of surficial products upon addition of FeO seems to increase, as formation of surficial products appears to be more extensive for samples with 1 and 2.5 wt.% FeO than those without FeO, despite being treated at the same temperature. For example, at T= 600 °C for the sample doped with 1 wt.% CaO, surficial products formed for samples doped with 2.5 and 1 wt.% FeO (panels g and d, respectively), display a more extensive coverage, than those formed for the sample without added FeO (panel a).

Based on the surficial products formed from HPG8 glasses of different compositions treated at 600-800 °C, the following broad observations can be done: 1) the treatment temperature of 800 °C seems to be, as in the case of the calc-alkaline rhyolite experiments, the most efficient temperature for formation of sulfur-bearing products (thus for SO_2-uptake) by rhyolitic glass, given the fact that a larger areas of the particles surfaces were covered by reaction products, hinting at higher reactivity of cations (specially Ca) with SO_2, 2) addition of FeO appears to increase formation of surficial products as well as to yield formation of more angular morphologies 3) addition of CaO also seems to enhance formation of surficial products upon SO_2 treatments, and 4) exposure temperature appears to be a controlling factor for SO_2 uptake.

3.3.2 Leachate analyses

After SEM-BSE analyses showed presence of extensive surficial products formed on the HPG8 samples surfaces upon performing high temperature SO_2-uptake experiments, as seen for the calc-alkaline rhyolite, the nature of the surface products was also determined. This was done by analyzing leachates of the samples, with ion chromatography (described in section 2.5.1, Chapter 2), for all the time-and temperature series of experiments of samples doped with 1 and 2 wt.% CaO and 0, 0.1, 1, 1.5, 2 and 2.5 wt.% FeO.

Results of leachate analysis are displayed in Figure 3.21, which shows, for each leached cation (Ca^{2+}, Na^{+} and K^{+}), its concentration obtained from each set of HPG8 samples, i.e., doped with 1 and 2 wt.% CaO, as upper and lower graphics, respectively. The treatment temperature of experiments is symbolized by the color of the outlines enclosing each data set, i.e., concentrations obtained from experiments performed at 600, 700 and 800 °C, are enclosed within a yellow, red and dark red outlines, respectively.

Concentration data points of the HPG8 set of experiments are shown as filled circles. The filling colors of the concentration data are blue, orange and grey and represent the experiment exposure times of 5, 15 and 30 min, accordingly. Furthermore, data points of the previous set of experiments, performed with the natural calc-alkaline rhyolite are also plotted within the HPG8 graphics, for comparison purposes, and are shown as filled squares.

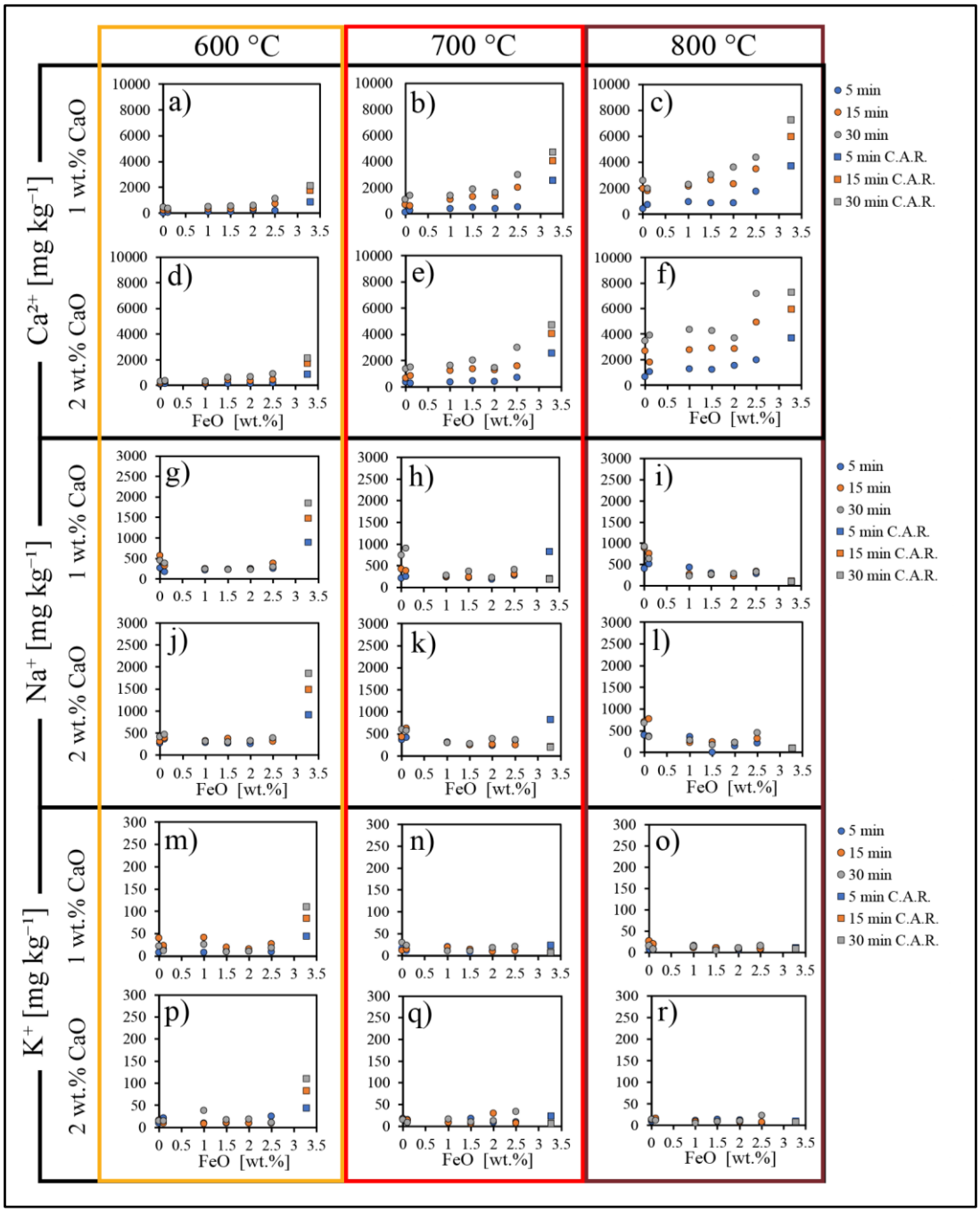

Figure 3. 21 Concentrations of leached cations from the HPG8 samples doped with 1, 2 wt. % CaO and 0, 0.1, 1, 1.5, 2 and 2.5 wt.%FeO. Concentrations of leached Ca^{2+} (a-f), Na^{+} (g-l), and K^{+} (m-r), from HPG8 samples treated with SO_2-Ar gas mixtures, for time and temperature-series of experiments are shown. Leachate data of temperature-series of experiments are displayed as vertical columns; from left to right, the data obtained at 600 (a,d,g,j,m,p), 700 (b,e,h,k,n,q), and 800 °C (c,f,i,l,o,r), while data of the time series of experiments, 5, 15 and 30 min., are plotted as blue, orange and gray circles, respectively. Additionally, as a comparison element, the data obtained under the same sample treatment but for the natural calc-alkaline rhyolite (denoted C.A.R. in the plot legend), is also shown for each graphic as squares, following this same time-color coding.

All concentration data points are expressed as mg kg^{-1}, and plotted against the amount of total iron, expressed as FeO (wt.%) of the sample. In the case of the HPG8 samples, this refers to the amounts of FeO added to each sample (0, 0.1, 1, 1.5, 2 and 2.5 wt.%), whereas in the case of the calc-alkaline rhyolite, this value represents its natural content of 3.26 wt.% FeO. Leachate data of the HPG8 samples seemed to broadly display similar trends to those observed for the calc alkaline leachate data.

For instance, that for all time- and temperature-series of experiments of both sets of HPG8 samples (doped with 1 and 2 wt.% CaO), concentrations of leached calcium were the highest obtained amongst all three cations, indicating formation of mainly Ca-bearing sulfur surficial products (i.e., $CaSO_4$). Also, that concentrations of leached calcium increased with increasing exposure time and temperature, as the highest concentrations of calcium were obtained at T=800 °C for the exposure time of 30 minutes of the samples doped with 1 and 2 wt.% of CaO, and correspond to 4357 mg kg^{-1} (panel c) and 7178 mg kg^{-1} (panel f), respectively.

Interestingly, the combined effect of adding CaO and FeO, appears to result in increasing leached calcium concentrations obtained for the HPG8 samples. This effect is perhaps clearer at T= 800°C for samples doped with 1 (panel c) and 2 wt.% CaO (panel f), where addition of FeO (0-2.5 wt.%) consistently results in increasing concentrations of leached calcium, indicating enhanced formation of $CaSO_4$. Addition of CaO, also results in enhanced formation of Ca-bearing surficial products, since concentrations of calcium leached at T=800 °C, are clearly higher than those obtained for samples doped with 1 wt.% CaO.

By comparing the natural calc alkaline calcium-data points with the doped CaO- and FeO-doped HPG8 samples, interesting observations can be done. Fist, concentrations of leached calcium of the HPG8 samples doped with 1 wt.% CaO, for all time- and temperature-series of experiments and all added FeO amounts, are much lower than the calcium concentrations obtained for the natural rhyolite, at the same temperature treatments and exposure times. This observation becomes more interesting, when the composition of the natural calc-alkaline rhyolite is considered. As described in Chapter 2, section 2.5.4, this material was Ca- and Fe-rich, 1.7 and 3.26 wt.% respectively, thereby, all concentrations of calcium leached from the HPG8 samples doped with 1wt.%CaO have less FeO and CaO than the calc-alkaline rhyolite, which seems to lead to lower Ca concentrations (i.e., lower Ca-

bearing surficial products formation), than for the natural rhyolite. For example, HPG8 samples containing 1 wt.% CaO and 2.5 wt.% FeO treated at 600, 700 and 800 °C for 30 minutes, had calcium concentrations 47, 36 and 39 % lower than those obtained under the same time- and temperature experiments of calc-alkaline samples. In the case of the HPG8 samples doped with 2 wt.% CaO, concentrations of calcium leached, appear to be similar to those obtained for samples doped with 1 wt.% CaO, at 600 and 700 °C, however at T= 800°C, calcium concentrations of HPG8 samples (panel f) are noticeable higher than in panel c.

Furthermore, the data point obtained for the HPG8 + 2wt.% CaO, treated at 800°C for 30 minutes seems to match the result obtained for the calc-alkaline sample (30 min C.A.R.) treated under the same conditions, being the first only 1.1 % lower than the HPG8 sample. For the same the same temperature (800 °C), the HPG8 sample treated for 15 minutes also shows a calcium concentration similar to that of the calc-alkaline rhyolite treated also for 15 minutes (15 min C.A.R.), only 17% lower, while for the exposure time of 5 min, calcium concentrations of the HPG8 sample is 46 %lower than that of the calc alkaline rhyolite (5 min C.A.R.).

These results might suggest that, although bulk iron content in the glass appears to enhance calcium mobility (thus, formation of leachable surficial $CaSO_4$), the amount of bulk Ca content in the particles is the strongest parameter controlling Ca-bearing surface products. Moreover, the temperature of 800 °C, seems to be, as for the calc-alkaline rhyolite-experiments, the temperature at which the highest Ca concentrations were obtained, thus formation of Ca-bearing soluble products, has the highest efficiency among the temperatures tested.

Concentrations of leached sodium and potassium of treated HPG8 samples also show some interesting features, although addition of CaO does not appear to have any effect on the leachate results. For all treated samples (HPG8 and natural calc-alkaline), sodium concentrations obtained are much less than those obtained for calcium (see y-axis scale), however at 600 °C, concentrations of sodium leached of HPG8 samples (doped with both 1 and 2 wt.% CaO) seem to be even lesser than those of the natural calc alkaline rhyolite (panels g and j), at 700 and 800 °C, this difference appears to decline, as sodium concentrations of calc-alkaline rhyolite decrease with increasing treatment temperature of the samples (see Figure 3.4).

However, for the HPG8 samples with no FeO added (i.e., 0wt.%FeO), this trend does not seem to occur, as seen in panels g-l, where concentrations of leached Na (of samples with 0 wt.%FeO) shows a slight increase upon increasing treatment temperature, unlike the case of the C.A.R. This result might indicate that absence of Fe positively influences mobility of Na, (thus Na-bearing surficial products formation). Leachate data for potassium does not display this trend, and in general concentration of potassium are even lesser than those of sodium (see y-axis scale), as previously seen for the calc-alkaline leachate results.

At 600 °C, concentrations of leached potassium show the greatest discrepancy among concentrations obtained by the other treatment temperatures, where HPG8 (doped with 1 and 2 wt.% CaO) samples experiments resulted in much less leached potassium than the calc alkaline rhyolite samples for all exposure times. Nevertheless, leachate results of HPG8 samples treated at 700 and 800 °C, seem to agree with those of the calc-alkaline rhyolite samples, i.e., negligible concentrations were obtained for all exposure times.

This shows (as in the case of the natural rhyolite), that K-bearing surficial product formation (e.g., K_2SO_4) is a rather inefficient reaction resulting of SO_2-glass particles interactions. After observing that, for all HPG8 treated samples, the main leached cation was calcium, I also proceeded to determine sulfate (SO_4^{2-}) concentrations and plot the molal ratios of Ca^{2+}/SO_4^{2-}, $2Na^{+}/SO_4^{2-}$ and $2K^{+}/SO_4^{2-}$, in order to confirm that $CaSO_4$ was the main product of high temperature SO_2-uptake reactions, as for the experiments performed with natural rhyolite.

Figure 3.22 shows the resulting plots of HPG8 samples doped with 1 and 2 wt.%CaO, expressed as molal concentrations (mmol kg^{-1}) of leached Ca (panels a and b), Na (panels c and d) and K (panels e and f), are plotted against molar concentrations of leached SO_4^{2-}. Each plot includes leachate data of all HPG8 treated samples, doped with the rage of 0-2.5 wt.% FeO and treated for the experimental exposure times (5, 15 and 30 min.), but no special symbol/color was used to distinct the FeO content or exposure time, only the treatment temperature is shown with the color-coding used before and explained in the plot-legends (as in Figure 3.5).

This was done to simplify the interpretation of the graphics, since the purpose of this figure was to confirm $CaSO_4$ formation, as a result of SO_2-uptake by HPG8 particles.

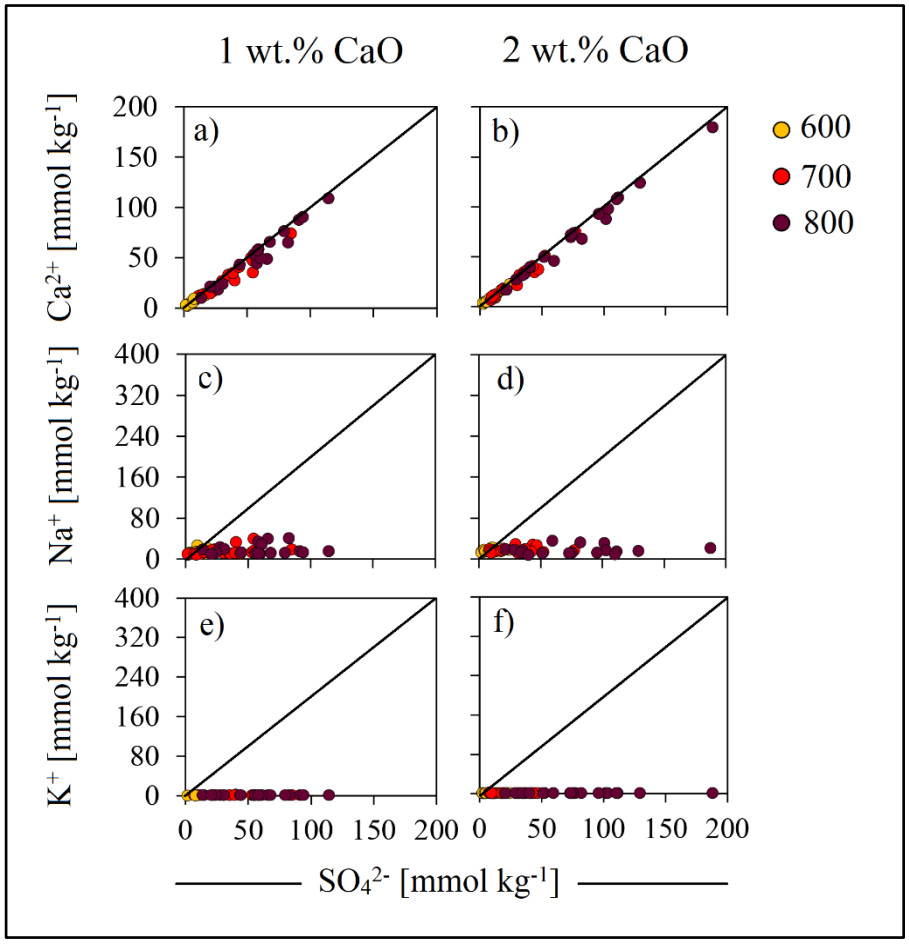

Figure 3. 22 Molal concentrations of leached cations and sulfate. Molal concentrations (mmol kg^{-1}) of leached cations, Ca^{2+} (a,b), Na^{+} (c,d) and K^{+} (e,f) are plotted against concentrations of leached sulfate for the two sets of HPG8 samples (doped with 1 and 2 wt.%CaO) treated with SO_2, at 600, 700 and 800 °C. All the time- and temperature-series of experiments are plotted, but in order to simplify the graphic, only the temperature-series are distinguished with the color code scale used previously, i.e., yellow (600 °C), red (700 °C and dark red (800 °C). The black lines show the molal relations for $CaSO_4$ (1:1), Na_2SO_4 and K_2SO_4 (both 2:1).

Coefficient of correlation R^2						
	1 wt.% CaO			2 wt.% CaO		
T (°C)	600	700	800	600	700	800
Ca	0.942	0.955	0.959	0.978	0.972	0.989
Na	0.107	0.205	0.007	0.149	0.019	0.012
K	0.048	0.092	0.054	0.005	0.109	0.024

Table 3. 4 Correlation coefficient values for molal ratios of leached HPG8 samples treated with SO_2. Correlation coefficients obtained from molal ratios of Ca, Na and K and of sulfate were obtain for HPG8 samples doped with 1 and 2 wt.% CaO for all treatment temperatures, from the plots in Figure 3.22.

Indeed, this was the case for all HPG8 treated samples, as implied by the previous leachate data of cations (Figure 3.21), where concentrations of leached calcium were the highest obtained among the other cations. By looking at the molar ratios of calcium and sulfate (panels a and b) a striking 1:1 behavior can be seen for all samples, indicating that the high concentrations of Ca obtained, resulted from dissolution of $CaSO_4$ surficial products formed on the HPG8 particles.

To better evaluate the correlation between molar concentrations of cations and sulfate, the coefficient of correlation, R^2, was calculated (as for the molar concentrations of the natural rhyolite experiments), and the results are shown in Table 3.4. For calcium data of samples treated at 600, 700 and 800 °C, values of 0.942, 0.955 and 0.959 are obtained for samples doped with 1 wt.% CaO, while for samples doped with 2 wt.% CaO are slightly higher; 0.978, 0.972 and 0.989, respectively, in both cases the strongest 1:1 relation between calcium and sulfate were obtained for samples treated at 800 °C.

This result is in strong agreement with the previous leachate results, of both HPG8 samples and natural calc-alkaline rhyolite experiments, for which, samples treated at 800 °C for all exposure times, CaO and FeO added amounts, showed to produce the highest amounts of surficial products, specifically $CaSO_4$. R^2 values obtained for Na, were lower than 0.3, for samples doped with 1 and 2 wt.% CaO treated at 600, 700 and 800 °C. The lowest R^2 values were obtained at 800 °C, which agrees with R^2 values obtained for the natural rhyolite treated samples.

Lastly potassium molar concentrations show even lower correlation with sulfate molar concentrations values for all temperatures, being R^2 for all temperatures <0.2. Results of molar ratios of monovalent cations vs sulfate, clearly show a less preferential reaction pathway between SO_2 and Na and K, to form surficial products, and in general, increasing of temperature results in even lower formation of these products, as also seen for the natural rhyolite leachate data (see Figure 3.5d-i).

3.3.3 Bulk FeO determination (iron redox state)

The bulk redox state of HPG8 iron-bearing samples (i.e., 0.1, 1, 1.5, 2 and 2.5) was also determined for the non-treated material and for some treated samples.

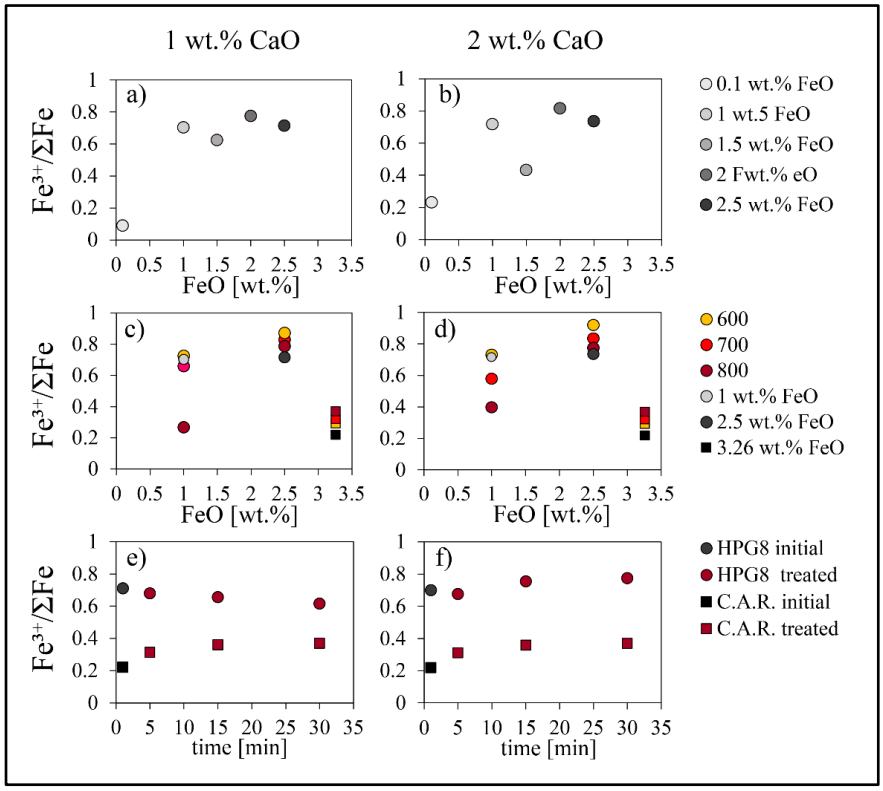

Figure 3. 23 Bulk iron redox state of the treated and non-treated HPG8 samples. Expressed as the ratio of ferric iron (Fe^{3+}) over the total iron (ΣFe). Initial Fe^{3+}/ΣFe values of the two non-treated sets of HPG8 samples are plotted against the bulk FeO content (wt.%). a) shows iron redox state of samples doped with 1 wt.% CaO and b) shows redox values of samples doped with 2 wt.% CaO. In both cases a gray scale of colors is used to symbolize different the FeO (wt.%) content. Plots c) and d) show redox values of samples doped with 1 and 2 wt.% CaO, respectively, and treated at 600, 700 and 800 °C, all for 30 minutes. Due to the large number of samples, only those containing 1 and 2.5 wt.% FeO were plotted. Plots c) and d) also show the initial values of each sample, distinguished by the gray colors to compare changes of the redox state of treated samples vs the non-treated samples, also the initial redox state of the calc-alkaline rhyolite (labeled C.A.R. in the legend) is plotted as a black filled square in each case. Plots e) and f) show the variation of redox state for the time-series of experiments performed at 800 °C for the samples doped with 1 and 2 wt.%CaO, respectively. In these graphics, also Fe^{3+}/ΣFe values of time-series experiments of the calc-alkaline rhyolite (C.A.R) are plotted as filled squares.

Figure 3.23 shows the results obtained for the Fe redox state determinations of non-treated HPG8 samples (i.e., only powdered and sieved glasses) doped with 1 and 2 wt.% CaO in panels a and b, accordingly. For comparison purposes, also the corresponding data of calc-alkaline rhyolite samples treated for the same exposure time and temperatures, and of the same grain size

distribution (63-90 μm) are plotted together with the HPG8 data, the latter being represented by filled circles and the first by filled squares, as for Figure 3.21. Each non-treated sample is color coded according to the amount of iron, with a gray scale; increasing iron contents have darker-gray colors (see legend). The results of the treated samples doped with 1 and 2.5 FeO wt.% FeO, doped with 1 and 2 wt.% CaO, showed in panels c and d respectively. These samples were treated with SO_2 for 30 minutes each, at 600, 700 and 800 °C (see legend), furthermore, as a reference data point, por each plot of treated samples, the initial redox state of iron of the untreated sample is also plotted. For example, in panel c, data points of the treated samples HPG8 + 1 wt.% CaO, doped with 1 and 2.5 wt.%FeO, treated at 600, 700 and 800 °C, can be seen as yellow, red and dark red filled circles, accordingly, while the corresponding initial redox state values of are shown as filled circles of pale gray (i.e., non-treated HPG8 + 1%FeO) and dark gray (i.e., non-treated HPG8 + 2.5%FeO), respectively. In all plots, redox state of iron is expressed as $Fe^{3+}/\Sigma Fe$ and plotted against the amount of total iron in the sample (wt.% FeO).

Generally high $Fe^{3+}/\Sigma Fe$ values obtained for the non-treated samples, HPG8 + 1 and 2 wt.%CaO, indicate that they were initially highly oxidized (panels a and b), with the exception of samples containing 0.1 wt.% FeO, which in both cases display rather reduced $Fe^{3+}/\Sigma Fe$ values of 0.08 and 0.23 in panels a and b, accordingly. Excluding these values, the other samples (HPG8+ 1, 1.5, 2 and 2.5 wt.% FeO), display $Fe^{3+}/\Sigma Fe$ values ranging from 0.62-0.77 and 0.4-0.8 for HPG8 samples doped with 1 and 2 wt.% CaO, respectively. Apart from the $Fe^{3+}/\Sigma Fe$ reduced values of samples with 0.1 wt.%FeO, samples with higher FeO contents show a broadly good agreement with each other, as standard deviation values are 0.06 for the 1wt.% CaO doped samples and 0.1 for those doped with 2 wt.%. Low $Fe^{3+}/\Sigma Fe$ values obtained for the 0.1 wt.%FeO-doped samples, could be due the analytical $K_2Cr_2O_7$ potentiometric titration method, since repetition of the measurements for these samples yielded to varying results and high standard deviations, within the same samples (0.1 wt.% FeO + 1, 2 wt.% CaO), which was not the case when measurements of samples of higher FeO contents were repeated.

This might suggest that, this analytical method to determine iron redox state of samples might not be suitable for samples with FeO < 1 wt.%. Regarding the values obtained for the treated samples (HPG8 + 1 and 2 wt.% CaO), these show some differences than for the natural rhyolite.

For the latter, the increase in treatment temperatures, consistently resulted in increasing of the $Fe^{3+}/\Sigma Fe$ values, i.e., the higher the treatment temperature the more oxidized became the iron in the sample. However, in the case of the analyzed HPG8 treated samples, this behavior seems to apply only for the samples with the highest FeO content i.e., 2.5 wt.% FeO, where samples treated at 600-800 °C display higher $Fe^{3+}/\Sigma Fe$ values for both 1 and 2wt.% doped HPG8 samples (panels c and), than the initial values of the corresponding untreated 2.5 wt.% FeO samples.

Yet, the iron redox state of the samples, does increase according to the treatment temperature, i.e., higher temperatures did not systematically yield higher $Fe^{3+}/\Sigma Fe$ values, for example in panel c, where the non-treated sample of 2.5 wt.%FeO had an initial $Fe^{3+}/\Sigma Fe$ value of 0.71, the most oxidized result of the treated samples was 0.87, obtained at 600 °C, followed 0.82 at 700 °C and 0.78 at 600 °C. From panel d, similar results can be seen for the treated samples containing 2.5 wt.% FeO, where the most oxidized Fe values (amongst the two 1 and 2 wt.% CaO doped set of samples) were obtained at 600°C, i.e., 0.92, followed by 0.83 at 700 °C and 0.77 at 800 °C.

Thus, for treated samples containing 2.5 wt.% FeO, lower treatment temperatures resulted in increasing iron oxidation of the sample. This was a contrasting result obtained for the treated HPG8 samples, when compared to those obtained for the natural rhyolite (see Figure 3.7). The discrepancy in the redox behavior of treated samples with that of the natural rhyolite, becomes even more evident when observing $Fe^{3+}/\Sigma Fe$ values obtained for the samples containing only 1 wt.% of FeO. For these samples, increase of treatment temperatures (700 and 800 °C) proportionally resulted in a decrease of the iron redox sate ($Fe^{3+}/\Sigma Fe$ values), for both 1 and 2 wt.% doped samples, for which the lowest values were obtained at 800°C; 0.26 and 0.39, followed by 700 °C; 0.65 and 0.57, respectively.

Only samples treated at 600 °C, resulted in slightly increased $Fe^{3+}/\Sigma Fe$ values (with respect to their initial redox state), of 0.72 and 0.73, for samples doped with 1 and 2 wt.% CaO, respectively. To also test the effect of exposure time upon changes in the iron redox state of treated samples, $Fe^{3+}/\Sigma Fe$ values of HPG8 samples doped with 1 and 2 wt.%CaO and 2.5 wt.% FeO each, treated at 800 °C for 5, 15 and 30 minutes are plotted in panels e and f, respectively.

As in the previous plots, s calc-alkaline rhyolite treated under the same conditions, and the initial iron redox state values of each material, are also plotted. In both cases, HPG8 samples doped with 2.5 wt.%FeO and 1 and 2 wt.%CaO, panels e and f, accordingly, the redox state of iron does seem to increase upon increasing exposure time, in the same manner as for the natural rhyolite treated samples.

Although, the $Fe^{3+}/\Sigma Fe$ values obtained for the time-series of experiments, display an analogous behavior to that of the natural rhyolite samples, discrepancies in the $Fe^{3+}/\Sigma Fe$ values obtained for the temperature-series of HPG8 samples point towards a more complex redox dynamic. HPG8 samples doped with 1 and 2.5 wt.%FeO (and 1 and 2 wt.% CaO each), displayed more oxidized and more reduced values, accordingly upon increasing temperature. This behavior and its implications for Ca mobility, will be further discussed in Chapter 4.

3.3.4 Raman spectroscopy

Characterization of the structural properties of both non-treated and treated HPG8 glasses was also done with Raman spectroscopy, to gain insights on the chemical dependence of the glass structure and the mineralogy of the surficial products formed. Spectroscopic analytical parameters were the same as those used for the calc-alkaline rhyolite, described in Chapter 2, section 2.5.5. Both analysis of non- and treated samples was done for samples as powders.

3.3.4.1 Raman spectra of the non-treated samples

Results of the Raman spectroscopy analysis of all initial HPG8 glasses, doped with 1 and 2 wt.%CaO and 0, 0.1, 1, 1.5, 2 and 2.5 wt.% FeO each is shown in Figure 3.24. Peaks relevant to glass structure, are high lightened for each one of the three regions characteristic of silicate glasses, i.e., low-, intermediate- and high-wavenumber regions (~200-300, ~300-900 and >900 cm^{-1}), and are distinguished with yellow, blue and green colored bands, respectively for each spectrum. Spectra of both set of samples containing 1 wt.% CaO (shown in panels a,c,e,g,i,k) and 2 wt.% CaO (panels b,d,f,h,j,l), display similar features characteristic of highly polymerized glasses (i.e., Si-rich).

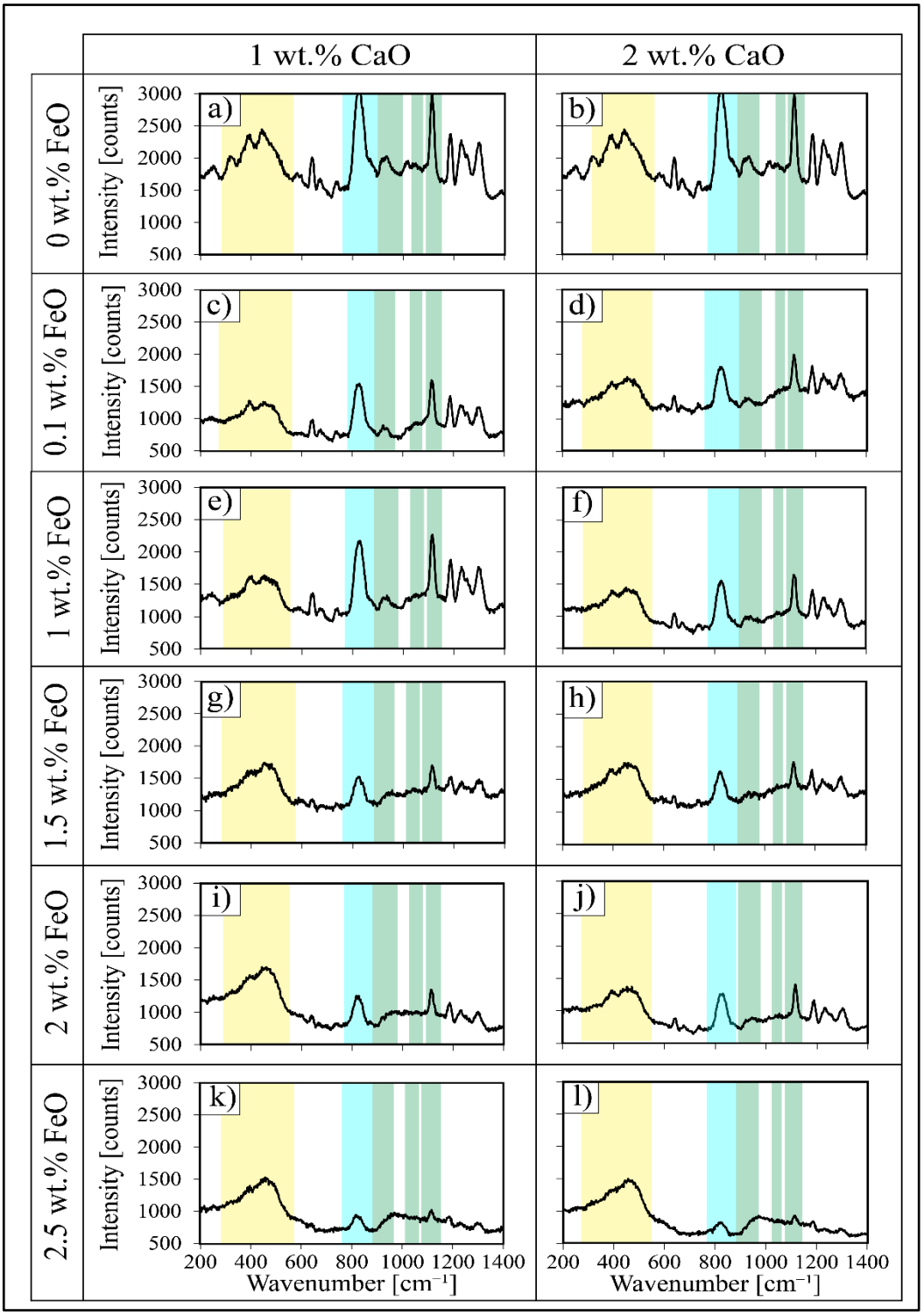

Figure 3. 24 Average Raman spectra of the non-treated HPG8 powdered glasses. Raman spectra were acquired for the two sets of HPG8 samples, doped with 1 (panels a,c,e,g,l and k) and 2 (b,d,f,h,j and l) wt.% CaO (each doped with 0, 0.1, 1, 1.5, 2 and 2.5 wt.% FeO). Relevant features related to the glass structure are high lightened with color bars, corresponding to the characteristic wavenumber regions of silicate glasses; yellow, blue and green bands represent the low-intermediate and high wavenumber regions, respectively.

At the low-waver region a prominent peak at ~470 cm^{-1} (yellow band), can be seen for the acquired spectra of all samples (panels a-l), which has been consistently linked in previous studies (e.g. McMillan 1982,1988; Neuville et al. 2014) to symmetric bending (V2) of bridging oxygens in the three-dimensional network structure. The peaks at ~980, ~1050 cm^{-1}, seem to decrease in intensity as FeO is added for both sets of samples. For instance, only spectra of samples doped with FeO ≤ 1 wt.%, all three peaks display distinguishable signals, while spectra of samples doped with FeO ≥1.5 wt.%, the only distinguishable peak is that of ~1120 cm^{-1} (see panels g-l).

3.3.4.2 Raman spectra of the surficial products formed

Mineralogy of the surface products was also determined by Raman spectrometry, to complement characterization of the products resulting from the high temperature SO_2-HPG8 glass reactions, as done for the calc-alkaline rhyolite treated samples (see section 3.1.1.4.1). Both sets of treated HPG8 samples, doped with 1 and 2 wt.% CaO were analyzed, but only the samples doped with 0, 1 and 2.5 wt.% FeO each, all treated at 800 °C for 30 minutes. The resulting acquired spectra is shown in Figure 3.25.

In all cases, the peaks corresponding to spectra of anhydrite determined in section 3.1.1.4.1 (see Figure 3.18 and Table 3.3) are seen for the HPG8 treated samples; the peaks corresponding to the SO_4 molecule vibrations modes V1, V2, V3 and V4 are seen at average values for the six spectra at 1015 cm^{-1} (V1), 412 and 501 cm^{-1} (V2), 1129 and 1167 cm^{-1} (V3), 623 and 686 (V4) and the peak attributed to the vibration of the bond between calcium an sulfate (M-O), a peak at an average value of 261 cm^{-1} is found for all spectra.

When comparing the position of these peaks with those of the reference material of anhydrite (see Table 3.3) a great agreement is found, strongly indicating that the main surficial product formed as a consequence of SO_2 uptake, is anhydrite ($CaSO_4$). This result agrees with that obtained for the natural rhyolite (see section 3.2), where also anhydrite was the main reaction product formed during high temperature SO_2 experiments. The implication of this is that for rhyolitic glasses, SO_2 uptake is limited by calcium mobility within the glass (i.e., diffusion).

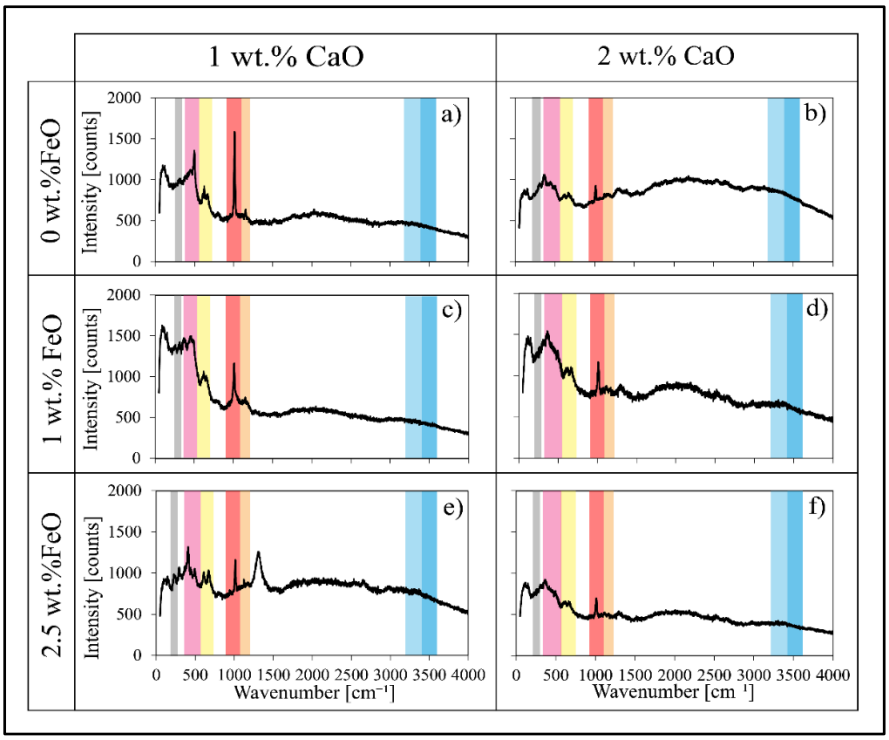

Figure 3. 25 Average Raman spectra of surficial products of treated HPG8 samples. Raman spectra acquired for treated HPG8 samples doped with 1 and 2 wt.% of CaO and 0, 1 and 2.5 wt.% FeO, treated at 800 °C for 30 minutes each are shown. Samples were analyzed as powders and for each spectrum, the location of peaks present in the anhydrite and gypsum spectra are high lightened with color bars. For anhydrite, the vibrations corresponding to the sulfate molecule V1 (1005 cm^{-1}), V2 (416 and cm^{-1}) V3 (1137 cm^{-1}) and V4 (622 and 673 cm^{-1}) are symbolized by the pink, yellow, orange and pale orange bars, while the peak corresponding to vibrations of the bond Ca-SO_4 located at 323 cm^{-1} is represented by a gray bar. To also test the presence of gypsum ($CaSO_4 \cdot 2H_2O$), in addition to the above-mentioned peaks, the peaks corresponding to vibrations of water molecules V1 (3403 cm^{-1}) and V3 (3490 cm^{-1}) are highlighted by blue and dark blue bars.

This was also confirmed by the absence of peaks related to vibration of water molecules at wavenumber ~3403, 3490 cm^{-1}, symbolized by blue bars in Figure 3.25, which would have implied presence of gypsum ($CaSO_4 \cdot 2H_2O$).

3.3.5 Electron probe micro-analyzer (EPMA) transect measurements

EPMA analyses were then conducted for treated samples prepared as polished thick sections, in order to detect cation depletion within the sample-particles.

For this, several spot-analysis were made for samples of diverse time- and temperature-series of experiments, along perpendicular transects of grain polished surfaces, as for the calc-alkaline rhyolite (transects depicted in Figure 3.11b-d), according to the analytical parameters described in Chapter 2, section 2.5.4. Due to the considerable amount of time that it would have taken to analyze all treated HPG8 samples, (doped with 1 and 2 wt.%CaO and 0, 0.1, 1, 1.5, 2 and 2.5 wt.% FeO each), EPMA analyses were done only for the treated samples doped with 1 and 2 wt.% CaO and 0, 1 and 2.5 wt.% FeO each, treated for 5, 15 and 30 minutes at 600, 700 and 800 °C.

Results of CaO, Na_2O and K_2O wt.% measured for transect spot-analysis can be seen in Figure 3.26, where data points are showed as circles filled with the color corresponding to the treatment temperature, and no distinction was made to differentiate the exposure times. All data in plotted against a ´Normalised transect distance´ which was an adjustment done to disregard differences in the distances of the transect measurements and be able to plot them all in a scale of 0 to 1, which represent the edges of the particle surface and 0.5 represents the middle. In each plot, the initial values of CaO, Na_2O and K_2O, (i.e., 1.19, 3.99, and 4.36, for samples doped with 1 wt.% CaO, and 2.17, 4, and 4.31, for samples doped with 2 wt.%, respectively), described as ´non-treated material´ in the plot legend, are plotted as a green constant line.

Data obtained of wt.% CaO treated samples doped with 1 wt.% CaO (panels a-c), seem to mimic those of the calc-alkaline samples (see Figure 3.13), in that near-edge depletion of calcium (expressed as wt.% CaO) can be seen for the three samples (doped with 0, 1 and 2.5 wt.%FeO), they behave however differently in each case; as the temperature dependence of Ca depletion appears to be influenced by the amount of Fe present in each sample. For example, for samples containing no Fe (0 wt.%FeO), most of the near-edge depletion seems to occur for those treated at 600 °C (see panel a), for samples doped with 1 wt.% FeO, near-edge depletion seems to occur mostly for higher temperatures, 700 and 800, whereas for the samples doped with 2.5 wt.% FeO, Ca depletion seem to occur mostly for samples treated at 800 °C. For the same set of samples (doped with 1 wt.% CaO), results of Na and K, also show interesting trends, when compared to the results obtained for the calc alkaline rhyolite.

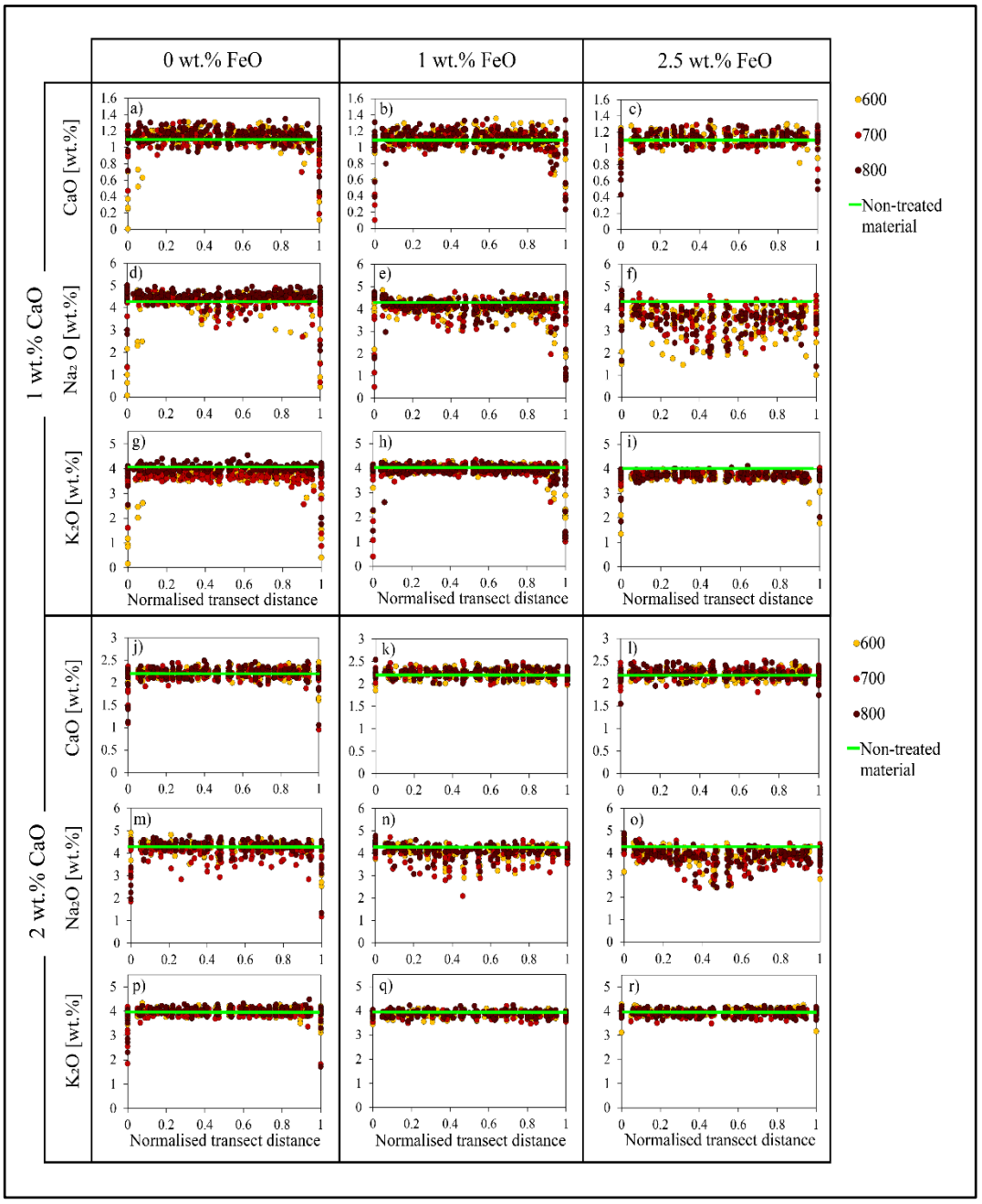

Figure 3. 26 Transect EPMA spot-measurements for Ca, Na and K of HPG8 treated samples. Spot-measurements performed along perpendicular transects of polished HPG8 samples doped with 1 and 2 wt.% CaO (a-i, and j-r, respectively) and 0, 1 and 2.5 wt.% FeO each, treated at temperatures of 600 (yellow filled circles), 700 (red filled circles) and 800 °C (dark red filled circles), all for 30 min. Bulk concentration of CaO, Na_2O and K_2O (wt.%) are plotted against a normalised transect distance. This was an arbitrary parameter used to dismiss the difference between the length of the transect measurements for all grain sizes, by dividing the spot-measurements distance by the total transect distance. Thus, the values of 0 and 1, represent the beginning and end of each transect, i.e., the edges of the particles. As a comparison reference, the initial bulk value of CaO, Na_2O and K_2O is shown in each plot as a horizontal green line.

For instance, previous results EPMA results for Na and K showed little to no near-edge depletion (see Figure 3.13, panels e and h), specially at high temperatures (at 700 and 800 °C), and in the case of Na, most depletion was due to scatter of data in the middle distances of the particle surfaces, due loss during measurements, whereas HPG8 treated samples do display near-edge depletion in both Na (panels d-f) and K (panels g-i). Interestingly, as in the case of calcium (panels a-c), depletion of both Na and K, seems to depend on both the treatment temperature and on the FeO content in each sample.

For samples with no added FeO, depletion of Na at near-edge distances is more notorious for samples treated at 600 °C (panel d), when 1 wt.% FeO is added, slightly less depletion is observed and appears to occur mostly for samples treated at higher temperatures of 700 and 800 °C (panel e), finally, the sample with 2.5 wt.% FeO added, shows less near-edge depletion (panel f), and also displays the most scatter. Results of K (panels g-i) display a similar behavior as Na results; where near-edge depletion decreases with increasing FeO content, and that T= 600 results in high depletion for samples with 0 wt.% FeO (panel g), whereas T= 700 and 800 °C produced most of the depletion for samples with 1 wt.% FeO added (h), and that the lowest near-edge depletion is seen for samples doped with 2.5 wt.% FeO (panel i).

The observed increased near-edge depletion of Na and K for samples with decreasing FeO content shows good agreement with the leachate data of these cations for the same samples (i.e., 1wt.%CaO + 0, 1 and 2.5 wt.% FeO), where generally, the highest concentrations of leached Na and K where obtained for the free-FeO samples (see Figure 3.21 panels g-i for sodium and m-o for potassium). Depletion trends observed for HPG8 samples doped with 2 wt.% CaO are similar than those obtained for samples doped with 1 wt.% CaO, they apear however, to be less clear.

Results for calcium for example, show highest near-edge depletion for samples containing no FeO (panel j), followed by samples doped with 2.5 wt.% FeO (panel k), while samples doped with 1 wt.%FeO showed the lowest near-edge depletion (panel l). Effect of temperature on calcium mobility seems to show that near-edge depletion occurs preferentially at T=800°C (see panels j and l). This might be attributed to the measurements and not to the real behavior of calcium for this set of samples.

Behavior of Na and K for this second set of samples (2 wt.% CaO), show more agreement with their counterparts of samples doped with 1 wt.% CaO, than Ca, especially for the enhancement of near-edge depletion observed for samples containing no FeO, as seen in panels m and p, accordingly. For the samples doped with 1 and 2.5 wt.% FeO, negligible near-edge depletion of Na and K can be seen in panels n-o, and q-r, respectively, which is also in agreement with the corresponding leachate data for Na and K (see Figure 3.21 panels j-l for sodium and p-r for potassium).

3.4 HCl uptake by natural calc-alkaline rhyolitic obsidian

3.4.1 HCl-anhydrous experiments

Additional to evaluating high temperature SO_2-uptake potential by natural and synthetic rhyolitic glasses, a set of time- and temperature-series of experiments was carried out to also test the potential of rhyolitic glasses to uptake HCl at high temperatures. This was done under both hydrous and anhydrous HCl-atmospheres, as described in Chapter 2, section 2.4.1, however only for the natural glass (calc-alkaline rhyolitic obsidian) and not for the set of HPG8 glasses doped with CaO and FeO. Experiments performed under anhydrous conditions, were performed analogously to the SO_2 anhydrous experiments, i.e., they consisted in treating 2 g of each grain size distribution (<63, 63-90 and >90 μm) with a gas mixture of 1 mol.% HCl and 99 mol.% Ar, for the whole range of temperatures 200, 300, 400, 500, 600, 700 and 800°C, for 1, 3, 5 15, 30 and 60 minutes each.

3.4.1.1 Scanning electron microscope (SEM) analyses

SEM images of treated particles were taken, to evaluate the morphology of surficial products formed during high temperature interactions between HCl and the natural calc-alkaline glass. Figure 3.27 shows several images obtained from particles treated with HCl. All pictures taken correspond to samples of the grain size distribution of 63-90 μm, treated at 400 and 600 °C for 60 minutes. A few interesting features can be seen in Figure 3.27, first, that the morphology of the surficial products appears to be more diverse in terms of shape, size and aspect ratio, in comparison with that seen for the samples treated with SO_2.

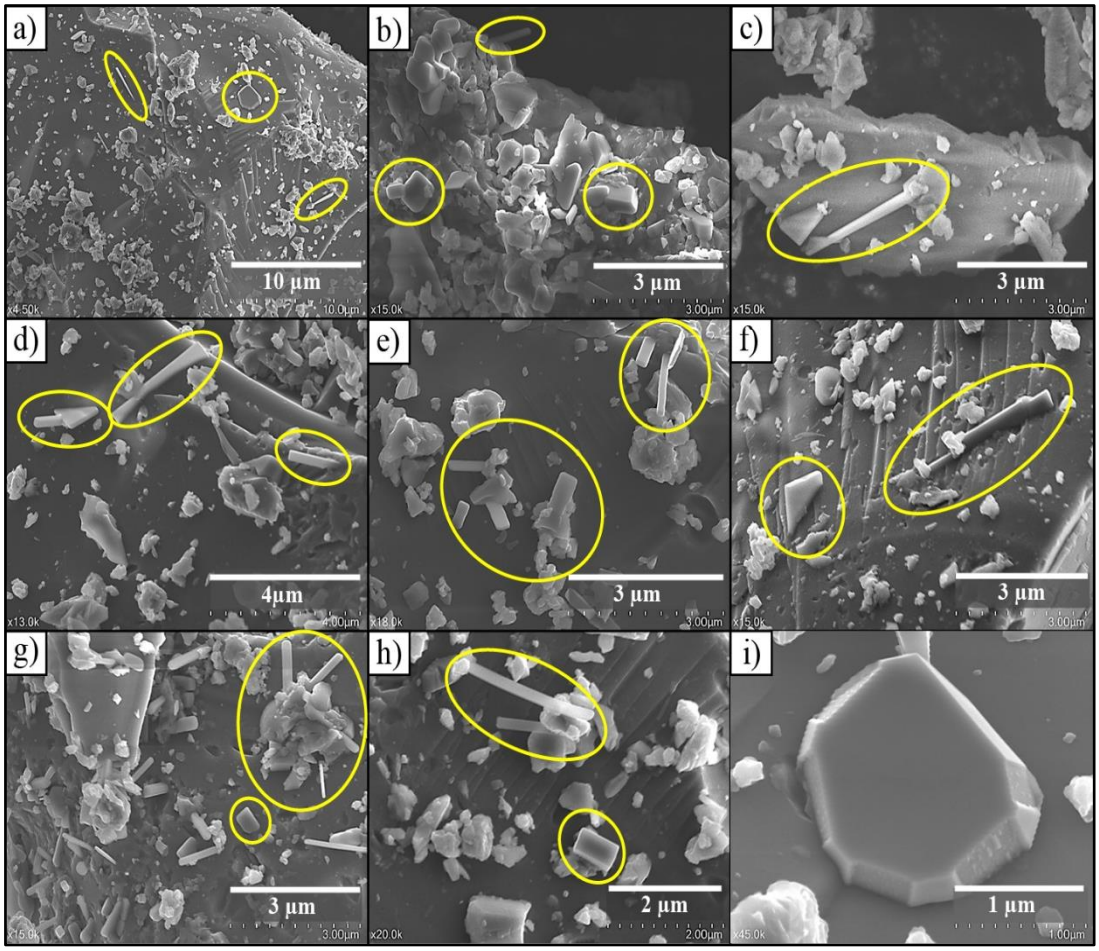

Figure 3. 27 SEM-BSE images of the morphology of surficial chloride-bearing salts SEM-images of sample surfaces of the grain size distribution 63-90 µm, treated at 400 and 600 °C with a gas mixture HCl-Ar for 60 min. each, treated with the HCl-Ar mixture. The reaction products seem to display more heterogeneous shapes and morphologies (e.g., cubic, elongated prisms, elongated polyhedra and what appears to be elongated crystals or spikes), in comparison with the products formed after the SO_2-experiments. Figures c) to h show several cubic, rhomboidal and elongated Cl-bearing products. The later show no apparent preferential growth orientation. Panel i) shows one of the largest (diameter approx. 2 µm) grown surficial product formed during either SO_2- or HCl-experiments.

Whereas images taken of samples treated with SO_2 mostly showed angular surficial products of small sizes (from a few hundreds of nanometers to one or two micrometers) and low aspect ratios (close to 1:1), the surficial products formed during high temperature HCl experiments, show mixed morphologies, such as cubic geometries (c,d,f,g), rectangular prisms of diverse heights (a,d,g), very elongated polyhedral or even tube-like products (a,b,d,e,f,g,h).

The overall size of these products also seems to be larger than that observed for the surficial products of samples treated with SO_2.

3.4.1.2 Leachate analyses

Treated samples were leached and analyzed with ion chromatography, as for previous samples, to quantitatively evaluate the surficial products chemistry, formed during reactions between the HCl gas mixture and the surface of the glass particles. The expected surficial products to have formed were chloride-bearing products (Cl^-), such as NaCl, KCl and $CaCl_2$. Results of cations leached for these set of experiments, presented in Figure 3.28, showed that both calcium (a-c) and sodium (d-f), were leached in similar concentrations, while, potassium concentrations were, as in the case of SO_2-treated samples, negligible, when compared with the calcium and sodium.

Leachate results of samples of the smallest grain size distribution, <63 μm showed the highest concentrations for all cations, being the highest 3054 mg kg^{-1} for sodium (sample treated at 400 °C for 60 min), accounting for ~10 % of the total bulk sodium concentration of the glass (30782 mg kg^{-1}), followed by calcium with 2460 mg kg^{-1} (for the sample treated at 600 °C for 60 min.), accounting for ~20 %of the total bulk calcium in the glass (11863 mg kg^{-1}) and 109 mg kg^{-1} for potassium, that represented only 0.47 % (for the sample treated at 200 °C for 30 min.) of the total bulk potassium concentration in the glass (23272 mg kg^{-1}).

Cation concentrations of leached treated samples of the grain size distribution, 63-90 μm, were 30, 20 and 35% lower, for sodium, calcium and potassium, respectively, than the concentrations obtained for the smallest grain size. While the difference between leached sodium and calcium concentrations was not overly high as for the grain size distribution <63 μm sodium concentrations remained broadly highest than those of calcium, i.e., ~10 % higher, being sodium maximum concentration 2160 mg kg^{-1} (for the sample treated at 400 °C for 60 min) that represented 7% of the glass bulk sodium, calcium maximum concentration of 1919 mg kg^{-1} (for the sample treated at 700 °C for 60 min) and accounted for 16 % of the glass bulk calcium concentration), and a maximum concentration of potassium of 70 mg kg^{-1} (from the sample treated at 200°C for 5 minutes), which represented 0.3 % of the total bulk potassium concentration in the glass.

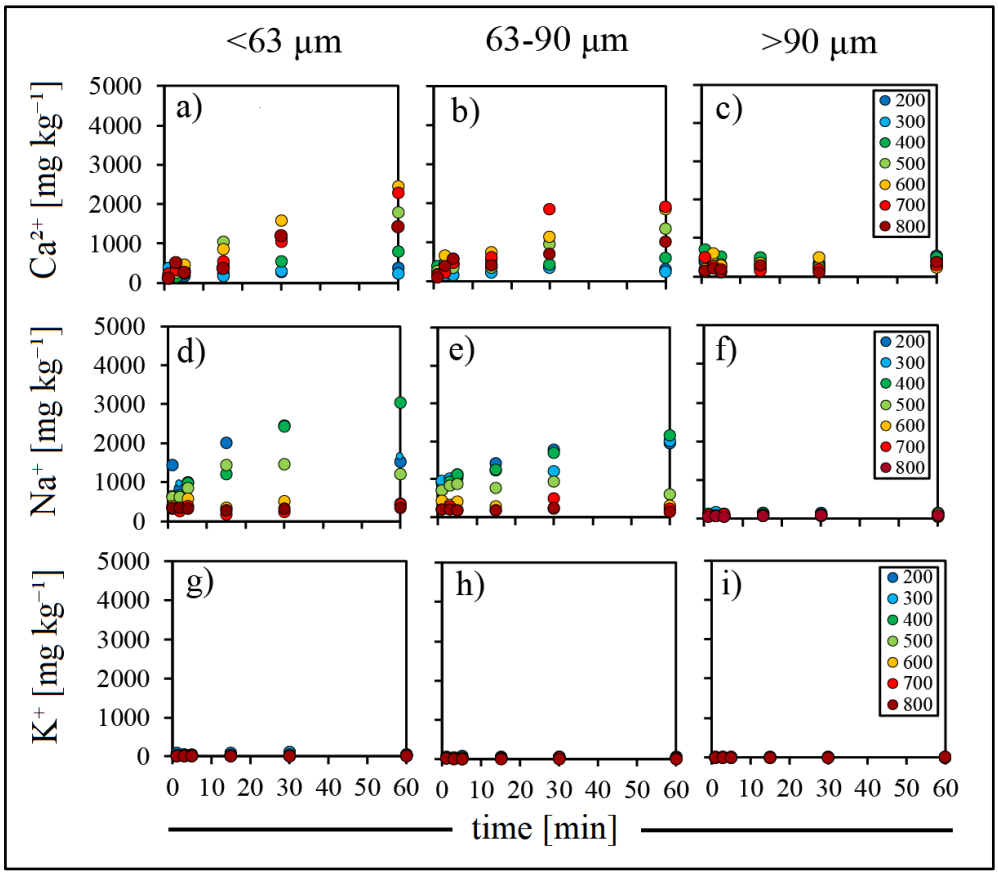

Figure 3. 28 Concentration of leached cation from the anhydrous HCl experiments. Concentrations (mg kg^{-1}) of Ca^{2+} (a-c), Na^{+} (d-f) and K^{+} (g-i) leached from samples treated at high temperatures (200-800 °C) under HCl atmospheres are plotted, for the three grain size distributions <63, 63-90 and >90 µm, as a function of time (1-60 min.). Data points are color-coded according to the legends.

Lastly, leachate results of the grain size distribution of >90 µm showed the lowest concentration values for all cations, with a maximum sodium concentration of 170 mg kg^{-1} (for a sample treated at 300 °C for 30 min.), accounting for only 0.55% of the bulk sodium, a maximum calcium concentration of 687 mg kg^{-1}(for a sample treated at 400 °C for 1 minute), accounting for 5% of the bulk calcium) and maximum potassium concentrations of 22 mg kg^{-1}(for the sample treated at 300°C for 3 minutes), which represents for 0.1% of the glass bulk potassium. These results showed similar trends in what the effect of grain size distribution had on the formation of surficial products for the set of SO_2-experiments, i.e., decreasing particle size, consistently increases concentrations of leached cations Ca, Na, and K, thus higher formation of surficial products.

The effect of the exposure time on the amount of leached cations, was similar to that observed for the SO_2-experiments in that, increasing exposure times proportionally increased concentrations of all leached cations, as an expected result for longer reaction times, as seen in Figure 3.28. The effect of temperature on the leachate results for each cation also shared similarities with that observed for the SO_2-experiments, namely that there were two distinct trends that described the behavior of monovalent cations and calcium concentrations upon temperature treatments.

Previous leachate results of the SO_2-experiments, showed that increasing temperatures resulted in higher concentrations of leached sodium and potassium (see figure 3.4d-f), being the highest sodium and potassium concentrations obtained for the 600 °C treatments, however at 700 °C, concentrations of leached Na and K for all grain size distributions displayed a significant decrease of up to 70 and 43 %, respectively, while at 800 °C the decrease was even higher for sodium, namely 83 % and slightly higher 47 % for potassium, again, when compared to concentrations of both cations obtained for samples treated at 600 °C.

In the case of leached sodium from the HCl-experiments, concentration of this cation showed a constant increase in the range of 200-400 °C, being the samples treated at 400 °C, those with the highest sodium concentrations (i.e., therefore, those that produce the most surficial products upon temperature treatments) for the grain size distributions of <63 and 63-90 μm, while for samples >90 μm, however the maximum concentrations were obtained at 300 °C. For potassium, the temperature-dependence of the leachate concentrations showed a rather unclear agreement for all three grain size distributions, being the highest concentration obtained at 200 °C, for the samples of <63 and 63-90 μm, while samples of the grain size >90 μm, the highest concentration was obtained for the temperature of 300 °C.

Leachate concentrations of calcium for the SO_2-experiments displayed an uninterrupted concentration increase with increasing temperature, which was more evident at 700 and 800 °C (see figure 3.4a-c), for which leached concentrations for the three grain size distributions increased up to 260 and 270 %, respectively, with respect to those obtained at 600 °C. In the case of HCl-experiments, leachate concentrations of calcium displayed a similar trend in that higher temperatures resulted in higher concentrations.

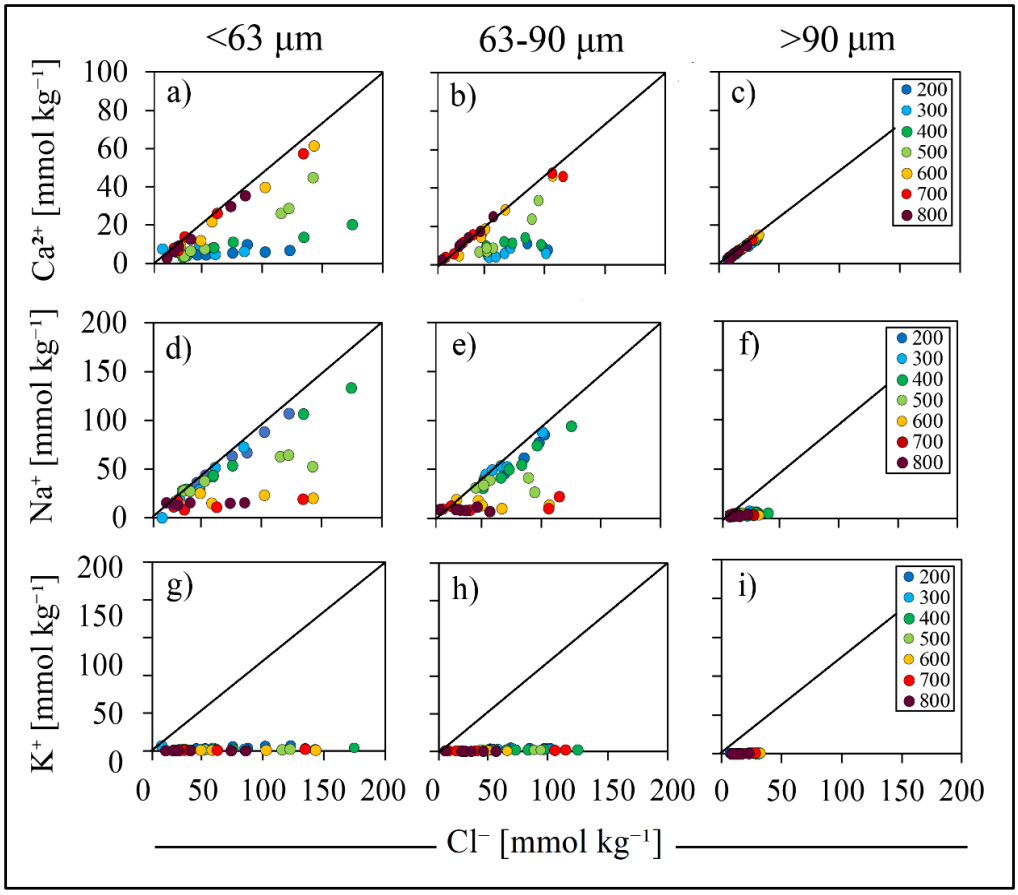

Figure 3. 29 Molal concentrations of leached cations and chloride. Molal concentrations (mmol kg^{-1}) of leached cations, Ca^{2+} (a-c), Na^{+} (d-f) and K^{+} (g-i) are plotted against concentrations of leached chloride for the three grain size distributions. To simplify the graphics, all time-series of experiments are symbolized with filled circles, and only the temperature of each experiment is showed with different colors, according to the temperature color-coding seen in the legends. The molal ratios of $CaCl_2$ (1:2), and NaCl and KCl (both 1:1) are shown with black lines.

	Coefficient of correlation R^2																					
PSD (µm)	<63							63-90							>90							
T (°C)	200	300	400	500	600	700	800	200	300	400	500	600	700	800	200	300	400	500	600	700	800	
Ca	0.291	0.05	0.948	0.951	0.99	0.992	0.998	0.293	0.197	0.113	0.945	0.988	0.988	0.99	0.981	0.896	0.989	0.972	0.995	0.972	0.973	
Na	0.986	0.98	0.99	0.818	0.166	0.278	0.108	0.949	0.963	0.984	0.945	0.271	0.398	0.042	0.424	0.54	0.334	0.235	0.156	0.013	0.26	
K	0.782	0.254	0.985	0.303	0.11	0.961	0.146	0.59	0.016	0.209	0.164	0.416	0.828	0.525	0.009	0.331	0.366	0.037	0.246	0.486	0.716	

Table 3. 5 Correlation coefficient values for molar ratios of leached calc-alkaline rhyolite samples treated with HCl. R^2values of the molal ratios obtained for concentrations of each cation versus chloride were calculated for all three grain size distributions, temperatures and exposure times (these values are integrated indistinctively in the temperature data), i.e., from the plots in Figure 3.29.

This can be clearly seen for samples of <63 and 63-90 μm, for which the highest concentrations were obtained at 600 and 700 °C respectively, while the temperature of 400 °C produced the most leached calcium for the grain size distribution of >90 μm. Concentrations of leached cations were also calculated as molal (mmol kg^{-1}) and plotted against molal chloride (Cl^-) concentrations, as shown in Figure 3.29, in order to confirm 1:1 behavior among monovalent cations and chloride concentrations, hence formation of NaCl, KCl, and 1:2 behavior in the case of $CaCl_2$. The correlation coefficient, R^2, was also calculated for each temperature-series of experiments of all grain size distributions and is shown in Table 3.5.

Plots for sodium vs chloride seen in Figure 3.29d-f, display a strong linear behavior for samples treated at 200, 300 and 400 °C, strongly indicating preferential formation of NaCl, especially for the grain size distributions of <63 (panel d) and 63-90 μm (panel e). Indeed, correlation coefficient values, R^2 (Table 3.5) of the leached samples treated at 200, 300 and 400 °C, are all greater than 0.9, being the R^2 value of samples treated at 400°C, 0.99, i.e., the highest value obtained for sodium among all temperature treatments, and grain sizes distributions.

Molal ratios of leached sodium and chloride of samples treated at higher temperatures, ≥500 °C, consistently result in lower R^2 values, especially at 700 and 800 °C., as seen also in Figure 3.28d-f, where temperatures above 500 °C, result in less linear molal ratios (lower slope of the plotted series), for all grain size distributions. In contrast, molar ratios of leached calcium and chloride display the most linear behavior at temperatures higher than 400 °C, for all grain size distributions (Figure 3.29a-c), note that in the case of calcium, the linear behavior represents a 1:2 ratio, since one mole of calcium reacts with two moles of chloride to form $CaCl_2$ (see the scale in the calcium graphics of Figure 3.29a-c).

This trend can also be seen for the R^2 values of calcium in Table 3.5, where all samples of the grain size distribution <63 μm treated at T ≥400 °C display high values (>0.9), being the highest value among all grain size distributions, 0.998, obtained at 800 °C. A similar behavior can be seen for the molal ratios of calcium for samples of the grain size distribution 63-90 μm, for which T≥ 500 °C show the most linear trends (see Figure 3.29b). This is consistent with the R^2 values calculated for this grain size, where all molal ratios of samples treated at T≥ 500 °C display R^2 values >0.94, being the highest value obtained again for T=800 °C (0.99).

Lastly, Figure 3.29, shows generally linear molal ratios for all temperatures, but also the lowest calcium concentrations among all grain size distributions (see panel c). Accordingly, fairly high R^2 values (>0.8) were obtained for this grain size distribution for all treatment-temperatures, being the highest, unlike in the previous grain size distributions, that obtained at 400 °C (0.989). Molal ratios of potassium showed the least agreement among all leached cations and chloride (see Figure 3.29g-i), as expected from the low concentrations previously observed seen in Figure 3.29g-i. By inspecting R^2 values presented in Table 3.5, is clear that, there are not consistent trends as those observed for calcium or sodium, where increasing temperatures resulted in higher and lower R^2 values, respectively.

There was, however, an overall positive increase of the R^2 values obtained with decreasing particle size, since the highest R^2 values, were 0.985, 0.828 and 0.716, corresponding to the grain size distributions of <63, 63-90 and >90 μm and for the temperatures of 400, 700 and 800 °C respectively. Although the leachate results for the set of anhydrous HCl-experiments showed a clear preferential formation of Na-bearing chloride surficial products, namely NaCl, unlike the SO_2-experiments (where the main cation found in the sulfate-bearing surficial products was calcium), there were noteworthy similarities between the two sets of experiments.

The first was that there was a general positive correlation between decreasing particle size and increasing leached cation concentrations, as the highest concentrations of cations were obtained for the grain size distribution <63, followed by 63-90 and >90 μm, analogously to the results observed in the SO_2-experiments. Second, that the temperature-dependences of leached Na and Ca, appeared to be comparable to those observed for the SO_2-experiments, i.e., that samples treated temperatures in the range of 500-800 °C resulted in increased concentrations of leached calcium, while concentrations of sodium also showed a positive correlation with increasing temperatures, up to 500 °C, temperature above which the leached concentrations of sodium sharply drop, although for the set of SO_2-experiments sodium and potassium concentrations decreased at T≥700 °C.

Finally, for both set of experiments, concentrations of leached cations were the lowest among the three cations analyzed, although, its behavior broadly followed the previous temperature-dependence trend displayed by sodium.

3.4.2 HCl-hydrous experiments

The influence of addition of water to the HCl-Ar gas mixture (1 mol.% HCl and 99 mol.% Ar, respectively) on formation of surficial chloride products (thus HCl uptake) was also tested, as done for the SO_2-set of experiments (see section 3.1.2). Water vapour was added to the HCl-gas mixture entering the AGAR reactor, as a nebulized flow, by coupling a quartz nebulizer to the reactor gas inlet, fed with deionized water by a peristaltic pump (see details in Chapter 2 section 2.4.1).

The amounts of water vapour added to the HCl-Ar mixture were the same as for the SO_2-experiments, namely: 0.01, 24.32, 38.16, 47.72, 62.3, 82.17, 90.04, 93.09, 94.71 and 96.41 mol.% H_2O, which were flown in the reactor to treat 2 g of sample at 400, 500, 600, 700 and 800 °C. All samples were treated for the longest exposure time, 60 minutes, and only the grain size distribution 63-90 μm was tested, this set of experiments had the purpose to test if addition of water to the gas mixture had a positive influence on high temperature HCl uptake by the calc-alkaline rhyolite, as there was a clear increase of concentrations of monovalent cations (specially sodium) for the range 0.01-82.17 mol.% H_2O added (see section 3.1.2.2 and Figure 3.16f-o).

3.4.2.1 Leachate analysis

Results of leached cations of the set of HCl hydrous experiments are shown in Figure 3.30, where the filled triangles symbolize the data point of leached calcium (panels a-e), sodium (panels f-j) and potassium (panels k-o) obtained for hydrous experiments and the prolonged colored line represents the value of the leachate result of experiments conducted at the same temperature, and time (60 minutes), but under anhydrous conditions.

The color coding for all data points is described in the inset legend for each plot. Some interesting trends can be seen for the leachate results of the hydrous HCl experiments. First, that concentrations of leached sodium appear to be ineffectively enhanced upon addition of water vapor (mol.%), and are rather very similar to those obtained under anhydrous conditions, as enhanced concentrations can only be seen for some mol.% of water vapour at temperatures of 400, 600 and 700 °C (panels f,h,i).

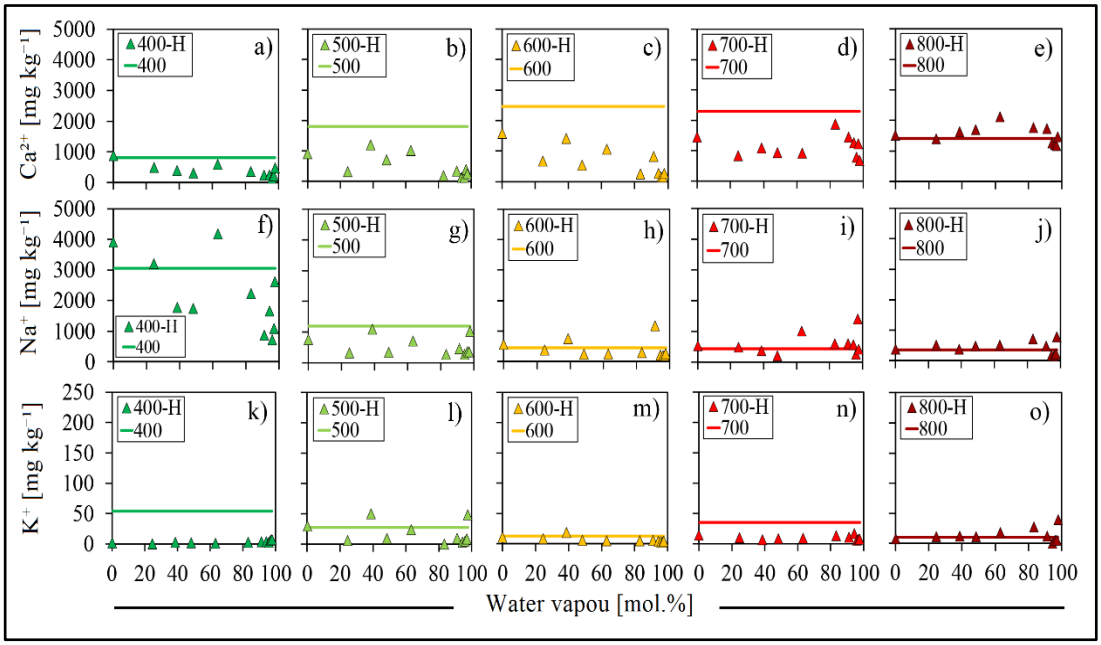

Figure 3. 30 Concentrations of leached cations from the water vapour- and temperature-series of hydrous HCl experiments. Leachate data for samples treated at 400-800 °C, for 60 minutes each under HCl-hydrous gas mixtures are plotted for Ca^{2+} (a-e), Na^{+} (f-j) and K^{+} (k-o) as a function of the range of water vapour tested (0.01-96.41 mol.% H_2O). For each temperature, leachate data of both hydrous and anhydrous conditions are plotted. Hydrous data are plotted as filled (filling colors represent the treatment temperatures) triangles and represent the concentration of a leached cation obtained for each water vapour amount (mol.%) tested, while anhydrous data is plotted as a constant value (no water vapour was added), described by a colored line (color of the line also represents treatment temperatures). The legend inset in each graph shows the hydrous data as the temperature value plus an "H" and the anhydrous data as only the temperature value.

These increased concentrations of leached sodium appear however to not follow a clear pattern but rather an ambiguous trend, unlike the clear trends observed for the leachate results of sodium of the hydrous SO_2-experiments (see Figure 3.16f-j). Concentrations of leached potassium also showed only a few scattered data points that were higher than the concentration obtained under anhydrous conditions for experiments treated at 500, 600 and 800 °C (panels l, m and o), but in general, the concentrations of potassium obtained under hydrous atmospheres appear to be lower than those obtained under anhydrous conditions.

In the case of calcium, leached concentrations under hydrous conditions also exhibit overall lower values than those obtained under anhydrous conditions (see panels a-e), except for a few data points corresponding to experiments performed with intermediate water vapour contents (38-90mol.% H_2O), only for experiments conducted at 800 °C (see panel j). Leachate results of hydrous HCl experiments showed that addition of water had a rather negative effect on leachate concentrations of cations (thus, surficial Cl-bearing products), and only in a few cases some water vapor amounts and temperatures inconsistently resulted in increased sodium, calcium and potassium concentrations.

These results strongly contrast with those obtained for the hydrous SO_2-experiments, where addition of certain amounts of water vapour, resulted in higher concentrations of leached sodium and potassium, while concentrations of calcium appear to remain unaffected by addition of humidity to the SO_2-Ar mixture (see Figure 3.16). Based on these results, a second set of time- and temperature-series of experiments aimed to track the time-dependence of enhanced leachate concentrations, was not conducted since the latter was not observed consistently enough to perform a second set of HCl hydrous experiments.

In what follows, the discussion of the results of this work will focus only on high temperature SO_2 uptake, given the minor relevance of HCl uptake observed by the rhyolites tested here, in comparison to that of SO_2. Nevertheless, previous studies have shown that HCl uptake could be more relevant for per alkaline magmas (e.g., Ayris et al., 2014).

Chapter 4

Discussion

4.1 Introduction

The results obtained from performing high temperature SO_2 uptake experiments by rhyolitic glasses will be discussed. First, the observed reactivity between SO_2 and glass surfaces will be addressed, particularly the preferential reaction with calcium than with other cations. The positive effect that increasing temperatures has on $CaSO_4$ formation will be address also in terms of crossing the glass transition of tested materials. Second, the mechanisms behind gas-uptake will be commented in terms of cation mobility, i.e., diffusion, reaction rates and limiting factors, as well as the implications for syn-eruptive gas-uptake occurrence. Finally, the findings from this study will be applied to evaluate the SO_2 uptake potential of the rhyolitic dome of Chaitén volcano (Chile).

4.2 SO_2 uptake

Both sets of rhyolitic glasses tested in this work were highly reactive to the SO_2-Ar gas mixture used for the high temperature gas-uptake experiments. During all temperature- and time-series of SO_2 uptake experiments, under both anhydrous and hydrous conditions, for the natural calc-alkaline obsidian and the HPG8 glasses (see sections 3.2 and 3.3, respectively), the main outcome of the solid-gas interactions, was the nucleation and growth of surficial sulfate-bearing minerals, consisting mostly in $CaSO_4$, further identified as anhydrite in all samples, by Raman spectroscopy analyses (see section 3.2.1.4 and 3.3.4.2). Additional formation of Na_2SO_4 and K_2SO_4 surficial minerals was also observed to occur during the solid-gas interactions, however at a much lesser extent than for $CaSO_4$ (see the leachate results in section 3.2.1.2 in Chapter 3).

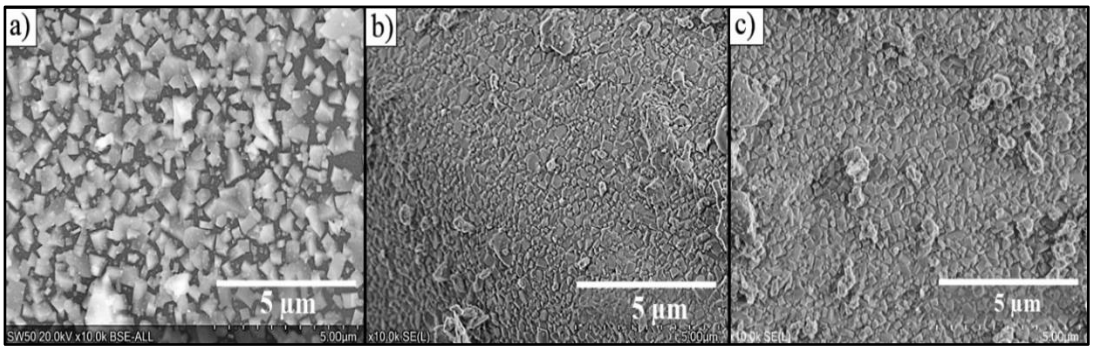

Figure 4. 1 Comparison between the surficial SO_2-glass products formed for three rhyolitic glasses. In a) the surficial products formed on the natural calc-alkaline rhyolite particles are shown, for a sample treated at 800 °C for 30 min. In b) and c) the surficial products formed for the HPG8 glasses doped with 1 and 2 wt.% CaO respectively are shown. In the case of b) and c), both samples were doped with 2.5 wt.% FeO total and were treated at 800 °C for 30 minutes each. All particles are of the grain size distribution 63-90 µm.

This result was consistent for both rhyolitic glass sets tested; the natural rhyolite and the two sets of HPG8 glasses (see sections 3.2.1.2 and 3.3.2, respectively). The minor concentrations of K^+ leached, suggest that accessory potassium-bearing salts were formed on the surfaces. Results from leachate analysis of the anhydrous SO_2-Ar atmospheres are consistent with the broad conclusions obtained by Ayris et al. (2013) using SO_2-air atmospheres, namely that: (1) total leached calcium increases with time non-linearly from values as low as 50 mg kg^{-1} at short exposure times to values approaching 10^4 mg kg^{-1} for longer exposure times (Figure 3.4a-c), (2) the time-dependence of the increase in leached Ca^{2+} is strongly dependent on particle size and exposure temperature, i.e., large particles or low temperatures produce less Ca^{2+} for leaching than small particles or high temperatures (Figure 3.4a-c) and finally, that (3) total leached Na^+ or K^+ shows similar features to Ca^{2+}, however, there is a switch from a positive temperature-dependence of the leached amount of these cations Na^+ and K^+ to a negative dependence on temperature at T>600 °C (Figure 3.4d-i).

This switch is similar in both Na^+ and K^+ data. At 800 °C the concentrations are negligible for all times of exposure.

4.2.1 Surficial and structural constrains of high temperature SO_2-glass reactions

Based on the vast characterization of the glass particles prior and after the high temperature SO_2 exposure, it was clear that uptake occurs on the surface of the particles, at the interface at which heterogeneous solid-gas reactions (i.e., reactions between two or more phases) take place. As proposed by Ayris et al. (2013), the initial step for this reaction is the chemisorption of the SO_2 gas molecule onto a reactive site (i.e., adsorption site) on the surface of glass. Whereas the amorphous nature of glass imparts chemically heterogeneity on the aluminosilicate structure, which poses challenges in predicting where initial adsorption will take place, it has been suggested that the most favorable adsorption sites for the SO_2 molecule are the oxo, M-O, or hydroxyl, M-OH, groups, where M is an alkali- or earth alkali-metal (e.g., Henley et al., 2015; Delmelle et al., 2018; Maters et al., 2016).

This is, because the dipolar nature of the SO_2 molecule prompts it to react as Lewis acid (i.e., species that accepts an electron pair) which favors interactions with Lewis bases (i.e., species that donates an electron pair), which in the case of aluminosilicates are most likely to be the M-O or M-OH groups (see Carre et al., 1992; Legrand, 1998). While both basic groups (M-O and M-OH) are present on natural aluminosilicates, the high temperatures at which the powdered glasses where exposed to SO_2, most likely caused the hydroxyl groups to become unstable and resulting in surficial de-hydroxylation (i.e., McDonald, 1958).

Furthermore, abundance of basic sites has been observed to be greater for fractured glass surfaces, which have more surficial defects, and so fractured aluminosilicate surfaces tend to be enriched in low coordination number atoms, such as alkalis or earth alkali (i.e., Batsanov, 1994; Carre et al., 1992; Pacchione et al., 1994). This observation is consistent with the results shown here, where the grain size distribution of the powdered glass samples (both natural and synthesized rhyolites) showed to have a strong influence on the amount of surficial sulfate-bearing products formed during the gas-uptake experiments (see leachate analysis results in Chapter 3). Availability of the "M" species, i.e., alkali or alkaline earth elements, to react with SO_2 upon high temperature exposure, can be explained by their role in the aluminosilicate glass structure.

Aluminosilicate glasses are amorphous solids mainly consisting in polymerized units of so called "network former cations" (Si^{4+}, Al^{3+}, also Ti^{4+}, Fe^{3+}, B^{3+} and P^{5+}) that form tetrahedral units bonded together by O^{2-} anions (Mysen et al., 1982) in the so-called T-O-T structures, where T is the tetrahedra unit, and O is a so-called bridging oxygen. Alkali and alkali earth elements present in the glass network do not form tetrahedral coordinated units, they play instead a dual role; acting either as "network modifier cations", when they are bonded to terminal oxygens in the tetrahedral network, or as "charge compensating cations" for the substitution of the trivalent cation into the network forming units formed by 3+ network former cations, i.e., Al^{3+} and Fe^{3+} (Mysen et al., 1982). Whereas both alkalis and alkali-earth cations can act both as network modifiers or charge compensating cation, some preferential structural roles, have been observed in each case, for instance, K-edge XANES spectra analysis of Ca and Na on soda lime aluminosilicate glasses, has showed that Ca^{2+} preferentially forms bonds with non-bridging oxygens (i.e., act as network modifier), while Na^{+} tends to charge balance Al^{3+} tetrahedra (Cormier and Neuville, 2004).

Furthermore, alkali earth cations tend to form rather unstable complexes when they charge-compensate Fe^{3+} in tetrahedral coordination in glass structures (Mysen et al., 1980;1985), in comparison with alkalis (Le Losq et al., 2014). Therefore, network modifier cations are likely to be more readily reactive due their relatively lack of structural-bonding to the tetrahedral network. While the basic sites M-O involve both the mono- and divalent- network modifiers Na^{+}, K^{+}, Mg^{2+} and Ca^{2+}, results of all SO_2-glass interactions that I performed consistently showed that, the most responsive cation to react with SO_2 at the ranges of temperatures chosen (200-800 °C) was Ca, whereas Na and K reactivity seemed to be much lower and temperature-limited.

Finally, Mg was not detected for any treated sample (see section 3.2.1.2) of the natural calc alkaline rhyolite. As the HPG8 glasses where Mg-free no $MgSO_4$ was expected to form, as it was the case. Absence of $MgSO_4$ in the treated natural obsidian could simply be due the fact that the glass Mg-poor and therefore the Mg available for reaction was not sufficient (bulk mean value of 0.08 wt.% MgO). Previous observations on Mg-bearing minerals, (e.g., $MgCO_3$, $Mg[OH]_2$), exposed to SO_2 for high temperature uptake experiments, have shown low SO_2-adsorption potential of these materials (i.e., Attig, 1968).

Ayris et al. (2013) also noticed minor formation of $MgSO_4$ upon exposing glasses with diverse compositions to SO_2 (at 25<T °C <800), in comparison to $CaSO_{24}$ formation. Renggli et al. (2011), explained this in terms of thermal stability of $MgSO_4$; by conducting a series of thermodynamic calculations for SO_2 reactions (at 500<T °C<1000) with albite, anorthite and diopside glasses, these authors found that $MgSO_4$ stability rapidly decreases at temperatures above 500 °C. Leached results of treated samples presented in this work showed compelling preferential uptake of SO_2 by reactions with Ca (i.e., $CaSO_4$ formation) for all high temperature experiments. This can be seen in Figure 4.2, where the normalised concentrations of cations leached from the SO_2 experiments are plotted against exposure temperatures.

Panels a and b show that the fraction of Ca mobilized, from the bulk glass to the surface, during the high temperature SO_2 exposure was up to 0.8 of the total bulk calcium for the calc-alkaline samples exposed to SO_2 (see section 3.2.1.2) and up to 0.62 and 0.74 for the HPG8 glasses doped with 1 and 2 wt.% CaO, respectively. The fraction of extracted monovalent cations from the glass network to grow sulfate-bearing products, was shown to be up to two orders of magnitude lower than that of calcium as the highest sodium fractions obtained during the SO_2 exposure experiments was 0.07 for the SO_2-treated calc-alkaline rhyolite, and 0.02 and 0. 05 for the for the HPG8 glasses doped with 1 and 2 wt.% CaO, respectively, while the fractions of mobilized potassium were only 0.006 for the calc-alkaline rhyolite and 0.001 for both sets of HPG8 glasses.

Furthermore, the solid-gas reaction efficiency was shown to be strongly temperature-dependent, as temperatures ≥ 600 °C, result in higher uptake of SO_2, via $CaSO_4$ formation, compared to that observed at lower temperatures. As seen in Figure 4.2a, at 800 °C, the fraction of calcium removed from the bulk glass is seen to be up to 8 times higher than that at 500 °C. The enhanced calcium mobility at T ≥ 600 °C, can be interpreted as a result of the onset of the glass transition, Tg. The glass transition temperature is defined as the temperature, at which the configuration (i.e., microscopic arrangement) of a liquid is "frozen in", becomes unrelaxed and structurally starts to behave as a solid (Mysen and Richet, 2005).

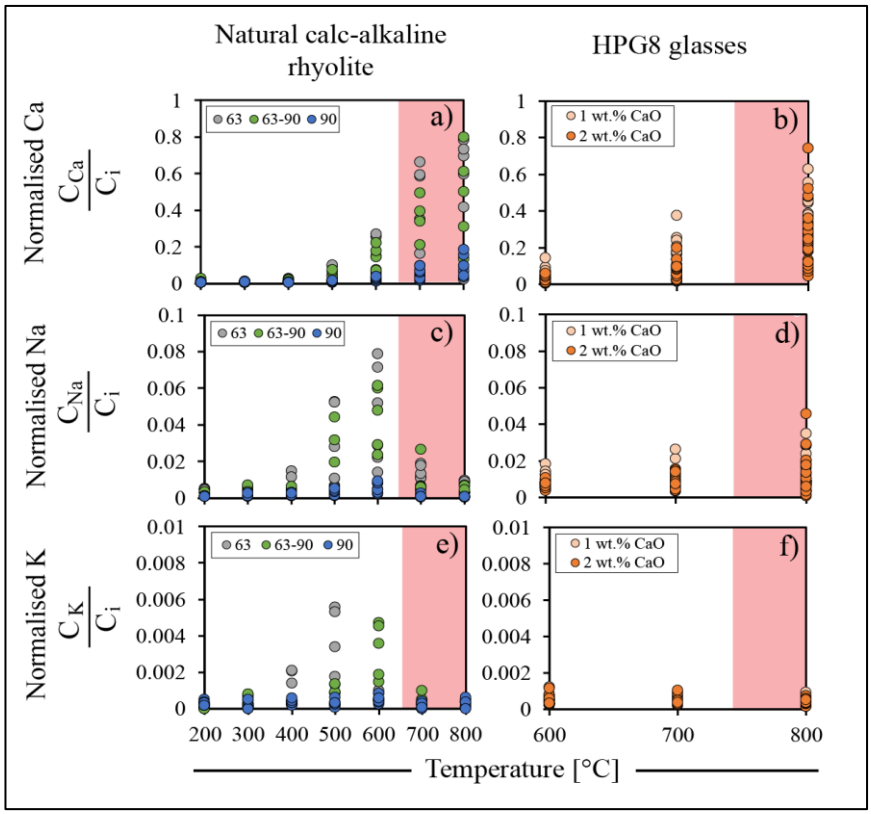

Figure 4. 2 Normalised fraction of mobilized cations. Fractions of leached cations shown on the Y-axis, of both natural and synthetic rhyolitic glasses treated with SO_2 are plotted versus the exposure temperatures, X-axis. Note that the scale of the Y-axis is different for each cation, to appreciate the different results. For each cation the normalised fractions, were obtained by dividing leachate concentrations by the bulk cation content of each cation in the corresponding glass. Note that only the normalised fractions, the temperature are plotted, additionally for the natural calc-alkaline graphics (a,c,e) the grain size distribution are shown, while for the HPG8 glasses (b,d,f) the calcium content is shown. All HPG8 samples were of the grain size distribution 63-90 µm. The pale red bars indicate temperature ranges above the glass transition, For the natural rhyolite Tg was ~ 680 °C, and ~811 °C and ~760-790 °C for the HPG8 glasses doped with 1 and 2 wt.% CaO, respectively

This temperature is not fixed for a given material, since it depends on the experimental parameters, such as cooling rates and timescales of experiments. Once the glass has crossed the glass transition, the thermal energy increases such that it can overcome the potential energy required to start configurational changes in the glass structure, which leads to atomic mobility and results in relaxation of the glass.

The glass transition temperature (Tg) for the natural calc-alkaline rhyolite was determined using a differential scanning calorimeter (Netzsch 4040 Pegasus DSC) by heating the sample from 25 to 1000 °C at a heating rate of 10 K min^{-1} and was found to be ~680 °C. Measured by the same method and under the same heating rate, Tg was estimated for the two sets of HPG8 glasses to be ~811 °C and ~760-790 °C, for the HPG8 glasses doped with 1 and 2 wt.% CaO respectively.

Tg of the HPG8 + 1 wt.% CaO remained consistent for all glasses, regardless of the FeO content (wt.%), while addition of FeO for the HPG8 + 2 wt. % CaO set, appears to have a slight effect on Tg, since increasing FeO content resulted in decreasing Tg. As seen for both set of glasses, samples treated at temperatures above the glass transition clearly showed enhanced Ca mobility as seen in Figure 4.2a,b. Interestingly, crossing the glass transition during experiments, also seems to affect mobility of the monovalent cations Na^{+} and K^{+}, however with the opposite effect than for calcium, as concentrations of both Na and K leached sharply decrease upon temperature treatments above Tg (see Figure 4.2).

In both cases, increasing temperatures (specially above the glass transition), seems to induce important structural changes on the physicochemical properties of the solid substrate, i.e., the glass, for the solid-gas reactions explored here. The reduced mobility of Na and K can be interpreted in terms of their preferential structural role as charge compensating cations. As seen in section 3.2.1.3, the Fe/Fe_{total} ratio systematic increased upon increasing experimental temperatures, thus prompting monovalent cations to serve as charge compensating cations for the increasing Fe^{3+} tetrahedra. Upon increasing experimental temperatures, the ratio Fe^{3+}/ Fe_{total} also showed to increase, from a fairly reduced value of 0.2, for the untreated powdered glass to a maximum measured value of 0.5, for samples treated at 800 °C.

It has been observed that upon oxidation of Fe^{2+} to Fe^{3+}, monovalent cations, there is a preferential association of Na^{+} and K^{+} (than with Ca^{2+} or Mg^{2+}), with Fe^{3+} to charge-balance its tetrahedral coordination with O^{2-} (Dickenson and Hess, 1981; Kress and Carmichael, 1988). This has been observed to have a close dependence on the ionization potential of network modifying cations (Z/r^2, Z=charge of the cation, r=atomic radii), which can be interpreted as a measure of the stability of their bonds with un-balanced tetrahedral units the higher the ionization potential of a cation is, the less stable the tetrahedra will be (Zahng et al, 2013).

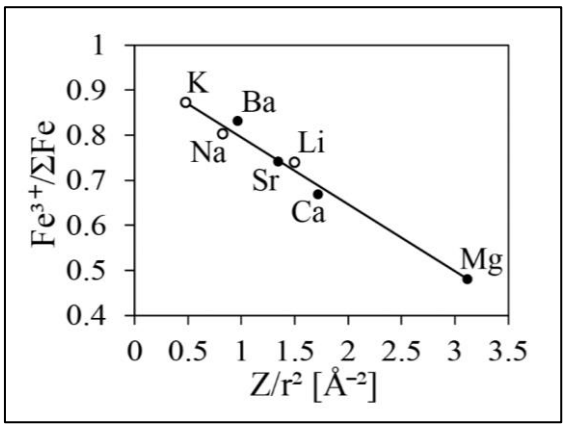

Figure 4. 3 Correlation between iron redox state and ionization potential of alkali- and alkaline earth-cations. Bulk iron redox state of K, Na, Li, (hollow circles), Sr, Ca and Mg (filled circles) in aluminosilicates is plotted against the ionization potential Z/r^2 of each cation, being Z, the formal charge of the cation, and r the ionic radii of each cation. Modified from Mysen and Richet (2005).

In fact, a clear correlation between $Fe^{3+}/\Sigma Fe$ and ionization potential of network modifier cations has been observed for alkaline- and alkaline earth-aluminosilicates. These findings, illustrated in Figure 4.3, and show that presence of cations with low ionization potential (i.e., alkalis) enhance an increase in the $Fe^{3+}/\Sigma Fe$ ratio of aluminosilicates, in comparison with alkali earth cations, implying a strong preference towards charge compensation of Fe^{3+} tetrahedra by alkalis.

Whereas determination of the redox mechanism(s) of iron in aluminosilicate glasses and melts is complex, mainly due to the multiple factors influencing it (i.e., chemical composition, oxygen fugacity, temperature), three kinetic mechanisms (or modes) have been proposed to cause Fe^{2+} oxidation in aluminosilicate glasses: (1) by diffusive flux of molecular oxygen O_2, (2) by diffusive flux of monoatomic O^{2-} anions charge-compensated by a counterflux of electron holes (h^+) a positive charge generated by the absence of an electron, and (3) by diffusive flux of network modifier cations which is also charge-compensated by a counterflux of electron holes (Cook et al.,1990; Cooper et al., 1996). These mechanisms are most likely to occur simultaneously, however, the dominant mechanism will be that which more efficiently dissipates the redox potential developed within the glass structure (Cook and Cooper, 2000).

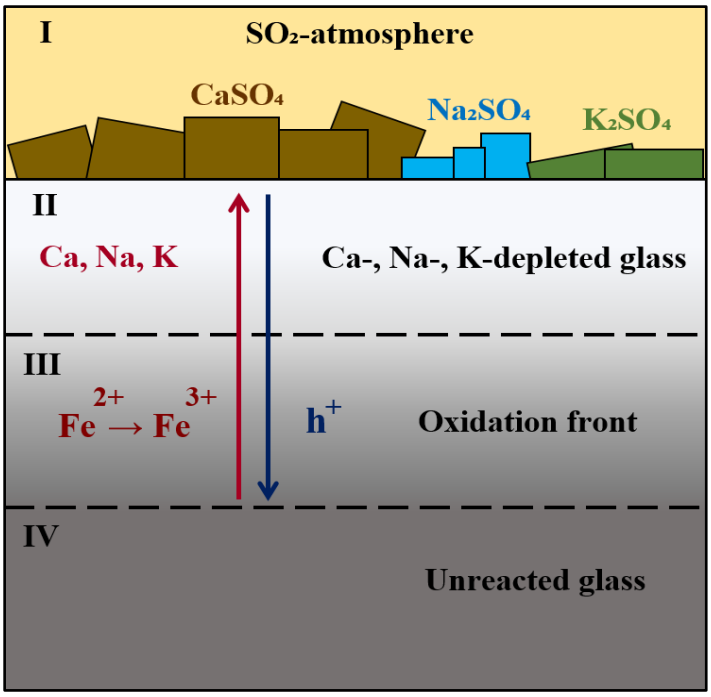

Figure 4. 4. Illustration of the cation diffusion process and the Fe redox response during SO_2 uptake experiments. A cross section of the aluminosilicate network exposed to SO_2 and the regions (I-IV) involved in the uptake process are depicted. The gray scale represents the concentration of cations in the glass network, darker tones indicate higher concertation and lighter grey/white represent lower concentrations. Region I, comprises the initial SO_2 chemisorption step, which forms sulfate minerals, and trigger chemical cation diffusion. Regions II and III represent where the chemical/structural changes within the glass occur, namely cation diffusion and Fe oxidation. Stage IV shows an unreacted glass depth. Modified from Renggli and King (2018).

Results of leachate and bulk Fe redox state analysis of both sets of rhyolitic glasses (natural calc-alkaline obsidian and HPG8 glasses) provide direct evidence that the dominant Fe redox mechanism taking place during the high temperature SO_2 uptake experiments, is the number 3, i.e., outflux of network modifier cations to the glass surface, counter-balanced by an influx of electron holes. Outward diffusion of Ca^{2+}, Na^{+} and K^{+}, was certainly evidenced by formation of surficial nano- to micrometer-sized Ca-, Na-, and K- sulfates during all sets of SO_2-glass experiments (see Leachate Analysis in Chapter 3).Chemical diffusion of cations is triggered by subtraction of Ca^{2+}, Na^{+} and K^{+} from surficial reactive sites upon initial SO_2 adsorption, which creates cation vacancies, that support cation diffusion to maintain growth of surficial sulfates (Ayris et al., 2013; Delmelle et al., 2018).

In Figure 4.4 a depiction of the cation diffusion process assumed to occur (mode 3) within the glass structure upon reaction with SO_2 is shown. The cartoon represents the 4 fundamental aluminosilicate network regions, involved in SO_2 uptake. Region I represents the initial interface reaction between the slightly negative SO_2 molecule and the slightly positive charged surficial cations, which leads to SO_2 adsorption on to the glass surface and further reactions which ultimately results formation of sulfate bearing minerals.

Region II, refers to the onset and development of cation diffusion driven by the chemical gradient generated by the extraction of cations in Region I, over time, loss of cations by outward diffusion (to further react with SO_2) causes the underlying glass to be depleted in Ca, Na and K and therefore enriched in Si and Al. Whereas the latter was not directly observed, depletion of calcium was ubiquitous upon inspection of SEM-EDS chemical mapping (see section 3.2.1.1), which showed indeed Ca-free zones underneath the treated particle surfaces. EPMA transect analysis showed likewise lower calcium concentrations of treated samples at near-edge distances (see section 3.2.1.5.

Region III illustrates cation (Ca^{2+}, Na^{+}, K^{+}) outward diffusion and the counter (inward) diffusion of electron holes, h^{+}, which ensure neutrality within the glass network. Such inward flux of electron holes, i.e., positive charges, most likely occurs simultaneously to Fe^{2+} oxidation. This argument is supported by the fact that aluminosilicates with polyvalent-transition metals, such as Fe, display a semiconductor behavior, meaning that electron mobility readily occurs (Schmalzried, 1984b; Cooper et al., 1996). Interestingly, it has been proposed that mobility of electron holes promotes electrical decoupling of diffusing cations from each other as well as from O^{2-} to which they may be bonded (i.e., Tuller, 1981; Schmalzried, 1981), thus, Fe^{2+} can easily release an electron (i.e., takes up an electron hole), which would result in Fe oxidation (Dickenson and Hess, 1986).

Upon oxidation, Fe^{3+}, is set to acquire a positive charge to stabilize its tetrahedral coordination with O^{2-} ions, which most likely becomes the structural role of Na^{+} or K^{+}. This process stage is of importance, because, it helps to explain the sharp decline of Na-, K-bearing sulfates formation, at $T > 600°C$ (at which $Fe^{3+}/\Sigma Fe$ ratios displayed their highest values). In this work, region III was evidenced by the presence of Fe-bearing nanolite structures, as seen in Figure 3.12. Lastly, region IV, represents a region of the material that is unaffected by either cation diffusion, or by electron hole diffusion, Fe^{2+} oxidation.

Occurrence of Stage IV was observed with SEM-EDS elemental mapping and EPMA transect analysis, as near-center depths with homogeneous spatial chemical distribution of cations, representative of the unreacted bulk glass composition. This implies that cation outward diffusion, thus, SO_2-uptake is not an unlimited sustained process. This might be due the fact that, depletion of cations Ca, Na and K shown in Region II, most likely results in an Si-, Al-, Fe^{3+}-enriched Region 3, which has been proposed to act as a structural barrier that impedes further Ca, Na, K diffusion (Renggli and King, 2018). These compositional/structural changes and their role in decreasing cation diffusion will be further addressed below.

4.2.2 SO_2-glass reaction mechanisms

Although the initial SO_2 chemisorption is a rather fast step and chemically favorable at high temperatures, i.e., >100 °C (Low 1971), the following formation and growth of surficial $CaSO_4$ follows a multi-step and temperature-dependent reaction. Several studies (i.e., Ward et al., 1966; Borgwadt, 1970; Allen and Hayhurst, 1996) aimed to characterize industrial gas desulfurization by reactions with CaO (as pure oxide, $CaCO_3$ or $CaMg[CO_3]_2$), showed that the overall reaction at high temperatures (up to 1230 °C), is:

$$CaO + SO_2 + {}^1/_2\, O_2 = CaSO_4 \qquad \textbf{Equation 4.1}$$

However, infrared spectroscopic analysis of CaO-SO_2 reactions suggest that the reaction begins with formation of SO_3 (Low et al., 1971), which promptly reacts in the presence of O_2 to form $CaSO_4$ (Allen and Hayhurst, 1996), as follows:

$$CaO + SO_2 = CaSO_3 \qquad \textbf{Equation 4.2}$$

$$CaSO_3 + {}^1/_2\, O_2 = CaSO_4 \qquad \textbf{Equation 4.3}$$

Formation of $CaSO_3$ to $CaSO_4$ could also be explained in terms of decomposition of the first, via disproportionation of SO_3^{2-} at temperatures >100 °C (e.g., Foerster and Kubel, 1924; McAmissh and Johnston, 1976) as shown in Equation 4.4:

$$4CaSO_3 = 3CaSO_4 + CaS \qquad \textbf{Equation 4.4}$$

In the presence of an oxidizing agent, such as O_2 (or in SO_2), it has been shown that both $CaSO_3$ and CaS readily oxidize to $CaSO_2$ (Ingraham and Marier 1971). In the context of high temperature SO_2 reactions with natural aluminosilicates, experimental observations between SO_2 and minerals, ash and glasses have shown similar reaction pathways (Douglas and Isard, 1949; Burnham, 1979; Fegley and Prinn, 1989; Ayris et al., 2013; Henley et al., 2015). A general reaction between SO_2 and aluminosilicate glasses can be described as that proposed by Burnham (1979):

$$2SO_2 + NMC\text{-}O\text{-}glass = NMC\text{-}SO_4 + S + glass\text{-}oxide \qquad \textbf{Equation 4.5}$$

where, "NMC" is a network modifier cation (e.g., Na^+, K^+, Ca^{2+}, Mg^{2+}), "O" is the oxygen anion (O^{2-}) bonded to these cations, "NMC-O-glass", represents the adsorption site, "NMC-SO_4" is the resulting sulfate formed, "S" is a reduced form of sulfur, and the "glass-oxide" term represents the reacted glass. Note that here, no sulfite is formed. Equation 4.5 describes a disproportionation reaction of sulfur (i.e., S_4^+), that simultaneously forms oxidized (S^{6+}) and reduced sulfur (as S^{2-}, S^- or elemental sulfur S^0), being the latter most likely present as gas (S_2 or H_2S) as observed by Burnham (1979), and Henley et al. (2015). In fact they found evidence, by experimental observations and thermodynamic modelling, that rapid sulfur disproportionation occurred upon exposure of anorthite glass to SO_2 at 700 °C (see Equation 4.6) and proposed that, in the presence of water vapor, S_2 becomes unstable and formation of H_2S is then favored, as seen in Equation 4.7:

$$2CaAl_2Si_2O_8 + 3SO_2 = 2CaSO_4 + 2Al_2SiO_5 + 2SiO_2 + 0.5S_{2(g)} \qquad \textbf{Equation 4.6}$$

$$3CaAl_2Si_2O_8 + 4SO_2 + H_2O = 3CaSO_4 + 3Al_2SiO_5 + 3SiO_2 + H_2S_{(g)} \qquad \textbf{Equation 4.7}$$

The results that I obtained by characterizing all sets of glasses treated with high temperature under anhydrous- and hydrous-SO_2 atmospheres, showed only presence of oxidized sulfur (i.e., sulfate)-bearing products (see Leachate

Analysis and Raman Spectroscopy sections in Chapter 3), and no intermediate oxidation products (i.e., sulfites). This strongly suggests that, the reactions showed in Equations 4.6 and 4.7, are most likely to have occurred under anhydrous and hydrous SO_2 atmospheres, respectively. As presence of sulfide-bearing surficial products was not detected for any treated sample, it can be assumed, that, according to Equations 4.6 and 4.7, reduced sulfur was released as gas (S_2 and/or H_2S). By the current experimental set up, determination of the latter could not be confirmed. Upon perming experiments in the AGAR device (see section 2.3), the reacted gas flow is carried out of the device and flows into the top of the fume hood for disposal.

Future work could be aimed to characterize the outlet gas flow in order to determine the chemical speciation of reacted gases, and to confirm occurrence of S_2 or H_2S upon SO_2 uptake by glasses. Nevertheless, the complexities of multicomponent aluminosilicate heterogeneous reactions in nature can rarely be described by a simplified reaction such as Equations 4.6 and 4.7, and in some cases formation of intermediate oxidation products can in fact occur. Further investigations aiming to precisely characterize SO_2-glass reaction pathways are required. These could by conducted, for instance, by preforming in-situ analysis of samples during the solid-gas reactions.

4.3 Analysis and interpretation of cation diffusion

In this section the experimental data obtained for outward cation diffusion from rhyolite particles will be treated to develop a simplified framework to analyze diffusion process in glass particles, for which it will be shown that temperature and cation concentration are first-order controlling variables. This framework will then be applied to the case-study of Chaitén volcano 2008 dome eruption, for which SO_2 emissions measured yielded to unexpected low values (Carn, 2009). Applying the findings of this work to understand Chaitén 2008 eruption is further relevant, given the rhyolitic composition of the erupted magma (Castro and Dingwell, 2009) and the high eruptive temperatures estimated (≥600 °C) for this eruption (Castro et al., 2012). Here, it is proposed that a large fraction of pre-eruptive degassing SO_2 flowing through ash-filled fracture networks may be ´sequestrated´ by permeable fractured rhyolitic domes.

Element	D_0 (m^2 s^{-1})	b (K)	Data Source
Ca	2.54 x 10^{-5}	29,830 ± 4,356	Mungall et al. (1999)
Na	1.34 x 10^{-6}	10,210 ± 243	Jambon (1982), Magariz and Hofmann (1978) and Watson (1981), in agreement with Zahng et al. (2010)
K	3.48 x 10^{-7}	12, 775 ± 927	Jambon (1982), in agreement with Zahng et al. (2010)

Table 4. 1. Published inputs to diffusion scaling. Reference diffusivities D_0 for each cation of interest and the corresponding *b* parameter values.

For Chaitén volcano 2008 eruption, this could have been the mechanism responsible for the ´strikingly low´ SO_2 emissions measured. To simplify the data analysis, only the results of the natural calc-alkaline rhyolite will be used in what follows. The overall SO_2-uptake reaction consists of several processes; i.e., adsorption, initial gas-glass reactions, and chemical diffusion, each of which can rate-limit the uptake reaction. Whereas, high temperature SO_2 uptake is initiated by rapid SO_2 chemisorption on to aluminosilicate surfaces (Henley 2015), it is dubious to assume that this is the rate-limiting process, given the fact that surficial sulfates are very rapidly formed in short period of times, specially upon higher temperatures (see Figures 3.4 and 3.21 in Chapter 3), as also observed by Ayris et al. 2013. Moreover, at the high temperature-regime at which the SO_2-glass interactions took place, activation energies of chemical gas-solid reactions can easily be overcome (Szekely et al. 1976).

Yet, the supply of cations (principally Ca^{2+}), in terms of chemical diffusion, was shown to be the controlling mechanism for the SO_2-uptake reaction rate. After initial SO_2 chemisorption and reaction on basic (Ca-, Na-, K-) surface sites, diffusive transport of cations takes place. Diffusion is in turn, limited by the value of the diffusivity D_x where x is replaced by the cation in question (e.g., D_{Ca} in the case of calcium diffusivity). Diffusivities of Ca, Na and K in aluminosilicates have been experimentally parameterized previously as a function of temperature (Zhang et al., 2010 and references therein), and have shown experimentally to have the Arrhenius form:

$$D_x = D_0 \exp\left(-\frac{b}{T}\right) \quad \textbf{Equation 4.8}$$

where D_0 is the reference diffusivity ($m^2\ s^{-1}$), b is an experimentally determined constant and T is the temperature. Both b and T are expressed in Kelvin. By using published parameters of D_0 and b; in rhyolitic samples, listed in Table 4.1, temperature-dependent diffusion laws can be obtained for $D_{Ca}(T), D_{Na}(T)$ and $D_K(T)$, which can be used to scale my experimental data for any temperature. For instance, the value of D_{Ca} for the anhydrous experiment (SO_2-Ar) at 800 °C and at 60 minutes, was found to be 2.15 $x10^{-17}$, for the natural calc alkaline rhyolite, which is similar to that obtained by Ayris et al. (2013), for rhyolitic glass powders treated at the same temperature and exposure time, e.g., 8.7 x 10^{-17} $m^2\ s^{-1}$. The characteristic timescale associated with diffusive mass transfer can be calculated by:

$$\lambda_D = R^2/D_x \quad \textbf{Equation 4.9}$$

where, in the case of pseudo-spherical volcanic ash particles, R, is the mean particle radius and particle angularity can be neglected (Wadsworth et al. 2017a). By using $D_x(T)$ described above and using the arithmetic mean of the distribution of particle sizes (R) as a proxy for the characteristic length in polydisperse particle distributions (Wadsworth et al., 2017b), λ_D can be defined for each suite of experiments at different temperatures, for different particle size distributions, and for each cation of interest. If it is assumed that the total amount of each cation available for mass transfer is the initial total concentration of that oxide in the starting glass (see Table 2.3), leachate concentrations can be normalized, by their respective initial bulk values according to Equation 4.10

$$\bar{C} = \frac{C_x}{C_{i,x}} \quad \textbf{Equation 4.10}$$

where $\bar{C}$ is a dimensionless normalised concentration, C_x, is the leachate concentration of the x cation (mg kg^{-1}), and $C_{i,x}$ is the initial bulk concentration of the cation x in the glass (mg kg^{-1}). By also normalizing the experimental time, t, by λ_D to give $\bar{t} = t/\lambda_D$, all the experimental data can be plot together can plot demonstrate that the data follows a consistent trend of $\bar{C}(\bar{t})$ for most datasets as shown in Figure 4.5.

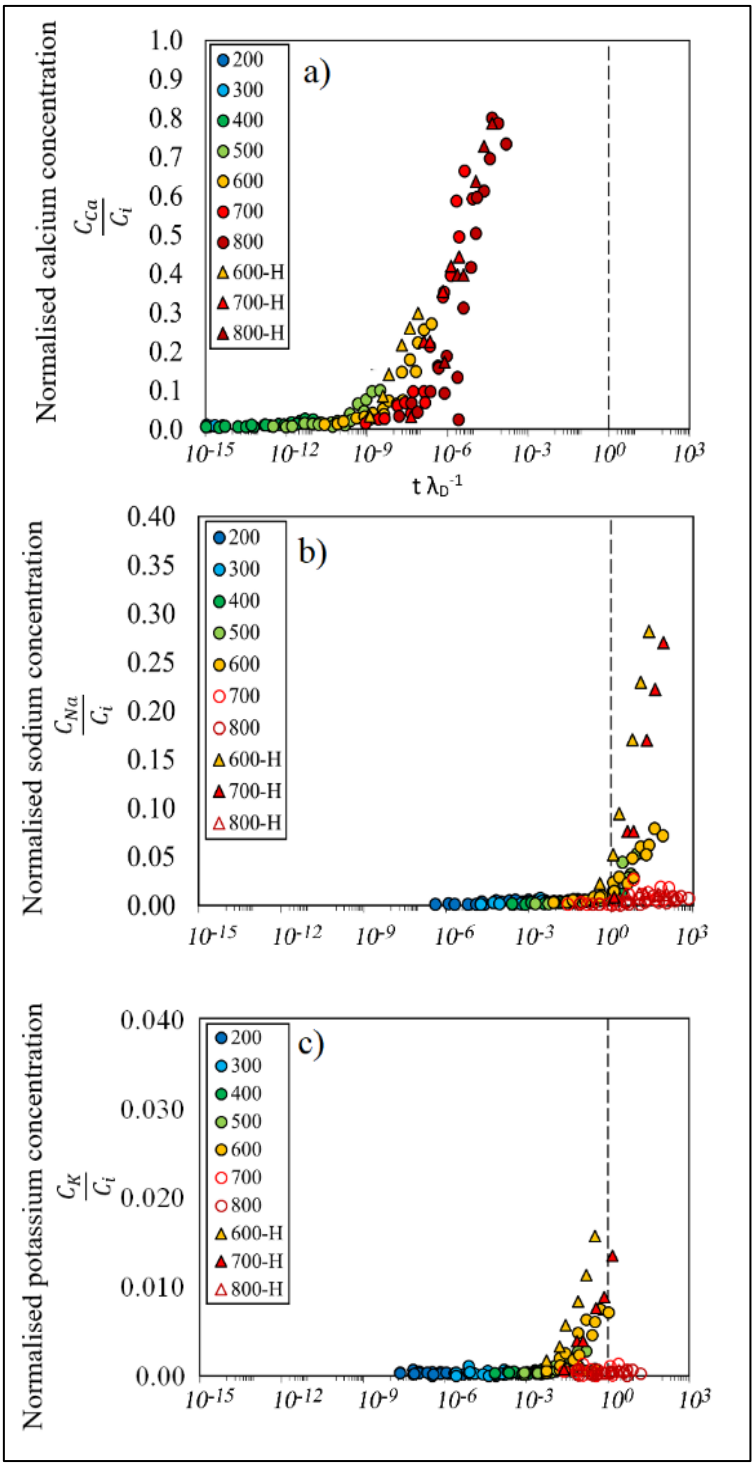

Figure 4. 5 The concentration of a given cation $C_x(t)$, i.e., C_{Ca}, C_{Na}, C_K, (a, b and c, respectively) normalized by the initial value of that oxide C_i giving $\bar{C} = C_x/C_i$, as a function of time t normalized by the diffusion time λ_D, giving $\bar{t} = t/\lambda_D$. Using $\lambda_D = \langle R \rangle^2/D_x$ collapses the data over all temperatures and particle size distributions below the critical oxidation temperatures (above which diffusive mass transport to the surface is negligible). Vertical lines simple guide the eye to a normalized time of unity.

Using the above scaling analysis, the apparent lack of Na and K diffusion above critical threshold temperatures (reflected in negligible concentrations in the leachate analyses; Figure 4.5b,c) can be clearly seen. For clarity, the 700 and 800 °C anhydrous time-series and the 800 °C hydrous time-series data are shown as unfilled data points in Figure 8. Using this distinction, it is clear to see that at these temperatures the diffusive extraction of Na^+ and K^+ to form surface salts is negligible compared with the consistent trend at lower temperatures. This is consistent with the observation that >600 °C and >700 °C are the threshold temperatures in anhydrous and hydrous conditions, respectively.

Here, these thresholds are interpreted as representing a transition from reduced to oxidized above those threshold temperatures, and consequently as the switch from Fe^{2+} to Fe^{3+} (see Figure 3.7), which has been shown to effectively capture Na^+ and K^+ for charge balancing (Cook and Cooper 2000; Cook et al., 1990; Cooper et al., 1996a,b;1997). In most cases, silicate liquid equilibrium oxygen fugacity will increase with increasing temperature, implying more oxidizing conditions at higher relative temperatures (e.g., Sack et al., 1980). On reheating in our experimental apparatus, the glass will relax above the glass transition temperature (~700 °C) using a viscosity threshold of 10^{12} Pa.s as an approximation of the glass transition, and using the model of Hess & Dingwell (1996) with a dissolved water content of 0.18 wt.%. Relaxation of silicate structure in our experiments will allow equilibration of the redox state, which in turn may be more oxidizing than the conditions locked in during cooling in nature (see Dingwell, 1990 for a review).

Although the data for $\bar{C}(\bar{t})$ fall to a universal trend in Fig. 8, in both the hydrous and anhydrous regimes, the data collected in hydrous atmospheres are at higher $\bar{C}$ for any given $\bar{t}$, consistent with the observations in dimensional plots (see Figure 3.17). Therefore, it is likely that a non-negligible effect of $\mathrm{H_2O}$ on the diffusive process. Koenderink et al. (2000) showed that diffusion of H^+ (or H_3O^+) in sodium silicate glasses containing Mg^{2+}, Ca^{2+}, $Sr^{2+}$and Ba^{2+}, can exchange with equi-valent Na^+ or K^+ generating ion exchange. Our inferred increase of the diffusive potential in the presence of H_2O vapour can therefore be interpreted as the effect of inward migration of H^+ enhancing the outward migration of Na^+ and K^+ up until the threshold temperature for surface oxidation described above.

Indeed, the fact that the threshold temperature for oxidative cut-off of diffusion of Na^+ and K^+ is dependent on H_2O (Figure 3.16) suggests that these effects of oxidation and ion exchange by motion of H^+ compete with one another. The implication is that this oxidation threshold is apparently higher in hydrous conditions at low H_2O activity when H^+ ion exchange dominates over oxidation but is independent of humidity at high H_2O when oxidation dominates over H^+ ion exchange.

4.4 A Case study: volcán Chaitén 2008 dome eruption

The finding of this work will now be applied to an in-dome scenario, a system that can be open, fractured and permeable to magmatic gas flow. Fractures in lava domes frequently host veins filled with fine-grained volcanic ash and host-rock material (i.e. tuffisites) and reflect processes occurring within the volcanic conduit (Tuffen et al., 2003; Kolzenburg et al., 2012). Taking the case of the lava dome erupted at Volcán Chaitén (Chile) in May 2008, scaling the amount of SO_2 sequestered can now be done in reasonable time limits. This study has found that the important parameters are temperature T, which conveys a diffusivity D_x, the timescale available at high temperature for sequestration t, particle size(s), captured by the arithmetic mean $\langle R \rangle$, and the initial amount of the cation in question C_i.

For the reactions involving Na^+ and K^+, it is additionally show that the presence of H_2O in the gas phase is an additional key parameter for their mobility. In-conduit or in-dome conditions are inevitably hot for longer than a rapidly ascending plume. Fracture networks are pervasive at silicic conduit margins (Farquharson et al., 2017; Gonnermann and Manga, 2003; Tuffen and Castro, 2009) and are advected up into domes, providing open-system pathways for gas transport bypassing melt. Such systems are typically in chemical disequilibrium at fracture and particle surfaces, especially while cooling, and gas-melt back-reactions can be common (e.g., Berlo et al., 2013; Schipper et al., 2015). Here, the possibility that ash-gas uptake reactions occurred during SO_2-rich gas transport through tuffisite veins in the dome of Volcán Chaitén soon after emplacement in May 2008 (Castro et al., 2012) is explored. Such a tuffisite vein is shown in Figure 4.5 collected as part of a larger bomb (analysis of this bomb appears in Saubin et al., 2016). Castro and Dingwell (2009) and Castro et al. (2012) provide a storage and ascent temperature estimate of $T = 825$ °C.

Figure 4. 6 Picture of a fracture in rhyolitic obsidian from Volcán Chaitén. This sample is from a larger bomb erupted from the 2008 dome. The fracture is filled with a polydisperse distribution of volcanic ash and glass fragments. This geometry is the basis for our calculated sequestration efficiencies.

Castro et al. (2012) additionally explore fracture dynamics at $T = 625$ °C, an estimated calorimetric glass transition temperature (Giordano et al., 2008). Both 825 and 625 °C represent the temperatures at which diffusion would have taken place within the tuffisites. The constraints presented previously were then used to find that $D_{\mathrm{Ca}} = 4 \times 10^{-17}$ m^2 s^{-1}, $D_{\mathrm{Na}} = 1.2 \times 10^{-10}$ m^2 s^{-1}, and $D_{\mathrm{K}} = 3.1 \times 10^{-12}$ m^2 s^{-1} for 825 °C, and $D_{\mathrm{Ca}} = 9.6 \times 10^{-20}$ m^2 s^{-1}, $D_{\mathrm{Na}} = 1.6 \times 10^{-11}$ m^2 s^{-1}, and $D_{\mathrm{K}} = 2.3 \times 10^{-13}$ m^2 s^{-1} for 625 °C. Such rhyolitic lava domes are frequently fractured and the fractures often host partially welded, initially granular tuffisites (e.g., Tuffen and Dingwell 2005). At Volcán Chaitén, the grain sizes in these tuffisites range approximately from 0.1 to 1 mm (see dense clasts in a "main vein" measured in Saubin et al., 2016).

This permits us to convert D_x to λ_D for each cation, and so, taking maxima and minima conditions (from maximum and minimum $\langle R \rangle$), and taking $T = 825$ °C, it was found that $10^8 < \lambda_D < 10^{10}$ s for Ca diffusion, $10^1 < \lambda_D < 10^3$ s for Na diffusion and $10^3 < \lambda_D < 10^5$ s for K diffusion. For $T = 625$ °C, these timescales would be $10^{11} < \lambda_D < 10^{13}$, $10^2 < \lambda_D < 10^4$, and $10^4 < \lambda_D < 10^6$ s, respectively.A first-order timescale for the time available for the diffusion-limited SO_2 sequestration process to occur is the timescale that these welding fractures can stay open and permeable (Wadsworth et al., 2014).

This is approximated by the sintering timescale λ_s for particles sintering at high temperatures, and is $\lambda_s = \mu\langle R\rangle/\Gamma$, where μ is the viscosity, and $\Gamma \approx 0.3$ N.m^{-1} is the surface tension with the gas phase (Wadsworth et al., 2016). In detail, Γ depends on the gas species available, but the value quoted here is an approximate and within the correct order of magnitude. Given the range of water contents 0.2-0.95 wt.% in the dome glasses (Castro et al., 2012), the viscosity model from Hess and Dingwell (1996) for rhyolites can be used to find that μ is of the order $10^7 - 10^9$ Pa s at this temperature. Here, it was found that $10^3 < \lambda_s < 10^{10}$ s. If λ_s, is taken to be approximately t (i.e., $\lambda_s \sim t$), this gives us $t\,{\lambda_D}^{-1}$ ranges of $10^{-7} - 10^{-2}$ for Ca^{2+}, $10^{-1} - 10^{4}$ for Na^{+}, and $10^{-2} - 10^{3}$ for K^{+} at $T = 825$ °C.

Referring to Figure 4.5, these $t\,{\lambda_D}^{-1}$ ranges would be sufficient for ~30-90% of the initial Ca^{2+} in the welding particles to be available for surface reactions with SO_2. Similarly, ~0-20% Na^{+} and negligible amounts of K^{+} would contribute in anhydrous conditions. In hydrous conditions, from Figure 4.5 it can be read that this would increase to ~0-50% of the initial Na^{+} and <5% of K^{+}. Interestingly, at the lower example temperature $T = 625$ °C, while the values of λ_D are increased relative to the higher temperature (see above), the overall value of $t\,{\lambda_D}^{-1}$ is increased because λ_s is much longer. This is of interest as it shows that across these range of conditions, the time for which the dome fractures can remain open exerts a controlling role during cooling compared with the time required for diffusion.

Next, the above constraints need to be scaled to dome conditions. Gonnermann and Manga (2003) computed a fractured zone at the margins of rhyolitic conduits of radius L that has thickness δ such that $\delta = FL\mu^{0.1}$ where $F = 0.01$ Pa.s$^{-0.1}$ is the given proportionality. Castro et al. (2012) constrained L to be 50 m on the basis of aerial views of the dome during the initial eruption and μ is given above. It was therefore found that δ is between 2.6 and 9.7 m for the range of parameters given above. Within the fracture zone δ it can be assumed that n fractures with thickness l_f and inter-fracture spacing l_s are present, such that $\delta = n(l_f + l_s)$. In cylindrical coordinates, the cross-sectional area of fractures that occupy the damage zone δ can be computed, which are termed A_f. A_T is then the total area $A_T = \pi L^2$. A_f then relates to l_f and l_s via

$$A_f = \sum_{j=1}^{n} A_{f,j} \qquad \textbf{Equation 4.11}$$

and the *jth* fracture has area $A_{f,j} = \pi\left[(2j-1)l_f^2 + 2l_f(L - \delta + l_s)\right]$. Converting A_f to the cumulative mass of glass particles m_g in the fractures will be necessary to compute mass fractions of SO_2 scavenged and can be achieved by

$$m_g = A_f H \rho (1 - \phi_i) \qquad \textbf{Equation 4.12}$$

where H is the vertical depth to which the fractures penetrate in the conduit, ρ is the glass density and ϕ_i is the initial porosity in each fracture. Wadsworth et al. (2016, 2014) found that an approximate value of $\phi_i = 0.5$ valid for most realistic packs of particles is of relevance to tuffisite emplacement. Knowing the mass of each cation in the glass that is available for reaction with the gas phase in the time available, m_x, by $m_x = C_x C_{i,x} m_g$, we can find the mass of SO_2 that will react with a given m_x by $m_{SO_2} = M_{SO_2} m_x / M_x$, where M_{SO_2} is the molar mass of SO_2 and M_x is the molar mass of the reacting cation species. Now the mass fraction of the total exsolved SO_2 that can be scavenged is $S = m_{SO_2}/\left(m_{SO_2} + m_e\right)$ where m_e is the total mass of exsolved SO_2 in the gas phase. As a limiting assumption, we simply take the value of the 500 mg kg^{-1} SO_2 (which we term C_{i,SO_2}) as the initial available proportion of the total mass that is released at the surface, measured in glass inclusions from the plinian pumice eruption in May 2008 (Castro et al., 2012). This amount can be converted to m_e by

$$m_e = \phi_i A_T H \rho C_{i,SO_2} \qquad \textbf{Equation 4.13}$$

This assumption requires that all the SO_2 that is exsolved into the gas phase originates from the same volume $A_T H$ in which the fractures occur. This simplifying assumption means the sequestration efficiency S is independent of the H over which the fractures occur. The initial amount of Ca, Na, and K in the glass phase can be estimated using the rapidly ejected pumice analyzed in Castro and Dingwell (2009) as $C_{i,x}$ of 0.014, 0.04 and 0.03 mass fraction, respectively (note that in Castro and Dingwell 2009, these values appear as wt.%). With these values and the inputs given above, it was found that the value of S that is attributable to calcium's role in the sequestration is 0.12-0.5. The amount attributable to Na is up to 0.4 in hydrous conditions.

Summing these contributions, it is predicted that between 12 and 90% of the eruptible sulphur dioxide can be scavenged during permeable flow through welding fractures (with 12% referring to the limiting 625 °C and 90% referring to the eruptive 825 °C, considered here). These estimates are maxima if it is acknowledged that the total erupted SO_2 may not be from the volume $A_T H$, and may only be from $A_f H$. Furthermore, these constraints would be overestimates if we consider that additional SO_2 may be bypassing the transiently open tuffisites from depths greater than H. Nonetheless, the results are striking that in-dome scavenging may be efficient over the timescales of open-system outgassing.

Additional complexities may arise from the intricate geomertries of many particles entrained and welded in tuffisite outgassing channels (e.g., Castro et al., 2012; Saubin et al., 2016). The result found above suggests that rhyolitic volcanic domes that are heavily fractured and for which the fractures are the dominant outgassing pathway (e.g., Castro et al., 2012; Tuffen et al., 2003; Cabrera et al., 2008), may act as efficient filters for the bulk SO_2 emitted. For the case of Volcán Chaitén (2008 eruption), this is broadly consistent with the "remarkably low" SO_2 measured in the plume above the emerging dome (Carn et al., 2009). Whereas no concrete evidence (i.e., $CaSO_4$, Na_2SO_4, etc. growth in tuffisite samples) for the Chaitén dome have been found, this could be attributed to dissolution upon contact with meteoric water.

Chapter 5

Conclusions and Outlook

In this thesis, the potential of natural and synthetic rhyolitic glasses to uptake two of the most environmental relevant gases, sulfur dioxide (SO_2) and hydrochloric acid (HCl), released during volcanic eruptions was tested. This was focused on high temperature gas-glass experiments, for which the effect of composition of the glass, the glass particle size distribution, exposure temperature and time, gas composition and humidity on the gas uptake was assessed. The rationale behind exploring this phenomenon with rhyolitic glass was based on the ubiquity of high silicic magmas in producing large- to very large volcanic events, which inject large amounts of fine ash (P_d< 63 µm) and gases into the atmosphere that can induce short- and long-term environmental and climate perturbances (e.g., Ayris and Delmelle, 2012; Jones et al., 2007; Robock, 2000).

During such large eruptive events, turbulent mixing of ash and hot gases, lead to heterogeneous reactions that result in effective gas removal from the atmosphere by growth of S- or Cl-bearing salts on ash surfaces. HCl uptake was not found to be sufficiently efficient to induce large changes in gas composition for rhyolitic eruptions and therefore, a principal conclusion of this work is that the rhyolite-SO_2 system is dominant for eruptions of high-silica magmas.

Here, it was found that the main mechanism by which SO_2 can be removed to form soluble anhydrite ($CaSO_4$) on rhyolite particles is Ca^{2+} diffusion (D_{ca}) from the bulk glass network to the surface, and that it shows its highest efficiency at T= 800 °C (compared with lower temperatures), with the inference that higher temperatures still would render this process more efficient. Diffusion of sodium and potassium was also observed to occur, however to an extent that could be considered negligible in comparison to calcium, in particular at T>600 °C, at which this work was focused.

Here, it is shown that the cation flux to the surface feeding the SO_2 reaction is electronically accommodated by the conversion of ferrous iron, Fe^{2+} to ferric iron, Fe^{3+}, which changes the structural role of Na and K, from network modifier to charge compensating cations for Fe^{3+} tetrahedra (Mysen et al., 1982). Calcium diffusion can be scaled using experimentally-determined diffusivity values and applied to any temperature. The role of hydrous atmospheres in high temperature SO_2 uptake by rhyolite was found to have a controlling effect of humidity (mol. % H_2O) in limiting the diffusion of Na^+ and K^+ to the ash surface because the diffusive influx of hydrogen takes the charge compensating role that other monovalent cations would normally take during the outward flux of divalent cations.

At water contents > 60 mol.% H_2O, concentrations of leached soluble Na_2SO_4 and K_2SO_4 were negligible, suggesting that highly hydrous atmospheres strongly hinder further diffusion of Na^+ and K^+. This is due to inward migration of protons, H^+, into the glass (e.g., Koenderink et al., 2000), which enhances oxidation of iron, thus inhibiting mobility of Na^+ and K^+. This finding is applicable for future studies aiming to model and predict ash-gas reactions, given the fact that all volcanic emissions are water saturated (> 60 mol. % H_2O), the contribution that Na and K can make in SO_2 uptake by rhyolite, can be greatly simplified.

Furthermore, at T>600 °C this can be neglected altogether. Yet, it was found that humidity is not limiting in Ca^{2+} diffusion, since under anhydrous- and water vapor saturated-SO_2 atmospheres, formation of $CaSO_4$, thus SO_2 uptake, were congruent with each other. Another key finding was the effect of iron oxidation dynamics on calcium diffusion. By synthetizing Fe-free and Fe-bearing rhyolites, and exposing them to hot SO_2, it was observed that higher Fe contents led to higher formation of $CaSO_4$. This has been suggested to occur due to intrinsic Fe redox-cation diffusion dynamics, where the outflux of cations (Ca^{2+}, Na^+, K^+), is charge compensated by the influx of electron holes (h*), which results in Fe oxidation (e.g., Cook and Cooper, 2000) at high temperatures (700-850 °C).

These studies have focused however, on oxidation dynamics of less silicic glasses (<60 wt.% SiO_2), which might not be fully applicable to rhyolitic glasses (≥70 wt.% SiO_2) and while they provide a basis for the understanding of cation diffusion and Fe oxidation dynamics, more experimental work is needed to better constrain the role of Fe oxidation on cation diffusion dynamics.

A direct application of the findings of this thesis was aimed to correlate the ´strikingly low´ SO_2 emissions measured for the 2008 dome-eruption at Chaitén volcano (Carn, 2009). Here, it is proposed that the permeable, fractured and degassing Chaitén dome could have acted as a filter for SO_2 emissions, previous to the 2008 eruption, given interactions between the fine ash-filled fractures (within Chaitén volcano´s pre-eruptive rhyolitic dome) and hot (>600 °C) degassed SO_2 (Castro et al., 2012; Castro and Dingwell, 2009).

From this, it was found that a fraction of up to 0.9 of the initial magmatic SO_2 could have been up taken by ash-gas reactions (Casas et al., 2019). Simple calculations led to suggest that relevant SO_2 uptake can occur at in-dome environments, can potentially reduce the amount of sulfur available for atmospheric interactions. The novel experimental approach applied here, and the wide range of variables tested, make the results of this work of great importance for future gas uptake research aimed to develop numerical models to predict the effective mass of SO_2 released during volcanic eruptions. To improve our estimations of net volcanic SO_2 emissions, by considering high temperature ash-gas reactions, is fundamental to better assess the environmental of climate impacts of large volcanic eruptions.

This thesis represents a coherent parameterization of the gas-glass reactions between SO_2 and rhyolitic volcanic glass. If we approximate natural volcanic ash as being dominated by volcanic glass (true in many cases; e.g. Heiken and Wohletz, 1992), then this thesis is a proxy parameterization of gas-ash reactions. The next step would be to upscale these reactions to volcanic conditions of in-plume hot reactions. To do this, the resultant model would have to be fully non-isothermal, non-isobaric in terms of the partial pressures of gas species, and coupled to a full volcanic plume model.

Ayris et al. (2014) achieved a simplification of this for HCl reactions with ash in plumes by using plume model output temperature fields to approximate an average flight path of ash, and calculate the diffusive flux of Na^+ that could feed HCl reactions. The output of the Ayris et al. (2014) calculation was a net HCl scavenged (in terms of molar ratio) during an eruption of a given size. However, to make a reliable quantitative prediction of this scavenging potential, a proper coupling of diffusion and cooling would need to be applied – which is yet to be done.

Future research aimed to develop predictive models of high temperature gas sequestration by ash, could be done by testing a wider range of magma compositions (basalt, andesite, dacite) under the same experimental variables described here. Nevertheless, rhyolite magmas remain the most relevant composition for large-scale sulfur uptake by ash, given their highly explosive behavior (thus, high fragmentation potential). Also, while in this work, great care was taken to accurately extrapolate the results from gas uptake by glass to gas uptake by ash, testing high temperature SO_2 (and HCl) uptake by natural ash should be conducted, in order to further validate this approach. Performing experiments with natural ash could also be helpful to compare if the evidence of the gas uptake by glass observed (e.g., calcium depletion beneath the particle surfaces) is also evident in natural ash, and therefore useful to recognize occurrence of high temperature gas-ash interactions.

Also, to improve the characterization of chemical reactions responsible for the uptake process observed here, experimental techniques should be developed to perform in situ analysis of samples during exposure to hot gases. Modifications of the advanced gas ash reactor (AGAR) used here could be done for this purpose, i.e., by coupling a mass spectrometer to the outlet of gases to monitor the gas products of the SO_2-glass reactions. Furthermore, isotopic tracer techniques could also be applied to determine sulfur partition coefficients upon reactions with glass (and production of anhydrite). Isotopic fractionation of sulfur during reactions with glass, might have a specific temperature-dependent value which could useful to fingerprint this process and to assess the extent of high temperature reactions in natural ash.

References

Aiuppa, A., Federico, C., Giudice, G., Gurrieri, S., Paonita, A., Valenza M. 2004. Plume chemistry provides insights into mechanisms of sulfur and halogen degassing in basaltic volcanoes. Earth and Planetary Science Letters. Volume 222, Issue 2. Pages 469-483. https://doi.org/10.1016/j.epsl.2004.03.020.

Allard, P., Aiuppa, A., Bani, P., Métrich, P., Bertagnini, A., Gauthier, P.-J., Shinohara, H., Sawyer, G., Parello, F., Bagnato, E., Pelletier, B., Garaebiti, E. 2016. Prodigious emission rates and magma degassing budget of major, trace and radioactive volatile species from Ambrym basaltic volcano, Vanuatu island Arc. Journal of Volcanology and Geotherm. Res. Vol 322, 119-143. https://doi.org/10.1016/j.jvolgeores.2015.10.004.

Allen, D., Hayhurst, A.N. 1996. Reaction between gaseous sulfur dioxide and solid calcium oxide mechanism and kinetics. J Chem Soc Faraday Trans 92:1227–1238. https://doi.org/10.1039/FT996 9201227.

Alidibirov, M. 1994. A model for viscous magma fragmentation during volcanic blasts. Bull. Volcanol. 56, 459–465.

Andersen, A., Kofstad, P. 1984. The reaction of Ni-20Cr with SO2at 600–900 °C. Corros Sci 24:731–743. https://doi.org/10.1016/0010-938X(84)90061-1.

Armienta, M.A., Martin-Del-Pozzo, A.,L., Espinasa, R., Cruz, O., Ceniceros, N., Aguayo, A., Butron, M.,A. 1998. Geochemistry of ash leachates during the 1994–1996 activity of Popocatépetl volcano. Appl Geochem 13(7):841–850.

Armienta, M.A., Cruz-Renya, S.D.L., Morton, O., Cruz, O., Ceniceros, N. 2002. Chemical variations of tephra-fall deposit leachates for three eruptions from Popocatepetl volcano. J Volcanol Geotherm Res 113(1–2):61–80.

Attig, R. C. 1968. Dispersed-phase Additive Tests for SO, Control. Interim report LR:68 :4078-01:9 by Babcock & Wilcox Co. for contract PH 86-67-127, pp. 4-5.

Ayris, P.M., and Delmelle, P. 2012. The immediate environmental effects of tephra emission. Bull. Volcanol. 74(9), 1905–1936.

Ayris, P.M., Lee, A., F., Wilson, K., Kueppers, U., Dingwell, D.B., and Delmelle, P. 2013. SO2 sequestration in large volcanic eruptions: high-temperature scavenging by tephra. Geochim. Cosmochim. Acta 110, 58–69. https://doi.org/10.1016/j.gca.2013.02.018.

Ayris P. M., Delmelle P., Cimarelli C., Maters E. C., Suzuki Y. J. and Dingwell D. B. 2014. HCl uptake by volcanic ash in the high temperature eruption plume: Mechanistic insights. Geochim. Cosmochim. Acta 144, 188–201. https://doi.org/10.1016/j.gca.2014.08.028.

Ayris, P. M., Cimarelli, C., Delmelle, P., Wadsworth, F. B., and Vasseur, J. Suzuki, Y. J., Dingwell, D.B. 2015. A novel apparatus for the simulation of eruptive gas-rock interactions. Bull Volcanol 77, 104. https://doi.org/10.1007/s00445-015-0990-3**.**

Barone, G., Mazzoleni, P., Corsaro, R.A., Costagliola, P., Di Benedetto, F., Ciliberto, E., Gimeno, D., Bongiorno, C., Spinella, C. 2016. Nanoscale surface modification of Mt. Etna volcanic ashes. Geochim. Cosmochim. Acta, 174 (2016), pp. 70-84 https://doi.org/10.1016/j.gca.2015.11.011.

Batsanov, S.S., 1994. Effects of Explosions on Materials: Modification and Synthesis Under High-Pressure Shock Compression. Springer-Verlag, New York, 194pp.

Bell, R.J., and Dean, P. 1972.The structure of vitreous silica: Validity of the random network theory. Philosophical Magazine, 25, 1381–1398.

Borgwardt, R.H. 1970. Kinetics of the reaction of sulfur dioxide with calcined limestone. Environ. Sci. Technol, 4, 1, 59-63. https://doi.org/10.1021/es60036a001.

Boudoire, G., Rizzo, G. A., Di Muro, Grassa, F., Liuzzo, M. 2018. Extensive CO2 degassing in the upper mantle beneath oceanic basaltic volcanoes: First insights from Piton de la Fournaise volcano (La Réunion Island). Geochimica et Cosmochimica Acta. Volume 235, Pages 376-401. https://doi.org/10.1016/j.gca.2018.06.004.

Brown, R.J. and Bonadonna, C. and Durant, A.J. 2012. A review of volcanic ash aggregation. Physics and chemistry of the earth, parts A/B/C., 45-46. pp. 65-78. http://dx.doi.org/10.1016/j.pce.2011.11.001.

Burnham, C.W. 1979. Magmas and hydrothermal fluids. In: Barnes HL (ed) Geochemistry of hydrothermal ore deposits. Wiley, Oxford, pp 71–136.

Buzgar, N., Buzatu, A., Sanislav, I. 2009. The Raman study of certain sulfates. Analele Stiintifice ale Universitatii "Al. I. Cuza" din Iasi. Seria Geologie. LV. 5-23.

Cabrera A., Weinberg R. F., Wright H. M. N., Zlotnik S. and Cas, R. A. F. 2011. Melt fracturing and healing: a mechanism for degassing and origin of silicic obsidian. Geology 39, 67–70.

Carey, S., Sigurdsson, H. 1982. Influence of particle aggregation on deposition of distal tephra from the May 18, 1980 eruption of Mount St. Helens volcano. J Geophys Res 87(B8):7061–7072.

Caricchi L., Burlini L., Ulmer L., Gerya T., Vassalli M. and Papale P. 2007. Non-Newtonian rheology of crystal-bearing magmas and implications for magma ascent dynamics. Earth Planet. Sci. Lett. 264, 402–419.

Carre, A., Roger, F., Varinot, C.1992. Study of acid/base properties of oxide, ox-ide glass, and glass–ceramic surfaces. J. Colloid Interface Sci.154 (1), 174–183. http://dx.doi.org/10.1016/0021-9797(92)90090-9.

Carlson, R., Smythe, W.D., Lopes-Gautier, R., Davies, A.G., Kamp, L.W., Mosher, J.A., Soderblom, L.A., Leader, F.E., Mehlman, R., Clark, R.N., Fanale, F.P.1997. Distribution of sulfur dioxide and other infrared absorbers on the surface of Io. Geophysical Research Letters 24. 10.1029/97GL02609.

Carn, S.A., Clarisse, S.A., Prata, A.J. 2016. Multi-decadal satellite measurements of global volcanic degassing. Journal of Volcanology and Geothermal Research,Volume 311, 99-134, https://doi.org/10.1016/j.jvolgeores.2016.01.002.

Casadevall, T.J., 1993. Volcanic hazards and aviation safety: Lessons of the past decade. Flight Saf. Found.-Flight Saf. Digest 1–9.

Casas, A.S., Armienta, M.A., Ramos, S. 2016. Sulfur speciation with high performance liquid chromatography as a tool for El Chichón volcano, crater lake monitoring. Journal of South American Earth Sciences, 72, 241-249. https://doi.org/10.1016/j.jsames.2016.09.001.

Casas, A.S., Wadsworth, F.B., Ayris, P.M., Delmelle, P., Vasseur, J., Cimarelli, C., Dingwell, D.B. 2019. SO_2 scrubbing during percolation through rhyolitic volcanic domes, Geochimica et Cosmochimica Acta, Volume 257, 150-162. ISSN 0016-7037, https://doi.org/10.1016/j.gca.2019.04.013.

Cashman K.V, Sturtevant, B., Papale, P., Navon, O. 2000. Magmatic fragmentation. In: Sigurdsson H, Houghton B,McNutt S, Rymer H, Stix J (eds) Encyclopedia of volcanoes. Academic, London, pp 421–430.

Castro, J. M. and Dingwell D. B. 2009. Rapid ascent of rhyolite magma at Chaite´n volcano, Chile. Nature 461, 10.1038.

Castro, J. M., Cordonnier B., Tuffen H., Tobin M. J., Puskar L., Martin M. C. and Bechtel H. A. 2012. The role of meltfracture degassing in defusing explosive rhyolite eruptions at volca´n Chaite´n, Earth Planet. Sci. Lett. 333–334, 63-69.

Cook, G. B., Cooper R. F. and Wu T. 1990. Chemical diffusion and crystalline nucleation during oxidation of ferrous iron-bearing magnesium aluminosilicate glass. J. Non-Cryst. Solids120, 207-222.

Cooper, R. F., Fanselow J. B. and Poker D. B. 1996a. The mechanism of oxidation of a natural basaltic glass: Chemical diffusion of network-modifying cations. Geochim. Cosmochim. Acta 60, 3253-3265.

Cooper, R. F., Fanselow J. B., Weber J. K. R., Merkley D. R. and Poker D. B. 1996b. Dynamics of oxidation of a basaltic melt. Science 274, 1173-1176.

Cooper, R. F., Smith D. R. and Cook G. B. 1997. Dynamic oxidation and the structure and crystallization of aluminosilicate glasses and melts. Electrochem. Soc. Proc. 97–39, 389-396.

Cormier, L., Neuville, D.R. 2004. Ca and Na environments in Na2O–CaO–Al2O3–SiO2 glasses: influence of cation mixing and cation-network interactions, Chemical Geology, 213, 1–3, pgs 103-113, ISSN 0009-2541. https://doi.org/10.1016/j.chemgeo.2004.08.049.

Cronin, S.J., Neall, V.E., Lecointre, J.A., Hedley, M.J., Loganathan, P. 2003. Environmental hazards of fluoride in volcanic ash: a case study from Ruapehu volcano, New Zealand. Journal of Volcanology and Geothermal Research 121 (3–4), 271–291.

De Kleer, K., De Pater, I., Ádámkovics, M. 2019. Emission from volcanic SO gas on Io at high spectral resolution, Icarus, Volume 317, 104-120,ISSN 0019-1035, https://doi.org/10.1016/j.icarus.2018.07.012.

Delmelle, P., Stix, J. 2000. Volcanic gases. In: Encyclopedia of volcanoes. Academic, New York, pp 803–815.

Delmelle, P., Villiéras, F., Pelletier,. 2005. Surface area, porosity and water adsorption properties of fine volcanic ash particles. Bulletin of Volcanology. 67.

Delmelle P., Lambert M., Dufrene Y., Gerin P. and Óskarsson N. 2007. Gas/aerosol–ash interaction in volcanic plumes: new insights from surface analysis of fine volcanic ash. Earth Planet. Sci. Lett. 259, 159–170.

Delmelle, P., Wadsworth, F.B., Maters, E.C., Ayris, P.M. 2018. High temperature uptake of volcanic gases on ash in eruption plumes. Rev Mineral Geochem 84:285–308.

Di Genova, D., Hess, K.U., Chevrel, M.O., Dingwell, D.B., 2016a. Models for the estimation of Fe3+/Fetot. Ratio in terrestrial and extra- terrestrial alkali- and iron-rich silicate glasses using Raman spectroscopy. Am. Mineral. 101, 943–952.

Di Genova, D., Sicola, S., Romano, C., Vona, A., Fanara, S., Spina, L., 2017b. Effect of iron and nanolites on Raman spectra of volcanic glasses: reassessment of existing strategies to estimate the water content. Chem. Geol. 475:76–86. https://doi.org/10.1016/j. chemgeo.2017.10.035.

Di Genova, D., Caracciolo, A., Kolzenburg, S. 2018. Measuring the degree of "nanotilization" of volcanic glasses: Understanding syn-eruptive processes recorded in melt inclusions, Lithos, 318–319, 209-218, ISSN 0024-4937. https://doi.org/10.1016/j.lithos.2018.08.011.

Di Muro, A., Métrich, N., Mercier, M., Giordano, D., Massare, D., Montagnac, G., 2009. Micro-Raman determination of iron redox state in dry natural glasses: application to peralkaline rhyolites and basalts. Chem. Geol. 259:78–88.https://doi.org/10.1016/j.chemgeo.2008.08.013.

Dickenson, M.P., Hess, P.C. 1981 Redox equilibria and the structural role of iron in alumino-silicate melts. Contrib. Mineral. Petrol. 78, 352-357.

Dingwell, D. B. 1990. Effects of structural relaxation on cationic tracer diffusion in silicate melts. Chem. Geol. 82, 209–216.

Dingwell, D.1996. Volcanic Dilemma-Flow or Blow?. Science. 273. 1054-1055. 10.1126/science.273.5278.1054.

Douglas, R.W. and Isard, J.O. 1949. The action of water and of sulphur dioxide on glass surfaces. J. Soc. Glass Technol. 33, 289–335.

Edmonds, M., Woods. A.W. 2018. Exsolved volatiles in magma reservoirs. Journal of Volcanology and Geothermal Research, 368,pp 13-30. ISSN 0377-0273. https://doi.org/10.1016/j.jvolgeores.2018.10.018.

Edmonds, M., Oppenheimer, C., Pyle, D.M., Herd, R.A.2003. Rainwater and ash leachate analysis as proxies for plume chemistry at Soufriere Hills volcano, Montserrat. In: Oppenheimer, C., Pyle, D.M., Barclay, J. (Eds.), Volcanic Degassing. Geological Society, London.

Farges F., Keppler H., Flank A. M. and Lagarde P. 2009. Sulfur K-edge XANES study of S sorbed onto volcanic ashes. J. Phys.: Conf. Ser. 190, 012177.

Fegley, B. and Prinn, R. G. 1989. Estimation of the rate of volcanism on Venus from reaction rate measurements. Nature 337, 55_58.

Fisher, R. V. 1961. Proposed classification of volcaniclastic sediments and rocks. Geological Society of America Bulletin. 72 (9): 1409–1414. https://doi.org/10.1130/0016-7606(1961)72[1409:PCOVSA]2.0.CO;2.

Foerster, F., and Kubel, K. 1924. Sulfurous acid and its salts II. Decomposition of sulfites at high temperatures. Z. Anorg. Allgem. Chem. 139, 261-92.

Folch A. and Marti J. 2009. Time-dependent chamber and vent conditions during explosive caldera-forming eruptions. Earth Planet. Sci. Lett. 280, 246–253.

Frogner, P., Gislason, S.R., Oskarsson, N. 2001. Fertilizing potential of volcanic ash in ocean surface water. Geology 29 (6), 487–490.

Furukawa, T., Fox, K.E., and White, W.B. 1981. Raman spectroscopic investigation of the structure of silicate glasses. III. Raman intensities and structural units in sodium silicate glasses. The Journal of Chemical Physics, 75, 3226.

Giggenbach, W. F. 1996. Chemical composition of volcanic gases. Pages 221–256 in ''Monitoring and Mitigation of Volcano Hazards'' (R. W. Scarpa and R. I. Tilling, eds.). Springer-Verlag, Berlin.

Giggenbach, W. F., Tedesco D., Sulistiyo Y., Caprai A., Cioni R., Favara R., Fischer T. P., Hirabayashi J.-I. Korzhinsky M., Martini M., Menyailov I. and Shinohara H. 2001. Evaluation of results from the fourth and fifth iavcei field workshops on volcanic gases, Vulcano Island, Italy and Java, Indonesia. J. Volcanol. Geotherm. Res., 108, 157-172.

Giordano, D., Russell J. K. and Dingwell D. B. 2008. Viscosity of magmatic liquids: A model. Earth and Planetary Science Letters, 271. Issues 1–4, 123-134. https://doi.org/10.1016/j.epsl.2008.03.038, ISSN 0012-821X.

Gislason, S.R., Hassenkam, T., Nedel, S., Bovet, N., Eiriksdottir, E.S., Alfredsson, H.A., Hem. P., Balogh, Z.I., Dideriksen, K., Oskarsson, N., Sigfusson, B., Larsen, G., Stipp, S.L.S. 2011. Characterization of Eyjafjallajökull volcanic ash particles and a protocol for rapid risk assessment. Proc Natl Acad Sci 108:7307–7312. https ://doi. org/10.1073/pnas.10150 53108.

Gilbert, J.S., Lane, S.J. 1994. The origin of accretionary lapilli. Bull Volcanol 56, 398–411. https://doi.org/10.1007/BF00326465**.**

Gonnermann, H. M. and Manga M. 2003. Explosive volcanism may not be an inevitable consequence of magma fragmentation. Nature 426, 432–435.

Graf, H.F., Feichter, J., and Langmann, B. 1997. Volcanic sulfur emissions: Estimates of source strength and its contribution to the global sulfate distribution. Journal of Geophysical Research 102: 10727–10738.

Gu, Y., Gierke, J.S., Bluth, G.J., Rose, W.I. 1999. A laboratory study of sulfur dioxide adsorption onto fine dacitic volcanic ash. EOS, Transactions, American Geophysical Union 80, F135. AGU Fall Meeting Abstracts.

Heiken, G. 1972. Morphology and petrography of volcanic ash. 1988. Geol Soc Am Bull 83(7):1961–1988.

Heiken, G., and Wohletz, K.H. 1985. Volcanic Ash. University of California Press, Berkeley, California, 246 pp.

Hess, K. U. and Dingwell D. B. (1996) Viscosities of hydrous leucogranitic melts: A non-Arrhenian model. Am. Mineral. 81, 1297–1300.

Henley, R. W., King, P. L., Wykes, J. L., Renggli, C. J., Brink, F. J., Clark, D. A., & Troitzsch, U. 2015. Porphyry copper deposit formation by sub-volcanic sulphur dioxide flux and chemisorption. Nature Geoscience, 8(3), 210–215. https://doi.org/10.1038/ngeo2367.

Holtz, F., Behrens, H., Dingwell, D.B., Taylor, R.P. 1992. Water solubility in aluminosilicate melts of haplogranitic compositions at 2 kbar. Chemical Geology,Vol 96, Issues 3–4, 289-302,ISSN 0009-2541,https://doi.org/10.1016/0009-2541(92)90060-I.

Horwell, C.J, Baxter, P.J. 2006. The respiratory health hazards of volcanic ash: a review for volcanic risk mitigation. Bull Volcanol 69(1):1–24.

Ingraham, T.R., and Marier, P. 1971. Note on the Mechanism of the Absorption of SO_2 by Limestone, Journal of the Air Pollution Control Association, 21:6, 347-351, DOI: 10.1080/00022470.1971.10469536.

Jambon A. 1982. Tracer diffusion in granitic melts: Experimental results for Na, K, b, Cs, Ca, Sr, Ba, Ce, Eu to 1300 _C and a model of calculation. J. Geophys. Res. 87(10), 10797–10810.

James, M.R., Lane, S.J., Gilbert, J.S., 2003. Density, construction, and drag coefficient of electrostatic volcanic ash aggregates. J. Geophy. Res. 108, 2435.

Jones, M.T., Sparks, R.S.J., Vades, P.J. 2007. The climatic impact of supervolcanic ash blankets. Clim Dyn 29(6):553–564.

Johnson, M.C., Anderson, A.T., and Rutherford, M.J. 1993. Pre-eruptive volatile contents of magmas. In: Carroll MR and Holloway JR (eds.) Volatiles in Magmas. Reviews in Mineralogy30: pp. 281–330. Chantilly, VA: Mineralogical Society of America

Kress, V.C., Carmichael, I.S.E. 1988. Stoichiometry of the iron oxidation reaction in silicate melts. Amer. Mineral. 73, 1267-174.

Klug, C., and Cashman, K. V. (1996). Permeability development in vesiculating magmas: Implications for fragmentation. Bull. Volcanol. 58, 87–100.

Kueppers, U., Scheu, B., Spieler, O. and Dingwell, D.B. 2006. Fragmentation efficiency of explosive volcanic eruptions: A study of experimentally generated pyroclasts. Journal of Volcanology and Geothermal Research, Volume 153, Issues 1–2, pp 125-135. ISSN 0377-0273. https://doi.org/10.1016/j.jvolgeores.2005.08.006.

Lane, S., Gilbert, J., Hilton, M. 1993. The aerodynamic behavior of volcanic aggregates. Bulletin of Volcanology. 55. 481-488. 10.1007/BF00304591.

Langmann, B., Folch, A., Hensch, M., Matthias, V. 2012. Volcanic ash over Europe during the eruption of Eyjafjallajökull on Iceland, April–May 2010. Atmospheric Environment,Volume 48,Pages 1-8,ISSN 1352-2310,https://doi.org/10.1016/j.atmosenv.2011.03.054.

Le Losq, C., Neuville, D. R., Florian, P., Henderson, G. S., Massiot, D. 2014. The role of Al3+ on rheology and structural changes in sodium silicate and aluminosilicate glasses and melts. Geochimica et Cosmochimica Acta, 126, 495–517. https://doi.org/10.1016/j.gca.2013.11.010.

Le Losq, C., Neuville, D.R. 2017. Molecular structure, configurational entropy and viscosity of silicate melts: Link through the Adam and Gibbs theory of viscous flow. Journal of Non-Crystalline Solids, 463, 175–188. https://doi.org/10.1016/j.jnoncrysol.2017.02.010.

Legrand, A.P., 1998. The Surface Properties of Silicas. John Wiley & Sons, Chichester, 494pp.

Magaritz, M. and Hofmann A. W. 1978. Diffusion of Sr, Ba and Na in obsidian. Geochim. Cosmochim. Acta 42, 595–605

Mandeville C. W., Carey S. and Sigurdsson H. 1996. Magma mixing, fractional crystallization and volatile degassing during the 1883 eruption of Krakatau volcano, Indonesia. J. Volcanol. Geotherm. Res. 74, 243–274.

Mastin, L.G. 2007. A user-friendly one-dimensional model for wet volcanic plumes. Geochem. Geophys. Geosyst. 8. http://dx.doi.org/10.1029/2006GC001455.

Maters, E. C., Delmelle, P., Rossi, M. J., Ayris, P. M., & Bernard, A. 2016. Controls on volcanic ash surface reactivity investigated with probe gases. Earth and Planetary Science Letters, 450, 254–262. https://doi.org/10.1016/j.epsl.2016.06.044.

Maters, E.C., Delmelle, P., Rossi, M.J., Ayris, P.M. 2017b. Reactive uptake of sulfur dioxide and ozone on volcanic glass and ash at ambient temperature. J Geophys Res Atmos 122:10077–10088.

Mayumi, M., Michihiko, N. 2014. A nanolite record of eruption style transition. Geology; 42 (7): 611–614. doi: https://doi.org/10.1130/G35553.1.

McAmish, L.H., Johnston, F.J. 1976. Sulfur exchange and decomposition kinetics in solid Na2S2O3, Journal of Inorganic and Nuclear Chemistry,Volume 38, Issue 3, pages 537-540. https://doi.org/10.1016/0022-1902(76)80299-0.

McDonald, R.S. 1958. Surface Functionality of Amorphous Silica by Infrared Spectroscopy. J. Phys. Chem. 1958, 62, 10, 1168-1178. https://doi.org/10.1021/j150568a004.

McMillan, P.,F., Piriou, B. 1982. The structures and vibrational spectra of crystals and glasses in the silica-alumina system. Journal of Non-Crystalline Solids. 53, 3,Pags 279-298. ISSN 0022-3093. https://doi.org/10.1016/0022-3093(82)90086-2.

McMillan, P.F., Piriou, B. 1983. Raman spectroscopic studies of silicate and related glass structure: a review. In: Bulletin de Minéralogie, 106, 1-2. Silicates liquides. https://doi.org/10.3406/bulmi.1983.7668.

McMillan, P.F. 1984. A Raman spectroscopic study of glasses in the system CaO-MgO-SiO2. American Mineralogist, 69, 645–659.

McMillan, P.F. 1988. Vibrational Studies of Amorphous SiO2. In: Devine R.A.B. (eds) The Physics and Technology of Amorphous SiO2. Springer, Boston, MA.

Molina, M.J. and Rowland, F.S. 1974. Stratospheric sink for chlorofluoromethanes: chlorine atomic-catalysed destruction of ozone. Nature 249, 811.

Morrissey, M., Zimanowski,. B., Wohletz, K., Buettner, R. 2000. Phreatomagmatic fragmentation. In: Sigurdsson H, Houghton B, McNutt S, Rymer H, Stix J (eds) Encyclopedia of volcanoes. Academic, San Diego, pp 431–445.

Mueller, S. B., Kueppers, U., Ayris, P. M., Jacob, M. & Dingwell, D. B. 2016. Experimental volcanic ash aggregation: Internal structuring of accretionary lapilli and the role of liquid bonding. Earth Planet. Sci. Lett. 433, 232–240. https://doi.org/10.1016/j.epsl.2015.11.007.

Mueller, S.B., Ayris, P.M., Wadsworth, F.B., Kueppers, U., Casas, A.S., Delmelle, P., Taddeucci, J., Jacob, M., Dingwell, D.B. 2017. Ash aggregation enhanced by deposition and redistribution of salt on the surface of volcanic ash in eruption plumes. Scientific Reports 7:45762. https://doi.org/10.1038/srep45762.

Mujin, M., Nakamura, M., Miyake, A. 2017. Eruption style and crystal size distributions: crystallization of groundmass nanolites in the 2011 Shinmoedake eruption. Am. Mineral. 102:2367–2380. https://doi.org/10.1186/s12986.

Mungall, J. E., Dingwell D. B. and Chaussidon M. 1999. Chemical diffusivities of 18 trace elements in granitoid melts. Geochim. Cosmochim. Acta 17, 2599-2610, 53.

Mysen, B.O., Seifert, F., and Virgo, D. 1980. Structure and redox equilibria of iron-bearing silicate melts. Amer. Mineral. 65, 867-884.

Mysen, B. O., Virgo, D., and Seifert, F. A. 1982. The structure of silicate melts: Implications for chemical and physical properties of natural magma, Rev. Geophys., 20(3), 353– 383, doi:10.1029/RG020i003p00353.

Mysen, B.O., Virgo D., Neumann E.-R., and Seifert, F. 1985. Redox equilibria and the structural states of ferric and ferrous iron in melts in the system CaO-MgO-A1203-SiO2-Fe-O: Relationships between redox equilibria, melt structure and liquidus phase equilibria. Amer. Mineral. 70, 317-331.

Mysen, B. O., and Richet, P. 2005. Silicate glasses and melts: Properties and structure. Boston: Elsevier, Amsterdam.

Mysen, B.O., and Toplis, M.J. 2007. Structural behavior of Al3+ in peralkaline, metaluminous, and peraluminous silicate melts and glasses at ambient pressure. American Mineralogist, 92, 933–946. https://doi.org/10.2138/am.2007.2334**.**

Naughton, J.J., Lewis, V.A., Hammond, D., Nishimoto D. 1974. The chemistry of sublimates collected directly from lava fountains at Kilauea Volcano, Hawaii. Geochimica et Cosmochimica Acta. 38. 1679-1690. https://doi.org/10.1016/0016-7037(74)90185-9.

Nehring, N.L., Johnston, D.A., 1981. Use of ash leachates to monitor gas emissions. In: Lipman, P.W., Mullineaux, D.R. (Eds.), The 1980 Eruptions of Mount St. Helens, Washington, USGS Professional Paper, pp. 251–254.

Neuville, D.R., and Mysen, B.O. 1996. Role of aluminium in the silicate network: In situ, high-temperature study of glasses and melts on the join SiO2-NaAlO2. Geochimica et Cosmochimica Acta, 60(10), 1727–1737. https://doi.org/10.1016/0016-7037(96)00049-X.

Neuville, D.R., de Ligny, D., and Henderson, G.S. 2014. Advances in Raman spectroscopy applied to earth and material sciences. Reviews in Mineralogy, 78, 509–541. https://doi.org/10.2138/rmg.2013.78.13.

Ninkovich, D., Sparks, R.S.J. and Ledbetter, M.J. 1978. The exceptional magnitude and intensity of the Toba eruption, Sumatra: an example of the use of deep-sea tephra as a geological tool. Bull. Volcanol. 41, 286–298. https://doi.org/10.1007/BF02597228.

Oppenheimer, C., Bani, P., Calkins, J.A., Burton, M.R., Sawyer, G. 2006. Rapid FTIR sensing of volcanic gases released by Strombolian explosions at Yasur volcano, Vanuatu. Applied Physics B. 85. 453-460. http://dx.doi.org/10.1007/s00340-006-2353-4.

Oppenheimer, C., Fischer, T.P., Scaillet, B., 2014. Volcanic degassing: processes and impact. In: Holland, H., Turekian, K. (Eds.), Treatise on geochemistry, second ed, vol. 4. the crust. Elsevier, Amsterdam, pp. 111e179. http://dx.doi.org/10.1016/B978-0-08-095975-7.00304-1.

Óskarsson, N. 1980. The interaction between volcanic gases and soild tephra. J. Volcanol. Geotherm. Res. 8, 251–266.

Pacchioni, G., Clotet, A., & Ricart, J. M. 1994. A theoretical study of the adsorption and reaction of SO2 at surface and step sites of the MgO(100) surface. Surface Science, 315(3), 337–350. https://doi.org/10.1016/0039-6028(94)90137-6.

Pallister, J.P., Major, J.J., Pierson, T.C., Hoblitt, R.P., Lowenstern, J.B., Eichelberger, J.C., Lara, L., Moreno, H., Muñoz, J., Castro, J.M., Iroumé, A., Andreoli, A., Jones, J., Swanson, F., Crisafulli, C. 2010a. Interdisciplinary studies of eruption at Chaitén Volcano, Chile. Eos, Trans Am Geophys Union 91:381–382. https://doi.org/10.1029/2010EO420001.

Papale, P., Neri, A., and Macedonio, G. 1998. The role of magma composition and water content in explosive eruptions I. Conduit ascent dynamics. J. Volcanol. Geotherm. Res. 87, 75–93. https://doi.org/10.1016/S0377-0273(98)00101-2.

Renggli, C.J., King, P.L., Henley, R.W., Norman, M.D. 2017. Volcanic gas composition, metal dispersion and deposition during explosive volcanic eruptions on the Moon. Geochimica et Cosmochimica Acta. Vol. 206, 296-311, https://doi.org/10.1016/j.gca.2017.03.012.

Renggli, C. J., & King, P. L. 2018. SO2 gas reactions with silicate glasses. Reviews in Mineralogy and Geochemistry, 84(1), 229–255. https://doi.org/10.2138/rmg.2018.84.6.

Renggli, C.J., Palm, A.B., King, P.L., Guagliardo, P. 2019a. Implications of reactions between SO2 and basaltic glasses for the mineralogy of planetary crusts. JGR Planets 124. https://doi.org/10.1029/2019JE006045.

Renggli, C.J., King, P.L., Henley, R.W., Guagliardo, P., McMorrow, L., Middleton, J.P. and Turner, M. 2019b. An experimental study of SO2 reactions with silicate glasses and supercooled melts in the system anorthite–diopside–albite at high temperature. Contributions to Mineralogy and Petrology, 174(1), p.3. https://doi.org/10.1007/s00410-018-1538-2.

Robock, A. 2000. Volcanic eruptions and climate. Rev Geophys 38:191–219. http://dx.doi:10.1029/1998RG000054.

Robock A., Ammann C. M., Oman L., Shindell D., Levis S. and Stenchikov G. 2009. Did the Toba volcanic eruption of _74 ka B.P. produce widespread glaciation? J. Geophys. Res. 114. http://dx.doi.org/10.1029/2008JD011652.

Rogers, N., Hawkesworth, C. 2000. Composition of magmas. In: Sigurdsson H, Houghton B, McNutt S, Rymer H, Stix J (eds) Encyclopedia of Volcanoes. Academic Press, London, pp 115–131.

Rose, W.I., Bonis, S., Stoiber, R.E., Keller, M., Bickford. 1973. Studies of volcanic ash from two recent Central American eruptions. Bull Volcano, 37: 338. https://doi.org/10.1007/BF02597633.

Rose, W.I. 1977. Scavenging of volcanic aerosol by ash: Atmospheric and volcanologic implications. Geology 5, 621–625. https://doi.org/10.1130/0091-7613(1977)5<621:SOVABA>2.0.CO;2.

Rose, W.I., Durant, A.J., 2009. Fine ash content of explosive eruptions. J Volcanol Geotherm Res 186(1–2):32–39. https://doi.org/10.1016/j.jvolgeores.2009.01.010.

Rossano, S., and Mysen, B.O. 2012. Raman spectroscopy of silicate glasses and melts in geological systems. EMU Notes in Mineralogy, 12, xvii + 504 pp., Chapter 9. https://doi.org/10.1180/EMU-notes.12.9.

Saubin, E., Tuffen H., Gurioli L., Owen J., Castro J. M., Berlo K., McGowan E. M., Schipper C. I. and Wehbe K. 2016. Conduit dynamics in transitional rhyolitic activity recorded by tuffisite vein textures from the 2008–2009 Chaitén eruption. Front. Earth Sci. 4, 59.

Sawyer, G.M., Oppenheimer, C., Tsanev, V.I., Yirgu, G. 2008. Magmatic degassing at Erta 'Ale volcano, Ethiopia. Journal of Volcanology and Geothermal Research. Volume 178, Issue 4. Pages 837-846. https://doi.org/10.1016/j.jvolgeores.2008.09.017.

Self, S. 2006. The effects and consequences of very large explosive volcanic eruptions. Philosophical transactions. Series A, Mathematical, physical, and engineering sciences. 364. https://doi.org/2073-97.10.1098/rsta.2006.1814.

Shapiro, L. and Brannock, W.W. 1956. Rapid analysis of silicate rocks. U.S. Geol. Surv. Bull. 1036C: pp. 32.34.

Sharp, T.G., Stevenson, R.J., and Dingwell, D.B. 1996. Microlites and "nanolites" in rhyolitic glass: Microstructural and chemical characterization: Bulletin of Volcanology, v. 57, p. 631–640. https://doi.org/10.1007/s004450050116.

Schipper C. I., Castro J. M., Tuffen H., Wadsworth F. B., Chappell, D., Pantoja A. E., impson M. P. and Le Ru E. C. 2015. Cristobalite in the 2011–2012 Cordo´n Caulle eruption (Chile). Bull. Volcanol. 77(34). https://doi.org/10.1007/s00445-015-0925-z.

Schlinger, C.M., Smith, R.M., Veblen, D.R. 1986. Geologic origin of magmatic volcanic glasses in the KBS tuff. Geology, 14, 959-962. https://doi.org/10.1029/JB093iB08p09137.

Schlinger, C.M., Griscom, D., Papaefthymiou, G.C., Veblen, D.R. 1988a. The nature of magnetic single domains in volcanic glasses of the KBS Tuff. J Geophys Res 93 :9137–9156.

Schlinger, C.M., Rosenbaum, J.G., Veblen, D.R. 1988b. Fe-oxide microcristals in welded tuff from southern Nevada: Origin of remanence carriers by precipitation in volcanic glass. Geolgy, 16, 556-519. https://doi.org/10.1130/0091-7613(1988)016<0556:FOMIWT>2.3.CO;2.

Schmalzried,H. 1984b. Oxide solid solutions and its internal reduction reactions. Ber. Bunsenges. Phys. Chem. 88, 1186-119l. https://doi.org/10.1002/bbpc.198400046.

Simons, G. & Garman, A. and Boni, A. 1987. The kinetic rate of SO2 sorption by CaO. AIChE Journal. 33. 211 - 217. 10.1002/aic.690330206.

Sorem, R.K., 1982. Volcanic ash clusters: tephra rafts and scavengers. J. Volcanol. Geotherm. Res. 13, 63–71.

Sparks, R.S.J., Wilson, L. 1976. A model for the formation of ignimbrite by the gravitational column collapse. J. Geol. Soc. London. 132:441-451. https://doi.org/10.1144/gsjgs.132.4.0441.

Sparks, R.S.J. 1986. The dimensions and dynamics of volcanic eruption columns. Bull. Volcanol. 48, 3–15. https://doi.org/10.1007/BF01073509.

Sparks, R. S. J., M. I. Bursik, S. N. Carey, J. S. Gilbert, L. S. Glaze, H. Sigurdsson, and A. W. Woods. 1997. Volcanic Plumes. 574 pp., John Wiley,New York.

Stoiber, R.E., Williams, S.N., Malinconico Jr., L.L., Johnston, D.A., Casadevall, T.J., 1981. Mt. St. Helens: evidence of increased magmatic gas component. Journal of Volcanology and Geothermal Research 11, 203–212. https://doi.org/10.1016/0377-0273(81)90023-8.

Stowe, L. L., Carey, R.M., Pellegrino, P.P. 1992. Monitoring the Mount Pinatubo aerosol layer with NOAA/11 AVHRR data. Geophys. Res. Lett., 19, 159-162. https://doi.org/10.1029/91GL02958.

Suzuki, Y. J. and Koyaguchi T. 2012. 3-D numerical simulations of eruption column collapse: effects of vent size on pressurebalanced jet/plumes. J. Volcanol. Geoth. Res. 221, 1–13.

Swanson, F.J., Crisafulli, C., Jones, J.A., Lara, A. 2010. Chaitén town (Chile) inundated by a complex multi-peaked volcanic flood in May 2008. Abstract V34B-06 presented at 2010 Fall Meeting, Am Geophys Union, San Francisco, 13–17 Dec.

Symonds, R. B., Rose W. I., Bluth G. J. S. and Gerlach T. M. 1994. Volcanic gas studies: methods, results and applications. In Volatiles in Magmas, Rev. Mineral. (eds. M. R. Carroll and J. R. Hollaway). Mineralogical Society of America, pp. 1–66.

Szekely, J., Evans, J.W., Sohn, H.Y. 1976. Gas–solid reactions. Academic,New York.

Taylor P. S. and Stoiber R. E. 1973. Soluble material on ash from active Central American volcanoes. Geol. Soc. Am. Bull. 84(3), 1031–1042. https://doi.org/10.1130/0016-7606(1973)84<1031:SMOAFA>2.0.CO;2.

Textor, C., Graf, H.-F., Timmreck, C., Robock, A. 2004. Emissions from volcanoes. Advances in Global Change Research. 18. https://doi.org/10.1007/978-1-4020-2167-1_7.

Tomita, K., Kanai, T., Kobayashi, T., Oba, N. 1985. Accretionary lapilli formed by the eruption of Sakurajima Volcano. J. Jpn. Ass. Min. Pet. Econom. Geol. 80, 49-54. https://doi.org/10.2465/ganko1941.80.49.

Tuffen, H., Dingwell D. B. and Pinkerton H. 2003. Repeated fracture and healing of silicic magma generate flow banding and earthquakes? Geology 31, 1089–1092.

Tuffen, H. and Dingwell D. (2005) Fault textures in volcanic conduits: Evidence for seismic trigger mechanisms during silicic eruptions. Bull. Volcanol. 67, 370–387. https://doi.org/10.1007/s00445-004-0383-5.

Tuffen, H., and Castro, J.M. 2009. The emplacement of an obsidian dyke through thin ice: Hrafntinnuhryggur, Krafla Iceland. J. Volcanol. Geotherm. Res., 185(4), 352–366. http://doi.org/10.1016/j.jvolgeores.2008.10.021.

Varekamp, J.C., Luhr, J.F., and Prestegaard, K.L. 1984. The 1982 eruptions of El Chichón volcano (Chiapas, Mexico): character of the eruptions, ash-fall deposits and gas phase. J. Volcanol. Geotherm. Res. 23, 39–68. https://doi.org/10.1016/0377-0273(84)90056-8.

Van Houte, G. and Delmon, B. 1978. Kinetics of the reaction of calcium sulfite with SO2. Bulletin des Sociétés Chimiques Belges. 87. 241 - 249. https://doi.org/10.1002/bscb.19780870401.

Wallace, P. 2003. From mantle to atmosphere: magma degassing, explosive eruptions, and volcanic volatile budgets. Developments in Volcanology. 5. 105-127. https://doi.org/10.1016/S1871-644X(03)80026-8.

Wadsworth, F. B., Vasseur J., Von Aulock F. W., Hess K. U., Scheu B., Lavalle´e Y. and Dingwell D. B. 2014. Nonisothermal viscous sintering of volcanic ash. J. Geophys. Res. Solid Earth 119, 8792–8804. https://doi.org/10.1002/2014JB011453.

Wadsworth, F. B., Vasseur J., Llewellin E. W., Schauroth J., Dobson K. J., Scheu B. and Dingwell D. B. 2016. Sintering of viscous droplets under surface tension. Porc. R. Soc. A.. https://doi.org/10.1098/rspa.2015.0780.

Wadsworth, F.B., Vasseur, J., Llewellin, E.W., Genareau, K., Cimarelli C. and Dingwell D. B. 2017a. Size limits for rounding of volcanic ash particles heted by lightning. J. Geophys. Res. Solid Earth 122. https://doi.org/10.1002/2016JB013864.

Wadsworth, F.B., Vasseur, J., Llewellin, E. W., Cimarelli, C. and Dingwell D. B. 2017b. Sintering of polydisperse viscous droplets. Phys. Rev. E 95. https://doi.org/10.1103/Phys-RevE.95.033114.

Wadsworth, F., Witcher, T., Vossen, C, Hess, K.-U., Unwin, H., Scheu, B., Castro, J. and Dingwell, D. 2018. Combined effusive-explosive silicic volcanism straddles the multiphase viscous-to-brittle transition. Nat Commun 9, 4696. https://doi.org/10.1038/s41467-018-07187-w.

Watson, E. B. 1981. Diffusion in magmas at depth in the earth: The effects of pressure and dissolved H2O. Earth Planet. Sci. Lett. 52, 291–301.

Wieczorek-Ciurowa, K. 1992. The thermal behaviour of compounds in the Ca–S–O system. J. Therm. Anal. 38, 523–530. https://doi.org/10.1007/BF01915517.

Wilson, L. 1980. Relationship between pressure, volatile content and ejecta velocity in three types of volcanic explosion. J. Volcanol. Geotherm. Res., 8; 297-313. https://doi.org/10.1016/0377-0273(80)90110-9.

Wilson, L. and Head, J. W. 1981. Ascent and eruption of basaltic magma on the Earth and Moon. J. Geophys. Res. Solid Earth 86, 2971–3001. https://doi.org/10.1029/JB086iB04p02971.

Witham, C.S., Oppenheimer, C., Horwell, C.J. 2005. Volcanic ash-leachates: a review and recommendations for sampling methods. Journal of Volcanology and Geothermal Research,141, Issues 3–4, 299-326. https://doi.org/10.1016/j.jvolgeores.2004.11.010.

White, S. 2009. Laser Raman spectroscopy as a technique for identification of seafloor hydrothermal and cold minerals. Chemical Geology. 259. 240-252. https://doi.org/10.1016/j.chemgeo.2008.11.008.

Zhang, Y., Ni, H., and Chen, Y. 2010. Diffusion Data in Silicate Melts. Rev. Mineral. Geochem. 72, 311–408. https://doi.org/10.2138/rmg.2010.72.8.

Zhang, X., Yue, Y. and Wu, H. 2013. Effects of cation field strength on structure and properties of boroaluminosilicate glasses. Materials Research Innovations. 17. 212-217. https://doi.org/10.1179/1433075X12Y.0000000051.

Zellmer, G., Sakamoto, N., Hwang, S.-L., Matsuda, N., Iizuka, Y., Moebis, A., Yurimoto, H. 2016. Inferring the Effects of Compositional Boundary Layers on Crystal Nucleation, Growth Textures, and Mineral Chemistry in Natural Volcanic Tephras through Submicron-Resolution Imaging. Frontiers in Earth Science. https://doi.org/4.10.3389/feart.2016.00088.

Zimanowski, B., Wohletz K., Dellino P. and Büttner R. 2003. The volcanic ash problem. J. Volcanol. Geotherm. Res. 122(1–2),1–5.